Aerogel and Fibre Optics

Grogan, Michael

Award date:
2010

Awarding institution:
University of Bath

AEROGEL AND FIBRE OPTICS

Michael David William Grogan

A thesis submitted for the degree of Doctor of Philosophy

University of Bath

Department of Physics

November 2010

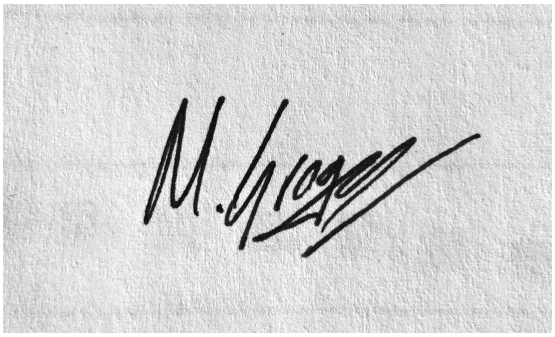

for my family

Abstract

This thesis presents the integration of aerogel and fibre optic technologies. We have developed several methods for fabricating aerogels that can transmit laser beams with low distortion and have a low attenuation of 0.07 dB/cm at 1310 nm. The refractive index of our aerogel can be varied between 1.025–1.05 by varying the density between 0.1–0.22 g/cm^3. These aerogels can be slightly birefringent, and we demonstrate that a 1 cm thick aerogel could be used similarly to a Babinet compensator. New methods have allowed us to controllably alter the optical properties of aerogel by the inclusion of dopants. Plasmonic aerogel created using our technique offers the unique opportunity to study unclustered and well-dispersed gold nanoparticles in an air-like environment, with applications in spectroscopic sensing and nonlinear optics. The simple and cheap method we have developed for doping aerogel with lanthanide ions could have a significant impact in the fabrication of glasses for laser materials.

We have created techniques for making aerogel in or around fibre optics so that we can use it to control the flow of light. Our method of filling a hollow-core fibre has enabled transmission through an unprecedented length of aerogel. The aerogel-filled fibre operates in a single mode at 1550 nm, with attenuation of 0.2 dB/cm. Also, we have encapsulated a range of different sized tapered fibres in aerogel with low attenuation. Tapered optical fibres are sensitive to their immediate environment because the optical field propagates right at the boundary between glass and air. Our lowest attenuation, 0.03 dB/mm at 1310 nm for a 750 nm diameter taper, represents an order of magnitude improvement over using other materials as the encapsulant. We have demonstrated the uses of tapered fibres packaged in aerogel as fused couplers, evanescent gas sensors, and in nonlinear light sources.

Contents

List of acronyms

APD Ambient Pressure Drying

BET/BJH Brunauer-Emmett-Teller/Barrett-Joyner-Halenda

BPR Back-Pressure Regulator

CCD Charge-Coupled Device

CQED Cavity Quantum ElectroDynamics

CS Condensed Silica

CVD/MCVD Chemical Vapour Deposition/Modified Chemical Vapour Deposition

CW Continuous-Wave

DCCA Drying Control Chemical Additives

DOS (photonic) Density Of States

ECDL External Cavity Diode Laser

EIT Electromagnetically-Induced Transparency

EMA Effective Medium Approximation

EPSRC Engineering and Physical Sciences Research Council?

FSM Fundamental Space-filling Mode

FEM Finite Element Method

FWHM Full-Width at Half-Maximum

GNP/NP Gold NanoParticle/NanoParticle

HC-PCF Hollow-Core Photonic Crystal Fibre

InGaAs Indium-Gallium-Arsenide

LT/HT aerogel Low-Temperature/High-Temperature aerogel

NA Numerical Aperture

NMR Nuclear Magnetic Resonance

OD Outer Diameter

OPA Optical Parameteric Amplifier

OSA Opitcal Spectrum Analyser

PCF Photonic Crystal Fibre

PMC Photonic MicroCell

PFD Process-Flow Diagram

RSCE Rapid SuperCritical Extraction

SA Saturated Absorption

SANS/SAXS Small Angle Neutron/X-ray Scattering

SCD Supercritical Drying

SEM Scanning Electron Microscopy

SERS Surface-Enhanced Raman Scattering

SMF Single Mode Fibre

TEM Transmission Electron Microscopy

TIR Total Internal Reflection

Chemical abbreviations

HOAc Acetic acid

HMDS/HMDZ Hexamethyldisilazane

HMDSO Hexamethyldisiloxane

MTMS Methyltrimethoxylsilane

PTFE Polytetrafluoroethylene (Teflon)

PMMA Polymethylmethacrylate

R An alkyl

ROH Alcohol (if R is CH_3 then this is methanol)

TEOS Tetraethoxysilane, *alternatively* Tetraethyl orthosilicate

TMCS Trimethoxycholorosilane

TMOS Tetramethoxysilane, *alternatively* Tetramethyl orthosilicate

TMS Trimethylsilyl

OAc Acetate ion

Acknowledgements

For their help and support, I thank wholeheartedly:

The people who have helped me prepare this thesis; particularly Tim and Viktoriya, who have patiently suggested better ways to communicate ideas, corrected my spelling mistakes, and put up with my frequent misuse of commas.

Sergio, for starting me on the right foot. The aerogel team at Bath; Limin, Mat, William, Richard, and all the other members who have come and gone. Paul and Wendy, for their advice and support. Other colleagues and friends at the University of Bath.

Stefan, for suggesting we should dope aerogel with gold nanoparticles. Susannah, for carrying out the modelling in chapter 6. Katie, for making and measuring almost all of the ytterbium-doped aerogels under my guidance: I'm so proud of what we achieved in such a short time.

Fernando, for BET measurements, and Ursula, for SEM and TEM images on our aerogel and gold nanoparticles.

Limin and Mat again, for providing me with the materials I needed to write chapter 7.

Brian, for providing the hollow-core fibre used in chapter 8. David Bird, for discussions about using the Bath PCF code to model fibres.

Fetah Benabid's group, especially Natalie, for providing the motivation for work in appendix A and for making anything that involved acetylene or sputter coating.

Viktoriya, with love.

And finally, from start to finish, Tim.

Publications list

1. M D W Grogan, S G Leon-Saval, R Williams, R England and T A Birks. "Optical Fibre with an Aerogel-Filled Core." In *Conference on Lasers and Electro-Optics/Qauntum Electronics and Laser Science Conference,* page CMW3. Optical Society of America (2009).

2. L M Xiao, M D W Grogan, S G Leon-Saval, R Williams, R England and T A Birks. "Tapered Fibres Embedded in Silica Aerogel." In *Conference on Lasers and Electro-Optics/Qauntum Electronics and Laser Science Conference,* page CFH6. Optical Society of America (2009).

3. L M Xiao, M D W Grogan, S G Leon-Saval, R Williams, R England, W J Wadsworth and T A Birks. "Tapered fibers embedded in silica aerogel." *Opt. Lett.,* **34**(18): pp. 2724-2726 (2009).

4. T A Birks, M D W Grogan, Z Chen, L M Xiao, S G Leon-Saval, C Xiong and R England "Modifying photonic crystal fibres." *(Invited paper)* In *14^{th} Opto-Electronics and Communications Conference* page FM3(2009).

5. N V Wheeler, M D W Grogan, P S Light, F Couny, T A Birks and F Benabid. "Large-core acetylene-filled photonic microcells made by tapering a hollow-core photonic crystal fiber." *Opt. Lett.,* **35**(11): pp. 1875-1877 (2010).

6. L M Xiao, M D W Grogan, R England, W J Wadsworth and T A Birks. "Tapered fibre-aerogel devices and applications." *(Invited paper)* presented at *Asia-Pacific Microwave Photonics Conference,* page MB2-4 (2010).

7. L M Xiao, M D W Grogan, R England, W J Wadsworth and T A

Birks. "Aerogel Package for Fused Fibre Couplers." In *Conference on Lasers and Electro-Optics/Qauntum Electronics and Laser Science Conference,* page ATuB6. Optical Society of America (2010).

8. N V Wheeler, M D W Grogan P S Light, F Couny, T A Birks and F Benabid. "Large Core Acetylene-Filled Photonic Microcells Made by Tapering the Hollow-Core Fiber." In *Conference on Lasers and Electro-Optics/Qauntum Electronics and Laser Science Conference,* page CTuS5. Optical Society of America (2010).

9. M D Rollings, M D W Grogan, L M Xiao, R England, T A Birks and W J Wadsworth. "Supercontinuum Generation in Tapered Fibres Embedded in Silica Aerogel." In *Conference on Lasers and Electro-Optics/Qauntum Electronics and Laser Science Conference,* page JTuD59. Optical Society of America (2010).

10. N V Wheeler, M D W Grogan, T D Bradley, F Couny, T A Birks and F Benabid. "Ultra-High Reflectivity Hollow-Core PCF Microcell using a Tapered Micro-Mirror." In *Conference on Lasers and Electro-Optics/Qauntum Electronics and Laser Science Conference,* page CThB3. Optical Society of America (2010).

11. L M Xiao, M D W Grogan, R England, W J Wadsworth and T A Birks. "Gas sensing with a sub-micron tapered fibre embedded in hydrophobic aerogel." In *Conference on Lasers and Electro-Optics/Qauntum Electronics and Laser Science Conference,* page JThB6. Optical Society of America (2010).

12. M D W Grogan, M D Rollings, L M Xiao, W J Wadsworth, R England, S A Maier and T A Birks . "Plasmonic Aerogel Doped with Gold Nanoparticles." In *Conference on Lasers and Electro-Optics/Qauntum Electronics and Laser Science Conference,* page JThE21. Optical Society of America (2010).

13. T A Birks, M D W Grogan, L M Xiao, M D Rollings, R England, W J Wadsworth. "Silica Aerogel in Optical Fibre Devices." *(Invited paper)*

presented at *the International Conference on Transparent Optical Networks,* page We.A2.4 (2010).

14. C Edwardson, M D W Grogan, T A Birks and P G Coleman. "Positron and positronium studies of silica aerogel." Presented at *the International Workshop on Slow Positron Beam Techniques* (2010).

15. N V Wheeler, M D W Grogan, P S Light, F Couny, T A Birks and F Benabid. "Developments in the application and fabrication of photonic microcells." Presented at *Photon 10.* Institute of Physics (2010).

16. M D W Grogan, S G Leon-Saval, R England, T A Birks. "Silica aerogel core waveguide." *Opt. Express,* **18**(21): pp. 22497-502 (2010).

17. M D W Grogan, S G Leon-Saval, R England and T A Birks. "Optical Waveguide with an Aerogel Core." To be presented at *MRS Fall meeting* (2010).

18. M D W Grogan, S C Heck, M D Rollings, L M Xiao, R England, W J Wadsworth, S A Maier and T A Birks. "Optical Quality Plasmonic Aerogel with Gold Nanoparticles." To be presented at *MRS Fall meeting* (2010).

19. L M Xiao, M D Rollings, M D W Grogan, R England, W J Wadsworth and T A Birks. "Optical Fibre Devices Packaged in Silica Aerogel." To be presented at *MRS Fall meeting* (2010).

20. M D W Grogan, S C Heck, K M Hood, S A Maier and T A Birks. "Structure of aerogel and the breakdown of the effective medium approximation." Submitted to *Opt. Lett.,* October 2010.

21. N V Wheeler, M D W Grogan, T D Bradley, F Couny, T A Birks and F Benabid "Multi-pass hollow core-PCF microcell using a tapered micromirror." Submitted to *J. Lightwave Technol.,* November 2010.

22. L M Xiao, M D W Grogan, W J Wadsworth, R England, T A Birks. "Stable Low-Loss Optical Nanofibres Embedded in Hydrophobic Aerogel." Submitted to *Opt. Express,* November 2010.

23. W J Wadsworth, M D W Grogan, L M Xiao, M D Rollings, R England and T A Birks. "Aerogel-enhanced tapers and fibres." *(Invited paper)* to be presented at *IEEE Winter Topicals Meeting* (2011).

24. M Dowson, M D W Grogan, T A Birks, D Harrison and S Craig. "Streamlined Life Cycle Assessment of Silica Aerogel made by Supercritical Drying." Submitted to *International Conference on Applied Energy* (2011).

25. M D W Grogan, S C Heck, L M Xiao, R England, S A Maier and T A Birks are preparing a manuscript called "Control of nanoparticle aggregation in aerogel hosts," to be submitted to *J. Non-Cryst. Solids.*

26. M D W Grogan and T A Birks are preparing a manuscript called "Low-refractive index, naturally birefringent aerogel," to be submitted to *J. Opt. Soc. Am. A.*

Chapter 1

Introduction

Silica aerogels are a unique type of transparent "solid" material with an extremely low refractive index, closer to that of gases than liquids or solids. This is due to their internal structure: a nanometre-scale open network of silica glass textured like a sponge, with air filling the pores. In fact, the volume of air in our aerogels often exceeds 95%, so perhaps they would be better described as a rigid rather than a solid!

A material with such a low refractive index has interesting uses in waveguides. As such, aerogel was chosen for our study to enhance fibre optics.

Optical fibres are ubiquitous in the telecommunications industry because they can efficiently carry light over many kilometres. However, the light is confined deep inside a region of solid silica glass, making it inaccessible for many other applications. Post-processing fibres to make them much thinner can release some of the light, but these fragile "tapers" need protection from dust and water in the surrounding environment. Due to the low refractive index and material compatibility, aerogels are ideal for providing this protection. Completely encapsulating the tapered fibre in the low refractive index aerogel does not significantly disturb the light, but the aerogel provides a mechanical shield from contaminants that would otherwise do so.

Unlike other methods of protecting tapered fibres, encapsulation in aerogel provides more than just a shield.

The open nature of the aerogel network allows gas to flow through the material

and into the vicinity of a tapered fibre. Here, it can interact with light in the evanescent field around the tapered fibre. Since many gases have distinct spectral signatures, optical detection methods can then be used for sensing. Hydrophobic aerogel could extend this sensing functionality to gases dissolved in water.

Aerogel could also hold dopants, which have interesting optical properties, in the evanescent field of a tapered fibre. For example, aerogel doped with well-dispersed nanoparticles could have applications in sensing, nonlinear optics, and (with co-dopants such as elements from the lanthanide series or laser dyes) plasmonic enhanced gain. The gases and dopants can interact with each other in the evanescent field. This could extend the range of detectable gases.

The evanescent field around a tapered fibre is weak, so we were motivated to use aerogel as the core of a waveguide. Again, we can find a solution from fibre optics: this time using special hollow-core fibres with a microstructured cladding. Unlike in the encapsulated tapered fibre, filling the core of a hollow optical fibre will strongly alter the waveguide properties. This is because, for some wavelengths, the effective index of the microstructured cladding is even lower than the refractive index of the aerogel. Thus, we have made an aerogel waveguide that guides light by total internal reflection, which is ideal for studying intensity dependent interactions between light and aerogel.

Overview

This overview is a guide to the rest of this thesis. It also separates my contributions from those of my collaborators. After this chapter, I adopt the more elegant use of the first person plural.

Chapters 2 and 3 provide background material about aerogel and fibre optics respectively. The aerogel chapter is relatively exhaustive, and the sections on sol-gel chemistry, supercritical drying, and the optical properties of aerogel particularly lay out the foundations for all of my later developments. The chapter on fibres, on the other hand, is a précis of a substantial field. The key points are about the properties of fibre tapers, the difference between step-index and microstructured fibres, and the methods for making each of the above.

Chapter 4 examines the work of others on combining aerogel and fibre optics. Most of this literature was published prior to the start of my project.

Chapter 5 is a full discussion of the facility I designed and built for making aerogel, and the properties of the aerogel produced here. Limin Xiao contributed the method for making low-temperature hydrophobic aerogel with HMDS, and Tim Birks derived the formulae for describing birefringent aerogel. Although the motivation for developing an aerogel facility was for post-processing fibres with aerogel, I believe that the key results presented in this chapter are more generally applicable to the optics community.

Chapter 6 discusses doped aerogel with different optical functionality. Firstly, the new method I developed for making plasmonic aerogel doped with well-dispersed gold nanoparticles is presented. The desire for aerogel doped with gold nanoparticles was partially motivated by Stefan Maier, who also suggested their useful applications. Comparing the measured optical properties of this doped aerogel to models that I specified, but which were computationally implemented by Susannah Heck of Imperial College London, has led to valuable insights about the environment around the gold nanoparticles. This is particularly useful when considering potential applications of the plasmonic aerogel. Secondly, the new method I developed for doping aerogel with ytterbium ions is presented. Katie Hood, an undergraduate student from the physics department, made most of the wet-gels and spectral measurements under my supervision as part of her summer project with us this year. This work is ongoing, and we hope it will be of considerable value to laser technologists.

Chapter 7 first discusses how the methods I developed for producing aerogel can be used for encapsulating tapered fibres, building on the initial work of Sergio Leon-Saval. Then, I report on measurements of tapered fibre devices made by Limin Xiao and Matthew Rollings. These devices include fused couplers, evanescent gas sensors, and tapered fibres for supercontinuum generation.

In chapter 8, I discuss an aerogel core waveguide, formed inside a hollow optical fibre. The behaviour of the waveguide is explained using comparisons between the measured and modelled properties of the fibre. The result of a basic nonlinear experiment is described.

Chapter 9 contains the conclusion of this thesis, recapping the achievements and significant results in combining aerogel and fibre optics. In it, I also suggests directions for future experiments, and outline those that follow directly from the results presented in other thesis chapters.

Appendix A temporarily moves away from aerogel to discuss tapering fibres for low-loss splice junctions with hollow-core fibres. These splices are used in the creation of photonic microcells by Fetah Benabid's group, particularly by Natalie Wheeler, who then used them to observe strong interaction between laser light and acetylene. Moving back to aerogel, the interaction between laser light and acetylene confined in an aerogel was investigated by Natalie Wheeler, and the spectral shape is promising for applications. Thus, I propose the fabrication of a photonic microcell using an aerogel-filled fibre, similar to an ordinary photonic microcell, but with potentially improved spectral characteristics.

Other contributions have been significant enough that they stretch over multiple chapters. William Wadsworth advised on topics relating to nonlinear optics, and some questions of chemistry. Sergio Leon-Saval conceived many of the initial ideas and helped to lay the foundations for this project. Richard England was frequently consulted on questions of chemistry. Finally, Tim Birks conceived the idea of combing aerogel and fibre optics and has supervised my project throughout.

Chapter 2

Building block 1: Aerogel

This chapter is intended to inform the reader about aerogel, an unfamiliar material to many. It begins with an introduction to the essential terminology. This is followed by a short historical account, summarising the milestones in aerogel development. We then present different methods for making aerogel from the literature. These methods lead to subtle difference in the aerogel properties, which are expanded upon in the final section of the chapter. The interested reader can find further information in the popular science article by Fricke [1] and in review articles [2–4].

2.1 Terminology

An *aerogel* is formed when the liquid component of a jelly is removed, taking care to leave behind the unaltered rigid skeleton. The notion of the foodstuff is not wrong, but it is misleading: most jellies are not wobbly, and they are often filled with liquids other than water. In modern nomenclature, this ambiguity is removed because jellies are often called *gels* instead. The solid and liquid components of a gel are both continuous, so the liquid component can be entirely replaced by different fluids, without altering the solid component. It is common practice to prefix the word gel with whatever makes up the fluid component. Thus, *alcogel* is filled with alcohol, *hydrogel* is filled with water, *wet-gel* is filled with a general liquid or mixture of liquids and *aerogel* is filled with air.

There are many different flavours of aerogel but, for brevity, within this thesis the word refers normally to silica aerogel. Where necessary, other types of aerogel are prefixed by their chemical composition (i.e. alumina aerogel, cellulose aerogel). The term aerogel has no formal definition, although it is implied that it refers to a solid gel structure filled with gas in the pores. However, following [4], we generally take aerogel to mean that the solid component account for no more than 10% of the volume. In fact, it is more common to refer to the corresponding air-fraction when describing an aerogel: a quantity known as *porosity*.

Photographs of the steps in the formation of aerogel are shown in Fig. 2.1. The first step is made from a mix of chemicals, which form a *sol*. A sol (the word is derived from "solution") is a suspension of colloidal solid components within a liquid host. To make wet-gel, the solid component sticks together, forming progressively larger chains. Eventually, a whole network is formed, extending through the whole volume and becoming rigid. This process is known as *gelation*[1].

After gelation, the alcogel spends some time *aging*. During this process, the chemical reactions continue and the structure evolves slightly, becoming stronger and making it slightly easier to remove the liquid component without fracturing. However, if the liquid is simply allowed to evaporate from the wet-gel, then the capillary force caused by the meniscus receding into the pores will alter the fragile structure. A different method for removing the liquid is needed.

[1] Sometimes spelled gellation

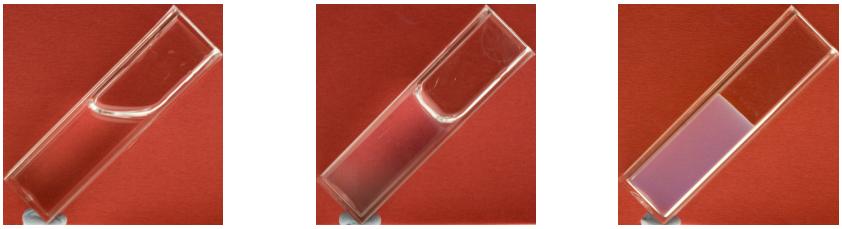

(a) sol **(b)** wet-gel **(c)** aerogel

Figure 2.1: The stages of aerogel fabrication. The transformation from (a) liquid sol to (b) rigid alcogel is known as gelation, and takes ~ 10 min. The liquid component is then carefully removed to make (c) aerogel.

The liquid component of wet-gel is removed by *supercritical drying (SCD)*. SCD is a method of transforming liquid to gas without the two phases being present at the same time, thereby allowing the structure of the gel to be preserved but the pores to be filled with gas. The transformation happens as the liquid is heated above some critical temperature, while always being held under an instantaneous pressure greater than the vapour pressure as the temperature rises. The arrows around phase space in Fig. 2.2 show a complete idealised SCD cycle.

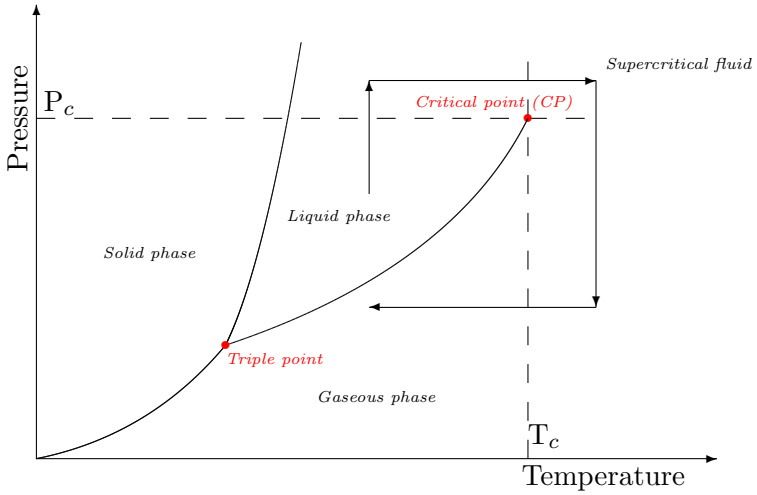

Figure 2.2: A schematic phase diagram for common liquids. Using temperature and pressure control to follow the path of the arrows can transform liquid to gas without the phases coexisting.

2.2 The history of aerogel

The first report of aerogel was enabled by the invention of SCD and appeared in a letter by Kistler [5], published in Nature (1931). The continuous nature of wet-gels was well understood at this time, but replacing the liquid phase with gas was hitherto impossible because capillary forces during evaporation destroy the fragile structures. In a supercritical fluid, there is no distinction between the phases, so there are no capillary forces. Converting the liquid in the pores to gas via a supercritical fluid changes the phase without damaging the solid component. The detailed experimental procedure is expanded upon in [6]. While wet-gel preparation methods have changed, the SCD cycle is very similar to those still used today.

The early aerogels are described as "opalescent, but quite transparent", with densities between 0.02–0.1 g/cm^3. Additional aerogels of alumina, nickel tartarate, stannic oxide, tungstic oxide, gelatine, agar, nitrocellulose, cellulose and egg albumin were reported. Rubber aerogel was attempted, but proved unsuccessful. In the organic aerogels, substitution of alcohol with propane was necessary to lower the critical temperature. Other supercritical-drying solvents including ether and CO_2 were also used for SCD. Table 2.1 gives the critical temperature and pressure of some commonly used supercritical-drying solvents.

Solvent	T_c °C	P_c bar
Methanol	240	79
Ethanol	240	63
1-propanol	265	51
1-butanol	290	43
Acetone	235	46
Ether	192.5	36
Water	375	220
Carbon dioxide	31.1	74
Nitrous oxide	36.5	72
Freon 116	19.7	30

Table 2.1: The critical point of many common solvents, collected from [7, 8]

Apart from an unsuccessful foray into industry, the research field lay dormant for $\sim$ 30 years. This was partially caused by the length of time it took to create

a single aerogel, which could be one month or longer. The original wet-gels were formed from acidified sodium silicate (waterglass), and all the salts and acid needed to be removed by washing with water. Around 50 washes with water were required to remove the salts [9], before that in turn was replaced with alcohol for SCD.

Teichner and Nicolaon [9] developed a new method for the production of alcogel using tetramethyoxysilane ($Si(OCH_3)_4$, TMOS) as the source of silica. TMOS reacts with water to produce silica and methanol, forming a wet-gel already filled with alcohol and thus does not require the long and tedious solvent-exchange steps of Kistler's original method. In fact, using this method it is possible to produce aerogel in half a day [10].

These aerogels were more transparent than those made from sodium silicate, and filled a refractive index range previously only accessible by high-pressure gases. Using sintering, aerogels could be used to fill the full refractive index range between gas and vitreous silica, Fig. 2.3. Aerogels produced from TMOS were quickly adopted by the nuclear physics community for use as a Cherenkov radiator [11]. The velocity of high-energy particles, such as protons and pions, through the aerogel causes the emission of Cherenkov light.

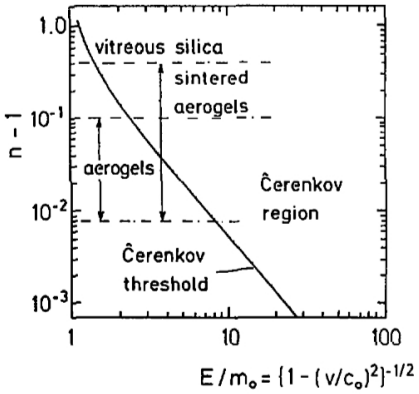

Figure 2.3: Aerogels and sintered aerogel can fill the whole refractive index range between high-pressure gasses and vitreous silica, [2].

The invention of wet-gels from TMOS spurred an increase in interest and the number of publications about aerogel rose steadily during the 1980's [2]. The middle of the decade saw the first International Symposium on Aerogel [12]. Along with this came the first report of aerogel dried at low temperatures in

CO_2 [8]. In this method, the alcohol in the pores is first exchanged with liquid CO_2. Then, the liquid is taken supercritical in the same way as alcohol, but the transition occurs at 31.1 °C. Whilst Kistler had reported this technique when attempting to make rubber aerogel, he had either not tried it or been unsuccessful in applying it to silica aerogel. The low-temperature process was significant because it reduced the hazards associated with aerogel production, making it cheaper and (according to the authors) faster.

Whilst the drying process was more-or-less the same as Kistler's invention, there was continued development in the way alcogel was made. Brinker *et al.* [13] and Tillotson and Hrubesh [14] investigated ways to control the rate of the two reactions that occur to create alcogel. In [13], some of the water is left out of the gel until a later time so the first-step reaction can only partially complete. This allows some control over the structural properties of the resulting gel. In [14], this process is extended to two completely separate reaction steps. In the first step, a condensed silica (CS) precursor is formed using an acid catalyst. This mixture can be stored in non-alcoholic solvents for a reasonable time without reversing the reaction. The CS precursor is then mixed with water and a basic catalyst to form wet-gel.

The two-step method improves control over the structural properties of aerogel, and allows exceedingly low densities. The lowest density aerogel that we have seen reported in the literature was made by Kocon *et al.* [15], and was just $0.003\,\mathrm{g/cm^3}$. This aerogel was a transparent uncracked monolith, but the low density altered some of the structural properties. Where regular aerogels can be handled with relative ease, the ultralow density aerogels deform even during careful handling. As a result these ultra-low density aerogels are less technologically useful, but as the lowest density solid they are an interesting footnote to our story.

In a significant departure from Kistler's SCD, Deshpande *et al.* [16] invented a process for sub-critical drying at ambient pressure. In this method, the internal surface of the alcogel is modified so that it contains molecules that reduce the contact angle between the liquid and glass. This correspondingly reduces the capillary force as liquid recedes into the gel body, and prevents the formation of new chemical bonds within the network. For sufficiently slow evaporation

rates the gel shrinks but does not crack, and can be coaxed back to its original volume using mild heating. Another significant benefit of this method is that the chemistry of the surfaces often renders them hydrophobic.

Throughout its history, aerogel has attracted interest because of many applications that benefit from its various exceptional properties. One of the most significant uses was in NASA's Stardust probe, launched in 1999 [17]. The probe collected tiny particles from the trail of a comet, which became lodged in the aerogel without destroying it. The light payload and low thermal conductivity, as well as the ability to survive in a vacuum, make aerogel well-suited to space-based applications.

Aerogel has an exceedingly low linear component of refractive index, but surprisingly, the intensity-dependent component is reported as being five orders of magnitude larger than ordinary silica [18–21]. If the source of the non-linearity is caused by the material's electronic (rather than thermal) properties, then aerogel could become an exceedingly useful medium in non-linear optics. One curiosity of this non-linearity is its negative sign, i.e. the refractive index is depressed by high intensities. This property opens up possibilities in optical power limiting, as well as new frequency generation and supercontinuum similar to what has been observed in silica fibres [22, 23].

In 2005, Tong *et al.* [24] used aerogel as a substrate for very small tapered fibres. The tapered fibre nanowires ranged in size from 140–900 nm, so a large component of light is guided in the evanescent field outside of the glass element. The fibres were sat on top of the aerogel without fastening. This caused low optical loss because the aerogel causes only a slight perturbation to the field around the fibre. Bent waveguides and coupled waveguides were also made this way, using bends annealed into the tapered fibres. This work is reviewed in more detail in chapter 4.

2.3 Methods of aerogel fabrication

2.3.1 Sol to alcogel

Chemistry of the sol

The synthesis of silica gels has been studied for nearly 200 years. The method of producing tetraethoxysilane ($Si(OC_2H_5)_4$, TEOS) by adding anhydrous ethanol to silicon tetrachloride ($SiCl_4$) was developed by Ebelmen in 1845 [25]. Subsequent work on hydrolysis led to gels that could, over a sufficiently long period, be dried to yield optical elements such as lenses [25]. There are two definitive texts on silica sols and gels, The Chemistry of Silica by Iler [26] and Sol-gel Science by Brinker and Scherer [25]. Far more information is contained between their covers than is presented here, and they can generally be consulted for points of clarity.

The formation of sol from a general tetraalkoxysilane occurs through three reversible reactions. The hydrolysis of the alkoxide to form silicic acid (R. 1), and polymerisation via either condensation of water (R. 2) or alcohol (R. 3) to form silica.

$$Si(OR)_4 + 4\,H_2O \underset{esterification}{\overset{hydrolysis}{\rightleftharpoons}} Si(OH)_4 + 4\,ROH \qquad \text{(R. 1)}$$

$$\equiv Si{-}OH + OH{-}Si\equiv \underset{hydrolysis}{\overset{condensation}{\rightleftharpoons}} \equiv Si{-}O{-}Si\equiv + H_2O \qquad \text{(R. 2)}$$

$$\equiv Si{-}OR + OH{-}Si\equiv \underset{alcoholysis}{\overset{condensation}{\rightleftharpoons}} \equiv Si{-}O{-}Si\equiv + ROH \qquad \text{(R. 3)}$$

However, the rate of the backward reactions is sufficiently low that it is not generally considered important except in a few special cases [27]. The two most commonly used alkoxides are tetramethoxysilane (R is CH_3) and tetraethoxysilane (R is C_2H_5). Neither are miscible with water so a homogenising agent, normally the parent alcohol (ROH), is used.

These reactions are controlled by the electrochemistry of the sol, as well as the ratio of reactants. In fact, the reason silica is one of the most studied materials is that the reactions are slower than in most other metal alkoxides [4, 25]. In practice, the rates of various reactions can be controlled to such an extent that

they are essentially independent [4].

The rates of the various reaction steps are controlled by the pH of the sol, Fig. 2.4. In acidic conditions, proton donors increase the rate of hydrolysis by attacking the $O(\delta^-)$ atoms from the alkoxy groups [4]. This is known from isotopic substitution, where the hydrolysis reaction is actually

$$(CH_3)_3{\equiv}Si{-}OCH_3 + H{-}{}^{18}OH \longrightarrow (CH_3)_3{\equiv}Si{-}{}^{18}OH + CH_3OH \qquad (R.\,4)$$

In basic conditions, the condensation reaction is favoured because the proton acceptors attack the partially positively charged $Si(\delta^+)$ [25, 27]. Condensation reactions reach a minimum around pH 2, which is the point of zero charge and the isoelectric point of silica [25].

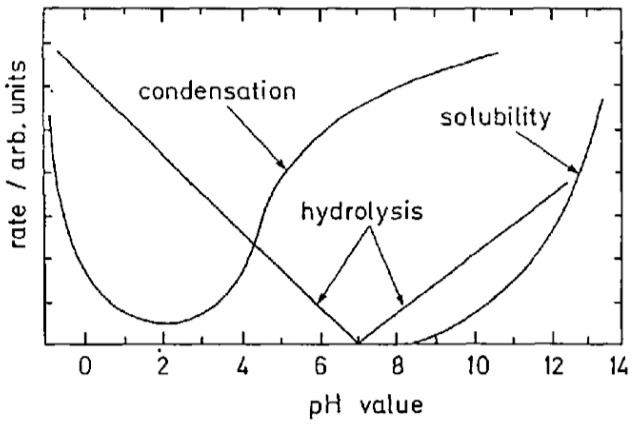

Figure 2.4: The rate of reactions (R. 1) & (R. 2) and the solubility of silica at various pH, from Fricke and Emmerling [2]

The aerogel reported in [10] was made using a TMOS precursor. The stoichiometric reaction of TMOS and water is

$$Si(OCH_3)_4 + 2\,H_2O \longrightarrow SiO_2 + 4\,CH_3OH \qquad (R.\,5)$$

so a sol only needs 2 water molecules per molecule of TMOS to become silica. Sol with varying degrees of water excess, from 2–20 mol per mol of TMOS, were investigated. Acid catalysed and neutrally prepared sols were reported not to form alcogel at ambient temperature. Instead, sometime during the SCD cycle, they became alcogel and the result was opaque aerogels. Basic catalysed alcogels

formed even at 0 °C and the solvent was removed to create a "consistent, almost transparent cake" [10].

Under basic catalysis, the rate of condensation is fast compared to hydrolysis, favouring the formation of dense colloidal silica particles [4]. This minimises the number of OH terminations, preferentially forcing them out to the particle surface. The size of these 'primary' particles is determined by the solubility of silica (also pH dependent), as smaller particles dissolve and precipitate onto larger particles. This mechanism is known as Ostwald ripening [26, p. 175]. If the particles are smaller than 7 nm, the sol is transparent like water. Larger particles of 10–30 nm give the sol a translucent appearance. If the particles are larger than 50 nm, the sol is white and milky-looking [26, p. 345].

In acidic conditions, fast hydrolysis and slow condensation reactions make chain-like silica structures. The length of these chain-like primary particles is dependent on the pH, as the formation of new material is preferentially directed onto the end of the chains by the acidic environment [28]. This maximises the number of internal OH surface terminations [25]. The pH of the sol changes over time as different amounts of silicic acid and particles of silica form. (Fig. 2.7 is a comparison of the structures in acid- and base-catalysed aerogels.)

When two primary particles come in close proximity, they are able to join together by continuing condensation reactions, Fig. 2.5. The new aggregate is able to continue moving around in the sol, coming into continued contact with more primary particles and extending in size. If primary particles join immediately upon touching, the kinetics of aggregation are said to be diffusion-limited. This describes basic sols quite well, since condensation reactions are rapid. If, on the other hand, many collisions occur before particles become joined, the aggregation is reaction-limited. The two processes favour slightly different structures, which we will discuss later in this section.

In both cases, the primary units aggregate until the point of gelation, when the network spans its container. As the units get larger, the viscosity of the sol increases. Initially, the increase is slow, but it becomes more rapid as the gel point approaches and the chains of silica become longer. Sol with a low initial pH has a slower increase in viscosity [29]. At the point of gelation, the viscosity rapidly tends to infinity.

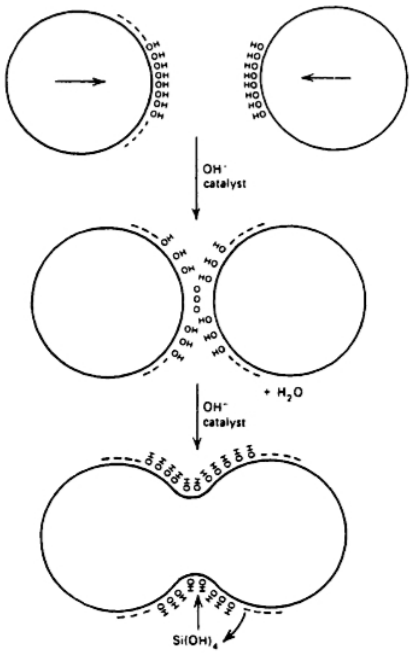

Figure 2.5: Mechanism for condensed silica particles to join together in a base-catalysed reaction, from [26, p. 224].

Although the gel-point demarks a change in state, the reactions continue in the wet-gel. Unreacted components within the pores are still causing the formation of new primary particles. Primary particles and aggregates that were not part of the first spatially extended aggregate join onto the network. This process continues until all the silicon from the sol has become joined into a single macromolecule.

Recipe 1: one-step sol

A typical recipe for producing alcogel from TMOS can be found in Roig *et al.* [30]. TMOS was added dropwise to methanol in a molar ratio $1:12.25$ and thoroughly mixed. The sol was made by adding water and ammonium hydroxide to the mix, in the molar ratio $4:6.5\times10^{-2}$ with respect to the original TMOS component. It was agitated for 15 min, then cast in test tubes and sealed until gelation, which typically took 3–7 min. Aerogels obtained by high-temperature SCD (see sec. 2.3.2) had shrunk linearly by 7%, and had a final density of $0.13\,\mathrm{g/cm^3}$.

The concentration of TMOS dissolved in methanol is used to alter the density of the resulting aerogel. Assuming there is no shrinkage during SCD, the limits

on the density of aerogel are imposed by the chemistry.

The upper limit of aerogel density is determined by the miscibility of the ternary TMOS + methanol + water system. The ternary phase diagram for TEOS, which is hopefully similar, is presented in Fig. 2.6(a) [25, 31]. (We have not been able to find a similar phase diagram for TMOS.) We have estimated the upper bound on density from the recipe that uses the minimum amount of methanol for homogenising the mixture, and the stoichiometric amount of water. The TMOS : water molar ratio should be 1 : 2, which is a volume ratio of 4 : 1. This requires 0.8 mol methanol per TMOS mol to homogenise [11], giving an overall TMOS : water : methanol volume ratio of 4 : 1 : 1. This produces 4.5×10^{-3} mol/ml of SiO_2. Silica weighs 60.1 g/mol, so the maximum density = 0.275 g/cm^3 — equivalent to 85% porosity.

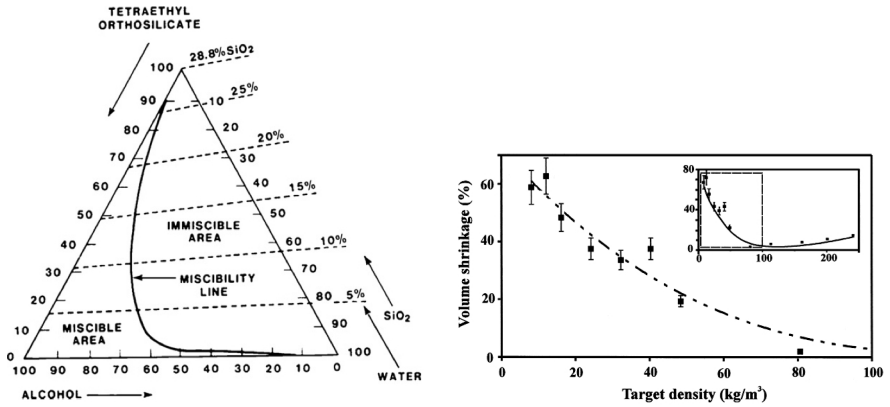

(a) **(b)**

Figure 2.6: (a) Ternary phase diagram of a TEOS-ethanol-water system, from [25, p. 109]. (b) Shrinkage of aerogel with different target densities, from [15].

The lower limit on the density of aerogel is determined by requiring a complete network to form. This is somewhat more complicated to calculate. In the normal one-step method for preparing sol, the density is adjusted by adding excess solvent. However, at the extremely high levels required for the ultra-low density aerogel, the reverse reactions of (R. 2) and (R. 3) are favoured and alcogel never forms [14].

The aerogel density can be increased by shrinkage during SCD or sintering. Kocon *et al.* [15] report that alcogels with target density of 0.100 g/cm^3 undergo

the minimum shrinkage during SCD, Fig. 2.6(b).

Recipe 2: two-step sol

The desire to make even-lower density aerogel for Cherenkov radiators and space payload led to the invention of Tillotson and Hrubesh's two-step process for alcogel formation. Using this method, aerogel with density down to 0.003 g/cm^3 can be produced [14, 15]. This was recognised as the lowest density solid in the world by the Guinness World Records book in 2002 [32].

In the first step of the procedure, a precursor of "condensed silica" (CS) oil is prepared from TMOS. In this step, hydrolysis occurs with very little condensation because insufficient water is added and the reaction is acid catalysed. The molar ratio of TMOS : methanol : water : HCl is $1 : 2.4 : 1.3 : 10^{-5}$. The water content can be increased to 1.6 without the solution forming a gel. Once the reaction is complete, the excess solvent is distilled off and the CS oil is diluted with a non-alcoholic solvent. This stabilises the silica oligomers by suppressing the esterification and condensation reactions. The CS oil can be kept in a sealed container for at least 1.5 years without changing significantly [14].

In the second step of the procedure, the CS precursor is mixed with more water, solvent and a base catalyst so that it forms a gel. The extra chemicals are added in proportion to the number of moles of TMOS in the first step. An additional 2.7 moles of water hydrolyses the remaining OCH_3 sites. The amount of additional solvent added, usually acetone or acetonitrile, is used to control the density. The base catalyst is typically ammonium hydroxide. Gelation normally occurs in around 30 min at room temperature.

The aerogel is made using high-temperature SCD (p. 36) at 300 °C, 136 bar. Other methods of drying cause too much shrinkage to produce ultra-low density aerogels [14]. High-temperature dried gels are stable, and have exceedingly low measured densities. The amount of shrinkage seen in these aerogels is not quoted, but a 2.5 cm thick, 0.004 g/cm^3 sample was measured optically [14] (see sec. 2.4.2) to have very low loss.

Other reported two-step processes, such as those of [27] or [33], do not separate the reactants so thoroughly. Instead, they simply slow the condensation

reaction during the first step (using HCl as a catalyst) so that the formation of primary particles is different. Upon the addition of the second-step materials, the ammonium hydroxide neutralises the HCl and condensation reactions become more common. All variations of the two-step process produce aerogels with significantly different structural properties compared with one-step base-catalysed aerogel.

The structure of alcogel

The structure of alcogel grows in stages: the nucleation of particles; the growth of particles; coagulation into particle aggregates; and reinforcement of the aggregate structure [26, 29]. The different preparation conditions considerably influence the structure of the wet-gel. In addition, it is difficult to measure accurately the structure of wet-gel. Often, measurements on aerogel can reveal information about the structure, but some evolution will have occurred after the alcogel formed.

There are many ways to investigate the structure of gels: transmission electron microscopy (TEM), small angle x-ray or neutron scattering (SAXS/SANS), nitrogen sorption analysis (BET/BJH), light scattering and nuclear magnetic resonance (NMR) studies all reveal vital clues. TEM and nitrogen sorption are practically restricted to aerogel, and NMR to alcogel. SANS and SAXS can be used for either, as can light scattering measurements with a sufficiently sensitive detector, but they only reveal more general features.

The generalised structure and dimensions of base-catalysed aerogels derived from SANS and SAXS measurements is shown in Fig. 2.7(a). They contain bead-like particles, which join into chains separated by $\sim 50\,\text{nm}$. The particles are $\sim 5\,\text{nm}$ across, and are themselves formed of tightly packed smaller ($\sim 1\,\text{nm}$) particles of fully dense silica. This structure of the network is confirmed by the high-resolution TEM picture of Fig. 2.7(b), although the size of the pores is difficult to infer from the image. BET and BJH analysis of nitrogen sorption can be used to calculate surface area and pore-size distributions for aerogel. Whilst this method has documented problems [34, and refs. therein], it is still often used for comparative analysis and gives results in reasonable agreement with other measurements.

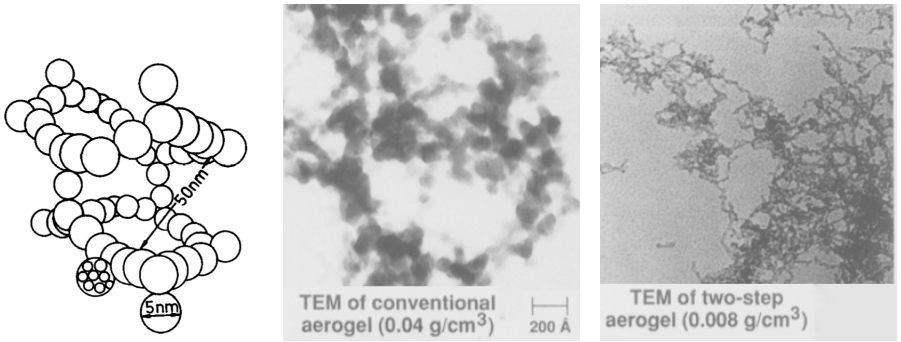

(a) **(b)** **(c)**

Figure 2.7: (a) A schematic picture of the structure of aerogel, from [34]. TEM images showing the structure of (b) base-catalysed aerogel and (c) 2-step aerogel with an acid-catalysed first step, from [14].

Different size structures within the gel evolve in different ways due to charge on the external OH or OR groups changing as the polymer length increases [28]. Acid catalysts create highly cross-linked polymer-like structures [25, 28]. This is especially true if there is insufficient water for complete hydrolysis [27], as the hydrolysis reaction is quicker in acid catalysts, and is almost complete before any condensation starts [25].

Since two-step aerogels have acid catalyst in the first step, the primary particles should have a significantly different structure. The TEM image in Fig. 2.7(c), which is directly comparable with (b), confirms that even though the second step is base-catalysed, the two-step aerogels have a more branched, polymeric structure. The average chain length of the primary particles is < 15 nm. Light-scattering measurements confirm that the smaller and more branched network causes less optical loss than a similar network of bead-like primary particles [14, 25].

After the alcogel is formed, the structure is not completely fixed. It can be significantly influenced by aging, drying, and post-processing using high temperatures (sintering). These aspects are expanded upon in the following section.

2.3.2 Alcogel to aerogel

Aging: structural evolution and strengthening

After an alcogel has been formed, a certain amount of aging is often beneficial to strengthen it before drying. Aging times from none to several months have been investigated with varying degrees of success. The results vary from paper to paper, but the consensus is that the optimum aging time ranges from a few hours to about a week. Aerogel made using the rapid supercritical extraction process has no aging time as the alcogel only forms during the heating process, yet it is reported to be monolithic [35]. Schwertfeger *et al.* [36] claim that, for their aerogel, an aging time of one week is ideal, based on NMR studies of unreacted chemicals within the pores. Few people report considerably longer aging times than these.

During aging, several mechanisms alter the structure of the wet-gel. The most obvious method for this we have already mentioned; the continuing reaction of silica precursor within the pores of the alcogel. Primary particles and aggregates strengthen the network simply by adding additional vertices and edges, mechanically bracing the existing skeleton. Unreacted chemicals strengthen the network by reacting with the silica surfaces, either by undergoing hydrolysis and then condensation or by alcohol condensation with the network providing the hydrolysed silica.

The network can strengthen itself using two subtly different mechanisms as well. Syneresis is the contraction of the gel, caused by the primary particles moving closer together and the joining region between them thickening. This process causes the expulsion of fluid from the pores, as the gel dimensions get smaller. Syneresis is more common in acid-catalysed wet-gels because of the greater flexibility of the polymer-like structure [25]. Redeposition of silica has a somewhat similar effect, Fig. 2.8(a). Differences in the effective radius of curvature cause silica to dissolve from the particle surface and deposit in the necks, strengthening the weak points in the structure [26, p. 230]. After sufficient aging, the structure of the wet-gel evolves into a more even network, Fig. 2.8(b).

If the aging time is too long, Haereid *et al.* [37] report that the network weak-

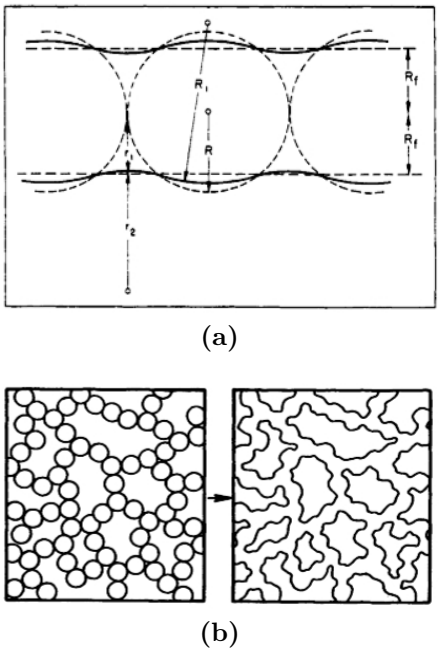

Figure 2.8: (a) Silica redeposits from areas of positive curvature to areas of negative curvature. (b) The wet-gel network evolves from quite discrete spheres to a more continuous structure. Figures from Iler [26, pp. 230-231].

ens and shrinkage increases after drying. If the wet-gel structure is sufficiently inhomogeneous, then redeposition of small silica particles onto larger ones causes a re-coarsening of the network. Dorcheh and Abbasi [31] present rates of the two processes (necking and coarsening), which cross at a point considered the optimum aging time. We are unaware of other reports (apart from by the same authors) of wet-gel weakening by aging for too long, despite the relatively conventional gel recipe used in [37].

Various treatments can be used to help produce stronger wet-gels and aerogels. The effect of temperature and aging liquid composition was extensively studied by M.-A. Einarsrud and colleagues [37–41]. The effect of temperature is simply in speeding up the aging process: gels aged at 100 °C aged 44× quicker than those aged at 40 °C [37]. Adding excess water in the pores increased the strength of the resulting gel by a factor of two.

Addition of more silica to the wet-gel during aging creates a stronger network as extra material is deposited on the existing structure [26, 41]. Aging alcogel with

TEOS in the pores resulted in gels with 15× the mechanical strength, without considerable increase in the density. Unsurprisingly (see Fig. 2.4), the addition of a basic catalyst increased the amount of silica bonded to the network, and higher pH gels were stronger. The strongest wet-gels were made by aging in a 70% TEOS-ethanol bath with a pH of 11. These were strong enough for ambient drying without surface modification.

During drying, the structure can continue its evolution, which is dependent on the process used. Low-temperature SCD does not promote any further reactions, thus the aerogel structure is similar to the alcogel's [42]. Any shrinkage that does occur arises from reorganisation of the aggregates during solvent exchange. High-temperature SCD causes structural modifications, which strengthen the aggregate network. The result is normally less-shrunken aerogel. Ambient pressure (evaporative) drying usually modifies the structure completely, resulting in a dense glass. However, we will presently discuss several methods for producing low density structures using this method.

It is worth noting at this point that most aging takes place in a somewhat larger volume of liquid, with the fortuitous consequence of removing water from the gels. Although this is seldom commented upon, we believe it is particularly significant to the success of low-temperature SCD.

High-temperature SCD

In high-temperature supercritical drying, the pore fluid of the alcogel is raised above its critical point. Whilst the temperatures are modest by glass technology standards ($< 300\,^{\circ}\mathrm{C}$), they are high enough to require some care as the solvents are flammable. This is particularly true for methanol and ethanol, where the high temperature is accompanied by a significant pressure as well.

The pressure-temperature phase diagram for methanol in Fig. 2.9 shows the conceptual picture of supercritical drying. The phase coexistence line is the equilibrium vapour pressure for a given temperature. During evaporative drying, molecules from the liquid phase evaporate so that the equilibrium pressure is reached. As the vapour diffuses into the atmosphere, or is carried away on air currents, more liquid evaporates and the meniscus recedes into the gel body.

This is equivalent to travelling through phase space on the red arrow marked in the figure. The capillary force from this meniscus causes cracking and shrinkage during evaporative drying. A more complete description of the development of stress and the evolution of the gel network during evaporative drying can be found in Brinker and Scherer [25, pp. 483–489].

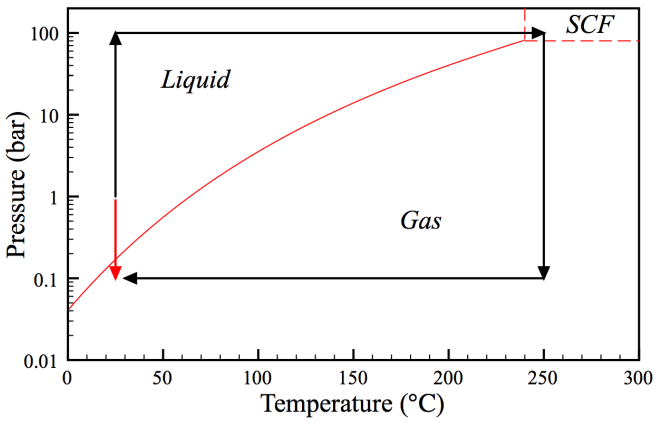

Figure 2.9: Pressure-temperature phase space for methanol. The line demarks liquid-vapour equilibrium and terminates at the critical point values of $P_c = 79$ bar, $T_c = 240\,°C$. SCF means supercritical fluid. Data from NIST [43].

If the gel is kept in an environment where the vapour pressure is somewhat above the critical pressure, then molecules can be slowly removed without the formation of any menisci [6]. The most practical way to achieve this is to fill an autoclave with methanol and heat it gently. Since the liquid is incompressible, thermal expansion will cause a very quick rise in pressure. Above the critical pressure, a valve can be opened to release the excess methanol until the critical temperature has also been exceeded. At this point, faster depressurisation can occur (but slow enough to maintain thermodynamic equilibrium), until the internal pressure is below the vapour pressure at room temperature. This prohibits any condensation inside the aerogel during cooling.

If the autoclave is only partially filled with liquid methanol at the start of SCD, then it contains a meniscus that can move up or down in the vessel [7]. The movement happens because gas is compressible (up), and liquid can evaporate from the surface (down). If these two rates are perfectly balanced, then the menisus does not move, but the capillary forces weaken until at the critical point

it vanishes. This critical specific volume, V_c, is the 'tipping point' between an expanding liquid phase (where critical conditions will always be met) and an expanding gas phase (where they never will). If the volume of methanol is slightly too small, this is equivalent to crossing the phase equilibrium line at a higher temperature, with a lower surface tension.

For methanol, $V_c = 3.67\,\mathrm{cm}^3/\mathrm{g}$ [7]. This is the inverse of the density of methanol required to make a single supercritical phase, and is useful because it is independent of the vessel volume. If the specific volume of liquid methanol $V > V_c$, high-temperature supercritical drying will progress with no meniscus passing through the wet gel. Our calculation of the amount of methanol required at ambient conditions comes from inverting V_c and multiplying by the volume of the actual vessel. The result is in grams, which can be converted to a volume using the density of methanol, $0.791\,\mathrm{g}/\mathrm{cm}^3$ at s.t.p. For a 1 L vessel, 344 ml room-temperature methanol is required.

Even with no capillary forces, stress during supercritical drying can still cause damage to the fragile gel structure. Continuing alcoholysis and condensation reactions can alter the structure, and syneresis is accelerated by the high temperatures. However, these are not the main causes of cracking in high-temperature SCD. The different thermal expansion rates, and the confining nature of the aerogel cast, cause cracking from compression [44]. If the cast is a cylinder, compression cracks run perpendicular to the length. Slow heating rates, which are dependent on the diameter of the wet gel, are required to prevent cracking. Scherer [44] reports that for a 2 cm diameter alcogel, the heating rate should not exceed 2 °C/min for a radially-unrestricted gel.

Since high-temperature SCD is often performed on samples that have not had any solvent exchange, the pore fluid often contains a binary mixture of methanol and water. The water volume depends on how much was in the sol compared to the stoichiometric ratio. Recalling reaction (R. 5), only 2 moles of water are used up in the sol formation. For a relatively normal gel (e.g. Recipe 1, p. 29) this leaves 2 mol of water per mol of TMOS in the pores of the alcogel, going into the autoclave for SCD. This small amount modifies the critical point of the mixture. A linear scaling of the critical point, based on the relative weight of methanol and water, is a sufficient adjustment [7].

Concentration gradients between the mixed pore fluid and the pure methanol external fluid can cause cracking in exceptionally fragile gels. This is particularly true if the target density is very low, as the highly branched structure cannot significantly strengthen itself. For these gels, it is important to consider to solubility of silica in high-temperature alcohol and mixtures. This is minimised for a mix of water and methanol in the molar ratio 1 : 4 [15]. It is perhaps surprising to note that the addition of zeolite, a porous non-soluble form of aluminosilicate which can partially trap water or impurities, reduces shrinkage during high-temperature SCD [15, 45].

An alternative method of high-temperature SCD has been demonstrated using an overpressure of inert gas, removing the need for excess methanol volumes [7]. In this method, the inert gas applies hydrostatic pressure to the liquid methanol in the alcogel, which is reported to force the liquid component to remain in that state during heating. If the gas pressure is insufficient, subcritical drying can occur at elevated temperatures - equivalent to having a subcritical excess solvent volume. This can lead to additional shrinkage during SCD. The most commonly used inert gasses for this experiment are nitrogen and argon. The arguments about thermal stress build up and heating rates for the gel still apply.

Rapid supercritical extraction (RSCE) is a high-temperature alternative drying scheme for expedited production of aerogel [35]. In RSCE, liquid sol is added to a pressure vessel. This becomes alcogel as the vessel is heated, presumably sometime before critical conditions are attained. The expansion of the sol is prevented by sides of container, until a pressure above P_c is reached. At this point, the liquid phase can escape through a relief system leaving the solid component in the vessel. Using this method, the production time of aerogel can be as quick as 5 h (hours) [46]. However, these aerogels often have large density fluctuations because of their method of production [35].

Low-temperature SCD

The discovery of supercritical fluids, including CO_2, predated Kistler's invention of SCD by $\sim$ 50 years [47]. This is testament to the ingenuity of the scientists and engineers of the day, who used miniature glass viewing cells over an excep-

tional range of pressures to understand how many liquids behaved under certain conditions. The disappearance of phase separation above the critical point must have been a surprise to those early pioneers, along with the unusual solvating properties of the supercritical phase. In fact, it is likely this solvating property is responsible for Kistler's failure to produce rubber aerogel using CO_2 [6].

Whilst Kistler was obviously undaunted by the high critical point of methanol, its hazardous nature is clearly present. This was particularly evident when, upon a gasket seal failure, the whole Airglass factory was destroyed by the explosion of a high-temperature SCD autoclave [1]. This explosion happened in 1984 [48], and within a year the first reports on the far safer low-temperature drying process were published.

The critical point and pressure-temperature phase diagram for CO_2 are presented in Fig. 2.10(a). One substantial difference between methanol and CO_2 is that the latter only exists as gas at s.t.p. and must be pressurised to ensure it is liquid. Thus, during the SCD cycle shown by the arrows in the figure, the first act is to jump across the phase coexistence boundary as CO_2 flows into the autoclave.

A schematic setup from Wagh *et al.* [50] is shown in Fig. 2.10(b). Liquid CO_2 flows into a vessel partially filled with excess methanol along with the alcogels for drying. Using the inlet and outlet valve, the liquid CO_2 is used to gradually purge methanol from the autoclave and, diffusively, from the alcogels. When the entire volume of methanol has been extracted, the vessel is sealed and the heaters are switched on so the temperature and pressure rise above the critical point. Slow depressurisation follows, at the end of which the aerogel is ready to be removed.

In addition to the safety of low-temperature processing conditions, Tewari *et al.* [8] claim the time it takes for SCD reduces from 2–3 days to 8–10 h. This claim is somewhat unusual, as high-temperature drying does not normally take so long. However, further clues later on reveal that they have difficulty with high-temperature SCD, observing cracking, shrinkage and lack of repeatability. These are not normally complaints levelled at the high-temperature process, but that is not the focus of the paper. Low-temperature aerogel is reported [8] to be repeatable, not too shrunken, and largely monolithic. The optical properties are acceptable (see sec. 2.4.2), and improve after heating at 450 °C for 4 h.

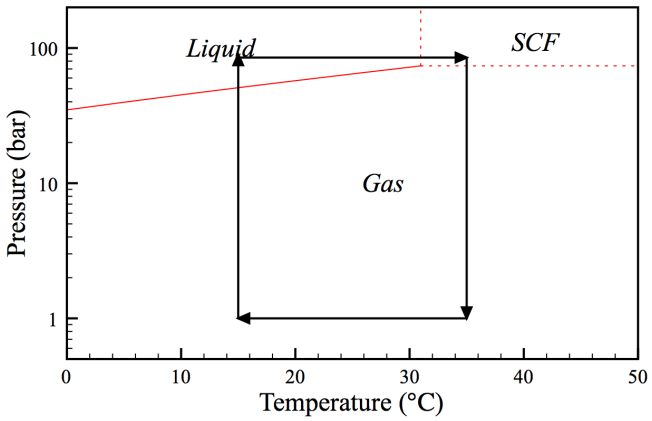

(a)

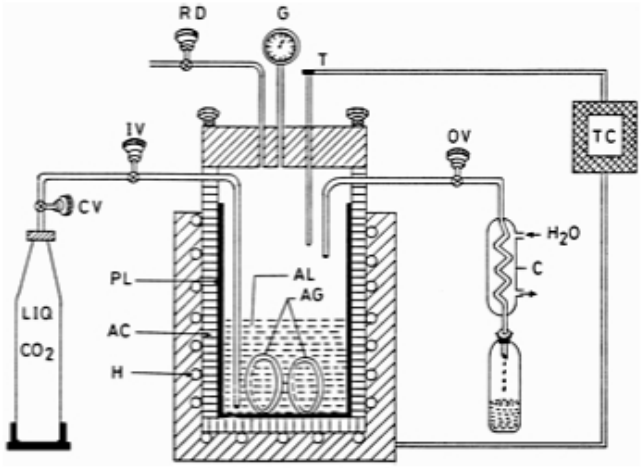

(b)

Figure 2.10: (a) Phase coexistence data for supercritical CO_2, from NIST [49]. (b) Diagram of LTSCD setup from Wagh *et al.* [50].

Shrinkage of low-temperature dried aerogel is thought to be due to mechanical stress during solvent exchange rather than chemical reactions [51]. The stress may be caused by concentration gradients between the sample (full of methanol) and the environment (full of CO_2). The diffusion rate is complicated by the scale of the pores and the large internal surface area, as both Knudsen and surface diffusion play a role [52, and refs. therein]. The miscibility between the two liquids is also important, as surface tension at liquid-liquid interfaces can still cause considerable damage to the wet-gel.

If solvent exchange is incomplete before the drying cycle has finished, then

the aerogel will be damaged. The site of the damage is at the centre of the gels and extending outwards towards the surface. Solvent exchange occurs faster at higher temperatures. Exchange of methanol with CO_2 in a paralleopiped sample with 10 mm smallest dimension can be shortened by 15 min by increasing from 20 °C to 25 °C [53].

At even higher temperatures, somewhat quicker solvent exchange is expected. In two papers, van Bommel and de Haan [52, 54] showed that injecting supercritical CO_2 could be used for making aerogel. This means the temperature can be increased rather arbitrarily, and in fact they produced crack-free aerogel at 70 °C, further shortening the time for SCD. However, the SCD cycle started (as in normally the case) with enough ethanol to completely cover the sample. This means a large initial volume of liquid ethanol present in the reactor, so consideration of the ethanol-CO_2 binary fluid phase is important.

Using a windowed autoclave and acetone co-solvent, phase separation of acetone rich and CO_2 rich phases are observed [55]. If the phase boundary is across the alcogel, then inter-surface forces cause catastrophic collapse of the structure, and results in white, powdery material. If the phase boundary is kept above the sample until sufficient exchange has occurred, then high-quality aerogel can be produced. This is probably comparable to the situation in methanol + CO_2 mixtures for producing aerogel.

In every procedure for low-temperature SCD, a large volume of additional solvent is added in the reactor at the start of the cycle. Most reports claim this is simply to prevent ambient drying. However, in chapter 5 we will discuss its importance in light of observations in our windowed autoclave. We will show that it also acts to reduce the diffusion rates of liquids through the alcogel by increasing the content of methanol within the chamber. This reduces the susceptibility of the aerogel to cracking due to concentration gradients.

Modified surfaces for hydrophobicity

Aerogels tend to be hygroscopic, that is, they absorb moisture from the atmosphere. This is because the surfaces are covered in hydroxyl groups that present sites for hydrogen bonding. These sites attract water, which condenses on the

internal surfaces. Liquid water drops are destructive because the large quantities of surface OH within the aerogel pulls the drop in, and the structure fractures into white powder because of capillary forces.

Aerogel becomes a much more useful material when prepared so that it is (at least mildly) hydrophobic. We have adopted a colloquial definition of the term hydrophobic, really meaning that the aerogel is not destroyed by contact with water. The quality of the hydrophobic properties can be quantified by looking at the contact angle with a water drop supported on the external surface. Ideally, complete modification of the surface chemistry makes it superhydrophobic (contact angle $> 160°$) [36, 56], and even moisture in the air will not condense on the internal surfaces. The methods for making hydrophobic aerogel depend on the drying method used to extract the pore solvent.

Immediately after high-temperature SCD, aerogel is moderately hydrophobic. This is because reesterification causes some of the aerogel surface to be covered with OCH_3 in place of OH terminations [25, p. 505]. The covering of methyl groups can be increased by treating the aerogel with hot methanol vapour [57]. Hydrophobic aerogels with larger contact angles can be obtained with higher alcohols, such as n-butyl alcohol [26, p. 573]. This process is not dependent on drying method, as the hydrophobic surface is added after the aerogel has already formed.

Improved hydrophobic properties can be obtained by linking CH_3 directly to Si in the network. *These methylated surfaces are often formed with co-precursors in the sol.* Methyltrimethoxysilane ($CH_3Si(OCH_3)_3$, MTMS) co-precursor provides three network bonding sites, and presents one external hydrophobic termination [36, 58]. With MTMS/TMOS = 0.2, hydrophobic, transparent aerogel with a contact angle of 50° can be made by high-temperature SCD. Increasing the MTMS fraction dramatically improves the hydrophobic properties, but the aerogels are translucent or opaque.

When only a single hydrophobic surface site is present, the siloxane bonds (Si−O−Si) are at the surface, and can be subjected to water attack, Fig. 2.11(a). This exposes several additional OH sites, somewhat reducing the effectiveness of the coating. With sufficient MTMS coating, this effect reduces because water is less able to get close enough to the underlying network to break it apart.

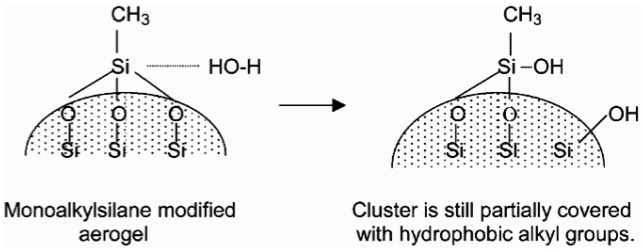

(a)

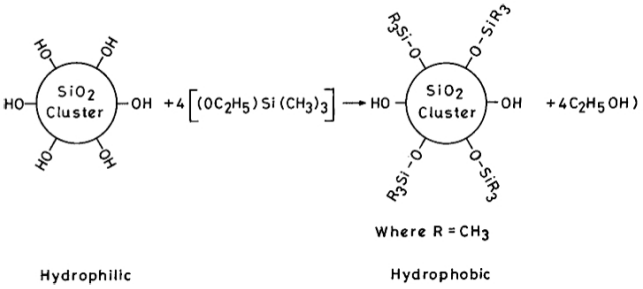

(b)

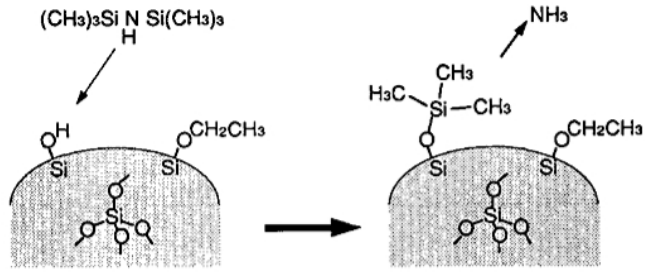

(c)

Figure 2.11: Different methods of producing hydrophobic aerogel. (a) Using a co-precursor with a slower gel time such as MTMS can coat the internal surfaces with a single hydrophobic (CH_3) group in place of the hydroxyl group. (b) A more effective co-precursor, TMES, replaces each surface hydroxyl with a Si connected to 3 CH_3 groups. (c) This same modification is possible after the alcogel has already formed, by washing in HMDS.

To prevent this degradation in hydrophobic properties, a branched molecule with multiple hydrophobic groups per surface site is used instead. One possible chemical modifier is trimethylethoxysilane ($(CH_3)_3Si(OC_2H_5)$, TMES), as demonstrated by Rao *et al.* [59]. The three methyl groups are connected the network via an Si−O−Si bridge, Fig. 2.11(b). Since hydrolysis of the ethoxysilane is slower than of methoxysilanes under the same catalysis, TMES effectively gels on the outside of the TMOS network. Aerogel made by high-temperature drying has a larger contact angle (105°) and a comparable transparency to those made with MTMS co-precursor.

In continuation of this work, Rao *et al.* [60] investigated many different co-precursors for high-temperature drying. For hydrophobic properties, trimethylmethoxysilane (TMMS) is the most effective precursor with TMOS. This result is somewhat surprising, as the hydrolysis reaction is quicker than the ethoxysilane reaction, and earlier formation should lead to less effective surface coverage (as some replaced groups will become trapped internally during cluster formation while OH will still present on the surface of the clusters). TMES aerogels have a higher transparency than TMMS aerogels for otherwise identical conditions. Explanation of the excess optical loss in the modified aerogels is not provided.

The addition of co-precursor greatly effects the gel time. Sols that would ordinarily gel in 4 h took up to 16 h when MTMS was included in the sol [58]. There are several possible reasons for this, all connected to the surface chemistry of the modifying elements. The Si−R groups do not participate in any of the reactions. If they form in the network during the initial stages of growth, they reduce the number of functional groups in the chains and change the formation of condensed silica particles. If they are forming on the condensed silica particles themselves, the network will be less susceptible to sticking via the mechanisms shown in Fig. 2.5. Alternatively, since the pH and particle growth is strongly influenced by the electrochemistry of the Si−OH bonding [25], different sized particles may result simply because of a different equilibrium.

Even a network with only three reactive sites and one non-reactive sites (reduced functionality), alcogel and aerogel can still form. Aerogel made from MTMS precursor alone exhibits superhydrophobic properties [56]. The contact angle of this aerogel can be up to 173°, which is exceptionally high and implies

almost every surface site contains a hydrophobic group. These aerogels have another interesting mechanical property: they can be incredibly flexible [61]. However, because of the oddities in structural formation, the aerogel is completely opaque.

Low-temperature SCD is not suitable for producing hydrophobic aerogel from co-precursors [36, 51, 58]. These results appear to be determined by experiment, as none of these papers explains this observation. It seems that liquid CO_2 can, when filling the pores, alter either the structure or the surface chemistry and revert the aerogel to presenting hydroxyl rather than alkyl groups (see chapter 5). Nevertheless, we tried drying alcogel made with an MTMS coprecursor and dried using our low-temperature process, and observed that our aerogels were hydrophobic (although the contact angle was low).

Alternatively, the aerogel can be made hydrophobic by washing the alcogel in different chemicals during aging. If the network is already stable (i.e. alcogel), the surfaces can be modified with little effect on the optical properties. Trimethylsilyl (TMS) modification of the surfaces is most effective, adding three hydrophobic groups per surface site on a branched, umbrella-like structure. Fig. 2.11(c). Surface modification techniques carried out in liquid alcohol and supercritical CO_2 were developed by Yokogawa and Yokoyama [62], using hexamethyldisilazane[2] ($(CH_3)_3SiNHSi(CH_3)_3$, HMDS) to provide TMS. In both media, the reactions are limited by the time it takes for the TMS modifier to diffuse into the gel, but this process is greatly accelerated when it is a component in a supercritical phase material.

Alcogel treated with HMDS and dried using low-temperature SCD can make aerogel with superhydrophobic properties. However, there are a few drawbacks caused by the structure and the reaction by-products. The umbrella-like structure prevents complete surface coverage, limiting it to 2.45 of a possible 4.1 groups nm^{-2}. Monolayers of water can still form on the remaining OH sites (they form underneath the TMS umbrellas), but multilayers are prohibited [26, p. 699]. Another reason for incomplete coverage of TMS on the surface is that the reaction is inhibited by the ammonia (as O−Si−O become more soluble in very basic solutions). Since ammonia is produced by the reaction of HMDS with the network, the

[2]Sometimes HMDS is called HMDZ

reaction is self-retarding. A mix of hexamethyldisiloxane ($(CH_3)_3SiOSi(CH_3)_3$, HMDSO) and trimethylchlorosilane ($(CH_3)_3SiCl$, TMCS) can lead to more complete surface coverage [63].

Hydrophobic modifications are an important factor in aerogel development. As well as making it waterproof, aerogel made to be hydrophobic often exhibits less shrinkage than equivalent unmodified aerogel, because the modified contact angle reduces any force build-up during SCD. This idea was extended further by Deshpande *et al.* [16] in the development of ambient-pressure drying (APD), which is the subject of the next section.

Ambient drying

If the evaporation rate from alcogel is sufficiently slow, evaporative drying can produce a shrunken but uncracked monolith of glass. This low porosity glass is generally known as xerogel, although this can lead to some confusion. The root of the word, xeros, means dry; literally speaking, aerogel is therefore a subtype of xerogel where the internal structure has been maintained to at least some degree. We have accepted aerogel defined by porosity$\geq$ 90%, but we should extend this to $\geq 87.5\%$ as this is the densest aerogel we can form with a preserved structure (recall the calculation for maximum density on p. 30). Historically, Kistler applied the term "aerogel" to xerogels produced by SCD, regardless of porosity but as long as the structure was relatively preserved. However, ambient drying techniques that preserve the structure were not available to him.

The capillary pressure arising during evaporative drying of wet-gels is large enough that it would cause liquid to rise up to 8 miles [26, p. 535]. However, we know from experiments with aerogel that the solid component of the network is actually quite strong even on macroscopic dimensions [1, 11]. The network itself is expected to be much stronger still on the dimension of the aggregates [42] (p. 32). This is why slow evaporation causes shrinkage: the gel compresses with the enormous applied force, but the network resists cracking. However, as parts of the network approach each other, condensation reactions expelling water cause irreversible bonds so the shrinkage cannot reverse as the effects of capillary pressure lessen. Even using low surface tension liquids, the network collapse is

permanent because of this effect.

If the internal surfaces are completely replaced with unreactive terminations, no additional bonds form and the gel can gently spring back once the liquid is completely removed [16, 26]. Thus, we can see it is no coincidence that aerogel produced this way has superhydrophobic properties. Fig. 2.12 shows the schematic evolution of the volume of gel during ambient drying procedure. Initially, the surfaces of wet-gels were modified with ammonium oleate and a high-boiling, easily oxidised oil [26, p. 537 and references therein]. More recently, HMDS, TMCS and hexamethyldisiloxane in various mixtures have been used in an easier process [63].

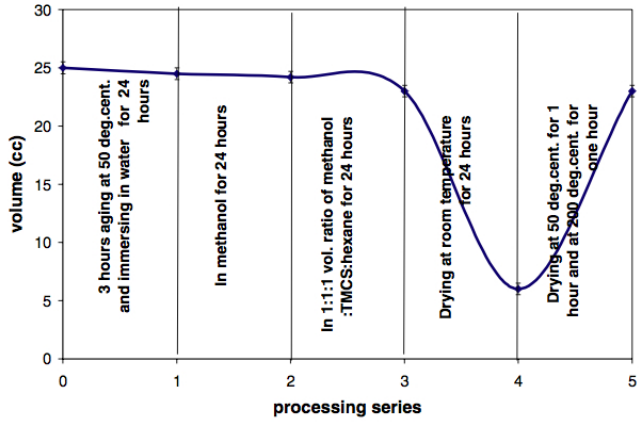

Figure 2.12: Evolution of gel volume during preparation and ambient drying, from [64]. The gel springback is caused by heating, and happens because unreactive surface terminations prevent the formation of permanent bridges between different strands of the glass network.

Using these methods, ambient drying can be used to produce xerogel of comparable porosity to all but the ultra-low density aerogel. The advantages of ambient drying are its cheapness and the reduction in hazards, because there are no high pressures. The disadvantage is, to encourage gel springback, high temperatures of 200 °C are still required, which is still larger than many organic and polymer elements can withstand.

There are two methods of ambient drying which do not use hydrophobic modifications: strengthening the structure using additional alkoxysilane [41, 65], and the addition of chemical additives to prevent cracking (DCCA's) [27, and refs. therein]. These methods are somewhat different, as they prevent the network

from shrinking in the first place, rather than relying on springback to achieve low densities. As a result, they cannot match the very lowest densities, but aerogel with 0.22 g/cm^3 and low shrinkage during drying has been obtained [41]. Despite the apparent ease of these methods, and the appeal of transparent, modestly low-density ambiently-dried aerogel, little work has been reported in the recent literature [66].

Drying methods: advantages and disadvantages

Each method for extracting the solvent has advantages and disadvantages, and is suited to different kinds of samples. Here, we attempt to review the methods with advice on their most suited applications.

Ambient drying is the most suited for industrial applications, particularly when the wet-gel is derived from waterglass. This is the cheapest method of producing aerogel, as it doesn't require any particularly specialised equipment and has fewer scale-up challenges. However, aerogel produced this way is not as transparent as when produced by SCD [63, 64]. Also, the inherent gel shrinkage before springback could cause embedded items to be displaced or broken. Finally, for efficient replacement of the surface chemistry with TMS, chemical modifiers must be introduced diffusively into the network. This step causes considerable restrictions on sample geometry, similar to those in low-temperature SCD.

Low-temperature SCD is often the default method of drying for aerogel. The safe working temperature and inert solvent means that, even in the event of seal or autoclave failure, risks are minimised. The low temperatures are compatible with many materials, extending the usefulness of aerogel as a host medium (à la chapter 6). This is particularly important when trying to incorporate organic chemicals or polymers in the matrix, which degrade rapidly above 100 °C [51]. The most significant disadvantage of low-temperature drying is the tedious solvent exchange for liquid CO_2, which is only partly sped-up by the use of all-supercritical CO_2 [52, 54]. This diffusion step effectively prohibits the aerogel exceeding 1.5 cm thickness in the smallest dimension.

High-temperature SCD is considered the least favourable method for drying aerogel, but is the most flexible method of the three. For example, the geometry

of the sample is less important, because there are no solvent exchange steps required. Also, high-temperature SCD is the only way of producing aerogels with exceedingly low density, as the low-temperature process seems to degrade the network too significantly. The obvious disadvantage is the significant hazard if there were a mechanical failure, caused by the high temperature and pressure. Other disadvantages include: the incompatibility between the high temperatures, alcohol, and many interesting organic and polymeric dopants; the high electricity cost of heating a vessel to supercritical temperatures; and the difficulty in industrial scale-up of suitable autoclaves.

Cryogel

The final route from liquid to gas, via an intermediate solid phase, is known as freeze-drying. The considerations of the pore fluid and the mechanism of freezing are of paramount importance. These difficulties have made it impractical to produce aerogel by freeze-drying, although fragments and fibres have been made this way [25, p. 506]. Tewari *et al.* [8] assert that this method has never been used to create transparent aerogel, so we only mention it here for the purpose of completeness.

2.4 Properties

Most of the properties of aerogel are derived from its structure. Hence, different methods of making aerogel produce structures suited to different applications. The properties are influenced by many aspects of the structure, such as the size of the elements, the amount of aging, and the method of supercritical drying.

2.4.1 Mechanical properties

Aerogel has a large internal surface area created by the large number of thin chain-like elements. The range of surface areas observed in aerogel span from $200\,\mathrm{m^2/kg}$ [42] to $950\,\mathrm{m^2/kg}$ [67]. This can be influenced by the preparation and supercritical drying conditions. Aging reduces the surface area, as the curvature

of the primary particles in the silica networks is reduced [37].

A number of applications are related to the high surface area of aerogels. For example, they promote catalytic activity, particularly when combined with iron oxide on silica or alumina aerogels [2, and refs. therein]. The electronic properties of aerogel are also related to the surface area, as well as the material, and can be used in creating supercapacitors. This is particularly useful with carbon aerogels of high surface area [68].

The thermal conductivity of aerogel is the lowest of any transparent material. This is because the porous structure minimises convective heat transfer, and the low-density network reduces conduction. Thermal transport in aerogel is therefore predominantly due to infrared radiative heat transfer, and is minimised by absorption losses in the infrared [69]. For this reason, aerogels have been proposed as a filling in the hollow of double-glazed windows, which would result in a 3× improvement in the insulating properties [1]. Even larger improvements can be obtained, albeit at the expense of the optical properties, by adding materials which absorb near-IR wavelengths as well.

The speed of sound in aerogel is 100–300 m/s, slower than in air and considerably slower than in fully dense glass (5,000 m/s). This interesting feature could lead to applications as an impedance matching material between piezoelectric transducers and air [1, 68].

2.4.2 Optical transmission

Optical transmission is a measure of the transparency of a material. Optical loss is a measure of light that is not transmitted, which may be due to scattering, absorption, reflection or some contribution from each factor. Often, the loss is strongly dependent on the wavelength of light. This means that spectral transmission or loss measurements are a useful tool for comparing similar objects.

Many factors affect the transparency of aerogel. For example, reports of one- or two-step procedure, water content, solvent, temperature during formation, density, hydrophobic properties, supercritical drying medium, and catalyst [3, 14, 50, 58, 62, 70–72] all show slightly different spectral transmission. There are so

many variables that few hard and fast rules exist for maximising the transparency of aerogels.

Worth bearing in mind is the ease with which the aerogel is fabricated. TMOS is more reactive and easier to condense than TEOS, so it is a natural precursor choice. In [50] the authors show that aerogel from TMOS causes less loss than aerogel from TEOS, Fig. 2.13(a). One-step aerogels are much easier to produce than two-step aerogels, but Fig. 2.13(b) shows that they also cause more loss. The additional expense and difficulty of the two-step methods may be worth it for some applications, but it is not universally adopted. High-temperature drying is generally reported to yield aerogel with less loss than identical low-temperature aerogels, Fig. 2.13(e & f). However, low-temperature aerogels can recover somewhat by heat-treating to 450 °C [8].

Almost all aerogel papers report on light transmission rather than loss. Whilst some display spectral measurements, others simply state values for white light. Very few standardise their measurements, and often the thickness is rather arbitrary because of shrinkage from the original cast. Commonly reported thickness range from 5–10 mm, but some spectra are through much thicker aerogels. Fig. 2.13 shows some typical examples of transmission spectra in various types of aerogel.

The spectral transmission through all different types of (transparent) aerogel is similar. At visible wavelengths, there is strong wavelength dependence, causing a sharp shoulder. All spectra show similar resonances in the infrared region, causing sharp dips in the transmission. These have been attributed to water (1.2, 1.4 and 1.9 μm) and O−H and Si−O at 2.2 and 2.6 μm respectively [8]. They raise the background loss by weakly absorbing even where they are not resonant, as they are quite broad features.

The spectra in Fig. 2.13(b & f) present the highest transmission we have come across in the literature. Both results are for two-step aerogels, although the second is using a commercially available CS precursor rather than controlling their own first step. From (b), at 800 nm, the transmission through a 0.04 g/cm^3 aerogel 2.5 cm thick is 95%. This is equivalent to an attenuation of 0.09 dB/cm. For the same wavelength, from (f) the transmission through 1 cm aerogel is 97% and the equivalent attenuation is 0.13 dB/cm.

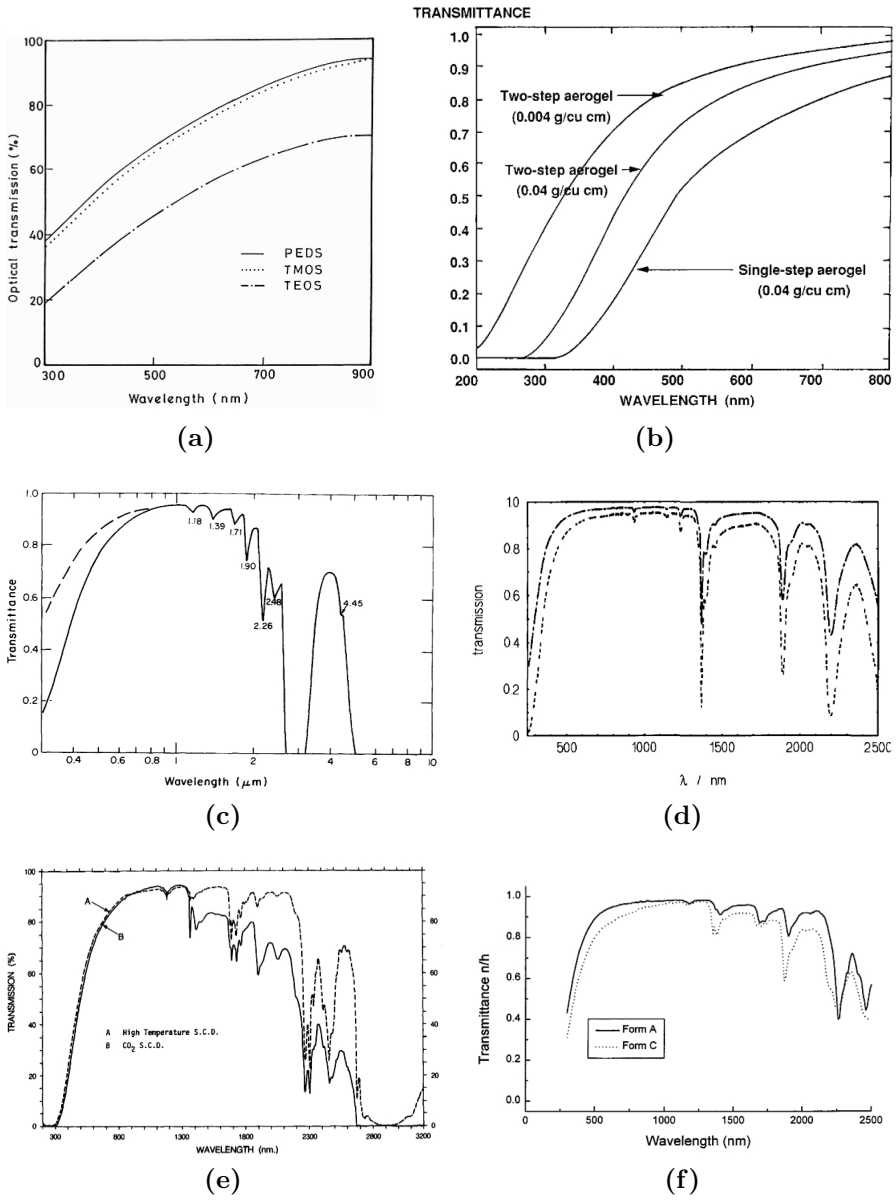

Figure 2.13: Aerogel transmission spectra. (a) Transmission through 10 mm aerogel made from different precursors, from [50]. (b) Transmission through 25 mm aerogel made using the one-step and two-step processes, from [14]. (c) Transmission spectrum of 4 mm thick ordinary aerogel to $\lambda = 10$ μm [73]. (d) Transmission spectrum through a 20 mm aerogel tile [74]. (e) & (f) Transmission spectra for otherwise identical aerogels, 3 mm and 10 mm thick respectively, dried using low (Form C) and high (Form A) temperatures [8, 71].

It is clear both from the appearance and spectra that aerogel causes Rayleigh-like scattering of visible light, Fig. 2.14. Aerogel appears slightly yellow when viewed on a white background, because blue light is preferentially scattered. Against a black background, back-scattered light is primarily visible, and the aerogel appears grey-blue like "frozen smoke" [73]. The wavelength dependence of the aerogel scattering has been experimentally determined as close to λ^{-4}, as expected from Rayleigh's theory [73, 75].

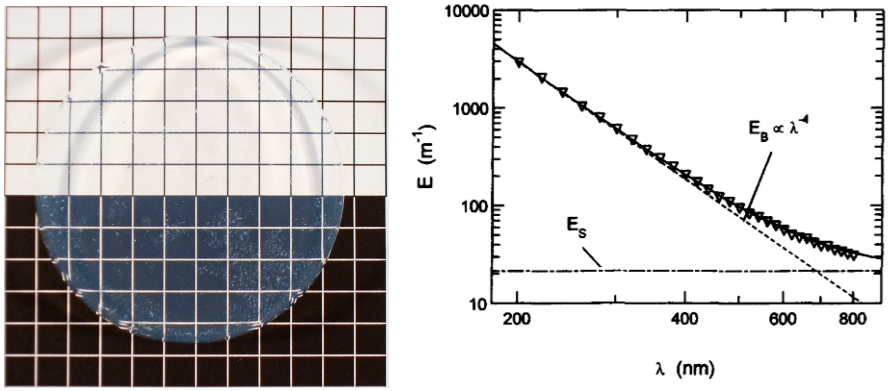

(a) **(b)**

Figure 2.14: (a) A disk of our aerogel appears blue against a black background, and slightly yellow against a white background. (b) Aerogel scatters visible light according to an approximate λ^{-4}, spectrum taken from [75].

If aerogel is considered to scatter light according like a Rayleigh scattering medium, the extinction coefficient α can be defined as

$$\alpha = 32\pi^4 \frac{\rho_{\text{agl}}}{\rho_{\text{SiO}_2}} \frac{a^3}{\lambda^4} \left(\frac{n^2 - 1}{n^2 + 2} \right)^2 \tag{2.1}$$

where ρ_{agl} and ρ_{SiO_2} are the densities of aerogel and silica, a is the radius of the scattering centre, λ is the wavelength, and $n = n_{\text{SiO}_2}/n_{\text{air}}$ is the relative refractive index of the aerogel [3]. Therefore, we expect less scattering in aerogel with a smaller network, or aerogel of lower apparent density. This explains why ultra-low density two-step aerogels have a higher transmission.

The light transmission also has loss components caused by the external surfaces of the aerogel [74]. Given that the refractive index is so low, Fresnel reflec-

tion is minimal and can safely be neglected. For example, we have calculated the Fresnel reflection coefficient at normal incidence for an aerogel with a refractive index n=1.05 to be 1.2×10^{-3}. Surface scattering, which can be caused by roughness, contamination, or fluctuations in refractive index, can only be neglected if special care is taken to ensure the surface quality.

Images viewed through aerogel can be slightly fuzzy [4, 75, 76]. This is a result of micrometre-scale inhomogeneity in the refractive index, and leads to decreased optical performance [77]. The quality of images through aerogel has been quantified using a modulation transfer function method by Beck *et al.* [74]. They found the aerogel strongly affects the quality of transmitted images, and this degradation could easily be detected by eye. Pajonk *et al.* [71] mention imaging systems when discussing transparency ratio (the ratio of diffuse to direct transmission), but this criteria is insufficient for estimating how good an aerogel will be in imaging applications.

Many optical measurements are combinations of diffuse and direct transmission. In addition, many measurements use integrating spheres on the output, collecting more of the scattered light, but reducing the collection efficiency. This makes it quite difficult to directly compare different aerogels and quote what the loss of any particular sample will be. Additionally, degradation over time, especially in hydrophilic aerogels from water absorption, causes significant change in the optical and physical properties.

2.4.3 Refractive index

Many people have studied the refractive index of silica aerogels, as good knowledge of this property is essential when designing and analysing the data from Cherenkov radiators [78]. Since the refractive index of aerogel is low, measurements require special methods. The most common method of measuring its refractive index is using an angular deflection measurement from a block of aerogel [78]. Other methods have included imaging a grid through a tilted aerogel [79] and examining the form of Cherenkov radiation which, by comparison with simulation, can be used to calculate the refractive index [80].

Carter [78] used the angular deflection method to measure the refractive index of many aerogel tiles, prepared by the Matsushita Electric Works company, as well as analysing the density variation by cutting up small cubes from the tiles. He found variations of 0.5% in refractive index within single aerogel tiles, and 1.3% variations between tiles which were, at least nominally, similar. These aerogels had densities around 0.15 g/cm^3, and although no published data exists on their fabrication, it is likely they were made via a two-step process. There is no mention of the supercritical drying conditions or hydrophobic properties. Carter suggests that material dispersion can be modelled by averaging the refractive index of fully dense silica and air, and verifies that for a small change in wavelength (from 633–544 nm) the experimental variation in refractive index is consistent with that predicted by the dispersion.

Danilyuk *et al.* [81] measured the refractive index of two-step TEOS aerogels dried at high-temperatures. These aerogels were heat-treated at 650 °C to remove remaining organic solvents (and presumably water as they are hygroscopic aerogels). They postulate that the refractive index scales linearly with density, in the form

$$n = 1 + k\rho \tag{2.2}$$

but specify that this is an explicit expansion of the effective permeability of the material

$$\epsilon = n^2 = 1 + \alpha\rho \tag{2.3}$$

The value of k reported in this paper is 0.206 ± 0.001 cm^3/g measured at 633 nm. This value is corrected using the known material dispersion of quartz so that $k = 0.213$ cm^3/g at 400 nm.

Richter and Lipka [79] used a sample of each of the aerogels mentioned above to measure the refractive index of aerogel in a vacuum. The aerogels, when placed under vacuum, are reported to outgas water vapour. This leads to changes in density, and possibly shrinkage, leading to a complicated change in refractive index. Their method of measuring refractive index is using an image magnified through a tilted aerogel onto a CCD camera. The shift in the image is simply related to

the refractive index, thickness and tilt of the sample. Aerogel refractive index is lower in a vacuum, and is unchanged between vacuum and 1 mbar pressure, for both samples. However, their measurement at atmospheric pressure (after pressure has been reintroduced to the sample) is $n = 1.095$ for a sample similar to Danilyuk *et al.* [81], 0.04 larger than expected from density measurements. The authors attribute this difference to water vapour penetrating the sample.

Wang *et al.* [82] investigate the relation between refractive index and density for low- and high-temperature dried aerogels, before and after heat treatment. They report several values of the constant of proportionality k in equation 2.2, but verify that it is constant for aerogels between 0.08–0.3 g/cm^3. They obtain a value of $k = 0.221\,\mathrm{cm}^3/\mathrm{g}$ before the samples are heat treated, dropping to $0.190\,\mathrm{cm}^3/\mathrm{g}$ immediately after. They report that $k = 0.198\,\mathrm{cm}^3/\mathrm{g}$ for a sample with just one hydroxyl group per surface silicon atom. Differing values of k are explained by different water residue content.

Villoro *et al.* [83] also uses aerogel made by Matsushita, specified to be hydrophobic. They quote a manufacturer-provided empirical relation for the refractive index with $k = 0.277\,\mathrm{cm}^3/\mathrm{g}$. They also consider material dispersion using a single-pole Sellmeier equation

$$n^2 = 1 + \frac{a_0\lambda^2}{\lambda^2 - \lambda_0^2} \tag{2.4}$$

where they find $a_0 = 5.36 \times 10^{-2}$ and $\lambda_0 = 91.82\,\mathrm{nm}$.

Bellunato *et al.* [80, 84] measure the refractive index of aerogel using the angular deflection method and from simulation of the photon emission by Cherenkov radiators made of aerogel. They again measure the refractive index uniformity, but this time using a beam deflection measurement that works on the scale of wavelengths of light. The consider four models for dispersion: no dispersion, one- and two-pole Sellmeier equations and a Clausius-Mossotti model.

2.4.4 Nonlinear refractive index

In silica glass (and in many other materials with Kerr nonlinearity), light of sufficiently high intensity alters the refractive index of the material [85] such that

$$n = n_0 + n_2 I \tag{2.5}$$

where n_0 and n_2 are the linear and nonlinear components of refractive index, and I is the intensity of the light. The nonlinear refractive index of silica is $\sim 2 \times 10^{-20}\,\mathrm{m^2/W}$, so observations of nonlinear effects need high-power light sources. Many types of pulsed lasers can reach the required peak powers needed to observe nonlinear effects. For example, Ti:sapphire lasers can have peak powers of 0.2 TW [86], and even lasers with more modest peak powers of 1.6 kW can cause striking nonlinear effects [22].

One interesting consequence of nonlinearity in silica is that, for certain input beam profiles, there is a lens-like focusing. Sheik-Bahae *et al.* [87] developed a method known as z-scan, which can be used to measure the nonlinearity of a material from its lensing effect. The concept of the method is simple: the sample under test is moved through the focus of a lens, and the power behind an aperture is measured using a photodiode (Fig. 2.15(a)). If the sample itself causes a lens effect, then this will move the position of the focal plane, and therefore change the amount of light that passes through the fixed aperture and onto the photodiode. Calculated examples of the z-scan traces are plotted in Fig. 2.15(b): the sign of the nonlinearity influences whether a valley-peak or peak-valley curve is measured.

Seo *et al.* [18] used the z-scan technique to measure the nonlinear refractive index of aerogel. In [18], 800 nm light from a Ti:sapphire laser with a 1 ps pulse duration and an 82 MHz repetition rate was used. The measured nonlinear refractive index was $-1.5 \times 10^{-15}\,\mathrm{m^2/W}$. In later publications [20, 21], the same authors switched to a 532 nm frequency-doubled Nd:YAG laser source, with 8 ns pulses and a 10 Hz repetition rate. Using this laser, the nonlinear refractive index was measured as $-4 \times 10^{-14}\,\mathrm{m^2/W}$. These measurements of nonlinearity are between five and six orders of magnitude larger than in pure silica, and notably have the opposite sign to the bulk material.

Seo *et al.* [20] propose the nonlinear contribution to refractive index arises from either quantum confinement of electrons in the nanoscale network or surface state

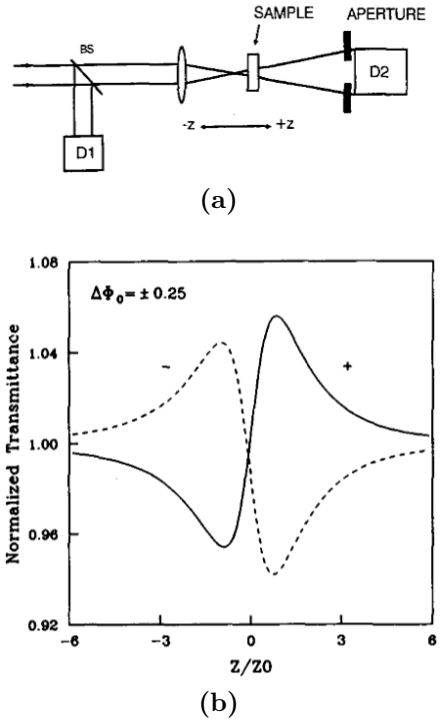

Figure 2.15: (a) Schematic of the z-scan setup. The ratio D2/D1 is recorded and plotted as a function of sample position. (b) Examples of calculated D2/D1 for positive (solid line) and negative (dashed line) values of n_2. Figures both from [87].

contributions. If one of these electronic effects is the source of the nonlinearity, and the measurements of n_2 are correct, then aerogel is a very promising material for nonlinear optics. However, the z-scan method is equally sensitive to thermal lensing effects [87], which is a less interesting form of nonlinearity as it does not contribute to nonlinear generation of new wavelengths. In fact, all the measurements of nonlinearity in aerogel are calculated from lensing properties rather than the generation of new wavelengths in sufficiently high-power pulsed lasers. Since the reports of large optical nonlinearity in aerogels come from only one research group, and the source of the nonlinearity is unclear from their measurements, there is plenty of scope for further investigation of this topic.

2.5 Conclusion

This chapter provides the background required for every subsequent chapter involving aerogels. In it, we have reviewed the sol-gel chemistry used to make alcogels, the supercritical drying methods for making aerogel, and their mechanical and optical properties. It is through our understanding of these topics that we have made progress towards our goal of combining aerogel and fibre optics, starting with the development of the facility for making aerogel at the University of Bath described in chapter 5.

Chapter 3

Building block 2: Fibre optics

This chapter is a review of several types of optical fibres. We start with the simplest case of a step index fibre, which guides light by total internal reflection at the boundary between a cladding and a higher refractive index core. Then we discuss fibre tapering, including why fibre tapering is useful and, in more detail, how our taper rig operates. In the next section of the chapter, we introduce photonic crystal fibres. Our particular focus in this section is on the properties of fibres that guide light in a photonic bandgap. Finally, we summarise two of the methods for making different types of fibre preforms. We recommend the books and review articles [88–92], which can be consulted for more information on various aspects of this chapter.

3.1 Step index fibres

Light incident on a boundary between two dielectric media is refracted according to Snell's Law,

$$n_i \sin\theta_i = n_r \sin\theta_r \tag{3.1}$$

where n is refractive index, θ is the angle that a ray makes with a normal to the boundary, and the subscripts i and r denote the incident and refracted media respectively. If $n_i > n_r$, then there exists an angle θ_i where the refracted ray just grazes the interface ($\theta_\mathrm{r} = 90°$). This angle is defined as the critical angle, θ_c such that

$$\sin\theta_c = \frac{n_r}{n_i}. \tag{3.2}$$

If $\theta_i > \theta_c$ then there is no refracted ray, and the light is totally reflected by the boundary.

If a second boundary is added parallel to the first, so that two identical low-index materials surround a high index "core", then light that is totally reflected at the first boundary will be totally reflected at the second as well. Thus, for certain wavelengths and angles of incidence, we say that light is confined in the structure by total internal reflection (TIR). A schematic picture of this kind of 'slab' waveguide is shown in Fig. 3.1.

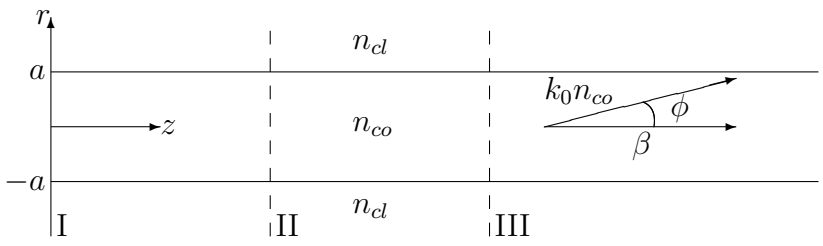

Figure 3.1: A schematic diagram of a slab waveguide. (Region I) The direction of the axes. (Region II) The refractive index distribution $n(r)$. (Region III) Light in the waveguide is described in terms of the wavevector (magnitude $k_0 n_{co}$) and propagation constant β.

Light in the core of a slab waveguide can be described by the axial and trans-

verse components of the wavevector k,

$$\beta \equiv k_z = k_0 n_{co} \cos\phi, \tag{3.3}$$

$$k_T = k_0 n_{co} \sin\phi \tag{3.4}$$

where $k_0 = 2\pi/\lambda_0$ is the free-space wavenumber and n_{co} is the refractive index of the core. From a geometric argument, the angle $\phi = \pi/2 - \theta_i$. If light is reflected at the boundary, then the angle $\phi \to -\phi$. Since $\cos\phi$ is an even function β is a constant and is used to describe a mode of propagation. β is known as the *propagation constant* of a waveguide mode.

A ray travelling perpendicular to the z axis has the maximum value of $\beta = k_0 n_{co}$. In order for light to be in a mode of the waveguide, we must have total internal reflection at the interface. This will only occur when the angle of incidence is greater than the critical angle. Using equation 3.2 and geometry, it can be shown that at the critical angle $\beta = k_0 n_{cl}$. Thus, the range of allowed propagation constants in a slab waveguide is given by

$$k_0 n_{cl} < \beta \leq k_0 n_{co}. \tag{3.5}$$

It is useful to define an effective index of a mode $n_{\text{eff}} = \beta/k_0$ so that this relation becomes $n_{cl} < n_{\text{eff}} < n_{co}$.

Light exits the slab waveguide at an angle that depends on β, shown in Fig. 3.2. Applying Snell's law to the interface between the core and the air gives

$$\sin\phi_{air} = n_{co} \sin\theta_c = (n_{co}^2 - \beta^2/k_0^2)^{1/2}$$

since $n_{air} = 1$. The bounds on $\sin\phi_{air}$ are set by the maximum and minimum values of β such that

$$0 \leq \sin\phi_{air} < (n_{co}^2 - n_{cl}^2)^{1/2}. \tag{3.6}$$

We can define the numerical aperture (NA) $= (n_{co}^2 - n_{cl}^2)^{1/2}$, so that light fills a cone with a half angle given from $\sin^{-1}(\text{NA})$. The same condition defines the acceptance angle at the start of the waveguide.

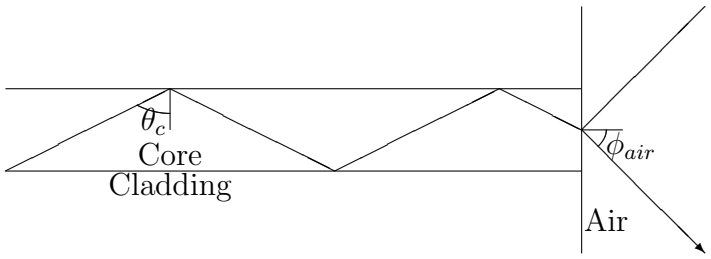

Figure 3.2: This figure shows the end of a slab waveguide. A ray with the minimum guided value of β hits the cladding interface $\theta_i = \theta_c$. All modes with larger β exit the waveguide with an angle less than ϕ_{air}.

Step index fibre has a similar structure to the slab waveguide, with a cladding tube surrounding a cylindrical core with a slightly raised refractive index. Therefore, light in the core can still be guided by total internal reflection. Fig. 3.3(a) is a schematic picture of the step index fibre geometry. The refractive index profile in the radial direction is pictured in Fig. 3.3(b). In fibres made from silica the difference in refractive index between the core and the cladding is normally achieved by doping the core region with germanium.

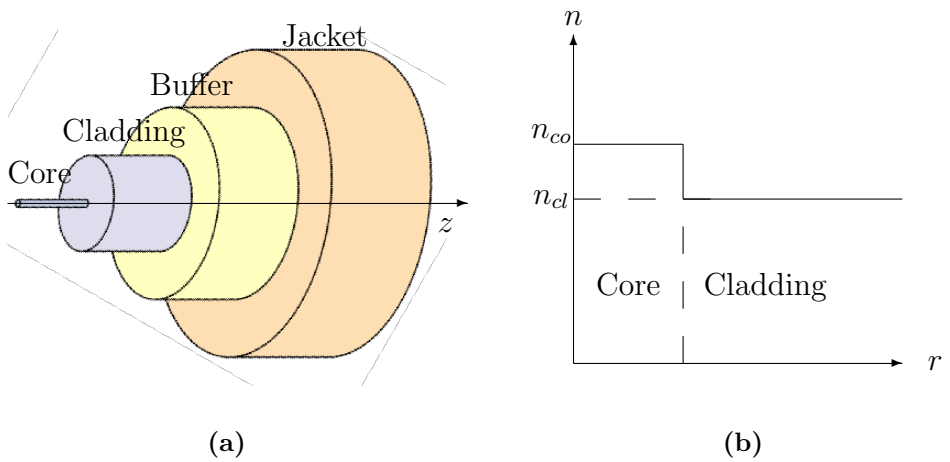

Figure 3.3: Schematic pictures of (a) a conventional step-index fibre (image from [93]) and (b) the refractive index profile of a fibre perpendicular to z.

Light in the fibre is guided by the core, but analysis of the waveguide using

Maxwell's equations reveals modes with quasi-exponentially decaying evanescent fields (see Fig. 3.4) supported in the cladding. This is similar to the exponential decay of the wavefunction of a particle in a finite square well, seen commonly in quantum mechanics. The exact solutions for Maxwell's equations in 2D polar coordinates are from the group of Bessel functions [88, 89].

The number of guided modes in a fibre is related to the size of the waveguide and the size of the index step in relation to the wavelength of light. It is convenient to define a normalised frequency parameter (V value)

$$V = \frac{2\pi\rho(\mathrm{NA})}{\lambda_0} \tag{3.7}$$

where ρ is the radius of the waveguide. From the theory of Bessel functions, if $V < 2.405$ then Maxwell's equations have only one spatial solution, but this one mode always exists. In this case, the fibre is said to be single mode (bar polarisation degeneracy), and the guided mode is the *fundamental* or LP_{01} mode. The fundamental mode is, by definition, the mode with the largest propagation constant in the waveguide.

For small $V \ll 2.405$ the fundamental mode is only weakly confined to the core and a lot of energy is contained in the evanescent field. As V increases, the fundamental mode becomes more tightly confined until the second mode becomes weakly guided. Fig. 3.4 shows the sketches of the field patterns for decreasing V. For large V, the number of guided modes $\approx V^2/4$.

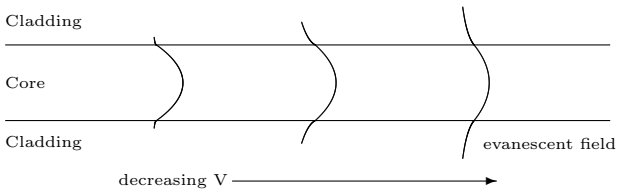

Figure 3.4: Sketches of different field patterns of the fundamental mode for decreasing V from $V \approx 2.405$. For smaller V, the field spreads further into the cladding and more light is contained in the evanescent field.

Real fibres can be made with $V < 2.405$ for a particular wavelength. For

example, Corning SMF-28 is a common type of step index fibre that guides in a single mode for wavelengths larger than 1260 nm. The wavelength at which $V = 2.405$ is sometimes referred to as the cut-off wavelength, as all higher-order modes are cut-off at longer wavelengths than this.

Loss in fibre optics is measured in decibels from the fractional power transmission

$$\text{loss(dB)} = -10 \log \left(\frac{P_{out}}{P_{in}} \right). \tag{3.8}$$

In a uniform waveguide the power $P_{out} = P_{in} \exp(-\alpha z)$, which gives loss $\propto$ length. Attenuation in fibres is the loss normalised over some appropriate distance, usually 1 km for low-loss fibres. The attenuation of SMF-28 is ≤ 0.22 dB/km at 1550 nm.

Fibre optics are made by heating and drawing down a preform of the desired refractive index distribution, but scaled to a larger size. This is described in more detail in sec. 3.4.

3.2 Tapered fibres

Tapered fibres (more colloquially called "tapers") are fibre optics with a changing radial dimension. They can be made either as the fibre is being drawn or in post-processing by re-heating and pulling on the fibre. Tapers made during the fibre drawing process are typically several metres long and the changes in the waveguide dimensions are gradual and often small. Post-processing fibre optics to make tapers on a tapering rig produces much shorter transitions and often much more extreme changes in dimension. Low loss tapers have been demonstrated that change the radial dimensions of the fibre from 125 µm down to just a few hundred nanometres (e.g. [94]).

The tapering rig at the University of Bath uses a travelling hot zone or "flame brush" [95] burning a mix of butane and oxygen to achieve similar temperatures to a fibre drawing furnace, Fig. 3.5(a). The small (~ 1 mm) flame sweeps quickly backwards and forwards along the fibre, which is simultaneously pulled from

both ends. Since the hot zone is small, only the parts of the fibre instantaneously within the flame are stretched. Each sweep of the fibre produces a region that is even in diameter along its length. By altering the length of the hot zone sweeps, the shape of the structure can be controlled into an arbitrary transition and a uniform waist section [95]. Fig. 3.5(b) schematically shows the shape of a tapered fibre.

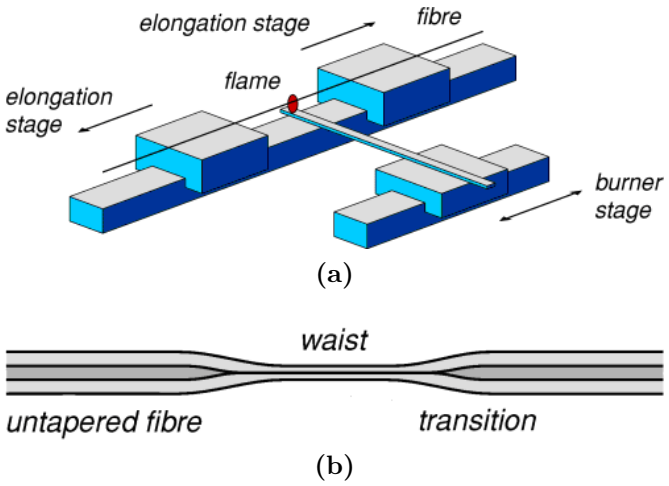

Figure 3.5: Schematics showing (a) the tapering rig and (b) the shape of a tapered fibre, from [96].

Our taper rig is controlled by a computer program that drives the three translation stages (the burner and elongation stages marked in Fig. 3.5(a)). The motion of the stages can be specified by the user for particularly unconventional processing. However, it is more common that we let the computer program calculate the burner motion given a set of desired parameters. Typically, we specify the sizes of the input fibres and the diameter and length of the desired taper waist. Additionally, we can specify the shape and length of the transitions (the default calculation is a simple linear transition), the speed of the stages, and many other parameters. SEMs on submicron tapered fibres made on our taper rig show that the calculated and measured diameters of the taper waist agree to within our measurement ability [94].

The modes of light that can propagate in a taper waist can be very different from in the input fibre. This can potentially cause loss because of poor mode overlap. However, the transition region can be used to effectively couple light

between the fundamental modes of the fibre and taper. If the taper transition is gradual enough, then light in the fundamental mode of the input fibre couples entirely to light in the fundamental mode of the taper waist. These gradual transitions are necessary to make adiabatic tapers from single mode fibre, failure to achieve this results in loss.

A full description of taper transitions requires coupled mode theory [88, chapter 28], and is beyond the scope of this introductory chapter. However, a simple physical description for adiabaticity using diffraction is instructive [97]. (It is easiest to picture this argument in transitions from the waist to the full-sized fibre.) Fig. 3.6(a) shows schematically a transition that is rapid compared to the diffraction of light at the end of the waist. The transition is too abrupt, and has no effect on the coupling. Alternatively, in Fig. 3.6(b), the transition is gradual enough that light is confined by the refractive index boundary and unable to diffract. It is channelled into the full-sized fibre with low loss.

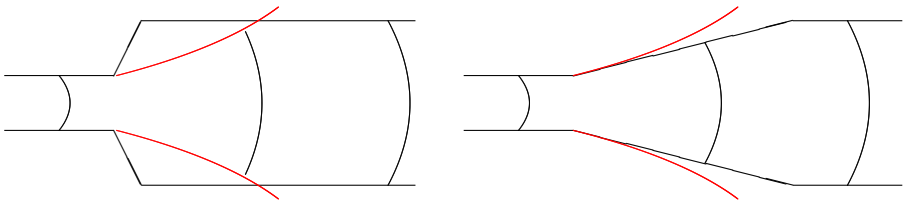

Figure 3.6: Schematics of coupling where the transitions are (a) shorter and (b) longer than the diffraction of light in the medium (marked in red, not exact).

Real tapered fibres can have exceedingly low loss. Tapers of 280 nm waist diameter have been fabricated on our tapering rig with attenuation of 0.38 dB/mm [94]: despite the fact that these measurements include transition losses, they are amongst the lowest reported for this size fibre. These loss measurements were made as the taper was formed, and are referenced to the light power in the untapered fibre. We regularly make tapers with diameters from $125 \rightarrow 1$ µm that have total insertion loss < 0.1 dB, despite being several centimetres long. We have also used the direct control over the stages to implement an "up-tapering" procedure similar to Kakarantzas *et al.* [98], who reported loss < 0.01 dB for a

240 μm diameter up-taper.

As a fibre changes size, the V-value will also change and the mode can become more or less confined. Fig. 3.7(a) shows the deliniation of taper regions by V-value, where the core and cladding can both be either single- or multimode waveguides. The finite size of the cladding is important for tapered fibres because, as we see in this figure, for some tapers it can also act as a single mode waveguide. Fig. 3.7(b) shows the absolute spot size of a tapered fibre versus the V-value of the core (bottom axis) and the cladding (top axis), calculated for a particular fibre [97]. The maximum spot size occurs where the effective index of the fundamental mode coincides with the cladding index [97].

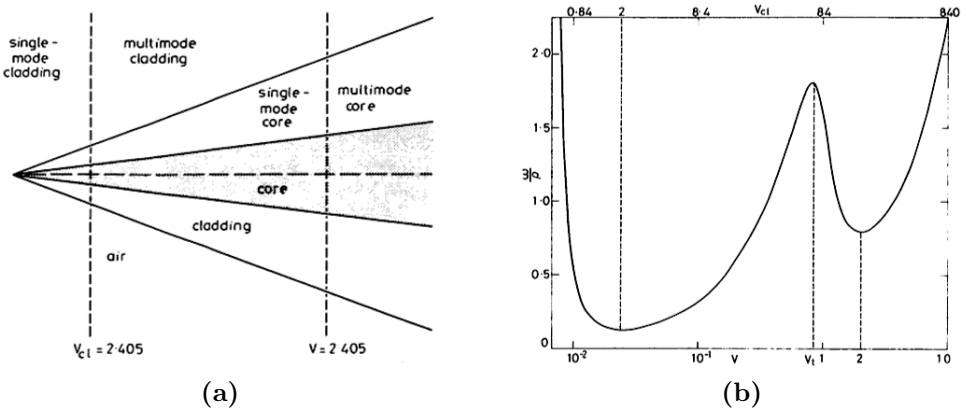

Figure 3.7: (a) Deliniation of single- and multimode regimes versus taper size. (b) Change in absolute spot size normalised to the core of the untapered fibre versus V. The calculations are for a fibre with $V = 2.3$, cladding radius 14× bigger than the core radius, and $V_{cl}/V = 84$. Figures reproduced from [97].

Tapered fibres can be used for different applications. For example, if two touching fibres are tapered together, they can become joined in a common waist. Such devices, called fused couplers, allow light to pass from one fibre into another and function as a fibre-optic beam splitter. By carefully choosing the input structures and the dimensions of the co-joined waist, the coupling ratio for a particular wavelength can be controlled [99]. (Fused couplers are discussed in more detail in sec. 7.3.1.) The wavelength-dependent operation of these couplers is useful for making fibre lasers, where pump light needs to be coupled into the cavity but the laser light needs to be reflected. Tapered fibres have also

been reported for supercontinuum generation [94, 100], sensing [101, 102], and as building blocks for microphotonic devices [103]. These are discussed in more detail in chapters 4 and 7.

3.3 Photonic crystal fibres

Photonic crystal fibres (PCFs) are a type of microstructured fibre where the waveguide properties arise from a regular lattice of media with different refractive indices. They are usually made from a two-dimensional microstructure of glass and air that is uniform along the fibre length. There are many different types of PCF, but we focus on the three shown in the SEMs of Fig. 3.8. The first of these confines light in a high index core by TIR, the other two have low index cores (filled, in the case of these images, with air) and therefore guide light by a different mechanism. This is discussed in more detail for the bandgap fibre (b) in sec. 3.3.2 and for the kagomé-lattice fibre (c) in sec. 3.3.3.

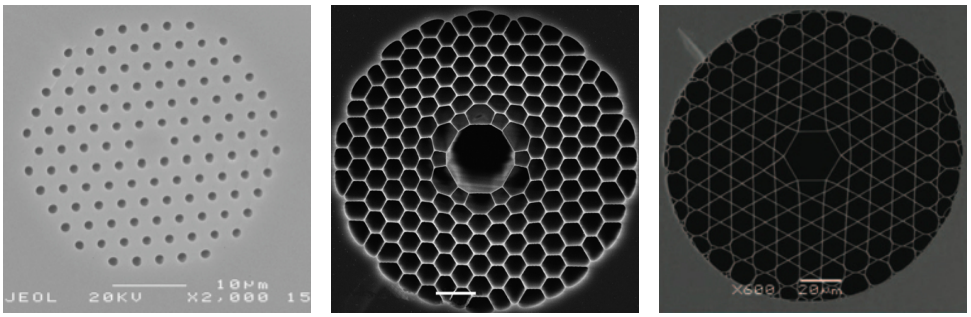

(a) **(b)** **(c)**

Figure 3.8: (a) Index guiding PCF, from [23]. (b) Bandgap guiding PCF with an air core (scale bar is 10 μm), from [104]. (c) Kagomé-lattice PCF, from [105].

PCFs usually contain hexagonal symmetry because this packs well into circular fibre. They are normally made using the "stack-and-draw" procedure described in sec. 3.4.

3.3.1 Index guiding PCF

Index guiding PCFs — such as that shown in Fig. 3.8(a) — are typically made from an array of circular holes of diameter d, separated by a pitch Λ. The "photonic crystal" is an array of air holes in a uniform background of silica, and the core (a defect in the structure) is formed by omitting one of these air holes. The cladding mode with the highest β, also known as the *fundamental space-filling mode* (FSM, lower-case as subscript), controls the number of guided modes in the core in a manner to a step index fibre: guided modes satisfy $k_0 n_{co} > \beta > \beta_{\text{fsm}}$, where n_{co} is the refractive index of silica [106]. In fact, there is a comparable equation for V value with the cladding mode index replaced by the effective index of the FSM $n_{\text{eff}} = \beta_{\text{fsm}}/k_0$, and the radius replaced by Λ. However, unlike in a step index fibre, as $\lambda \to 0$, V tends to a limiting value that depends on d and Λ [106]. Therefore, if the relative size of the air holes is sufficiently small, then the fibre operates in a single spatial mode for all wavelengths.

In the long wavelength limit, light in the FSM becomes less tightly confined in the regions of silica. This has the effect of averaging out the structure in such a way that the effective index tends to the weighted average of the materials' dielectric constants [106]. (The root-mean-square weighted average of the materials' refractive indices.) In fact, this long wavelength limit is applicable to any fibre cladding with the same crystal lattice. This includes fibres like the bandgap fibre in Fig. 3.8(b), despite having a much lower glass fraction. Although this is not relevant for bandgap guidance, we will return to this result in chapter 8 when we discuss our hollow-core fibre filled with aerogel.

3.3.2 Bandgap guiding PCF

A hollow core PCF cannot confine light by TIR, since no solid materials have a refractive index lower than air. However, several other mechanisms can cause light to become trapped in the low-index core of a photonic crystal fibre. This section concerns using a photonic bandgap to create a range of wavelengths that are guided in an air core [107]. In fact, bandgaps are not limited to hollow-core fibres [108, 109] but other structures will not be discussed here.

For certain structures with a 2D periodic lattice, such as the cladding of the fibre in Fig. 3.8(b), there are combinations of wavelength and effective index where light cannot propagate in the third dimension (along the fibre) [91, 110]. Some of the bands where propagation is forbidden lie below the refractive index of air. If the lattice contains an enlarged central core hole (a structural "defect"), then light that cannot propagate in the cladding becomes trapped in this defect. The wavelength range of light guided in photonic bandgap PCF is typically quite small, for example the fibre in Fig. 3.8(b) had a measured bandgap with a minimum attenuation of 15 dB/km at 1550 nm, but the bandgap was only 300 nm wide [104].

Using computers to model PCF claddings and create "finger-diagrams" such as the one in Fig. 3.9(b) can be a useful aid when explaining the fibre's optical properties. There are many available tools for modelling bandgap PCFs, but we have chosen to use an in-house program provided by a collaborator within the Department of Physics. The model uses a fixed-frequency plane-wave expansion for solving Maxwell's equations in a periodic medium [111]. It can be used to calculate the density of photonic states (DOS) for an idealised cladding structure over a range of wavelengths and effective indices, or to plot the mode patterns of particular states. More advanced "supercell" calculations can be used to model the core as well. We modelled an example cladding and DOS (Fig. 3.9) to help us explain bandgap guidance.

The white shaded regions of the DOS plot in Fig. 3.9 are combinations of wavelength and effective index where there are many cladding modes. Diminishing shades simply mean that the number of cladding modes is decreasing. Regions of red have no cladding modes: in the upper left corner, the red region is bound by the effective index of the FSM; other red regions are due to photonic bandgaps in the cladding (apart from the bottom right corner, which is an artefact of the computational parameters we used in this simulation). The blue line marks the effective index of air. Low loss modes in a hollow core must have an effective index below this line. Hence, the range of bandgap guided wavelengths is actually shifted to smaller values of $k_0\Lambda$ (longer wavelengths) than those at which the black and blue lines in the figure intersect (circled). Theoretically, modes can even exist deep in the "pit" of the bandgap (with $k_0\Lambda \approx 14$ and $\beta/k_0 \approx 0.97$ in

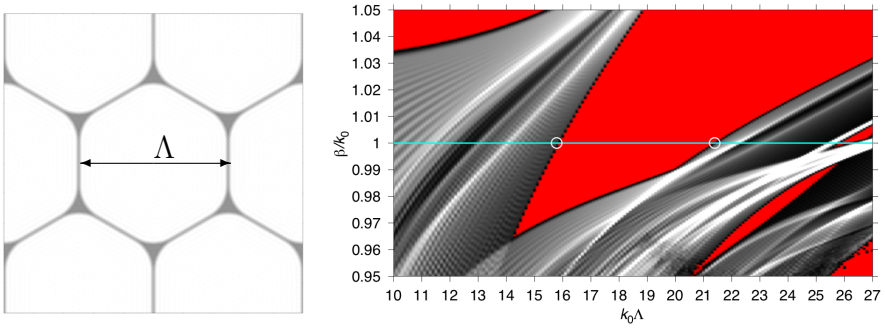

(a) **(b)**

Figure 3.9: (a) A simulation of the dielectric structure of a bandgap PCF cladding and (b) the calculated density of states (DOS) in the same structure. Calculations in our software are normalised to the pitch Λ. In the DOS plot, the white areas mark regions where there are a large number of cladding modes. Black areas mark low numbers of cladding modes and red areas indicate areas where there are no cladding modes. Guidance in a hollow-core mode can occur anywhere the red "fingers" drop below the blue line ($n = 1$).

this simulation).

There are several ways to extend the useful range of bandgap-guided wavelengths in PCFs. Poletti [112] proposed a different lattice design that can cause bandgap guidance for wavelengths from 1000–2000 nm, over three times wider than the region of bandgap guidance for the fibre in Fig. 3.8(b). However, this lattice is more difficult to stack and (to our knowledge) a real fibre with this lattice has not yet been reported. Alternatively, Light *et al.* [113] designed and fabricated a fibre with a similar lattice to the other fibres described in this section, but with the structure optimised to open up a second bandgap-guided region. In these fibres they were able to observe two bandgaps: the long wavelength bandgap extened from 1400–1750 nm, and the second shorter-wavelength bandgap from 1050–1150 nm.

3.3.3 Kagomé-lattice PCF

Kagomé-lattice PCF does not have any photonic bandgaps, instead the fibre confines light because the spatial period of the cladding and core modes are very

different (for the same β) [92, 114]. This leads to a broadband confinement, but with more loss than in bandgap fibres. Typically, kagomé-lattice PCF has attenuation of ~ 1 dB/m in two broad transmission bands, one covering the visible (500–800 nm) and the other covering the infrared (1100–1700 nm) [105]. Recently, low-loss kagomé fibre was reported with attenuation of 0.25 dB/m with similarly broad-band guidance [115]. In addition, kagomé fibre can be made with relatively arbitrary core sizes: Fig. 3.10 shows some SEMs and photographs of large-core kagomé fibres from [105]. Some applications of kagomé-lattice fibre are discussed in more detail in appendix A.

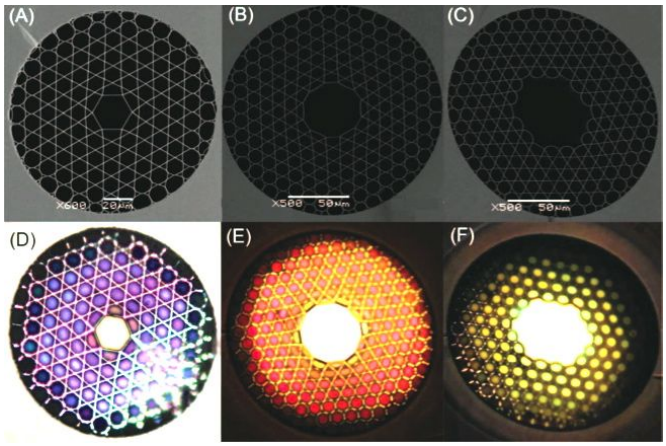

Figure 3.10: (A)-(C) SEMs and (D)-(F) optical micrographs of kagomé fibre made with different sized core defects. The defects were made by inflating the central 1-cell (A & D), or omitting the seven (7-cell, B & E) or 19 (19-cell, C & F) central capillaries during fabrication. Pictures from [105].

3.4 Fibre fabrication

Fibre fabrication is generally a two-stage process. In the first stage, a fibre preform is made, with the desired refractive index distribution scaled to a much larger dimension so that it is easier to make. This is then drawn to fibre by feeding the preform into a furnace at a low speed, and pulling the other end at a high speed. If the preform is completely solid, then the structure is preserved by the drawing process. If the preform includes air holes (for example, for PCFs),

then the structure can be changed during the fibre drawing process by introducing pressure differences.

Modified chemical vapour deposition method

There are several chemical vapour deposition methods for making high-purity preforms for optical fibres [116]. Most of them involve of silicon tetrachloride ($SiCl_4$) and germanium tetrachloride ($GeCl_4$) reacting with oxygen to produce silica (or doped silica) soot. Fig. 3.11 is a diagram of one such method, a modified chemical vapour deposition (MCVD) lathe. In MCVD, a preform is made using a fused quartz tube, which is rotated and simultaneously heated to 1500 °C with a moving flame. The gaseous $SiCl_4$ and O_2 are flowed through the tube, depositing layers of silica that get consolidated by the flame. Adding $GeCl_4$ to the reactants raises the refractive index so that a core region can be deposited. Finally, once the desired refractive index profile has been achieved, the tube is collapsed so that it forms a completely solid fibre preform.

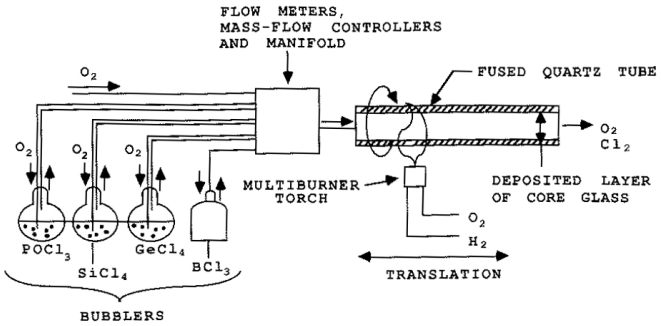

Figure 3.11: The MCVD method for fabricating fibre preforms, from [116]. Various reactant chemicals are fed into a heated, rotating silica tube where they deposit silica soot.

The MCVD process has several advantages when fabricating low-loss fibres [116]. All the deposition happens inside a protective silica tube with gas flowing out of it, so airborne contamination is minimised. Also, $SiCl_4$ and $GeCl_4$ are available at high purities, and their reaction in pure oxygen helps to minimise the number of loss-causing OH groups in the fibre. Finally, because the preform is a solid glass rod, the different thermal expansion coefficient of the doped glass core does not result in cracking even when high doping compositions are used [116].

Stack-and-draw method

An alternative to vapour deposition is shown in the schematic Fig. 3.12. For a given stack design, the first step is drawing the many capillaries and rods that are required. Then, these capillary tubes and rods are stacked into the desired pattern, and this is inserted into a larger jacket tube so that it can be drawn into a preform. Finally, the preform is put in a second jacket tube and drawn to fibre, taking care to preserve the structure as much as possible.

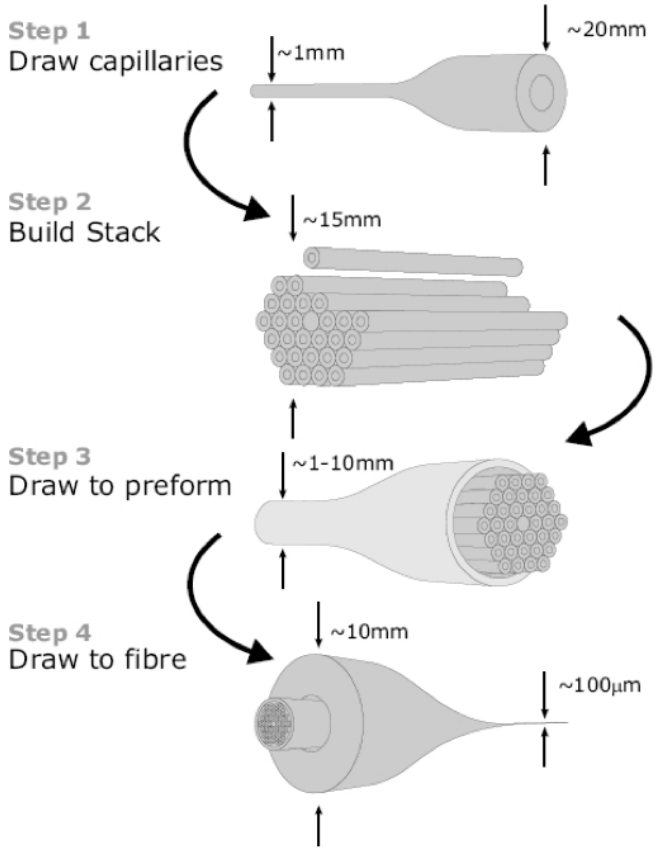

Figure 3.12: The stack-and-draw method for fabricating fibre, from [117].

3.5 Conclusion

This chapter provides the background required for subsequent chapters involving fibre optics. We have reviewed different types of fibre, including step index fibres

and PCFs. We have also described the operation of the taper rig, which is used for making the various tapered fibres discussed in chapters 7 and A. Two different methods are presented for fabricating fibres.

Chapter 4

Combining aerogel and fibres: previous publications

This chapter highlights existing reports of aerogel being used in fibre optics. The first part of the chapter introduces sol-gel methods for making glass. This is a well-established field, and we only present a small cross-section of it. We examine in some detail reports and industrial processes for making glass from aerogel, including using aerogel in preforms for fibre fabrication. In the second part of the chapter, we review the few papers that report aerogel integrated with waveguide devices. To our knowledge, these papers represent everything that has previously been published on combining optical fibres with aerogel. We hope that the reader will recognise the sparseness of the chapter as evidence that there is plenty of scope for further developments of composite fibre–aerogel technologies.

4.1 Fibre fabrication

Sol-gel technology has been developed extensively in the formation of glasses. Historically, it was used to produce optical elements, such as lenses, at low temperatures [25, p. 97]. In these applications, where visible transparency is the primary requirement, xerogel elements such as those in Fig. 4.1 are adequate. However, fibre fabrication requires glass with low visible and infrared loss over many kilometres. This requires special treatments to reduce impurities. Although no longer state-of-the-art, methods of forming glass preforms and specialist shapes can be found in [118, part IV].

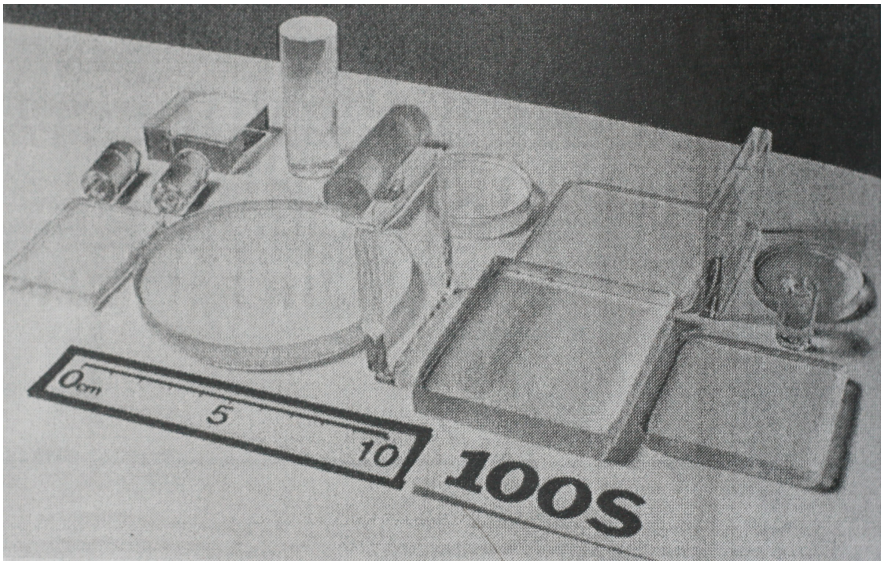

Figure 4.1: Densified glass xerogels can be produced in a variety of shapes, such as those shown in this photograph, from [25, and refs. therein].

Modifications in the processes discussed previously (chapter 2) are required to produce fibre quality glasses. Special sol, formed from fumed silica, is used so that preforms with higher density and purity of SiO_2 are achievable. Conventionally dried xerogel still retains too much porosity, and further consolidation by heating is required. The commercially protected Novara Process® uses TEOS to aid in the gelation of a fumed silica sol [119]. This sol can be precisely cast into arbitrary shapes depending on the application.

Glass preforms for overjacketing can be derived from this sol simply by casting

in a tubular mould [120, 121]. However, even this high quality product needs further adaption to produce glass for fibres. The presence of surface OH causes large attenuation at infrared wavelengths. Careful dehydroxylation of the surfaces can be done using Cl_2, followed by consolidation of the glass at $\approx 1200\,^{\circ}\mathrm{C}$. The resulting glass was demonstrated as a fibre overjacket by MacChesney *et al.* [120, 121], with excellent optical performance and low breakage rates.

PCFs (sec. 3.3) are made from a single type of optical glass interspersed with air holes. Normal fabrication uses the "stack and draw" method (see sec. 3.4), with sometimes hundreds of tiny capillaries. Instead of this tedious process, a sol can be cast in the shape of a holey preform [122]. The wet-gel can then be removed from the mould and converted to xerogel. Heat treatment can be used to remove the hydroxylated surfaces and further sintering can fully consolidate the glass regions. Using this method, relatively arbitrary geometries of fibre could be realised, simply by alterations in the mould.

Thus far, glass production from ambiently dried xerogel has been discussed. As well as xerogel, aerogel can also be sintered to produce glass [25, p. 701 and refs. therein]. There is little published research on glass produced from aerogel. In one of the only papers we have found, a consolidated aerogel was shown to yield glass of a high enough optical quality to form the core of optical fibre with attenuation $\approx 2\,\mathrm{dB/km}$. There are industrial applications of glass produced from aerogel: Evonik Industries [123] use consolidated aerogel glass for UV and IR LEDs, amongst other applications.

The one instance of fibre fabrication directly from aerogel was an attempt to make a cladding containing random holes [124]. Random-hole fibres have interesting sensing properties, with a wavelength-dependent loss sensitive to strain. A stack containing a solid overjacket tube, an aerogel cladding tube, and a solid core rod was drawn to fibre using a conventional tower. The resulting fibre had a large amount of optical loss. Closer inspection revealed that the aerogel had completely consolidated during the drawing process, leaving the core rod attached to the outer jacket. Since drawing from aerogel did not produce the desired structure, the method was abandoned in favour of using silica powder and a gas-producing agent instead.

4.2 Device fabrication

In the previous section, we discussed how aerogel and xerogel have both been used to make consolidated glass. Now we will discuss waveguide devices with an integral aerogel component. In all cases, aerogel is used as a waveguide cladding, so the field there remains evanescent. The benefits of aerogel claddings are the low refractive index, low loss and hydrophobic properties, as well as implicit material compatibility with silica fibres.

Solid-core fibres

Aerogel clad fibre with a solid, high-index core enables fibre with very high numerical aperture (NA) [125]. This is particularly valuable in situations where it is advantageous to increase the collection efficiency. The NA of the aerogel-clad fibre is only slightly less than that of the core simply suspended in air, but the aerogel protects the fibre from loss mechanisms such as scattering by dust particles on the surface. It also supports the fibre in a uniformly low refractive index medium, so light is not lost in the structure used to suspend a core in air (as it would be if the core were suspended by thin glass struts). Additionally, hydrophobic aerogel protects the fibre from moisture, which reduces the likelihood of surface cracking and hence mechanical weakness.

Aerogel clad silica fibres can be made by coating a solid silica fibre with silica aerogel. However, the aerogel can rub off so an additional sheath is required. Sprehn *et al.* [125] used a 12-inch long stainless steel tube with glass rings fitted to hold the silica fibre in the centre while the wet-gel was formed. Alternative sheaths could be made from heat-shrink or plastic wrap. The protective sheath means that high-temperature SCD is the only practical way to make these aerogel clad fibres.

Sandler *et al.* [126] used a 12-inch aerogel clad fibre made using this method as part of an astronomical detector. The fibre reportedly had NA = 1.1, compared to NA = 0.49 for a commercially available alternative. In this case, the acceptance angle more than doubled, and collection efficiency was improved by a factor of three. However, the short length and relative frailty of the fibre meant that, apart

from in exceptional circumstances, it is of limited practical use.

This strictly multi-mode waveguide has an NA > 1, since the refractive index of aerogel is so low compared to the core refractive index. However, there is nothing unphysical about this result, it simply means that some waves guided in the waveguide (determined by the critical angle of the core-cladding boundary) are incident on the output face at an angle greater than the critical angle between the core and air at the output face. These waves cannot couple into or out of the waveguide at a core-air boundary, but could easily be accessed by immersion in water or index matching fluid. Only modes with NA < 1 can be coupled into the waveguide at the core-air interface, and modes with a large NA can only be weakly coupled because of the strong Fresnel reflection at such steep incidence.

It is somewhat easier to cover the fibre core with alcogel by dip-coating, and hence realise thin surface films of around 20 μm [127]. Treating the films to make them hydrophobic makes them less likely to break during solvent exchange with CO_2. Given the thin nature of dip-coated films, exchange and supercritical drying can be completed in less than 30 min. Using this method, considerably longer coated fibres can be prepared.

An even more straightforward, although slightly less successful, scheme is to surround the core with beads of powdered aerogel and use heat-shrink to seal it in place. According to [127], this still creates a fibre with a large NA. This method also removes the need for supercritical drying with the fibre *in situ*, simplifying the fabrication process. However, the patent does not comment on the optical loss introduced by the aerogel beads or powder. A later patent, [128], suggests the scattering is high and can be used as the basis for a side-illumination fibre.

Fluid-filled fibres

Hydrophobic aerogel can form the cladding for a water waveguide [129]. The advantages of an aerogel cladding are that the refractive index is low enough to allow total internal reflection, the material is transparent enough to not cause much additional loss, and the ambiently dried aerogel is inexpensive to produce. In these waveguides, strength and support comes from an external tube, usually made from glass. The inner surface of the tube is coated with alcogel, which is

then modified for hydrophobic properties and dried at ambient pressure. The waveguide is filled with water, and transmits 700 nm light with ~ 10 dB/m attenuation.

Optical nanowires

Optical nanowires are sub-wavelength glass strands usually made by tapering standard optical fibres. Using a two-step drawing technique, where a micron-sized fibre taper is drawn down further by winding around a heated sapphire taper, optical nanowires as small as 50 nm can be fabricated [103]. Nanowires made this way can be tens of millimetres long, with excellent uniformity along the length. They can be bent and coiled to make devices such as couplers and resonators, and are a promising building block for microphotonic devices.

Supporting the optical nanowires and holding them in position so that the properties of devices remain constant is a significant challenge. For example, in an optical nanowire coil, the resonance due to coupling shifts quickly and irregularly as the fibre moves in air currents [102]. These shifts are over seconds or minutes. Since many devices rely on coupling between two adjacent wires, and the coupling conditions are strongly affected by separation, a way of fixing the positions greatly increases the usefulness of devices.

Tong *et al.* [24] used silica aerogel as a substrate to hold optical nanowires, which they cut and manipulated with the probes of scanning tunnelling microscopes. The nanowires fix to the aerogel through short-range van der Waals attraction and can be manipulated, but will hold their positions when untouched. The methods of fabricating tapered nanowires and the application of the aerogel substrate are described in detail in the patent of ref. [130]. Several example photographs, from [24], are presented in Fig. 4.2. The relatively tight bend (e) does not introduce much excess loss, as measured in (f).

Evanescent coupling between parallel nanowires is strongly affected by the separation distance. In fact, variable splitting ratios were observed from 5–90% simply by changing the separation of two 420 nm nanowires bends over 3 μm [24]. By contrast, the splitting ratio of fused couplers is fixed once they are made. The nanowire coupler introduced an excess loss of just 0.5 dB.

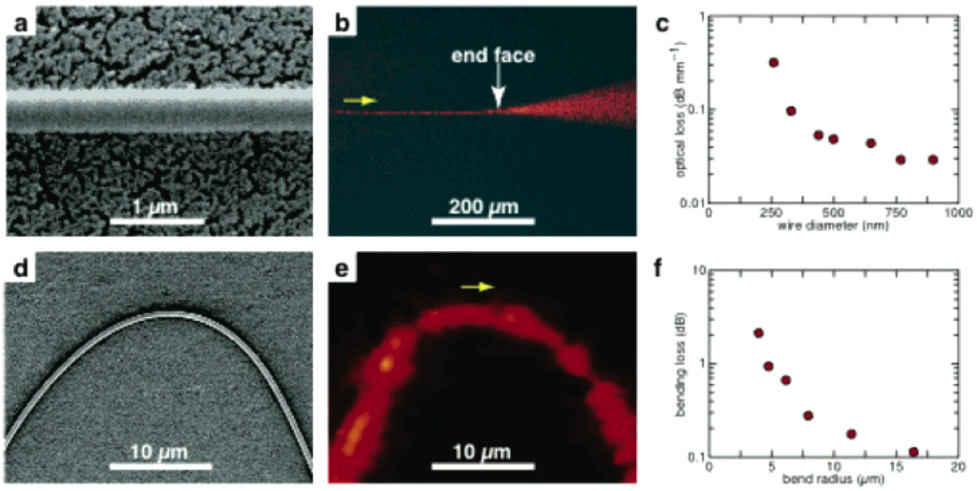

Figure 4.2: SEMs and optical micrographs of 380 nm (a & b) and 530 nm (d & e) optical nanowires illuminated with 633 nm light. (c & f) Measured loss of different diameter optical nanowires and bend-introduced loss for a 530 nm taper at different bend radii. Figure from [24].

Nanowires lying parallel to each other interact strongly by evanescent coupling, but those lying perpendicular do not. The crosstalk between perpendicular wires is −35 dB, so overlapping rotated circuits have virtually no effect on each other's operation.

Nanowire devices on aerogel substrates have two types of instability. Firstly, contaminants such as dust and moisture from the air can easily cause light to scatter from the fibre. Secondly, relative movements between two coupled nanowires cause a significant change in the evanescent coupling. This second instability only affects devices such as couplers or nanowire coils.

In an optical nanowire coil, the aerogel can be used as 'bread', sandwiching the resonator between two sheets. The stability of the resonator is significantly improved, and it was observed to remain stable even after one day [102]. However, the sheets of aerogel do not prevent movement or ingress of water, and eventual degradation of the optical properties is inevitable. Encapsulation of the tapered fibre in Teflon could be more appropriate in some situations [102], but at the expense of greatly increased attenuation.

4.3 Conclusion

We have discussed how sol-gel methods have been previously used in the fabrication of glass, as evidenced by some of the publications we have reviewed. Aerogel has also been used as an intermediate step in glass formation, producing glass of a high optical quality and from a range of materials. However, all this work simply derives high-quality silica glass, rather than incorporating aerogel in waveguides.

There have only been a few significant investigations of aerogel incorporated in waveguides. To our knowledge, they are: three patents for aerogel-clad solid fibres, and a further patent for a fluid waveguide with an aerogel cladding; two reports of aerogel-clad fibres being used in experiments; and two reports and one patent concerning aerogel as a substrate for tapered optical nanowires. In all the aerogel-clad fibres, a further protective layer is required to ruggedise the device for use in applications. However, this additional protection prevents gases from diffusing to the fibre core via the aerogel and interacting with the evanescent component of the guided light.

We believe that the dearth of publications on aerogel in optics is not because it has no uses. Rather, we suspect that general unfamiliarity with aerogel, coupled with the relative complexity of the fabrication process, has put people off. In the remainder of this thesis, we will discuss our development of a facility for making optical quality aerogel and combining it in waveguides. This has allowed us to create encapsulated tapered fibres (discussed in more detail in chapter 7) and aerogel-core waveguides (chapter 8).

Chapter 5

Making and improving aerogel

From this chapter on, this thesis predominantly describes the Ph.D. work of the author rather than background knowledge. This chapter describes the facilities and methods we have developed for working with aerogel, building on the ideas introduced in chapter 2. It begins with an account of work done previously at the University of Bath on sol-gel and aerogel fabrication. This is followed by a description of the procedure we developed for making aerogels, using both the low- and high-temperature supercritical drying rigs we built. Finally, the mechanical and optical properties (including refractive index, transparency and birefringence) of our aerogels are discussed. The developments presented in this chapter were essential to enable work presented later in this thesis.

5.1 History

Sol-gel work began at the University of Bath when Kakarantzas *et al.* [131] investigated making long-period gratings on tapered fibres using xerogel films. The sol was formed from acid catalysed TEOS precursor. Tapered fibres were dip-coated using a travelling bead of sol, which left behind a thin film that gelled quickly on exposure to air. The xerogel layer was consolidated using a CO_2 laser, which could be swept at different rates to create variations in refractive index along the length. Different refractive index modulations could be used to write long-period gratings on the tapered fibre.

Tapered fibres made by S. G. Leon-Saval were transported to Bratislava where they were embedded in aerogel made using high-temperature supercritical drying (SCD, sec. 2.3.2) for the first time. These relatively large tapers (20 μm in diameter) were bent so that the holders were easy to engineer, and completely uncoated because of the temperature range. Because of the sample geometry, the loss was quite large, even though the tapers were big. Smaller tapers were hard to transport, but the principle of embedding tapers in a low-index aerogel was proven.

The first low-temperature SCD aerogel made at the University of Bath was a collaboration between the Departments of Physics and Chemical Engineering, with S. G. Leon-Saval and R. Williams making an acid-catalysed TEOS-precursor aerogel 1 cm thick [132]. A photograph of the aerogel, Fig. 5.1, shows reasonable transparency although the aerogel had cracked in two. The initial rig design was later modified to use a different top-loading pressure vessel. The rig did not produce consistent results, and still struggled to accommodate tapered fibres. In addition, the cycle was long and required an almost-constant user presence for manual pressure adjustments.

In parallel to the low-temperature SCD equipment, a small high-temperature SCD experiment was set up for trying to make aerogel inside a hollow-core PCF. An alcogel-filled fibre was put in a stainless steel pipe, and heated using a pair of hot plates at 500 °C. It was hoped that the fibre itself would act to prevent ambient drying during heating until the methanol in the pores became supercritical. Nitrogen gas at 100 bar was used to provide an inert atmosphere and reduce

Figure 5.1: Photograph of aerogel made by R. Williams as part of his Masters project [132].

the flow rate of methanol out of the fibre before critical conditions were reached. This is similar to the second high-temperature SCD method described on p. 39. No fibres were successfully filled with aerogel using this method.

Alcogel preparation was altered to use TMOS as a precursor, in an effort to obtain more transparent aerogel [50]. The chemical recipe used was similar to Recipe 1 in sec. 2.3.1, with TMOS : methanol : water (containing ammonia) mixed in the ratio 2 : 2 : 1 by volume [133]. The reaction was catalysed with ammonium hydroxide with a few drops mixed in 100 ml water. Gel times were difficult to control exactly, but they ranged from 3–15 min, which is acceptable for making aerogel.

Based on this work, and the potential for continuing and significant results, an EPSRC grant was awarded [134]. The scope of the grant was to investigate ways to combine aerogel with fibre optics. The grant was awarded slightly before the author started this Ph.D. work, but funding from the grant did not start until February 2008. The rest of this chapter discusses our development of equipment and methods related to aerogel since then.

5.2 Making aerogel

In this section, we discuss how our aerogel is made. It combines the theory developed in chapter 2 with our own research and development into the best way to make monolithic aerogel with high optical quality. To begin, we summarise our

baseline method of making "standard" aerogel using low-temperature supercritical drying (SCD). Then, we present a contrasting method for making a similar aerogel using high-temperature SCD. This is followed by a brief discussion on controlling the gel time of a sol. Finally we discuss how we have made high- and low-temperature SCD rigs, describing their operation both in principle and in practice.

5.2.1 Standard aerogels by low-temperature SCD

Aerogel produced by this standard procedure is hydrophobic and dried at low-temperature using supercritical CO_2 (LT aerogel). This procedure forms the building block from which all our other aerogel recipes have developed. The sol is similar to that made by Leon-Saval, but we have altered everything else to improve the resulting aerogel. A considerable amount of development has therefore gone into determining this recipe. The summary here is our most current version, which includes several modifications that provide improved optical quality. These are further expanded upon in later sections.

The alcogel is made from a base-catalysed TMOS precursor process. Instead of the ammonium hydroxide catalyst, we use ammonia dissolved to 2.0 M (molar) in methanol. This means the TMOS, methanol and ammonia can be homogenised before any water is added, which we find makes the gel time easier to control. The purity of the TMOS is 99%.

We find it easier to describe chemical ratios in volumes rather than moles. Table 5.1 shows the equivalent volumes, moles and molar ratio of the components used in making our sol. The TMOS : water ratio is particularly important, and is far in excess of the 1 : 2 stoichiometric molar ratio (R. 5) so that all TMOS can hydrolyse to silicic acid.

The chemicals are combined into sol that is thoroughly mixed, then (optionally) gently agitated by swirling until ~ 2 min before gelation is expected. The motion of the sol under the gentle agitation helps create a more optically homogeneous alcogel on a macroscopic scale. At this point, the sol is poured into PMMA cuvettes $1 \times 1 \times 4\,\mathrm{cm}^3$. In the given chemical ratio, gelation should occur in 8–12 min, but sometimes small adjustments to the ammonia concentration are

Chemical	Volume	Moles	Molar ratio
TMOS	4 ml	2.68×10^{-2}	1
MeOH	4 ml*	9.88×10^{-2}	3.67
H_2O	2 ml	1.11×10^{-1}	4.13
Ammonia	–*	80×10^{-6}	3.0×10^{-3}

Table 5.1: Ratio of chemicals used in making a sol for standard LT aerogel. *A 3.96 ml volume of pure methanol combined with 40 µl of methanol containing dissolved ammonia at 2.0 M.

required to ensure that it does. After gelling in the cuvette, a small amount of methanol is added before sealing the top with Parafilm (a chemical-proof form of cling-film).

The methanol top prevents evaporative drying, and can also (with extreme care) be used remove the meniscus caused by wetting forces at the interface between sol and air. Since gelation is not an abrupt transition, the surface can support methanol slightly before the gel has stopped flowing. The alcogel is mostly methanol so pure methanol is miscible with the pore-fluid. This means there are no wetting forces between the liquid in the gel body and the sides of the cuvette, so the meniscus from the surface disappears since there is no longer a liquid-vapour interface in line with the surface of the gel.

The alcogel needs time to age before SCD. We have discovered that aging times of at least a week help to reduce cracking during SCD. However, while the aerogel is aging we often perform other solvent exchange steps in parallel. During these "washes", the chemicals in the pores of the alcogel are replaced diffusively with the chemicals in the wash solution.

After a day of undisturbed aging, the cuvettes are added to a (sealed) wash of pure methanol so the alcogel can be removed. The cuvettes are carefully placed so they are not touching each other in the wash. After 48 h (hours) the cuvettes become soft, and the alcogel can be removed by simply tipping it out. Sometimes, small cuts on the corners of the cuvette are necessary to help the alcogel come out without breaking.

The alcogel is removed from the cuvette to speed up diffusion and reduce the solvent exchange time in subsequent washes. The important length for diffusion is now 0.5 cm, since all sides of the cuboid-shaped alcogel will allow liquid diffusion.

The alcogels are washed in fresh methanol twice more, for a minimum of 24 h each wash. The fresh methanol reduces the water concentration within the alcogel body, and the time allows the aging process to continue.

The alcogel surfaces are altered so they contain trimethylsilyl (TMS) bonds to make them hydrophobic (see p. 42). This is achieved by diffusing a wash of HMDS : methanol mixed in the volume ratio 1 : 4 into the alcogel. The HMDS breaks down to become TMS and ammonia, but the production of ammonia reduces the chance of TMS bonding to the alcogel surfaces. Normally alcogel is washed in sealed containers, but if the container is left ajar during this wash then some of the excess ammonia can escape and the reaction can continue further. The silylating mixture is washed out after two days using a final wash in pure methanol. This HMDS process is adequate to ensure hydrophobicity, and no study has been undertaken to further optimise the hydrophobic property.

The alcogel is transformed to aerogel using low-temperature SCD. The alcogels are placed in a 500 ml pressure vessel (also known as an autoclave) under 100 ml methanol to reduce the likelihood of cracking. CO_2 is introduced to the autoclave and pumped in until the pressure is 90 bar, then the vessel is heated to 45 °C. The system is held in these conditions for ~ 2 h, which we determined experimentally to be long enough for solvent exchange to complete. The autoclave is depressurised and cooled to ambient conditions over ~ 1 h, a slow enough rate that no condensation occurs. Finally, the aerogel is removed from the autoclave.

Aerogel produced this way has a density of $\sim 160\,\mathrm{g/cm^3}$, and a refractive index ~ 1.04. It typically exhibits 1–5% linear shrinkage. The transparency is generally good, as evidenced by the photograph of aerogel on the Sulis-head background, Fig. 5.2(a).

Water can form droplets on the surface of our standard LT aerogel with a contact angle in excess of 90°. The photographs in Fig. 5.2(b & c) show the contrast between standard aerogel, and aerogel made by the same procedure but with no HMDS washing step. The hydrophobic aerogel, made with an HMDS wash, naturally supports water drops that act as lenses when appropriately illuminated. The scattering of the aerogel makes the shadow region and the lensing effect of the drop visible in the light pattern. The hygroscopic aerogel, made with no HMDS wash, is rapidly destroyed by contact with liquid water drops on the

(a)

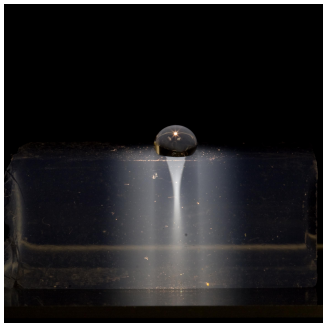

(b)

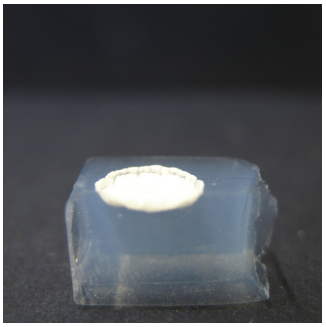

(c)

Figure 5.2: (a) Photograph of a standard LT aerogel, produced as we have described in this section. (b) & (c) Photographs of aerogel with water droplets placed on the surface. The hydrophobic aerogel in (b) supports the droplet. The hydrophilic aerogel in (c) is destroyed at the point where liquid water was in contact with it.

surface. On longer timescales, it linearly shrinks by $\sim 20\%$ as it absorbs moisture from the atmosphere over several weeks even without exposure to liquid water.

Previously, it has been reported that aerogel prepared with MTMS as a co-precursor in the sol is not hydrophobic when dried at low-temperature in CO_2 (p. 46). In our experience, this is not the case: aerogel made this way is not destroyed by contact with liquid water. However, drops sitting on the surface are wetting and do leave more residue and surface damage than those washed in HMDS.

5.2.2 Standard aerogels by high-temperature SCD

Making LT aerogel relies on sample shapes with short diffusion lengths, otherwise exchanging the pore solvent for CO_2 takes a prohibitively long time. Since we hope to make aerogel inside fibres, long diffusion lengths are inevitable. For this reason, despite the more hazardous nature, we have developed a similar standard procedure for making aerogel using high-temperature SCD (HT aerogel).

Since our HT aerogel will have long diffusion lengths, obtaining the hydrophobic property by diffusing HMDS into the alcogel is unsuitable. Instead, we use MTMS as a co-precursor in the sol to create alcogel with slightly hydrophobic internal surfaces. The MTMS causes a single alkyl group per surface site, rather than the three alkyls provided by HMDS. This gives our HT aerogel have a lower contact angle than LT aerogel, but it is still resistant to liquid water.

Table 5.2 shows the modified chemical ratio of components used to make sol in preparation for high-temperature SCD. The ratio of TMOS : MTMS has been optimised slightly to give a good combination of hydrophobic and optical properties in the final aerogel. Once the sol has become alcogel, it does not need an HMDS wash to be hydrophobic after SCD.

Chemical	Volume	Moles	Molar ratio
TMOS	3.6 ml	2.41×10^{-2}	1
MTMS	0.4 ml	2.79×10^{-3}	0.12
MeOH	4* ml	9.88×10^{-2}	4.08
H_2O	2 ml	1.11×10^{-1}	4.59
Ammonia	–*	80×10^{-6}	3.3×10^{-3}

Table 5.2: Ratio of chemicals used in making a hydrophobic aerogel dried at high temperature. *Again, this methanol is composed of 3.96 ml pure methanol and 40 µl methanol containing ammonia dissolved in it to 2.0 M.

The sol made for high-temperature SCD is also gently agitated until shortly before gelation, but it is usually left in test tubes or poured into glass cuvettes rather than PMMA cuvettes. It is possible to make aerogel in these containers because the diffusion length is not as important for high-temperature SCD. Of course, alcogel removed from PMMA cuvettes would also be fine, but more care needs to be taken when removing and handling unprotected alcogel.

Once formed, the alcogel is immersed in methanol and left for at least two weeks of aging.

The alcogel is made into aerogel using high-temperature SCD. The alcogels are placed in a 1 L autoclave with 400 ml methanol. Nitrogen gas is used to test for leaks and to create an inert atmosphere before heating starts. The autoclave is heated over ~ 2 h to 280 °C and the pressure simultaneously rises above 100 bar. The autoclave is then depressurised over ~ 30 min and cools to ambient conditions in approximately ~ 4 h, at which point the aerogel can be safely removed. More precise timings are described in sec. 5.2.4.

Aside from the shape, aerogel produced this way has similar properties to LT aerogel. The subtle differences in its properties will be discussed later in the relevant sections.

5.2.3 Gel time

Many factors affect how long sol takes to become alcogel. The most significant of these, and the easiest to control, is the initial pH of the sol, controlled by the catalyst concentration. Other important factors are the ratio of reagents, their dilutions in the sol, the temperature, how well mixed the sol is, and the mould or container. It is difficult to completely separate many of these factors, but in most cases it is the overall gel time that is our primary concern.

Taking care to control out as many other factors as possible, we studied the gel time of three sols with different methanol concentrations and a wide range of catalyst concentrations. The results are shown graphically in Fig. 5.3. Although the absolute value of ammonia concentration may be slightly different from the quoted values, care was taken to ensure that the relative changes are correct. The gel-time was defined in this study as the time between mixing the chemicals and the point when sol was no longer able to move when tipped. This is an overestimate for the strict definition of gel time, when the first container-spanning network forms, but it is possible to measure using only a stopwatch. All the sols were made by adding the chemicals in the same order (TMOS mixed with methanol containing ammonia, then water), then mixing for 30 s.

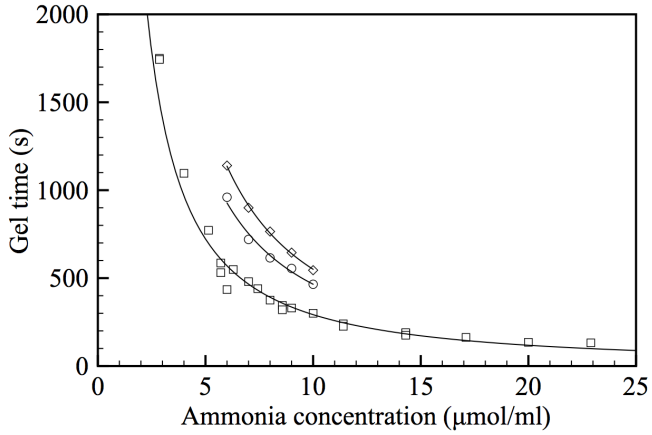

Figure 5.3: The effect of methanol and ammonia concentration on the gel time. The different data sets are for sols made from TMOS : MTMS : methanol : water volume ratios of 3.6 ml : 0.4 ml :x ml : 2 ml, where x = 2 ml (squares), x = 4 ml (circles, as in Table 5.2) and x = 5 ml (diamonds).

During gelation of a sol containing a high ammonia concentration, a lot of heat is generated. This is caused by the acceleration of the hydrolysis reaction (R. 1). We know hydrolysis evolves heat, as acid-catalysed sols get hot and then cool back to ambient temperature in the first ~ 10 min, but gelation does not occur until hours or days later. Sol with less ammonia does not heat up as much, and the slowest-gelling sols barely heat up at all.

The quality of the resulting aerogel is strongly influenced by the gel time. If the sol gels too rapidly, then bubbles and cracks form in the alcogel. This could be because of the temperature change caused by the hydrolysis reaction. Such a temperature change could create a stressed network as components change sizes while they cool down. Alternatively, it could simply be that the increased reactivity creates a weaker network because the primary particles are smaller. If the sol forms too slowly, larger primary particles are formed that cause more scattering loss in the aerogel.

5.2.4 High temperature SCD

High-temperature SCD is simple because (approximately) the same fluid fills the pores and the autoclave. Since the autoclave is sealed, heating causes thermal

expansion and the pressure increases. The whole volume of methanol will become a supercritical fluid (SCF) as long as the initial volume of methanol in our 1 L vessel is above the critical volume of 344 ml (see p. 38). In this case, no evaporative drying will occur in the sample.

The photograph in Fig. 5.4(a) is of the high-temperature SCD rig. The vessel (marked A) is loaded from the top, and sealed with a PTFE gasket. The temperature is measured using a thermocouple in a stainless steel sheath. The oven (outer box B) provides a shield in case of a leak, and the air temperature in the oven does not exceed 160 °C throughout operation. The vessel is heated by an electrical ceramic heater in close contact. The gas outlet line bubbles through water (C), which condenses the methanol exhaust and prevents all but ∼ 10% from leaking into the room.

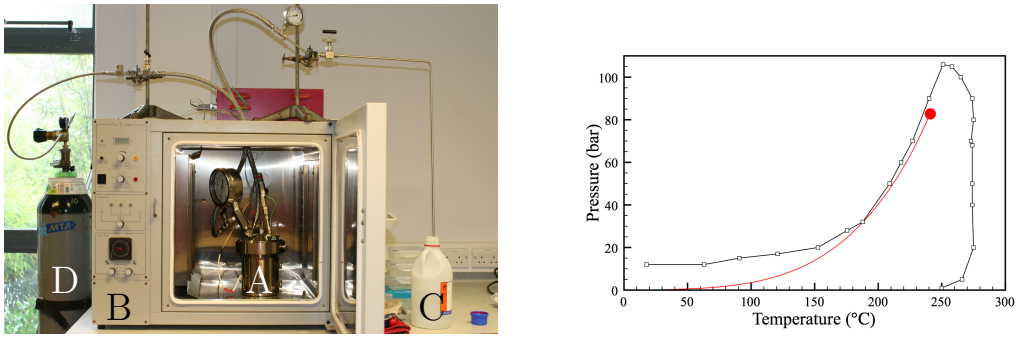

(a) **(b)**

Figure 5.4: (a) A photograph of the high-temperature SCD rig. (b) An example of the pressure and temperature evolution throughout a high-temperature supercritical drying cycle (joined data-points), plotted over the phase coexistence diagram from Fig. 2.9.

The vessel has enough space for up to 12 test tubes in a single cycle. These are put in, along with ∼ 400 ml methanol, and pressurised to 100 bar with nitrogen gas (D). The nitrogen is used to check for leaks, and create an inert atmosphere inside the vessel before heating starts. The gas is released until there is 10 bar pressure remaining.

The sealed vessel is then heated, and the pressure simultaneously rises until the supercritical conditions have been exceeded. The rate of heating is critical to the production of monolithic aerogel. If heating is too rapid, the mismatch between the expansion rate of the solid and liquid components of the gel is large

and the gel cracks. For alcogel of 2 cm diameter, a heating rate 2 °C/min is suitable. If the alcogel is larger, between 4–6 cm diameter, the heating rate must be lowered to 0.3 °C/min [44] otherwise cracks will form. Typically, we have 1.5 cm diameter gels in test tubes, and heating at 2.5 °C/min produces crack-free aerogel. We have noticed that heating from room temperature to 100 °C can be sped up to 15–20 min without resulting in cracked aerogel.

The atmosphere in the vessel is kept at supercritical conditions for 5 min, then the outlet valve is opened to allow depressurisation to 1 bar over 15–30 min.

Fig. 5.4(b) shows a complete SCD cycle marked onto the phase diagram of methanol. The first 7 data points are separated by 10 min, thereafter the interval is 5 min. Although the conditions in the vessel appear to touch the phase coexistence line during the cycle, the additional volume of methanol ensures that the vapour phase is always significantly above the sample level. The critical point of methanol, at the high temperature and pressure termination of the red line, is marked by an enlarged red dot.

The cycle shows that during SCD, the critical point of methanol is exceeded by a considerable margin. We do this to account for water left in the sample from incomplete solvent exchange. In samples that are long and thin (e.g. fibres filled with alcogel), the solvent exchange process takes a long time and there is a significant chance the pore-fluid has not been fully exchanged before drying. This means that the pore fluid could be composed of 5–10% water, modifying the critical point. Assuming a linear interpolation between the critical points of water and methanol, this binary fluid critical point will be at 260 °C, 100 bar.

5.2.5 Low temperature SCD

We have designed and built a flexible supercritical CO_2 rig for drying aerogels at low temperatures. The principal operation of the rig is to provide on-demand CO_2 at user-specified temperature and pressure for solvent exchange and extraction. A process flow diagram (PFD) of the rig is presented in Fig. 5.5, and the complete operation is described in the following paragraphs.

Liquid CO_2 comes from two unregulated cylinders with dip tubes, supplied

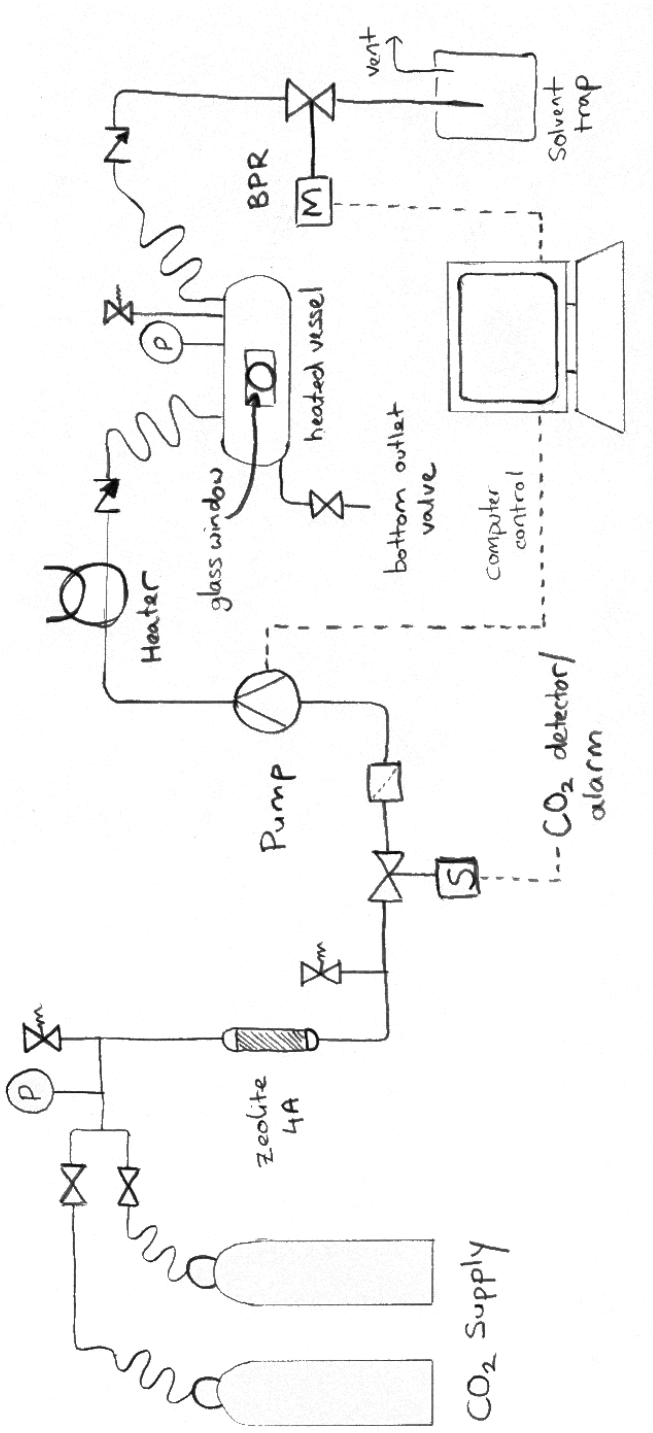

Figure 5.5: The process flow diagram for the low-temperature SCD rig.

by the BOC gas company. The cylinders are filled to 50 bar pressure at 15 °C, and in the warm lab this often rises to 60 bar. The dip tubes ensure that fluid is drawn from the liquid phase of the CO_2. The liquid flows through a drying column filled with Zeolite 4A to remove water, and a 5 µm particulate filter in case of any contaminants.

The line pressure is increased using a dual-piston pump so that strong mechanical shocks are avoided. The liquid state is maintained by chilling the pump heads to 5 °C. On the pump outlet, the high pressures ensure the CO_2 maintains a liquid or supercritical phase. After travelling through the pump the liquid CO_2 flows through a line heater, which can be used to change the temperature of the fluid. This enables supply in either the liquid or supercritical fluid phase.

The fluid flows into a custom-designed vessel, which has a cuboid-shape cavity and a pair of windows so that samples in the vessel are visible. The vessel is top-loaded and big enough to fit multiple samples side-by-side. The dimensions of the vessel allow quite long tapered fibres (chapter 7) to fit without having to bend them tightly. This reduces the likelihood of the tapers breaking in the aerogel.

The vessel outlet is controlled by an automated valve that acts as a back-pressure regulator (BPR). In the configuration we use it, the BPR maintains the vessel pressure for a given pump flow. The outlet line vents the exhaust CO_2 and methanol away from the operator, and contains a solvent trap to collect the methanol whilst allowing CO_2 to escape to the environment. The Joule-Thompson effect causes the outlet gas to be very cold, so condensation and freezing occur in and around the line. This helps the methanol to condense, and enables the solvent trap to operate very efficiently with no extra cooling required. The valve seat is heated to prevent choking caused by the Joule-Thompson effect.

Cracking

Our windowed vessel allows insight into what is occurring during each stage of supercritical drying. In particular, it can help us correlate the appearance of cracks in the sample with events (such as changes in temperature or pressure) during SCD. This has helped us to design a standard operating procedure that enables rapid production of crack-free aerogel.

Almost all previous reports of low-temperature SCD start with the vessel filled with alcohol (see, for example, Tewari *et al.* [8] or van Bommel and de Haan [52]). According to these papers, the excess alcohol prevents cracking caused by ambient drying while the vessel is sealed and the pressurised liquid CO_2 is flowing in. However, using our windowed vessel we have observed that even with no excess methanol, after 10 min the sample is uncracked and not noticeably shrunk. The same alcogel, removed from the vessel and left on the bench, cracked within 1–2 min. Inside the autoclave, the cracking is prevented because the chamber very quickly becomes saturated with methanol vapour.

We attempted solvent exchange with CO_2 starting with no excess methanol in the vessel and opening the supply. The state of the inlet CO_2 was changed by altering the temperature and pressure in the supply line and vessel.

To observe solvent exchange in pure liquid CO_2, alcogel was placed in the vessel with no excess methanol and the vessel and line were not heated. As the CO_2 flowed into the vessel, the liquid level rose up over the sample, and the sample cracked immediately. The reasons for this cracking and solutions to prevent it were not obvious from this experiment.

We tried a similar experiment, but using supercritical CO_2 introduced into the autoclave. An alcogel was placed in the vessel under an excess volume of methanol, and the vessel and line were heated above the critical point of CO_2. This took about 30–45 min, and during this time the excess methanol prevented cracks from forming in the alcogel. When the vessel had reached a high enough temperature of $> 35\,^{\circ}\mathrm{C}$, almost all the excess methanol was drained through the bottom outlet on the vessel, leaving ~ 25 ml left behind. The supercritical CO_2 was introduced at this point, and although there was no rising meniscus (the CO_2 is only ever gas or supercritical phase), the sample still cracked within the following 1 min.

We can speculate on two possible reasons that these gels were cracked by immersion in liquid or supercritical CO_2. Firstly, the concentration gradient between the pore fluid and the pure CO_2 could have caused large osmotic forces as the solvent's tried to exchange through the tiny pores of the alcogel. Alternatively, binary mixtures of methanol and CO_2 have been observed to have complicated phase behaviour [135], with menisci separating several different CO_2-

rich and methanol-rich phases even above the critical temperature of CO_2. This phase behaviour could have been replicating in the alcogels' pores with disastrous consequences.

Fig. 5.6 shows the critical point of a binary mixture of methanol containing x_2 molar fraction of CO_2 [135]. The triangles correspond to the critical pressure at different CO_2 fractions (right hand axis). These show a very large deviation from a linear interpolation between the critical points of methanol and CO_2, to a pressure that is too high for our equipment to reach. This means that as CO_2 diffuses into the pores, the methanol alters the critical point and the fluid is no longer supercritical. Below the critical point, there is coexistence between liquid and vapour phases and surface tension forces can cause cracking.

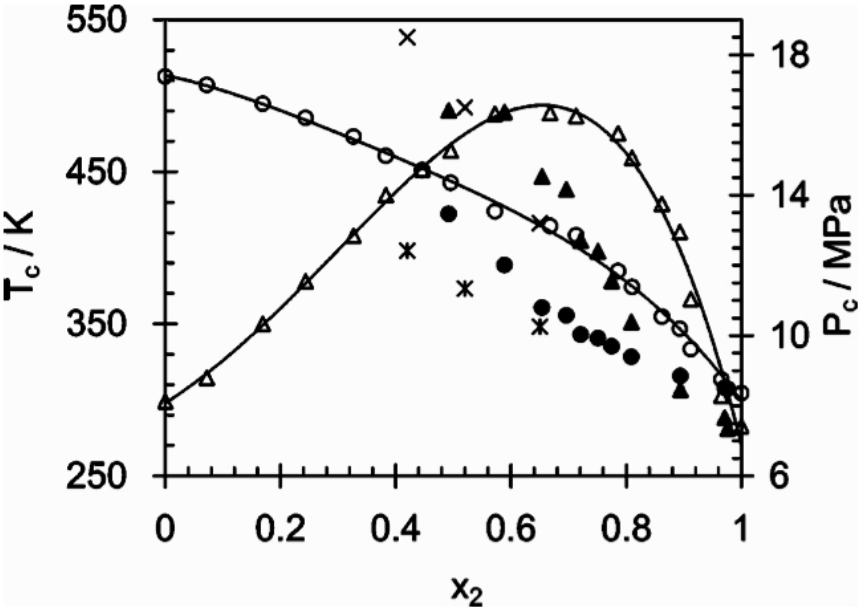

Figure 5.6: Binary critical point of a fractional molar mixture of CO_2 and methanol, from [135]. The triangles are binary critical pressure (right axis), and the circles are binary critical temperature (left axis).

We have observed that adding different amounts of excess methanol to the vessel altered the phase behaviour of the mixture when CO_2 was added. An added complication is that the composition of the fluid in the vessel changes constantly as methanol and CO_2 mixtures flow out and fresh CO_2 flows in. An example of the behaviour of mixture is shown in the series of photographs taken

through the vessel window in Fig. 5.7. For these photographs, 50 ml of methanol was initially added to the vessel, and, as CO_2 was added the mixture eventually seemed to form two distinct phases. Heating the vessel causes the interface to vanish, forming a single phase.

Figure 5.7: Heating causes a change in the phases present in a methanol + CO_2 mixture. These photographs were taken every minute, the vessel pressure was 100 bar, and the internal measured temperature rose from 20–25 °C.

We have experimentally determined that adding 100 ml of excess methanol to the vessel with the alcogel significantly reduces the chances of cracking. This amount of methanol is large enough to move all the phase-separation menisci so that they are above the alcogels in the vessel. It is possible that having the alcogel in a single phase is reducing the chance of cracking, or it could simply be that the osmotic forces are reduced because the concentration gradient is smaller with the methanol in the vessel. Either way, since there is considerably less methanol than if we were to start SCD with a completely full vessel, the duration of a drying cycle can be shorter as there is less methanol to remove.

Some alcogels do still crack during the early stages of SCD, but the appearance of cracks no longer seems correlated to any particular temperature or pressure changes, or any obvious events inside the vessel. We put this down to alcogels with less mechanical strength. Some other factors related to alcogels cracking during SCD include the gel time, aging medium and TMOS purity. If the gel time is too short, cracks often form in the alcogel before SCD starts. Often, we discard these alcogels before SCD as there is no way for the cracks to heal. Since the gel time is related to the dimension of the network, and faster gel times lead to smaller primary particles, it is not too surprising that this has an effect.

If the aging time is insufficient, then alcogel cracks during SCD because the network has not developed enough strength. This cause of cracking is common to

both low- and high-temperature SCD, and we have observed that aging for less than a week results in cracked aerogel regardless of the process.

An extra aging step in a mixture of water and methanol has been reported to strengthen the network [37]. We have observed that similar batches of alcogel are less likely to crack during SCD if the aging procedure includes a step in a methanol–water mixture. However, care must be taken to remove this water before SCD, otherwise it can cause cracking because it is poorly miscible with CO_2.

Different sources of TMOS can strongly influence the propensity of the aerogel to crack during low-temperature SCD. We tested three different types of TMOS, one from Fisher (99% pure) and two from Sigma Aldrich (98% pure, 99% pure). The results of the test are presented graphically in Fig. 5.8. Even with the low number of gels we have in this experiment, it is obvious that higher purity TMOS has a large influence on the number of cracked samples, and this finding is confirmed by later experience. It is more surprising that TMOS from Fisher gives a slightly higher yield than the same nominal purity from Sigma Aldrich, but even small differences in purity seem to have a large effect on the cracking in low-temperature SCD.

The distinction between different TMOS sources does not make any difference to cracking during high-temperature SCD.

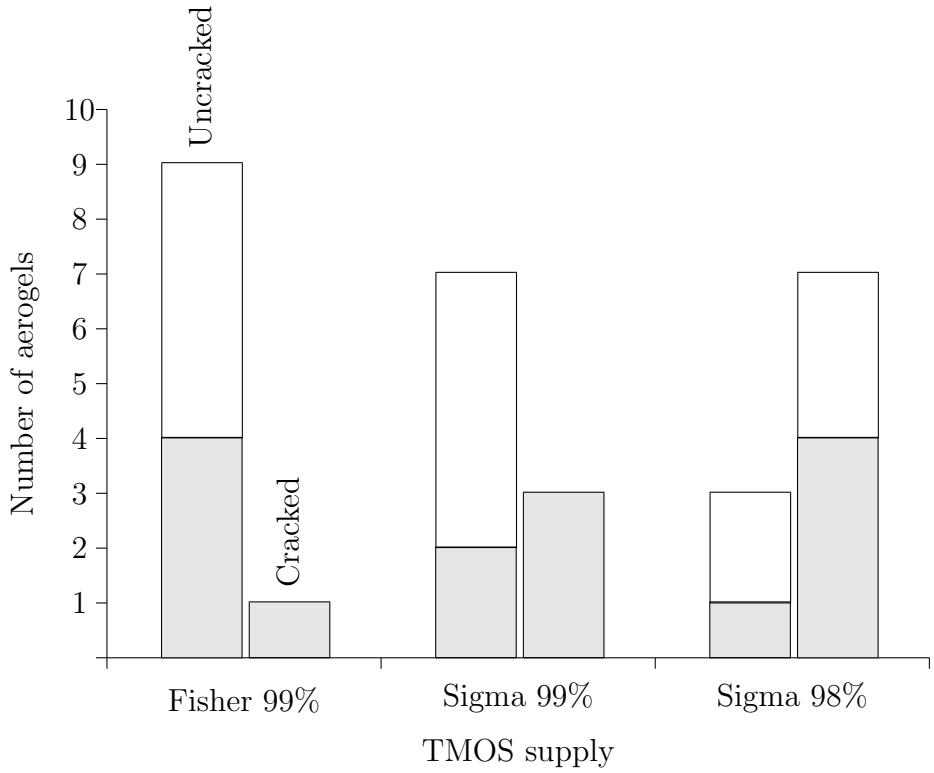

Figure 5.8: The ratio of uncracked (left columns) to cracked (right columns) for aerogels made using different sources of TMOS. The shaded regions represent aerogels that gelled in 7 min, compared to 13 min for the aerogels represented by the clear regions.

Normal operation

The normal operation of the rig for supercritical drying is as follows:

- Alcogel + 100 ml methanol added to vessel
- BPR switched on, CO_2 bottle opened and bottle pressure reached
- Pump switched on, liquid CO_2 pumped in to 85 bar, flow rate 10 g/min
- Temperature gradually increased to 45 °C over 1.5 h
- Pressure increased to 90 bar, flow rate reduced to 5 g/min for 1.5 h
- Flow rate reduced to 2 g/min over 3 min
- Pressure reduced to 80 bar bar over 10 min
- Pump switched off
- Pressure reduced to atmospheric over 15–20 min

During this procedure, cracks still sometimes occur, but seemingly at random rather than associated with any particular event. For some samples, longer depressurisation times up to 3 h are beneficial.

Many factors outside of our control seem to alter the optimum conditions for supercritical drying. For example, the amount of CO_2 remaining in the supply has been observed to cause differences. We also suspect the lab temperature causes differences, especially as the supply pressure can change by ∼10 bar between hot and cold days.

5.3 Mechanical properties

5.3.1 Handling & mechanical strength

Aerogel is quite brittle, breaking when not handled carefully. Nevertheless, with practice even low-density aerogels can be picked up and manipulated by hand.

High-density aerogels are generally quite robust. Aerogel will often survive being dropped with only minor damage.

The natural oils produced by the body cause damage to the external surface of the aerogel, so handling with gloves is advisable for aerogel used in optical experiments. The aerogel captures, quite beautifully, an image of a fingerprint in the damage on its surface when no gloves are used.

Aerogel, especially dried by low-temperature SCD, has a slight electrostatic attraction. This causes dust and contaminants from the air to stick to it, marring the external surface when left in an uncontrolled atmosphere. This type of degradation is easily prevented using a sealed box, and these contaminants can often be washed from the surface by either gentle blowing with dry air, or (if the aerogel is hydrophobic) by immersing it in water. Some aerogel also sticks on certain types of plastic, with a large enough attraction that it breaks when removed. It is not clear what causes this sticking.

When cutting and polishing aerogel, it is nearly impossible to retain the high-quality surfaces and large porosities. In our experience, even using a diamond saw blade to delicately slice the aerogel causes glass fragments to separate from the network and wedge in the pores. The cut aerogel has a matt appearance. Efforts to improve the surfaces by polishing just led to breakages with the same surface quality as the cut.

Instead of cutting, aerogel can be cleaved with relative ease. A slight score on the external surface creates a mechanical weak point, similar to cleaving in a fibre. However, the cleaving planes are much harder to control, and often the surface is angled. Since the refractive index of aerogel is so low, a slightly angled surface does not cause much refraction and is adequate for most purposes.

5.3.2 Density & Shrinkage

The density of aerogel can be controlled by changing the ratio of chemicals in the sol, as adding relatively more of the TMOS precursor increases the number of Si atoms within a unit volume and so increases the density. It is particularly convenient to alter the TMOS: methanol ratio and fix the TMOS: water ratio,

as methanol has only a weak effect in the reactions that lead to gel formation. By keeping the ammonia concentration within the methanol constant, similar gel times for different density gels are maintained.

Using this method, we have made aerogel with densities from 0.10–0.22 g/cm^3 in both high and low-temperature SCD. The density of aerogel is measured using simple methods to measure the mass and volume.

The mass is measured on a top-pan balance, which is accurate to ± 0.001 g. However, we have noticed the aerogel mass seems to fluctuate in time more than other materials, so the error is closer to ± 0.005 g. If the aerogel is hygroscopic, moisture absorption from the atmosphere can lead to a change in mass $\sim 5\%$ on timescales of 10 min.

The volume of aerogel is calculated from measurements of the aerogel dimensions. Measurement techniques using vernier callipers are reasonably accurate for samples made in cuvettes, as the aerogels have regular shapes. The error introduced by the surface meniscus, the dimple in the base of a cuvette, and the slight 'give' in the aerogel contribute to a volume error of ± 0.15 cm^3. Taking into account this inaccuracy gives density measurements within ± 0.025 g/cm^3 for a ~ 2 cm^3 aerogel.

As an alternative, estimating the volume from the known initial alcogel volume and the shrinkage is very useful for samples with irregular geometries. This is particularly true with the aerogel made in test tubes using high-temperature SCD, where the rounded test-tube base makes accurate measurements very difficult. The error here is somewhat larger, arising from the uncertainty of the initial volume of alcogel (we estimate the error to be closer to ± 0.25 cm^3). Carrying this error forwards gives density accurate to within ± 0.05 g/cm^3 for a ~ 2 cm^3 aerogel.

All our aerogel exhibits a small amount of shrinkage during supercritical drying regardless of composition and drying method. High temperature SCD causes $\sim 5\%$ linear shrinkage, seemingly irrespective of the target density. Low temperature SCD causes similar linear shrinkage in hydrophobic aerogel. Higher target density aerogels have lower shrinkage, probably due to a stronger network created by more material. Taking extra care over each of the steps, these high target

density gels can have shrinkage $\sim 1\%$.

5.4 Optical properties

Optical measurements are aided by making aerogel with flat and parallel surfaces. This is why we choose to form alcogel in cuvettes (PMMA cuvettes for LT or HT aerogel, glass ones for HT aerogel only). This has the added advantage that it is simple to measure the transmission spectrum of the alcogel as well. This is particularly relevant when trying to dope the aerogel, as we will discuss in chapter 6.

The high optical quality of our aerogel surfaces reveals that the aerogel has an internal structure of large refractive features resembling schlieren. These are responsible for distorting beams passing through the aerogel, and can be seen as regions of shadow in light passing through the aerogel. The comparison between the beam of a red laser (Fig. 5.9(a)), and the same beam with an aerogel in between the source and the screen (Fig. 5.9(b)), show this difference very clearly. Although the patterns produced are different in all aerogels, they always lie in the same direction, i.e. in line with the long axis of the cuvette. Similar structures have been observed in other aerogels, always aligned with the longest axis.

In contrast, gently agitating by swirling the sol until just before it turns to alcogel creates a very homogeneous structure. In aerogel prepared using this method, a transmitted beam has virtually no degradation caused by macroscopic inhomogeneity (Fig. 5.9(c)). This development means that devices such as lenses made from aerogel could be used in optical systems as they preserve the quality of the image.

5.4.1 Refractive index

We have tested several methods for measuring the refractive properties of aerogel directly. Unlike the methods discussed in sec. 2.4.3, these measurements do not require two flat faces joined by a particular angle. The first two methods require only a single interface, and measure either the critical angle for total internal

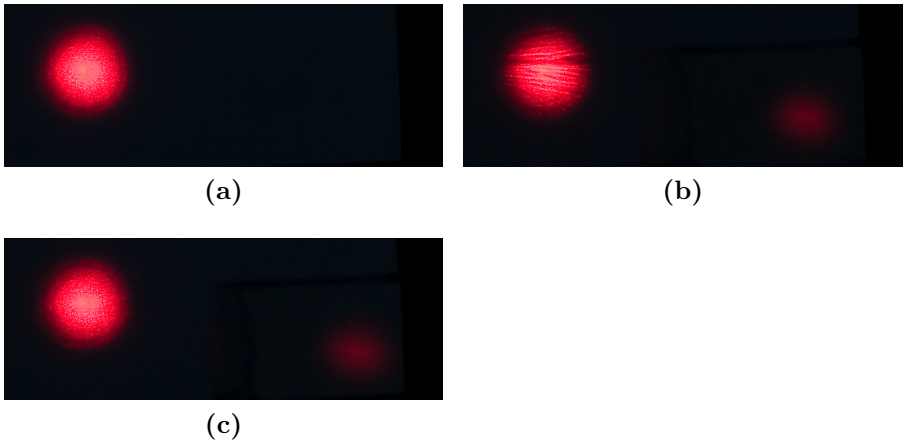

Figure 5.9: Photographs of a red laser spot imaged through a 10× microscope objective. (a) the laser spot, (b) the spot imaged through LT aerogel without gentle agitation of the sol, (c) the spot imaged through a standard LT aerogel (with the agitation). The schlieren-like structure that causes the shadows in (b) is virtually eliminated in (c) and the beam quality is high.

reflection or the Fresnel reflection due to the refractive step. The third method is a measurement of the refractive properties of an aerogel cylinder, and is suited to measuring the aerogel we make in test tubes using high-temperature SCD.

Total internal reflection

A block of aerogel can be arranged so that light in the aerogel is incident on an external surface at the critical angle, θ_c. The critical angle is determined by monitoring the refracted ray while adjusting the incident angle; the critical angle is the point when the refracted ray disappears. A top-down photograph is analysed using a suitable computer program, such as ImageJ, to measure the angle between the incident and reflected rays. This measured angle is $2\theta_c$. As an example, two photographs of different refractive index aerogels with light at incident at the critical angle are presented in Fig. 5.10.

The refractive index can be calculated from the critical angle using the simple relation

$$n_{\text{agl}} = \frac{1}{\sin\theta_c} \tag{5.1}$$

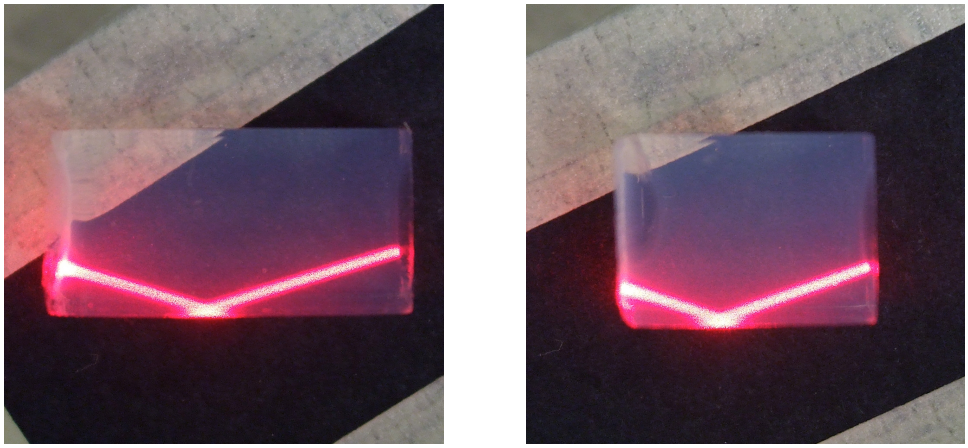

(a) **(b)**

Figure 5.10: Photographs of aerogel with different refractive index, with critical angles of 73.5° (a) and 71.5° (b).

from Snell's law. For the aerogels in Fig. 5.10, the critical angles of 73.5° and 71.5° correspond to refractive indices of 1.043 and 1.054 respectively. The angular measurements are accurate to $\Delta\theta_c \pm 0.25°$, corresponding to an error $\Delta n_{\text{agl}} \pm 0.002$. A more significant source of error arises from the difficulty of estimating when the incident light is exactly at the critical angle. We estimate the error in this measurement to be $\Delta\theta_c \pm 0.5°$, which equates to a total error in refractive index $\Delta n_{\text{agl}} \pm 0.005$.

Fresnel reflection

The Fresnel reflection coefficients [136, p. 114] for light incident at an angle θ_i on a planar boundary between materials of index n_i and n_r are

$$\mathrm{R}_\perp = |r_\perp|^2 \tag{5.2}$$

$$\mathrm{R}_\parallel = |r_\parallel|^2 \tag{5.3}$$

where

$$r_\perp \equiv \left(\frac{E_1'}{E_1}\right)_\perp = \frac{n_i \cos\theta_i - n_r \cos\theta_r}{n_i \cos\theta_i + n_r \cos\theta_r}, \tag{5.4}$$

$$r_\parallel \equiv \left(\frac{E_1'}{E_1}\right)_\parallel = \frac{n_r \cos\theta_i - n_i \cos\theta_r}{n_r \cos\theta_i + n_i \cos\theta_r} \tag{5.5}$$

are for plane polarised waves with electric field vectors perpendicular and parallel to the plane of incidence respectively (θ_r is the angle of the refracted ray). For a circularly polarised light source, half of the light is in each polarisation and the overall reflection coefficient becomes

$$R = \frac{1}{2}(R_\perp + R_\parallel). \tag{5.6}$$

At normal incidence with $n_i \approx n_r$, this simplifies to

$$R \approx \frac{\delta n^2}{2n} \tag{5.7}$$

where $\delta n = n_i - n_r$. This quadratic dependence on the difference in refractive index is useful for trying to measure small changes in n, such as the step between aerogel and air.

Exact graphical solutions for varying incident angles to a boundary of $n_i = 1$ and $n_r = 1.05$ are shown in figure 5.11 for both polarisation states and circularly polarised light. These indicate that, for angles less than 10°, the reflected intensity is only weakly dependent on the polarisation. They also show that the reflected intensity will be $\mathcal{O}(10^{-3})$ for most of our samples.

The weak dependence on angle and strong dependence on refractive index should make this method generally applicable to relatively arbitrary samples. However, there are several practical reasons that Fresnel-based measurement of refractive index is difficult. In aerogel that has not been made under continuous agitation - where there is a structural element to the bulk - the reflections are influenced by the internal structure. Even when the aerogel has been made with continuous agitation of the sol, back-reflections, bulk scattering hitting the detector and diffraction from sub-wavelength structures have made measurements using this method impractical.

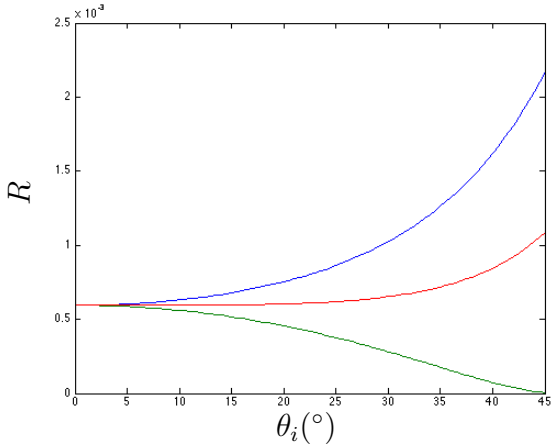

Figure 5.11: The Fresnel reflection coefficient of an index step $\delta n = 0.05$ for parallel (blue), perpendicular (green) and circularly (red) polarised light incident between 0° and 45°.

Refraction by a cylinder

The curved surface of an aerogel cylinder acts as a lens. Scanning a small beam up and down the surface, its change in position at a known distance can described by geometrical optics. The schematic picture of Fig. 5.12(a) shows an aerogel cylinder of radius R, with a ray incident parallel to the axis at height y_1. This is diffracted twice, as it enters and leaves the aerogel. The incident angle can be calculated from geometry, $\sin\theta_i = y_1/R$. The relation between incident and refracted angle is $\sin\theta_i = n_{\mathrm{agl}} \sin\theta_r$, from Snell's law. The output angle and distance d determine the height the ray hits the screen, such that

$$y_2 = R\sin(2\theta_r - \theta_i) - d\tan(2\theta_i - 2\theta_r) + R\cos(2\theta_r - \theta_i)\tan(2\theta_i - 2\theta_r). \quad (5.8)$$

If d is larger than the focal length of the cylinder lens, then y_2 will be a negative for positive values of y_1.

Fig. 5.12(b) shows an example measurement of refractive index using this method. The cylinder radius was measured as 7 mm, and the screen was 570 mm from the cylinder centre. Input positions were altered using a stable translation stage with a vernier handle. The experimental zero-position was determined by adjusting the aerogel height in the beam until no deflection was observed. The position y_1 was altered in 0.5 mm steps, and the y_2 positions were measured.

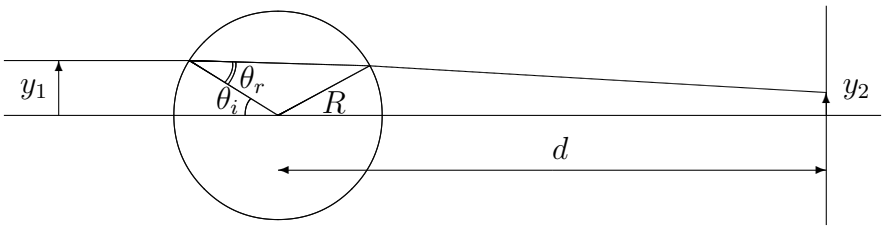

(a)

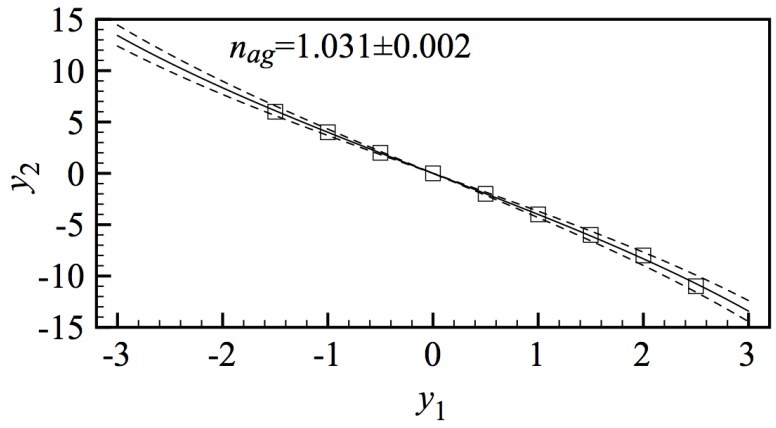

(b)

Figure 5.12: (a) A schematic of refraction by a cylinder of low-index aerogel. (b) measured (squares) and calculated (lines) deflection of a light ray by a 7 mm diameter aerogel cylinder on a screen at $d = 570$ mm. The calculated lines are for a refractive index of 1.031 (solid line) ±0.002 (dashed lines).

The refractive index was fit as a parameter until good agreement with the measured data was observed. The best fit is shown by the solid line, but the physical size of the data (which approximates the error in the measured y_2) means it can be described by the dashed lines as well. This gives us a similar error as the TIR method, $\Delta n_{\mathrm{agl}} \pm 0.002$. This is sufficient for most of the measurements we are interested in.

Relation between density and refractive index

We checked the relationship between aerogel density and refractive index for samples made using low- and high-temperature SCD, measured using both TIR and refraction from a cylinder. The results are presented in Fig. 5.13. The data all lie near to the linear relationship of equation 2.2, $n_{\mathrm{agl}} = 1 + k\rho_{\mathrm{agl}}$, with a value of $k = 0.26$. This value is within those reported in the literature as we reviewed in sec. 2.4.3.

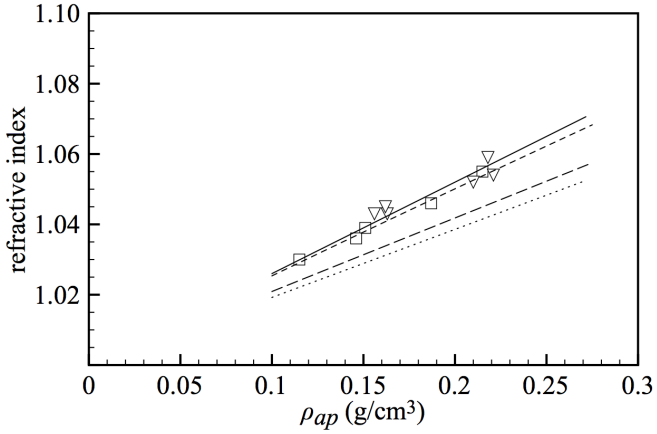

Figure 5.13: The refractive index of aerogel versus density. The squares are measurements on high-temperature dried aerogels using the cylinder refraction method. The inverted triangles are measurements of refractive index from TIR on low-temperature dried aerogels. The solid line is the linear relation $(n-1) = 0.26\rho_{\mathrm{agl}}$, the long and short dashed lines are average n and average n^2 effective indices, and the dotted line is the Looyenga effective medium approximation [137].

There are several other possible scaling laws that could describe a relationship between refractive index and density. For example, the long dashed line and short dash line of Fig. 5.13 are respectively the linear and root-mean-square (r.m.s) porosity-weighted averages of the refractive indices of glass and air for each aerogel. They are calculated from

$$\langle n \rangle_{lin} = P n_{\mathrm{air}} + (1-P) n_{\mathrm{SiO_2}} \tag{5.9}$$

$$\langle n \rangle_{rms} = [P n_{\mathrm{air}}^2 + (1-P) n_{\mathrm{SiO_2}}^2]^{(1/2)} \tag{5.10}$$

where the porosity can be taken to be $P = 1 - \rho_{\text{agl}}/\rho_{\text{SiO}_2}$, and we have used $n_{\text{SiO}_2} = 1.45$. The dotted line fit is the calculated Looyenga effective medium approximation for n_{agl} [137].

It is interesting to note that of the three effective index calculations, the most accurate at describing the experimental observations in aerogel is the r.m.s average. Since $\epsilon = n^2$, this is the linear average of the materials' dielectric constants. Naively, this is what would be expected from aerogel, as the internal structures should be sufficiently small and with no preferred direction.

5.4.2 Optical transmission

Aerogel formed in cuvettes has less surface scattering and does not cause focusing or beam walkoff. This makes it straightforward for measuring the optical loss caused by scattering, absorption, and Fresnel reflection (the last of which we have seen is negligible in aerogel).

Our spectral measurements are made using a Bentham single grating monochrometer and a photodiode, controlled by a computer program that measures the photodiode current at each wavelength. A schematic of the monochrometer setup is shown in Fig. 5.14. It is clear that in this configuration, the spectral measurements include light that is scattered in the aerogel but still hits the detector: the near-normal diffuse transmission. This means that most of our estimates for transmission will be a slight overestimate of the normal-direct transmission. We have fitted slits to the monochrometer that give it a 1 nm resolution when operating with the appropriate diffraction grating. The aerogel transmission is calculated at each wavelength from the current, as measured by the photodiode with the sample present compared to a suitably chosen reference, such that

$$I_{\text{T}} = \left(\frac{I_{\text{sample}}}{I_{\text{ref}}} \right) \tag{5.11}$$

This is converted to optical loss (also called extinction in chapter 6, particularly when referring to plasmonic aerogel) using

$$\text{Loss (dB)} = -10 \log(I_{\text{T}}) \tag{5.12}$$

When defined this way, loss is positive and gain is negative. For an aerogel on its own, the reference is the spectrum measured by the equipment when no sample is present. For alcogel, finding a suitable reference is difficult as the cuvette introduces loss that is hard to correct. This will be discussed in a little more detail in chapter 6.

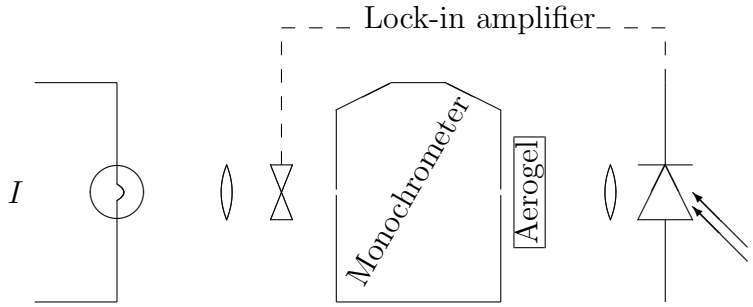

Figure 5.14: A schematic of the monochrometer setup for measuring the transmission through aerogel.

Fig. 5.15 shows the transmission and loss spectra of two different density aerogels made by low-temperature SCD. The transmission spectra are comparable with those in sec. 2.4.2, although our aerogels are not quite as transparent as the most transparent aerogel reported in the literature. The dips in transmission are caused by the resonance of molecular bonds in the network or on the surface. In particular, we expect the double-peaked loss at 1400 nm is caused by the OH in the bulk and on the internal surface of the aerogel [138]. We believe the other double-peaked absorption at 1700 nm arises from a CH resonance in hydrophobic (methyl) groups and unreacted methyoxy groups in the network [139].

The normalised loss spectra show that in the infrared, away from the molecular resonances, the aerogel has attenuation of ~ 0.1 dB/cm. This ignores the Fresnel reflection, which is small. The attenuation in dB is useful for calculating the loss through thicker pieces of aerogel or for aerogel incorporated into waveguides.

The red lines marked on the spectra of Fig. 5.15(b) were fit using the parameter A in

$$\text{Loss (dB)} = A\lambda^{-4} \tag{5.13}$$

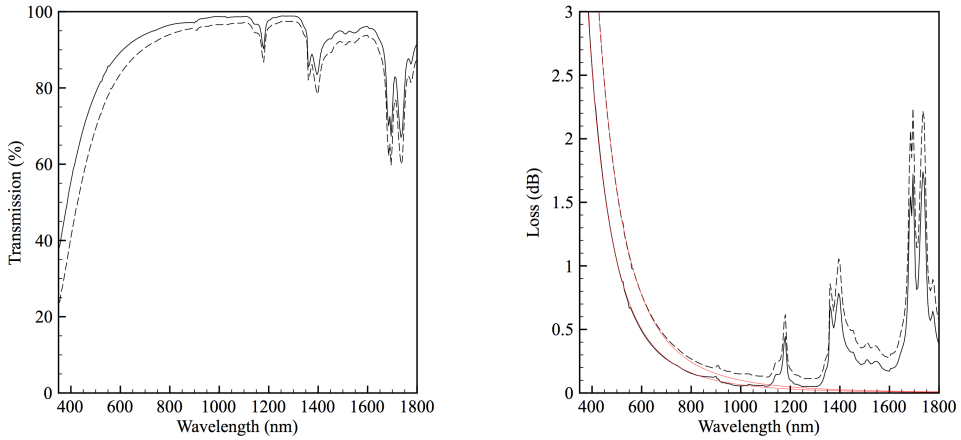

(a) **(b)**

Figure 5.15: (a) The spectral transmission of aerogel with low (solid lines, ρ_{ap}=0.16 g/cm^3) and high (dashed lines, ρ_{ap}=0.21 g/cm^3) densities. (b) the same results converted into loss in dB. The red lines are for a fit $\propto \lambda^{-4}$. The aerogels were 10 mm thick.

This is the expected form for the relationship between loss and wavelength for Rayleigh-like scattering [140]. For visible wavelengths (< 900 nm), the aerogels closely follow the Rayleigh scattering formula. In the infrared, as we have discussed, the spectra are dominated by resonant absorption features.

The loss spectra in Fig. 5.16 are for similar density aerogels made with an MTMS co-precursor and dried using high-temperature SCD. The spectra have a similar shape to their low-temperature counterparts, but the differences in the details are intriguing. In the visible range, the aerogel has slightly more Rayleigh-scattering loss, despite the fact that the network is expected to become more uniform during high-temperature SCD. In the infrared, the molecular resonances are reduced despite the fact that these aerogels have a lower contact angle (and so would be expected to contain more OH groups). Interestingly, the low-density aerogel contains $\approx 50\%$ less material, and the resonant absorptions are reduced by approximately the same amount. This suggests that these loss-peaks are introduced by the bulk, rather than the surface.

Aerogel made with 0.2 mol MTMS precursor per TMOS mol and supercritically dried at high-temperature has attenuation of 0.07 dB/cm at 1310 nm. This is, to our knowledge, lower than any other published values for aerogel. However,

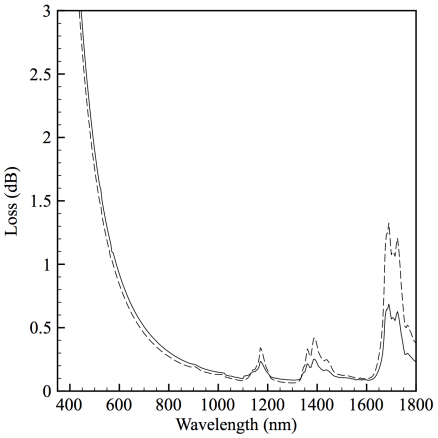

Figure 5.16: Loss spectra for high (dashed lines, $\rho_{\mathrm{agl}} = 0.19\,\mathrm{g/cm^3}$) and low (solid lines, $\rho_{\mathrm{agl}} = 0.11\,\mathrm{g/cm^3}$) density aerogel made by high-temperature SCD. The aerogel was treated with MTMS to make it hydrophobic.

it is likely this is because of the improvements to the surfaces and bulk homogeneity, rather than a reduced amount of Rayleigh scattering in the aerogel itself. We believe that other spectral measurement techniques (using similar spectrometer setups or integrating spheres) will have a comparable amount of experimental uncertainty between the diffuse and direct transmission.

5.4.3 Birefringence

Birefringent materials have different refractive properties depending on the polarisation state of light. Linearly birefringent materials have two orthogonal axes, often referred to as fast and slow. If light is polarised exactly along either axis, the polarisation state will be unaltered. However, if the incident light has some component on each of the axes, then the phase of the slow component will be retarded and the output will in general have a different polarisation state. If light is polarised equally on both axes (45°) and the slow axis is retarded by a quarter of a wavelength, then the output light is circularly polarised. If the slow axis is retarded by a half wavelength, the polarisation state rotates 90°.

Birefringence normally arises because of material anisotropy, but it can also be induced by applying stress. Both of these effects clearly introduce a preferred

direction on a molecular level within the material. Long-chain polymers in alignment, such as those in sellotape, have an obvious structure and exhibit strong birefringence with one of the axes aligned with the chains and the other orthogonal to them. Almost all materials have birefringent properties when stressed, but these are generally difficult to control.

Aerogel is generally considered an isotropic material on macroscopic scales [141]. Some natural birefringence has been commented on in [142, 143], but not thoroughly investigated. The two previous detailed reports of birefringence in aerogel, by Bhupathi *et al.* [141] and Pollanen *et al.* [143] show birefringence using applied stress. In addition, Pollanen *et al.* [143] show that uniaxial shrinkage can also cause birefringence.

We have observed position-varying birefringence in aerogel samples "as made", i.e. not subject to any kind of post-processing or external stress. Fig. 5.17(a) shows a piece of our aerogel back-lit with white light and viewed through crossed polarisers. A significant volume (marked D) exhibits smoothly spatially-varying birefringence. This behaves like a Babinet compensator and could be used as such, but with adjustment via sample position rather than by overlapping wedge-shaped elements.

We measured the birefringence of our aerogel using the following set-up. White light from an incandescent lamp was collimated and delivered to the aerogel via a chopper, a 10 nm bandpass filter, and an input polariser. The beam was directed at right angles to the long axis of the sample and near the centre line, i.e. out of the page around the letter D in Fig. 5.17(a), and the beam diameter was 0.8 mm. The transmitted light passed through an output polariser before being detected using a photodiode with lock-in amplifier. Positional variations were controlled using a calliper mounted on a stable translation stage.

Locations in the aerogel behaved as half- and quarter-wave plates for a range of wavelengths. For example, Fig. 5.17(b) is the transmission for $\lambda = 550$ nm and various output polariser angles, with the input polariser oriented at 45° to the long axis of the sample. The output polariser angle is relative to the input polariser angle and the power is normalised to the maximum transmission without the aerogel. Without the aerogel, the extinction ratio (the ratio of maximum to minimum transmitted powers) was 22 dB, representing the quality of our po-

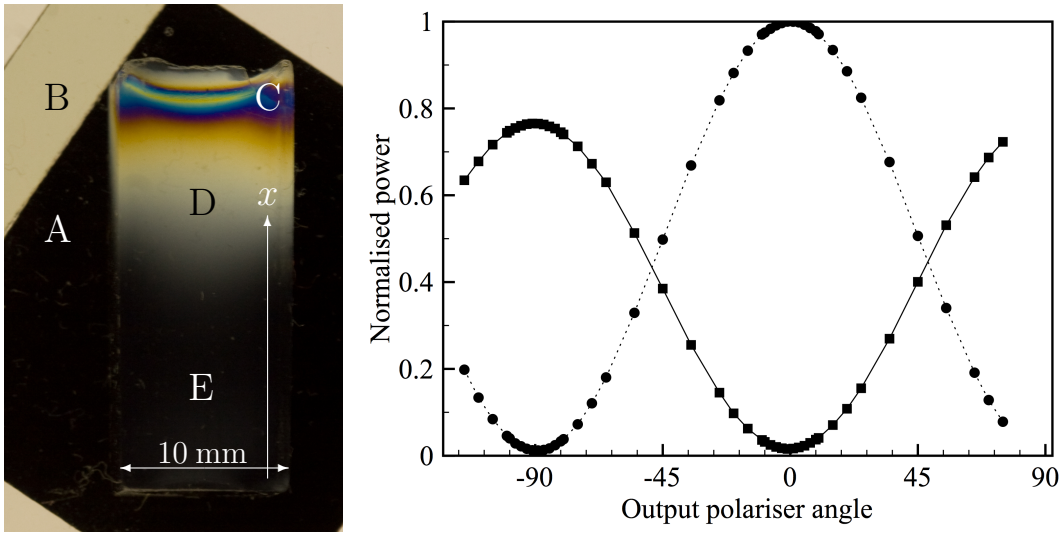

(a) (b)

Figure 5.17: (a) An aerogel sample viewed between crossed polarisers. A shows the extinction through crossed polarisers. At B the transmission through aligned polarisers is shown using a third polariser. Coloured fringes at C shows a strong wavelength-dependent birefringence at the top end of the aerogel. D looks like a zero-order half-wave plate where almost all light is transmitted. At E, the base of the aerogel, birefringence is small. (b) Transmission versus output polariser angle for 550 nm light without the sample (dashed line) and with the sample positioned as a half wave plate (solid line).

larisers. With the aerogel in place and positioned to act as a half-wave plate there was a 90° shift of the response (as expected for a half-wave plate) and the extinction ratio was 18 dB. The insertion loss (due to Rayleigh scattering in the aerogel) was 1.2 dB; working at longer wavelengths reduced scattering loss but maintained a similar change in extinction.

Measurements of transmission versus output polariser angle were made at different positions x along the sample. These resembled Fig. 5.17(b) but with raised mimima P_{min} and lowered maxima P_{max}. The retardance angle δ was found using $\cos\delta = R$, where the contrast is $R = (P_{max} - P_{min})/(P_{max} + P_{min})$. For $\lambda = 550$ nm these quantities are plotted against x in Fig. 5.18(a) and (b). There is a gradual variation of retardance with position, including both quarter- and half-wave birefringence. It can be shown that retardance values correspond

to birefringence $\Delta n = |n_{slow} - n_{fast}| = \lambda\delta/2\pi L$, which are indicated on the right-hand y axis of Fig. 5.18(b). The birefringence is $\mathcal{O}(10^{-5})$, but it is worth remembering that the mean index of the material is very small, measured at ~ 1.03.

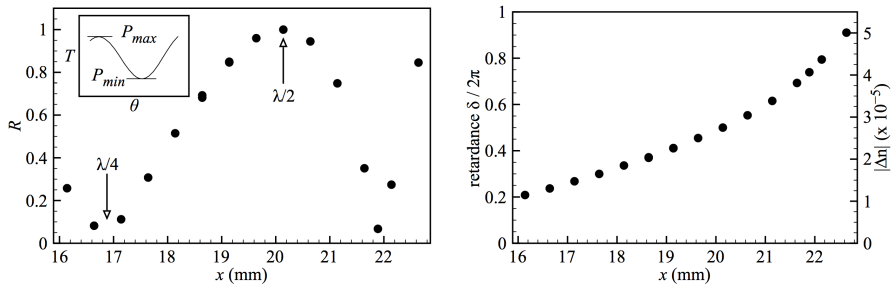

(a) **(b)**

Figure 5.18: (a) Contrast R versus position x for 550 nm light. (b) Retardance δ (left axis) and birefringence Δn (right axis) versus x as deduced from the data in (a).

The wavelength dependence of this birefringence was determined by repeating these measurements with different bandpass filters. The birefringence versus wavelength for three positions in the aerogel separated by 0.5 mm is plotted in Fig. 5.19. The birefringence is nearly constant, as expected for a material anisotropy.

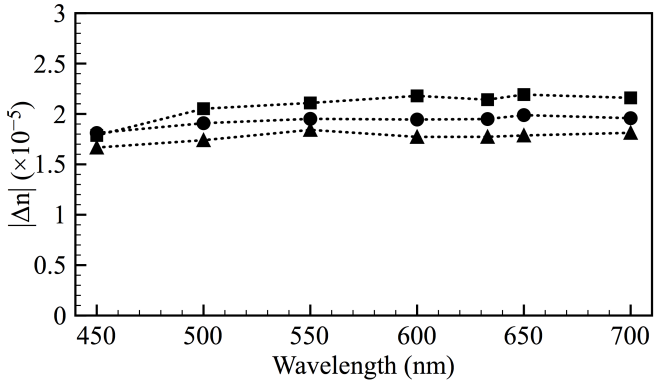

Figure 5.19: Birefringence Δn versus wavelength for x values of (bottom to top) 18.5, 19 and 19.5 mm.

We have demonstrated a position-dependent linear birefringence in a block of silica aerogel. No special measures were taken to produce this behaviour, and

no external stresses or other post-processing was applied. The results presented here were for one sample, but the effect was reproducible in other similar samples. The aerogel could immediately be used as a substitute for a Babinet compensator but with no internal surfaces; the low refractive index of the aerogel minimised Fresnel reflection at all wavelengths without optical coatings.

We have not established the cause of the birefringence, though it is clearly related to the exposed meniscus as the gel was formed. However, the properties of the aerogel are engineerable during its formation. Identification and control of the cause of the anisotropy could allow us to make spatially patterned birefringent elements such as those used to form radially- or azimuthally-polarised beams [144], simply by varying the processing or composition of the gel when it is made. The porosity of the aerogel may also be exploited to demonstrate gas sensors in which the aerogel birefringence is modified in the presence of certain gases.

5.5 Conclusion

In this chapter, we have discussed how we developed methods for making aerogel using both low- and high-temperature supercritical drying. The optical transmission and refractive index of our aerogel is important for the later work presented in this thesis, particularly in chapters 6, 7, and 8. The curious birefringence of our aerogel is also noted, and a potential application as a compensator is discussed.

Chapter 6

Doped aerogel

This chapter describes the preparation and properties of doped aerogels. We have developed new methods for the doping procedure, which have been inspired by the existing literature and our knowledge of aerogel formation. Although we have only focussed on two dopants, we believe the developed methods are generally applicable to other similar materials.

6.1 Motivation

The purpose of the dopants is to add new optical functionality to aerogel, e.g. making it sensitive to oxygen [145] or adding materials with optical nonlinearity. The two dopants we studied in detail are 50 nm gold nanoparticles (GNPs) and ytterbium (Yb^{3+}) ions. Each dopant gives the aerogel different optical properties.

Well-dispersed GNPs have a distinct, visible spectral absorption feature because of a localised surface plasmon resonance. GNPs are large enough to be 'locked' in place during the formation of the glass network. However, their optical properties are compromised because they aggregate in alcohol — a key ingredient in the sol. We have developed a method for adding GNPs to sol while preventing them from aggregating, making aerogel containing well-dispersed GNPs. These "plasmonic aerogels" have been investigated using imaging, spectra, and computational modelling to gain understanding of the local environment of the GNPs. We believe that, especially when combined with the waveguide devices presented in later chapters, these aerogels could be used for studying plasmonic gain, and have applications in sensing and nonlinear optics.

In contrast, Yb^{3+} causes a narrow absorption feature in the IR spectrum. The atomic scale of Yb^{3+} means that it must bond to the network to prevent it from escaping during solvent exchange or SCD. The ionic nature of Yb^{3+} means that another ion (the anion) is required for it to dissolve in water. Either ion can significantly alter the chemistry of the initial sol, manifesting in long gelation times and opaque (or at best translucent) alcogels. However, we have found that it is possible for the Yb^{3+} to attach on the network after gelation. By diffusing ytterbium acetate solution into alcogels, we were able to create otherwise-normal aerogel with a resonant loss of 12 dB at 975 nm. When illuminated with sufficiently high intensity laser light, the Yb^{3+} causes fluorescence at infrared wavelengths. These aerogels are subject to ongoing investigation to determine if they can provide optical gain, possibly enabling a whole new class of laser materials.

6.2 Plasmonic aerogel

A medium containing well-dispersed GNPs appears coloured because of wavelength dependent loss (also called extinction) caused by a strong coupling between an incident electromagnetic field and the metal's conduction electrons [146]. The motion of the conduction electrons is known as a localised surface plasmon. Light that excites this state is scattered and absorbed. The complete curved surface allows direct-illumination coupling between the electromagnetic field and the surface plasmon. When the motion of electrons around the surface is resonant with the field, the extinction is greatly enhanced. Consequently, the size and shape of the nanoparticles has a large effect on the peak wavelength of the surface plasmon resonance (λ_{SPR}). The resonant wavelength is also intimately related to the refractive index surrounding the nanoparticles.

For 50 nm GNPs suspended in water, $\lambda_{\mathrm{SPR}} \approx 530$ nm and the extinction feature is ~ 100 nm wide, Fig. 6.1. The peak extinction is controlled by the concentration of the GNPs. The short-wavelength extinction visible in the spectrum occurs because light excites electrons between bands within the gold, although these are non-radiative transitions [146].

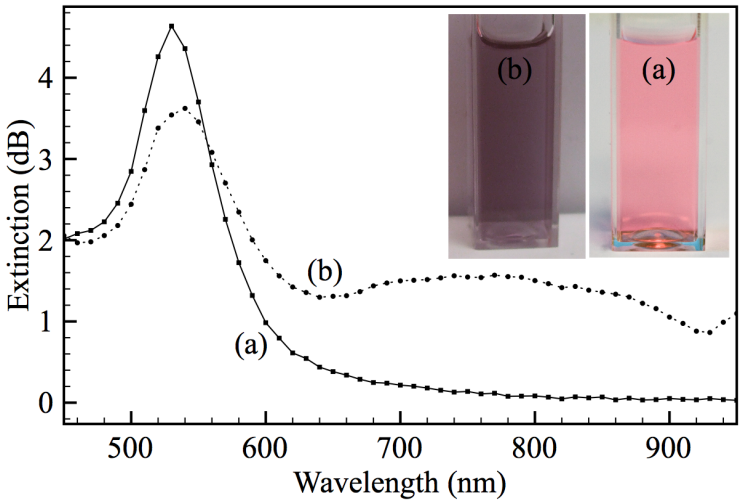

Figure 6.1: (a) A photograph and extinction spectrum of a 1 cm thick, 50 nm GNP suspension in water. (b) A photograph and extinction spectrum of a 1 cm thick, 50 nm GNP suspention in a mix of water and methanol: the purple colour is caused by GNP aggregation.

In water, the large extinction of green and partial extinction of blue light makes the suspension red in colour. However, suspensions of GNPs are not stable in water, and trace amounts of citrate ions are required to prevent them from aggregating. Even so, the GNPs settle over moderate timescales, with visible non-uniformity in the suspension appearing over the course of a day. Furthermore, the citrate stops stabilising the particles in the presence of alcohol, and the particles aggregate within an hour. The transmission electron micrographs (TEMs) of Fig. 6.2 show how significant this aggregation is, just 20 min after mixing the suspension with methanol. The extinction spectrum and photo marked (b) in Fig. 6.1 shows that the mixture has turned purple and no longer has a distinct spectral feature: eventually the colour completely disappears once all the gold precipitates out of the solution. Aggregated GNPs do not have such interesting optical features as there are no simple resonances from which the field build-up can arise.

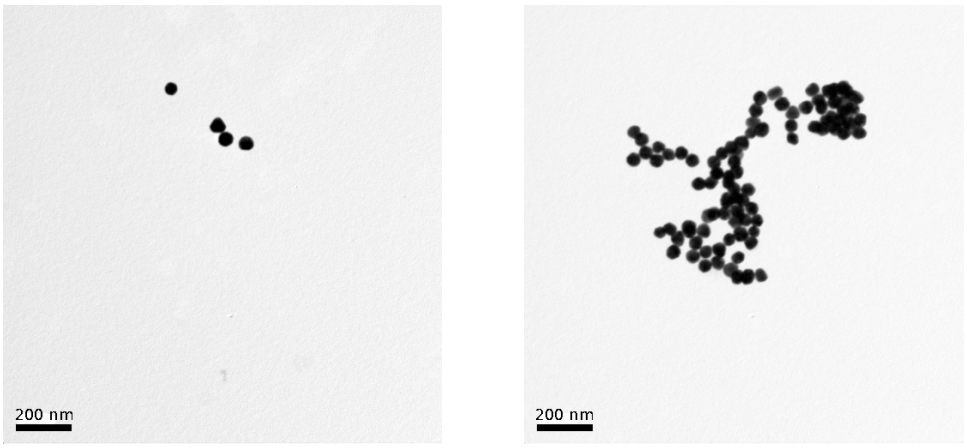

(a) **(b)**

Figure 6.2: TEMs of 50 nm GNPs, precipitated out of an equal mix of the aqueous suspension and methanol (a) immediately and (b) after 20 min.

We will use the purple colour and the longer wavelength spectral feature as an indicator for aggregation in subsequent alcogel and aerogel.

The surface plasmon resonance, and corresponding enhancement of optical field at the surface of the GNPs, can be used in many applications. One of the oldest (albeit somewhat unwitting) uses was in making decorative glass such as

that in the Lycurgus cup [146]. Since the λ_{SPR} depends on the local refractive environment, single GNPs have been used for environment sensing by linking them to a fibre optic tip [147]. The field enhancement around the GNPs surface can be used to enhance Raman scattering signals, a technique known as SERS [148, 149]. The GNPs also enhance both thermal and fast electronic nonlinearity. They have a reported electronic $n_2 = -2 \times 10^{-18}$ m^2/W [150], which is two orders of magnitude larger than silica.

Adding GNPs to the pores of aerogel immobilises them in a true 3D distribution. Looking forward, this could be interesting for interactions with the evanescent field outside of thin fibre tapers as in chapter 7 or in filled hollow-core PCFs from chapter 8. The open nature of the aerogel network could invite applications in gas catalysis [151], as GNPs are reported to catalyse the reaction of CO to CO_2 amongst others [152].

6.2.1 Existing literature

Several methods of combining GNPs with aerogel have been investigated previously. Many of the methods are designed to solve the aggregation problem, but introduce additional drawbacks (while not always solving the aggregation problem). It is quite difficult to make comparisons between all the methods because the spectral measurements are presented in arbitrary units.

The most straightforward way of eliminating aggregation is to remove the alcohol component from the gel chemistry. By adding aqueous GNPs drop-wise to TMOS, Yazawa *et al.* [153] were able to form a rigid gel with the only alcohol present being that produced during the hydrolysis reaction. The authors suggest this method only works with TMOS (rather than TEOS). The wet-gel was ambiently dried into xerogel, with different concentrations of GNPs introduced in the sol. While the authors claimed the GNPs were uniformly dispersed, the spectra they present suggest otherwise. The spectra have been reproduced in Fig. 6.3(a): the spectra show increasing loss as the as the wt% of GNPs increases from 0.01–0.05. The lowest doping concentration shows something close to an extinction spectrum of unaggregated GNPs in the xerogel, with a reasonably isolated optical feature. However, the xerogel with 0.05 wt% GNPs shows very significant

evidence of aggregation; the spectrum is almost flat and very attenuating, even at 800 nm.

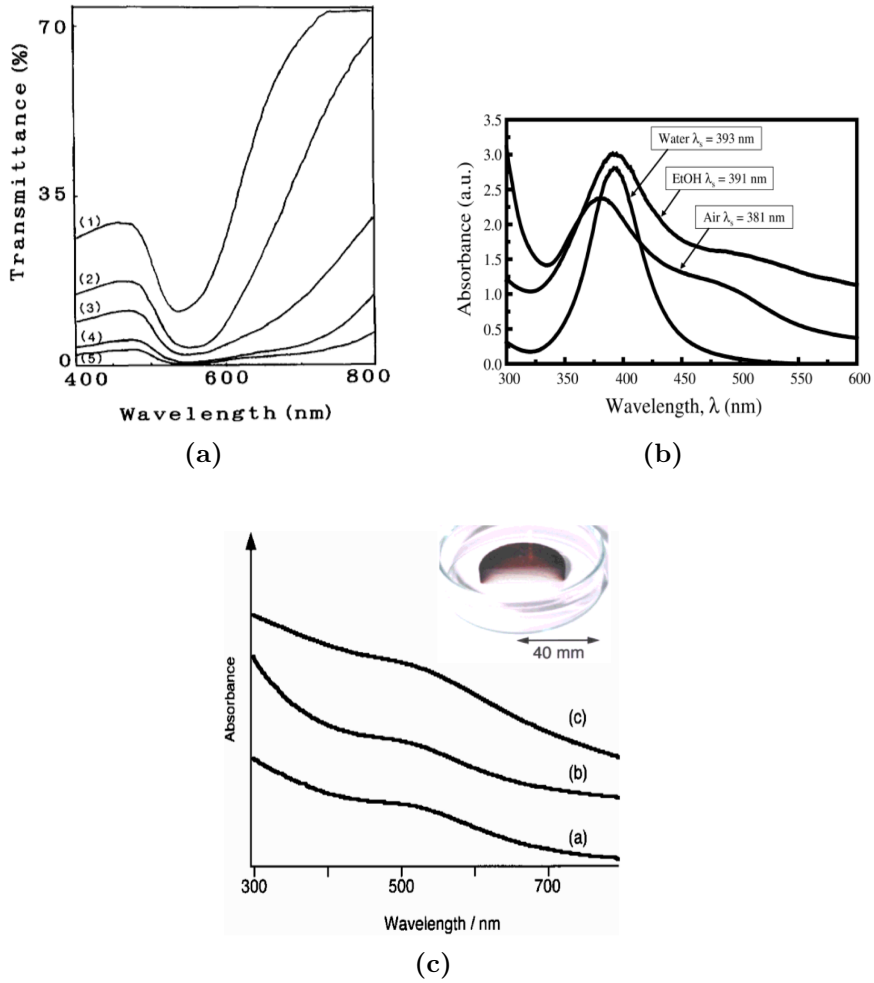

Figure 6.3: The spectra of doped gels containing GNPs, from papers by (a) Yazawa *et al.* [153], (b) Smith *et al.* [151] and (c) Tai *et al.* [154].

Smith *et al.* [151] used the same method as [153], but extended the procedure to supercritical drying. In order to do this, the gel containing the GNPs was washed in ethanol. During the solvent exchange, significant aggregation of the GNPs occurred. This can be seen in the spectra of the alcogel and aerogel in Fig. 6.3(b). The spectrum of the GNPs in water has no extinction beyond 450 nm, but the alcogel and aerogel spectra have strong extinction even beyond 600 nm.

Diffusing the GNPs into the network after formation is possible, on the con-

dition that they are much smaller than the aerogel pores. Tai *et al.* [154] added ~ 2 nm GNPs to a wet-gel that had been washed to contain toluene. This way, no alcohol is present during the diffusion process and the NPs themselves can actually stick to the glass component of the gel. In fact, after nearly 2 days of immersion, all the GNPs had been taken up by the wet gel. The wet-gel was supercritically dried to make aerogel, and the spectra of the different stages are reproduced in Fig. 6.3(c). Unfortunately, the concentration of GNPs throughout the gel was very uneven, as can be seen in the inset photograph.

An alternative method of creating composite aerogels, doped with a GNP suspension added to an about-to-gel sol so that it acts as a "nanoglue", was developed by Anderson *et al.* [155]. (The same method is more generally applicable to a wide range of aqueous nanoparticles [156].) The spectral results from this paper (Fig. 6.4) are not easy to interpret because the normalised units are offset and the signal shows a 'ripple' at long wavelengths that could be either aggregation or noise. On top of this, there is very little sign of Rayleigh scattering, a feature that is present on all aerogels. Finally, both sizes of GNPs in aerogel have signs of apparent aggregation within the spectra. This manifests itself as slight secondary peaks from 550–600 nm. However, the main surface plasmon extinction peak is reasonably distinct, and TEM images of crushed aerogel show a single NP embedded in the matrix with no others in the field of view, as shown in Fig. 6.4.

6.2.2 One-step doped aerogel

The simplest method of introducing GNPs into aerogel is by replacing the reagent water with an aqueous suspension of GNPs. Introducing GNPs this way has no impact on the reaction chemistry, but the alcohol causes aggregation as described above. It is worth noting that while the mixture is still a sol, the colour evolves as aggregation occurs. However, once the alcogel is formed there is little change in the colour before the solvent is removed.

We recap the procedure for making a standard one-step aerogel (sec. 5.2.1), with the water replaced by an aqueous suspension of GNPs from British Biocell International (available from www.buybbi.com). The sol is mixed from TMOS,

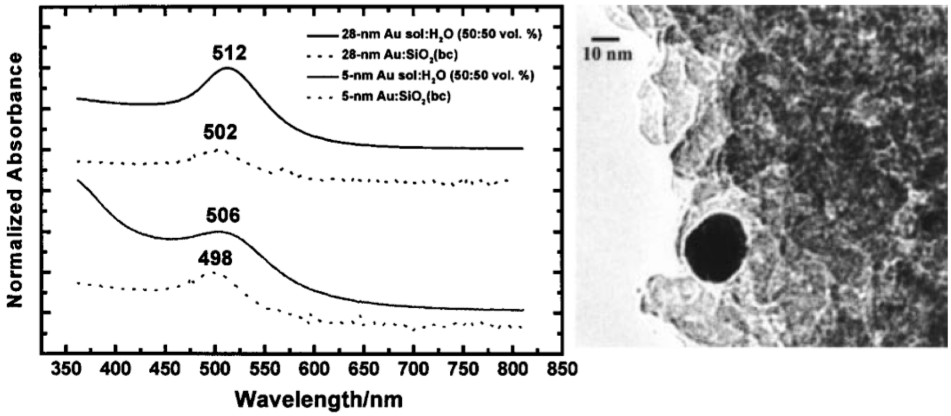

Figure 6.4: Spectra for 28 nm and 5 nm GNPs in aqueous suspension and embedded in aerogel. The TEM shows a 28 nm particle in the aerogel, prepared for microscopy by crushing to a fine powder. These figures are reproduced from [155].

methanol, GNP suspension, and ammonia in the molar ratio $1 : 4.6 : 10.3 : 3 \times 10^{-3}$. Expressed in terms of volume rather than amount, the ratio of the first three chemicals was $2 : 2.5 : 2.5$. The solution contains 5 μmol of ammonia, dissolved in the methanol of the sol (i.e each 1 ml of methanol contains 2 μmol ammonia). Typically, all 2.5 ml of the water contains GNPs. This is a considerably higher water content than the recipes presented in sec. 5.2, to enable a higher concentration of GNPs in the mixture. The aging and (low-temperature) supercritical drying procedures are as described in sec. 5.2.5. For comparison, we also prepared aerogels without GNPs, but with otherwise the same chemical recipe.

The spectrum of the aerogel is shown in Fig. 6.5, compared with an undoped aerogel made at the same time. As in Fig. 6.1, the spectral features and the purple colour of the aerogel imply the GNPs have aggregated during the fabrication process.

6.2.3 Two-step doped aerogels

We developed a method to prevent aggregation of GNPs during the formation of alcogel. This method is similar to that of Anderson *et al.* [155], Morris *et al.* [156] in that the nanoparticles are added to an already-made sol. However, the sol is not on the verge of gelation. Our method also shares common ground with

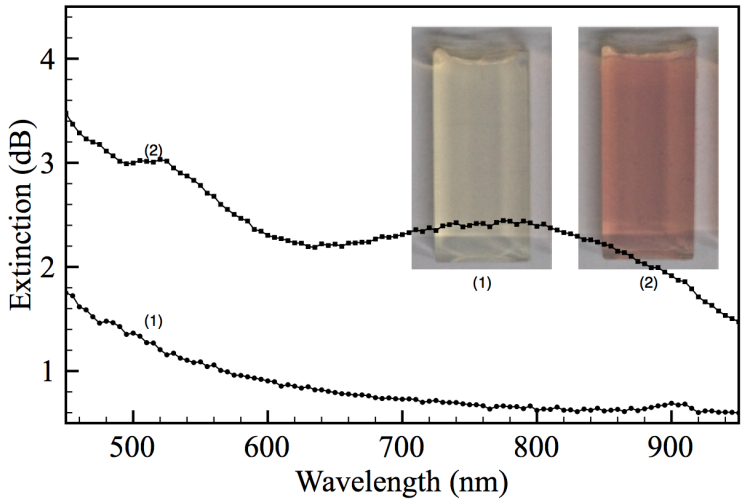

Figure 6.5: Photographs and spectra of doped aerogel containing aggregated GNPs and undoped aerogel prepared with the same conditions.

the approaches to two-step alcogel formation in [13, 14]. Our method is based on the following ideas: the time GNPs spend in liquid methanol should be reduced, which will limit the amount of aggregation; and a number of silica particles should be allowed to form a colloid before the GNPs are added, which will inhibit the motion of GNPs after they are added.

In our two-step sol, the ingredients of the one-step process are split so that the TMOS and methanol are separated from most of the water for as long as possible. In the first step, 2 ml of TMOS, 1.5 ml methanol, and 0.25 ml water with no GNPs are mixed. The second step, after a chosen delay, is to add the remaining 1 ml of methanol and 2.25 ml water with the GNPs. With some care, this method can produce a sol with a similar colour as the water with the GNPs before mixing, indicating the GNPs are not aggregating.

The first-step time (chosen by the experimenter) is the delay before adding the remaining chemicals; the second-step time is the (observed) further time until the sol has become alcogel. The amount of ammonia in the sol is crucial when determining the first step time, and controls the overall gel time as well. If the first-step time is sufficient, then the GNPs do not aggregate when added in the second step. This means the second-step time can be controlled up to a maximum of 35 min (the time the sol takes to gel if no additional ammonia is present in the

second-step methanol). This nice feature means that the sol containing GNPs can be cast in various moulds such as the fibres we describe in chapter 8.

The spectra of Fig. 6.6 show the effect of varying first- and second-step times on the aggregation state of the GNPs. The measurements were made on rigid alcogel cast in PMMA cuvettes. In the left-hand panel, the reduction of the long-wavelength peak shows that aggregation disappears for first-step times between 15–20 min, with a second-step time of 7 min. When the first-step time exceeded 25 min, the final gel lost transparency and became very milky in appearance, though the pink colour was still visible. For a fixed first-step time of 15 min, the right-hand panel shows that changing the second-step time between 5 and 35 min has little effect.

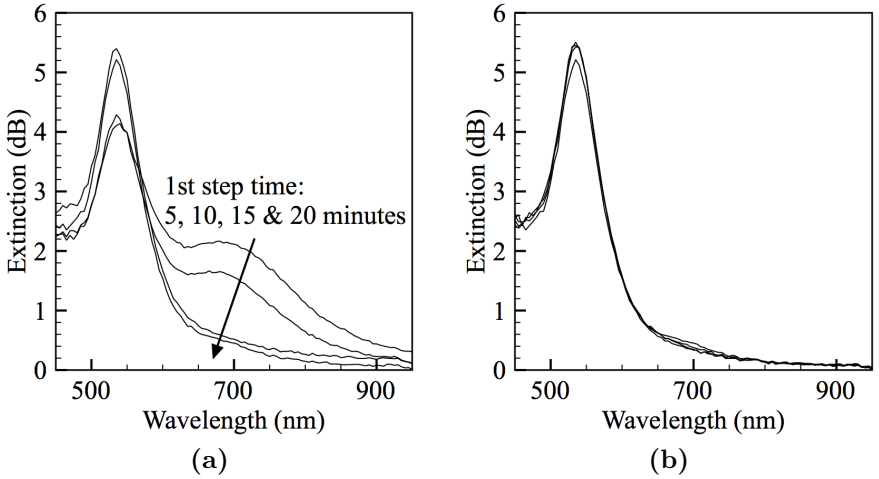

Figure 6.6: The extinction spectra of two-step alcogels while (a) varying first-step time for a fixed second-step time of 7 min, and (b) and varying second-step time (from 5–35 min) for a fixed first-step time of 15 min.

The alcogel was made into aerogel by our normal low-temperature method (see sec. 5.2). The cuvettes were softened in methanol so the alcogel could easily be removed. The total aging time was approximately two weeks, in several washes of fresh methanol. The alcogel was then treated with HMDS to make the resulting aerogel hydrophobic. Finally, supercritical drying in CO_2 was used to remove the solvent and the resulting aerogel appeared pink. The spectrum and a photograph of the aerogel are compared with an undoped aerogel made using

the same method, Fig. 6.7. With small modifications, the procedure is equally suitable for high-temperature SCD resulting in similarly doped pink aerogels.

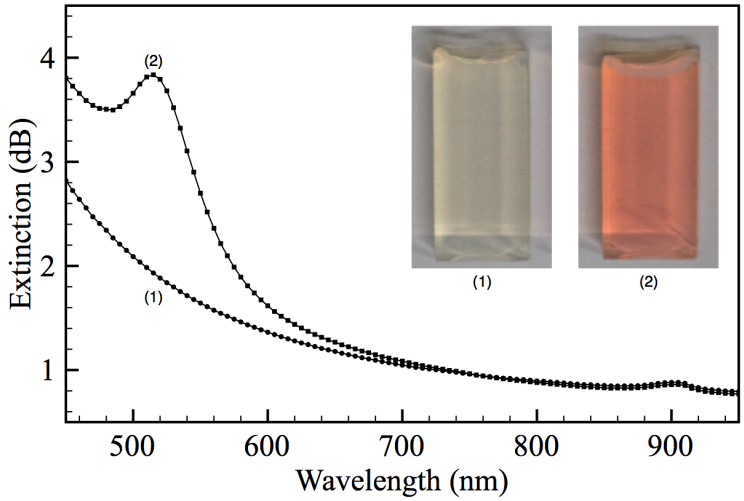

Figure 6.7: Photographs and spectra of doped aerogel containing dispersed GNPs and undoped aerogel prepared with the same conditions. The doped aerogel spectrum shows none of the signs of aggregation that are apparent in Fig. 6.5.

For visible light, both one- and two-step aerogels exhibit the $\propto \lambda^{-4}$ response characteristic of Rayleigh-like scattering. The two-step aerogel has slightly more loss at 800 nm, 0.14 ± 0.04 dB compared with 0.09 ± 0.04 dB for the one-step aerogel. The measured BET surface area [157] of two-step aerogels was $1000 \pm 20\,\mathrm{m}^2/\mathrm{g}$, compared with $700 \pm 10\,\mathrm{m}^2/\mathrm{g}$ for the corresponding one-step aerogels. BJH pore-size analysis [157] suggests that this difference is due to a large mesoporous regime in the two-step aerogel. A larger number of bigger pores is consistent with the increased light scattering observed in the two-step aerogels.

Using different mixtures of water and GNP suspension in the second step allows control of the GNP concentration. Fig. 6.8 shows spectra for doped alcogels and aerogels, with the magnitude of peak extinction shown in the inset. (The spectra of the corresponding undoped materials have been subtracted to isolate the effect of the GNPs. This is why the normal Rayleigh-like scattering of the aerogel is not visible in the spectra.) The height of the surface plasmon resonance peak is linearly proportional to the particle concentration in both, as expected.

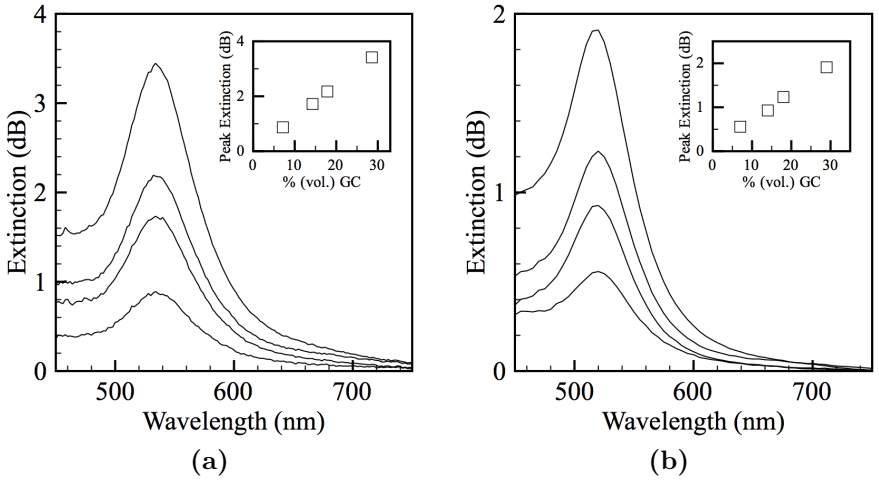

Figure 6.8: The extinction spectra for different concentrations of GNPs in (a) alcogel and (b) aerogel, higher peaks corresponding to greater concentrations. The wavelength shift of the peak between (a) and (b) is due to the difference in refractive index. The height of the surface plasmon extinction as a function of colloid concentration is inset in each graph.

6.2.4 λ_{SPR} and the structure of doped aerogel

For a given particle concentration, the height and wavelength of the surface plasmon resonance are different in the aerogel compared to the alcogel (and indeed the original aqueous suspension of GNPs). The wavelength was 531 nm in the aqueous suspension, 535 nm in the alcogel, and 519 nm in the aerogel. This difference is a consequence of the different refractive indices around the particles [146], which we explored by numerical modelling.

All of the simulations that we discuss in this section were performed at Imperial College London, though we specified the systems to be modelled. The simulations were finite element method (FEM) calculations in Comsol Multiphysics 3.5. The 3D simulation space was a sphere representing a single GNP, a cubic boundary at which the extinction cross-section was calculated, and a spherical perfectly matched layer. The software's free-meshing algorithm was used to partition the space into tetrahedral finite elements no bigger than 10 nm on the sphere and the cube for the simulation to converge. The dielectric properties of gold were taken from Johnson and Christy [158].

Small variations in the GNPs can be seen in the TEM images presented in Fig. 6.2. The average size and size range is 51 ± 3 nm and most of the GNPs are spherical, with only a few oddly shaped rods and triangles. Size and shape dispersion act to broaden the surface plasmon resonance lineshape, but do not result in a shift in the peak wavelength. A comparison between the modelling and experimental spectra of GNPs in aqueous suspension, Fig. 6.9(a), shows only a very slight amount of broadening, indicating these features are having little effect. The simulated and measured extinction spectra are normalised to the peak wavelength from here onward to enable easy comparisons.

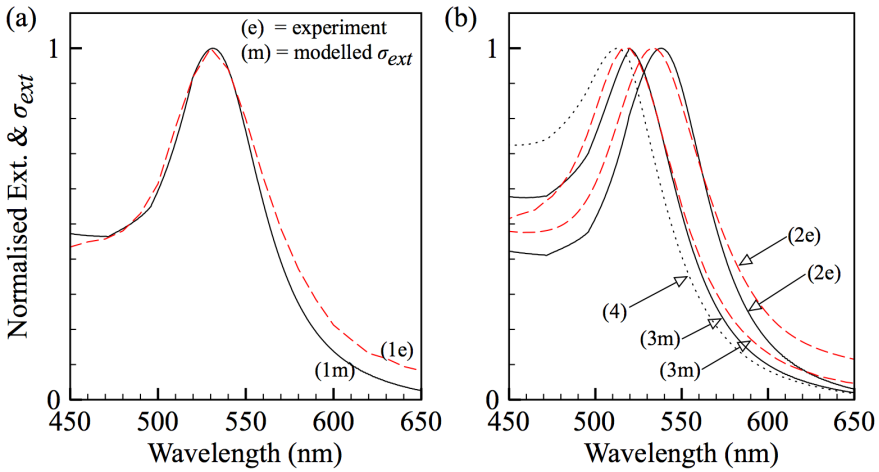

Figure 6.9: (a) Comparison of modelled (m) and experimental (e) extinction spectra of GNPs in water. (b) Modelled and experimental extinction spectra of GNPs in alcogel (2) and aerogel (3). (4) The expected extinction spectrum for a GNP surrounded by an effective refractive index of 1.05 (n_{agl}).

Changing the index of the material surrounding the GNP in the simulation causes the peak wavelength to shift. In [151, 159, 160], the two-component medium of aerogel (or alcogel) around the GNPs is represented as an effective medium, considering different effective medium approximations (EMA). Simulations with effective media of 1.4 and 1.2 were fitted to the λ_{SPR} for alcogel and aerogel, respectively, Fig. 6.9(b). Concentrating on aerogel, this value of effective index is significantly different from the measured $n_{\mathrm{agl}} \approx 1.05$. (Although we have not measured the index of alcogel, we believe the effective index is closer to 1.33 than 1.4 as alcogels are hard to see in the methanol wash solutions.) The curve

marked (4) is the modelled extinction spectrum that would be observed for a GNP in an effective medium of 1.05, which does not have λ_{SPR} at the predicted wavelength.

Smith *et al.* [151] attribute this inadequacy of EMA to interface properties and aggregation. However, the spatial extent of the surface plasmon suggests that the aerogel is not a homogeneous effective medium on these length scales. Fig. 6.10 shows the electric field in the vicinity of the gold nanoparticle, normalised to the incident electric field: the electric field enhancement caused by the GNP surface plasmon has decayed by $1/e^2$ within 25 nm of the nanoparticle's surface. This means λ_{SPR} is affected only by the material immediately around the GNP rather than the host medium as a whole. Therefore, EMAs should be used with extreme care, as the scale of the medium's internal structure is similar to the surface plasmon decay length.

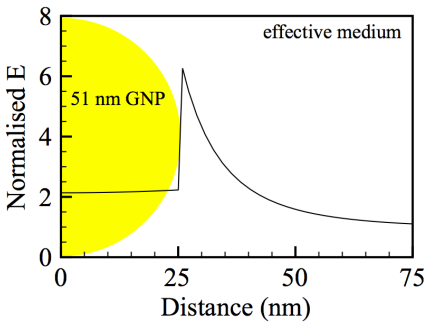

Figure 6.10: The spatial extent of the electric field around a GNP in water. The electric field has been normalised to the incident field away from the nanoparticle. The field enhancement in the vicinity of the GNP is because of the surface plasmon, as the simulation is at the SPR resonant wavelength.

A model in which the immediate environment of the particle differs from the bulk of the aerogel or alcogel seems more appropriate. We considered a 51 nm spherical gold particle with a 5 nm silica coat, embedded in a spatially extensive medium. We call this model the wedge model, as opposed to the effective medium model studied earlier. This model reflects the structure of aerogel [25], as the glass elements in aerogel are 5 nm thick, and the pores ($\sim$ 40 nm) are slightly smaller than the GNPs so the GNPs will fill them.

We tested this model for three different pore fluids: air (aerogel), methanol

(alcogel), and toluene (in wet-gel). The toluene-filled wet-gel was made by gradually replacing the methanol via successive steps containing 10%, 25%, and 50% volume toluene solutions to avoid cracking. The modelled λ_{SPR} is within ± 1 nm of the experimental measurement in each case, as shown in Fig. 6.11. We therefore conclude that the GNPs are completely wedged in place in the pores and almost entirely surrounded by strands of silica of ~ 5 nm thickness in both wet-gel and aerogel.

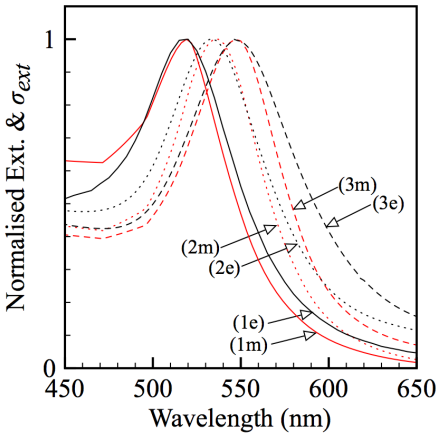

Figure 6.11: Comparison between the experimental (e) and wedge model (m) extinction spectra of GNPs in aerogel (1), alcogel (2), and toluene-filled wet-gel (3).

GNPs have proposed applications in sensing and fluorescence imaging [146, 161]. Our modelling predicts only a small decrease in the λ_{SPR} sensitivity to changes in the pore refractive index. The change in λ_{SPR} per unit change of pore refractive index is 52 nm for the wedge model, compared with 60 nm in the effective medium model. This is surprising, as the coating might be expected to decrease the amount of electric field in the pores. Plotting the spatial extent of the electric field at resonance provides useful insight, Fig. 6.12. In this figure, we see that although the boundary of the nanoparticle causes a field enhancement, the coated nanoparticle has a second field enhancement at the edge of the silica as well. The enhancement at the silica surface is large enough that the power contained in the electric field in the space around the nanoparticle is comparable. The coat also does not have a large effect on the decay length of the field enhancement in either air or methanol. The electric field enhancement at λ_{SPR} decays to $1/e^2 \sim 2$ nm closer to the external silica surface of the wedged GNP

than the ~ 25 nm of the effective medium particle in air. These factors combined explain why the theoretical sensing potential of the GNPs in the wedge model is comparable to that of GNPs in a simple effective index.

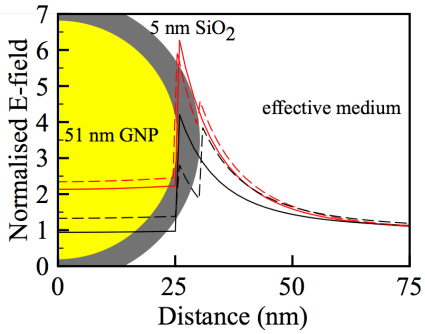

Figure 6.12: Simulations of the electric field in the vicinity of a GNP (solid lines) and a silica-coated GNP (dashed lines), normalised to the incident electric field. The field enhancement at the GNP is caused by the surface plasmon resonance, and the simulations were at resonant wavelengths of doped aerogel (red lines) and alcogel (black lines).

The results of our modelling indicate that GNP doped aerogel could have sensing applications once optimised using non-spherical and core/shell particles which have a larger wavelength shift per unit index change [162, 163]. The presence of a glass layer around the GNPs separates them from direct contact with the probe material, which is not promising for catalysis applications as contact with the metal surface is important. However, the glass layer is of benefit in SERS [149] as well as enhancing the emission [161, 164] from dye and emitter-doped aerogels, which have been proposed for sensor and laser applications [68, 145, 165]. It will also help in exploiting nanoparticles of more reactive materials, as they will be enclosed in silica.

6.2.5 Nonlinear properties of gold-doped aerogel

We probed the nonlinear properties of aerogel doped with GNPs using a high-power green laser. This laser was chosen because its wavelength (~ 540 nm) is close to the measured λ_{SPR} of the aerogel. The laser pulse duration was 400 fs, the repetition rate was 20 MHz, and the average power could be adjusted up

to 1 W. The laser was collimated and focused onto the aerogel using a 10× microscope objective. A multimode fibre near the output face of the aerogel collected scattered light and coupled it into an OSA using a multimode fibre.

A typical spectrum of the laser light taken with no aerogel in the setup is plotted in Fig. 6.13 (black line): the measured average power was 700 mW. The light spectrum was observed to shift wavelengths slightly over time, changing by approximately ±0.25 nm whilst maintaining a consistent spectral shape over the course of our measurements. We measured the spectrum of light with undoped and doped aerogel (made with the full 2.25 ml of GNP suspension in the sol) in the experiment and observed no change. However, we measured 1 nm of spectral broadening with an aerogel doped with half as much of the GNP suspension in the sol, Fig. 6.13 (red line). The spectrum of the laser light through this aerogel gradually returned to its normal shape as we reduced the power to below 500 mW.

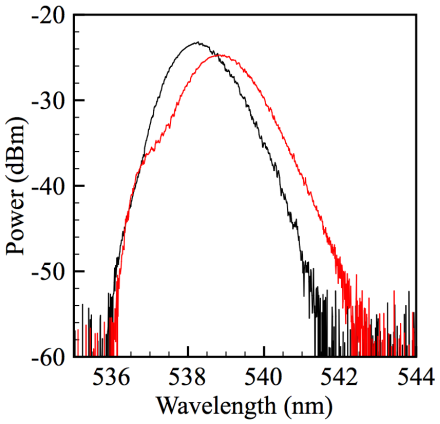

Figure 6.13: The spectrum of a high-power pulsed laser light, measured on an OSA (black line). The spectrum of the laser light after travelling through 1 cm of aerogel doped with GNPs (red line). The measured average power was 700 mW.

We believe this is the first observation of new wavelengths being generated by a nonlinear process in any aerogel, doped or otherwise. However, we feel it prudent to mention that the beam significantly distorts over the course of seconds and minutes: an indication of a significant thermal component of nonlinearity as well. After the high power laser is switched off, there are permanent deformations in the bulk of the aerogel, indicating structural alteration caused by thermal effects. It is worth noting that these effects are significantly enhanced by the

gold nanoparticles, and aerogel with no gold nanoparticles does not start to alter until much higher powers.

We suspect that the GNPs provide enhancement to both the thermal and electronic properties of aerogel, similar to the enhancement reported by GNPs in caster oil [150]. However, in aerogel, the heat has nowhere to go, as the material is a very good insulator. Since thermal nonlinearity tends to cause a negative lens effect [166], the peak intensity at the focus will reduced. (Indeed, we believe this may be what Seo *et al.* [18] measured in undoped aerogel.) Hence, at high GNP concentrations, the thermal nonlinearity dominates and stops new wavelengths from being generated by the weaker electronic nonlinearity. We believe that our lower-concentration plasmonic aerogel created a balance in which the nonlinear effects attributed to electronic nonlinearity could be observed.

6.3 Lanthanide-doped aerogel

Elements from the lanthanide series, also known as rare-earths, are commonly used in laser materials because of their electronic properties. A good review of lanthanide doped fibre lasers can be found in [167]. The transitions of the $4f$ electrons can be excited optically, giving lanthanide-doped materials a distinct transmission spectrum. As the excited electrons return to the ground state, they emit light with a characteristic fluorescence spectrum. The fluorescence lifetime depends on the environment around the ions: non-radiative transitions caused by clustering and OH [168] mean shorter lifetimes. Long fluorescence lifetimes are necessary for applications where the lanthanide provides gain or lasing.

The $4d$ and $5p$ electron shells shield the $4f$ electrons from the host, therefore the lanthanides are able to lase in many materials, including glasses and crystals. By contrast, other elements such as titanium or chromium require a specific environment for lasing [167]. Whilst most lanthanides can be used in lasers, significant interest in optics focuses on neodymium, erbium, and ytterbium. All three have been used as lasers when doped in crystals such as yttrium-lithium-fluoride and yttrium-aluminium-garnet, as well as in silica glass. However, there is little published research on the optical properties of lanthanide doped aerogel.

6.3.1 Doping glass with lanthanides: prior art

There are several ways to create glasses doped with lanthanide elements: vapour phase depositions into glass, solution doping glass made by chemical vapour deposition (CVD), and low-temperature doped-sol-gel glass formation. Whilst ion implantation of lanthanides into glass is possible, the other methods are generally easier to control and produce better results. Solution-doping CVD methods are well-established and have the following advantages: they produce a high yield, are easy to control, and have the desired optical characteristics for creating lasers [169].

The most common method of solution-doping uses lanthanide halides, such as $YbCl_3$. Solution-doping can also be used to introduce co-dopants such as $ErCl_3$ at the same time, whilst retaining control of the relative concentrations. Fibre preforms made using MCVD can be solution-doped with ease, following the method of Townsend *et al.* [169]. The fibre cladding is prepared according to normal MCVD procedure (sec. 3.4). The core is then deposited at a lower temperature, forming unsintered porous soot. The whole tube is filled with a solution containing the required dopant (typical concentration 0.1 M) for up to an hour. The water is replaced with acetone, and then the preform is treated with chlorine gas and heated to remove chemically bonded surface OH. After collapsing using heat, the preform is then drawn to fibre in the conventional manner. The absorption spectrum of a fibre containing 1200 ppm Er^{3+} and 4600 ppm Yb^{3+} is shown in Fig. 6.14.

Adding dopants to glass made via sol-gel methods also has some merit, as the low temperatures make it easy and cheap to produce doped glass. During the sol-gel process there are several points at which the dopant may be introduced into the network. Probably the most obvious approach is to mix the dopants into the sol, before gelation [170–176]. Other approaches have exploited the porous nature of gels after the pore solvent has been removed. Immersing aerogel [177] or xerogel [178] in dissolved lanthanide salts leads to take-up in the network. The doped re-wetted gels can then be fully densified to glass.

Sol-doping methods have used both one- and two-step procedures and a variety of lanthanide salts. Historically, neodymium-doped glass attracted more

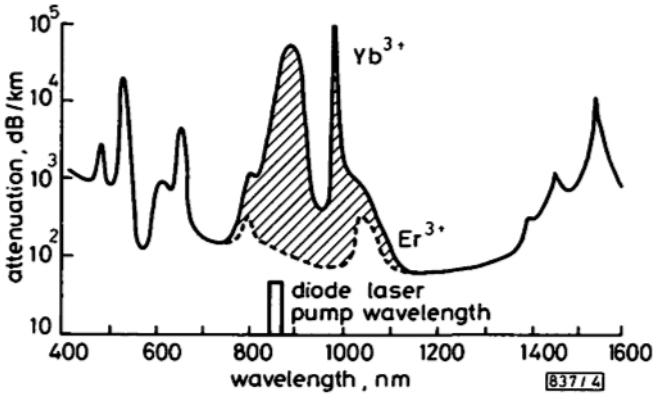

Figure 6.14: Spectrum of a fibre made by MCVD, doped with erbium and ytterbium, from [169].

interest because of its superior lasing qualities [168]. However, simply homogenising TMOS and water containing $Nd(NO_3)_3$ leads to poor fluorescence lifetimes $\sim 10\,\mu s$ because of clustering [168, 171]. Co-doping the sol with aluminium or phosphorous is known to reduce clustering in lanthanide-doped silica glasses [168, 171, 172]. This can increase the fluorescence lifetime by an order of magnitude, but is still less than expected from studies on glass formed in other ways. Berry and King [168] attribute this to residual OH, typically 2000–3500 ppm in densified xerogel. However, Pope and MacKenzie [170] make reference to a patent-pending (but still unpublished) process which can reduce the hydroxyl levels in dense glass to below 1 ppm with easy repeatability.

Recently, more focus has been given to erbium, using $Er(NO_3)_3$ [175] or $ErCl_3$ [174] dissolved in the sol before gelation. Tillotson *et al.* [174] used a two-step method with lanthanide-halides in the sol to produce clear but cracked aerogel using low-temperature SCD. High-temperature SCD did not produce transparent aerogel. The spectroscopic properties of aerogel made using this method were reported in [179]. The erbium modifies the normal photoluminescence of aerogel with a strong, narrow peak at 550 nm. Glauser and Lee [179] suggest that modified aerogels could be used in display materials. The original motivation for making lanthanide-doped aerogels was that they are reported to sinter to full-density glasses with better homogeneity than the corresponding xerogels [173].

Xu *et al.* [175] and Strek *et al.* [176] focused on making glass from xerogels, which could then be drawn to fibre. The fibre preform was made from a doped, sintered sol-gel glass in a freon atmosphere. The resulting fibre attenuation spectrum, Fig. 6.15(a), is reported to contain less than 2 ppm of OH, but even at this low level the attenuation of light over a kilometre is considerable. Electronic transitions in the erbium are clear from the spectrum, and have been identified with transitions from the ground state to the various excited states as marked. Two fibres with different erbium-concentrations of 100 ppm and 1000 ppm were investigated by pumping at 980 nm. The low concentration fibre has strong emission at 1550 nm. However, in the high concentration fibre there is strong green upconversion. The authors propose this happens from energy coupling from two excited erbium atoms, implying quite close proximity during the sol formation.

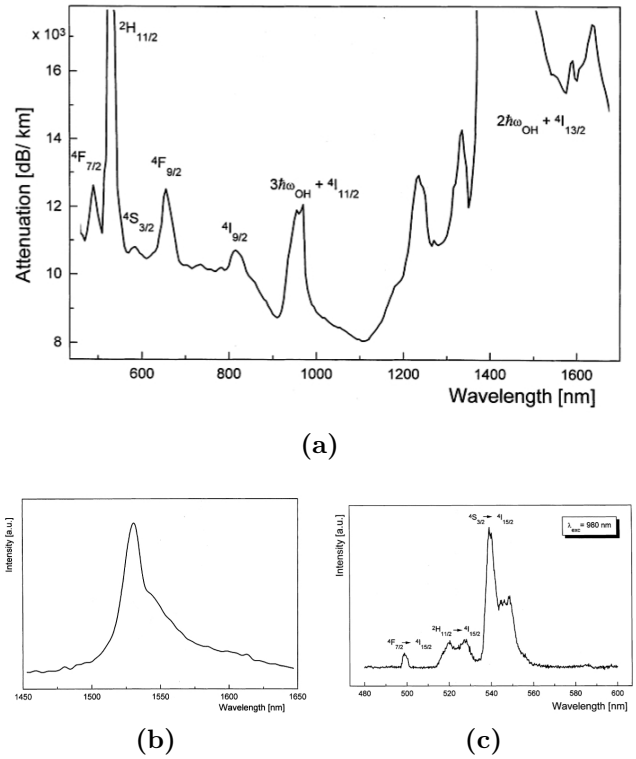

Figure 6.15: (a) Attenuation spectrum of a fibre made using a sol-gel preform doped with erbium. The emission of the fibre doped with (b) 100 ppm and (c) 1000 ppm, excited using 980 nm pump light. From [176].

Doping dried xerogel with lanthanide before finally consolidating it to dense

glass step can produce a high degree of homogeneity, but suffers from hydroxyl quenching [178]. Normally prepared alcogel, aged and dried at 45 °C for 2 weeks and then heat-treated at 1000 °C for an hour, can be immersed in aqueous salt solutions to introduce dopants in the network. Biswas *et al.* [178] used erbium acetate and an additional soaking step with a potassium (K^+) salt to reduce the hydroxyl content of the densified glass to 40 ppm. The potassium soaking creates alkali glass, with a significantly lower consolidating point of 850 °C. The fluorescence lifetime measurements of the doped alkali glass were 17 ms, indicating the erbium was well distributed and not being quenched by hydroxyl ions. This fact is directly attributed to the effect of the potassium. The potassium also leads to a narrower emission linewidth and a large increase in fluorescence efficiency.

We have decided to focus on ytterbium in doping experiments because of the availability of pump lasers and the relatively low price of hydrated ytterbium salts. For comparison with our later results, Fig. 6.16 is the absorption and emission spectrum of ytterbium in doped glass prepared using solution doping [180]. There is a strong narrow absorption at 975 nm, and a weaker but broader absorption around 915 nm. The emission spectrum of ytterbium is approximately a reflection of the absorption in the strong absorption line. The fluorescence lifetime was measured to be 0.8 ms. All of the measurements on doped glass are highly sensitive to the local environment. Glass made by ion-exchange, for example in [181], is reported to have longer fluorescence lifetimes (1.2 ms), but there is also significant alteration in the absorption and emission spectra.

6.3.2 Doping sol with lanthanides

Our early attempts to make doped aerogel were using a standard one-step low-temperature procedure, with ytterbium chloride ($YbCl_3 \cdot 6\,H_2O$) dissolved in water. The sol contained 2 ml TMOS, 2.5 ml methanol containing 50 µmol dissolved ammonia, and 2.5 ml aqueous $YbCl_3$ solution. The aqueous solution was made by mixing 1 g of $YbCl_3 \cdot 6\,H_2O$ in 6 ml water, so the solution was almost saturated. The sol was added to cuvettes which were topped with Parafilm to slow down evaporation from the surface.

Gelation did not take place within the normal 10–15 min, but a rigid alcogel

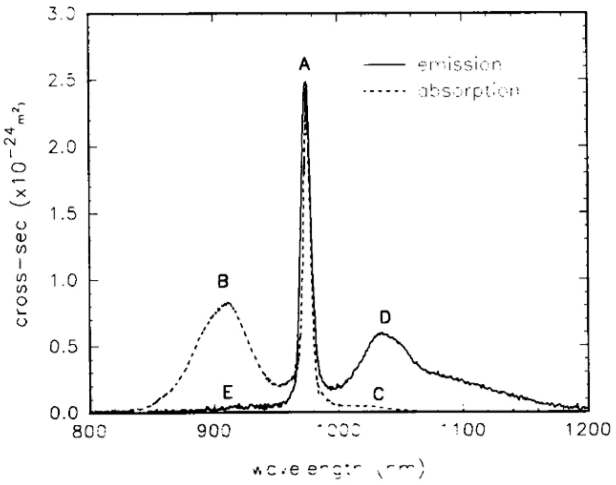

Figure 6.16: The absorption and emission spectra of ytterbium-doped glass, from [180].

formed after ~ 12 h heating at 60 °C. The alcogel was transparent and rigid, with a slight blue tinge. We believe that the change in the gel chemistry altered the structure of the network so the features were larger, and caused stronger scattering. It is not clear whether this change is due to either one or both of the ions in the solution, or simply due to the reduction in reaction rate.

The alcogel was made into aerogel following a normal low-temperature procedure, with ~ 2 weeks aging time and hydrophobic properties from immersion in HMDS solution before SCD. The gel shrunk by 10%, and was milky-coloured and mostly opaque to visible light. However, there was still adequate transparency at around 980 nm to see a small additional attenuation of 0.26 dB/cm due to remaining Yb^{3+} ions in the aerogel, Fig. 6.17(a). Although the loss is large, and the absorption due to the Yb^{3+} is small, it is clear that at least some of the Yb^{3+} remained in the network throughout multiple washes and SCD.

The spectra in this section are normalised using either a suitable control gel or (where none was available) air as the reference. The normalised spectra are then scaled to the peak of the ytterbium absorption. This makes comparison between the shapes of different spectra more distinct. We also specify the absolute attenuation at the peak absorption wavelength, so that the normalised spectrum in dB can be recovered. In this instance we did not have an appropriate reference, so the loss measured in the sample (1.07 dB) is normalised to air. The effect of

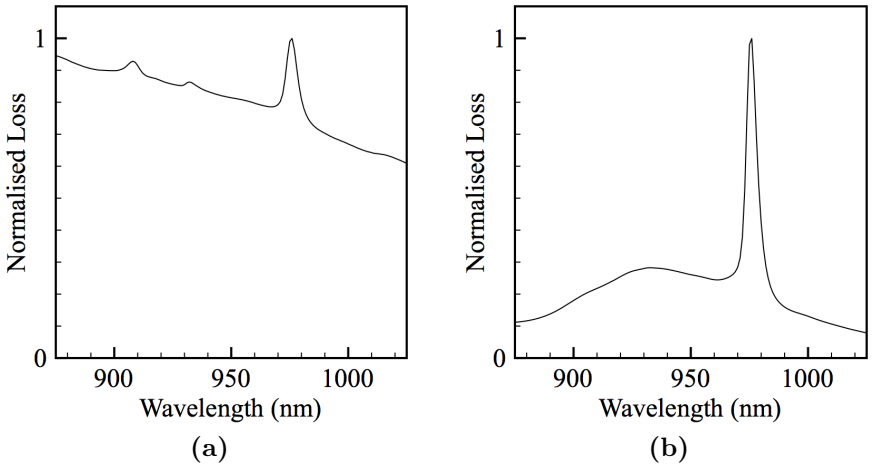

Figure 6.17: (a) The spectrum of aerogel made with a saturated solution of $YbCl_3$ in water. The excess loss is believed to be due to larger glass structures causing increased scattering, and the hump in the spectrum is due to resonant absorption by Yb^{3+}. The peak loss is 1.07 dB at 976 nm. (b) The spectrum of aerogel made with ytterbium acetate and acetic acid. The peak absorption is ~ 4 dB at 976 nm.

the Yb^{3+} was calculated using an approximate straight line fit between points where there was no resonant effect (0.84 dB). This gave an absorption due to Yb^{3+} of 0.23 dB in a 0.9 cm sample, equivalent to 0.26 dB/cm.

It was thought the long gel times could have been caused by the chloride ion, so we tried a similar experiment with ytterbium acetate (we write acetate as OAc from here on in). Using approximately the same dilution (1 g $Yb(OAc)_3 \cdot 6\,H_2O$ in 6 ml water) produced an opaque sol that did not become a gel. A two-step approach, similar to that used in doping with GNPs (sec. 6.2.3) was employed with moderate success to make semi-transparent alcogel, with gel times in excess of 2 h. This method is more complex and the alcogel was still not good quality, so alternative approaches were sought.

Consulting the literature for similar doping strategies, we note that [175] catalyse an erbium nitrate sol with nitric acid to generated a transparent sol. Similarly, we found that if sufficient quantities of acetic acid (HOAc) were added to the methanol in place of the ammonia, transparent sol would form in < 2 h. The volumes of components used to create transparent sol was 2 ml TMOS,

2.32 ml methanol, 0.18 ml HOAc, and 2.5 ml aqueous $Yb(OAc)_3$ solution. We used this alcogel to make aerogel using high-temperature SCD and, despite significant shrinkage and a slight reduction in transparency, we were able to obtain the spectral measurement in Fig. 6.17(b). The attenuation due to the Yb^{3+} at 976 nm is ≈ 4 dB/cm.

6.3.3 Solution-doping alcogel

All of our attempts at doping the sol caused disruption to the chemistry of gelation, and the eventual aerogels had worse properties than we normally observe in terms of shrinkage and transparency. However, the difficulty in stabilising the $Yb(OAc)_3$ in the sol hints that it might be possible for it to attach to the *already-formed* surface of an alcogel. Alcogel has been doped in this way before, but never with any of the lanthanides (in contrast to the solution-doping of xerogel and aerogel discussed on p. 143). Previous doping using this method has included gold nanoparticles [154, 182] and coumarin laser dye [183]. Neither of these dopants are ionic, so the solution chemistry is likely to be quite different in those cases.

Fig. 6.18 shows the normalised spectra for similar concentrations of aqueous $YbCl_3$ (dashed line) and $Yb(OAc)_3$ (solid line) solutions, with 1 g of the ytterbium salt dissolved in 6 ml deionised water. The spectra were referenced to that of deionised water, so the only effect is caused by the salt. The peak attenuation in the chloride salt was 4.8 dB/cm, compared to 4.6 dB/cm in the acetate. The slight broadening and peak shift are surprising, but the overall shape is quite similar between the two.

Transparent alcogel was made from 2 ml TMOS, 2.5 ml methanol, 2.5 ml water, and enough ammonia to gel in 10 min. The sol was added to cuvettes, and then immersed in methanol once it had gelled. The alcogels were removed from the cuvettes after 48 h. At this point, a set of 5 alcogels was added to a wash solution (wash solution 1) composed of 70 ml methanol and 30 ml aqueous $Yb(OAc)_3$ solution. The wash solution started to diffuse into the network, and alcogels were removed for measurement after 24, 48, 72, 138 and 166 h. The spectrum of each alcogel was recorded (Fig. 6.19(a)), then it was put back in a pure methanol

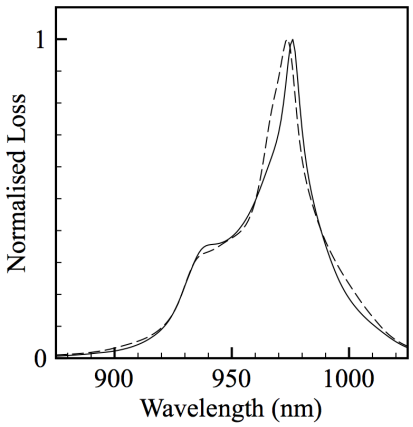

Figure 6.18: The normalised absorption spectra for $YbCl_3$ (dashed line) and $Yb(OAc)_3$ (solid line) dissolved in deionised water.

wash (wash solution 2) for 136 h, after which the spectrum was measured again (Fig. 6.19(b)). The spectra were normalised using an identical batch of gels that had been processed in a wash of 70 ml methanol and 30 ml pure water before being returned to pure methanol. The alcogel spectra clearly show that the Yb^{3+} is fixed place despite only being introduced by washing.

A spectrum of wash solution 1 at the end of the experiment has absorption due to Yb^{3+} of 2 dB at 975 nm. The spectrum of wash solution 1 before the experiment started was the same shape, and the difference between the two is roughly congruent with diluting the Yb^{3+} concentration by the volume of methanol in the alcogels. A spectrum of wash solution 2 at the start and end of the experiment has no detectable signal due to Yb^{3+}. In the beginning, this is because there is no Yb^{3+} in the solution, whereas at the end we believe the Yb^{3+} concentration is simply too small to measure. This implies that the overwhelming majority of the Yb^{3+} introduced diffusively into the network has become stuck, and cannot be removed by the same mechanism.

Diffusing alcogel with wash solution 1 has resulted in the Yb^{3+} ions becoming somehow attached to the network. This is confirmed by the fact exchanging the pore-fluid with wash solution 2 does not significantly reduce the amount of ytterbium in the gel, but it does remove the water from the pores. The difference in spectral shape and peak attenuation (comparing Fig. 6.19(a) and (b)) clearly show that the Yb^{3+} in the alcogel has a different local environment compared

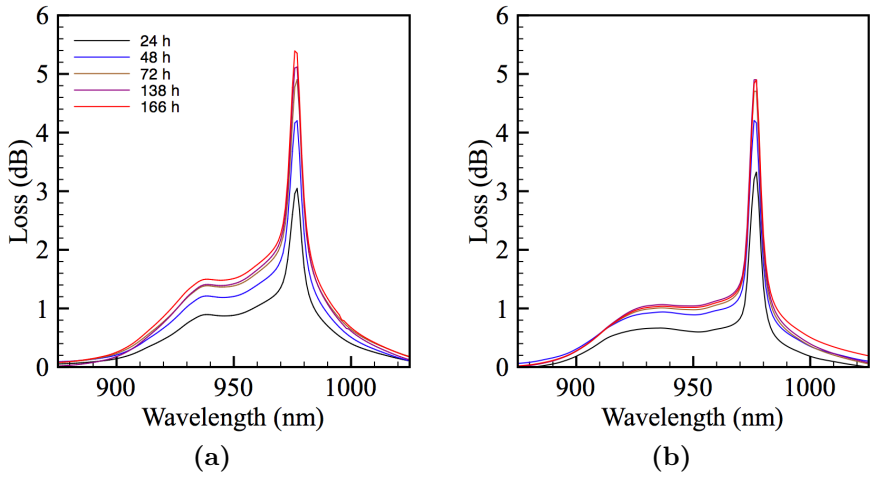

Figure 6.19: (a) The spectra of alcogels immersed in a solution containing $Yb(OAc)_3$ for up to 166 h. (b) The spectra of the same alcogels, washed with methanol so that ytterbium not attached to the structure is removed.

to the Yb^{3+} in the wash solution, although neither spectrum looks like that of Yb^{3+} in glass. Additionally, after replacing the pore-fluid with wash solution 2, the absorption due to Yb^{3+} surprisingly only drops by 0.5 dB. The pore fluid of the gels before this step (wash solution 1) has a measured absorption of 2 dB through 1 cm. Even taking into account that the alcogel contains $\sim$ 10% glass, that means the pore fluid should cause 1.8 dB/cm attenuation. That the absorption only changes by 0.5 dB when the pore fluid is exchanged for one that contains no Yb^{3+} ions is a peculiar result indeed.

It is clear from Fig. 6.19 that the amount of Yb^{3+} taken by the gel from wash solution 1 reaches some fixed level over time. In fact, after the first 48 h the wet-gel already appears to have taken up 85% of the Yb^{3+} that it can. Without further investigations, we can only speculate on the reasons for this. One possible reason could be that the pore fluid pH is altered, perhaps as the Yb^{3+} attaches to the network and displaces hydrogen ions that form acetic acid.

Refreshing wash solution 1 with a fresh, but otherwise identical, solution every 24 h leads to a higher uptake of ytterbium. The spectra in Fig. 6.20 show first the absolute scale, and then the same data normalised to the peak height so that differences in spectral shape would be more apparent. The three curves are for

24 h and 72 h in wash solution 1, and 72 h in an equivalent of wash solution 1 refreshed every 24 h. The identical shape of the curves suggests that the local environment of the Yb^{3+} is virtually unchanged, but that refreshing the solution simply leads to a larger amount of ytterbium being taken up by the network.

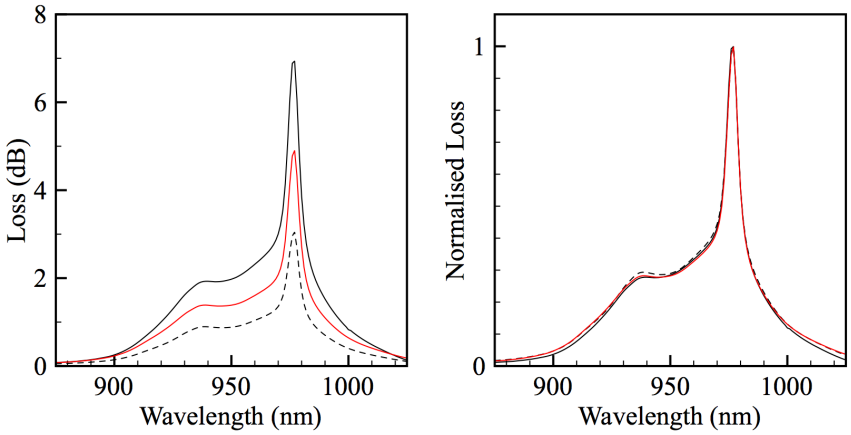

Figure 6.20: (left) The absorption spectra of gels diffused with wash solution 1 for 24 h (dashed line), 72 h (red line) and 3 × 24 h in fresh wash solutions 1 (solid black line). (right) The normalised spectra.

Adding ammonia can increase the amount of ytterbium contained in the wet-gel by a significant fraction. Adding 1 ml of 2.0 M ammonia dissolved in methanol, 69 ml methanol, and 30 ml water with dissolved $Yb(OAc)_3$ to create wash solution 1a can increase the amount of ytterbium taken up in the wet-gel by $\sim 15\%$. There are no differences in the spectral shape, so the ammonia does not appear to be having any effect on the Yb^{3+} environment.

The physical mechanism that causes an increase in the uptake of ytterbium when the wash solution contains ammonia is not understood, but we can speculate on what it may be. Initially, we considered that ammonia could act as a catalyst helping the Yb^{3+} to stick on the network more easily. Alternatively, increasing the pH makes the silica more soluble (Fig. 2.4 in sec. 2.3.1), which could make it easier for the Yb^{3+} to become embedded in the glass. Finally, the ammonia could simply be changing the distribution of charge in the solution in a favourable way by partially counteracting the acetate anion. A quick calculation from the masses of the components reveals approximately 1 mol ammonia per mol of ytterbium, for which there are 3 mol acetate.

6.3.4 Solution-doped aerogel

The alcogel described in the previous section was washed in pure methanol several times to remove excess water, and then the solvent was removed using low-temperature SCD. We made some aerogels hydrophobic by modifying the internal surfaces with HMDS. The Yb^{3+} did not seem to have any effect on the hydrophobic properties, as the aerogel was still able to support water droplets on the external surfaces. Nor did the HMDS significantly affect the spectrum of the ytterbium-doped aerogel, as can be seen in the comparison of hydrophobic and hydrophilic aerogel in Fig. 6.21. For comparison, we made some undoped aerogel that was treated in the same way apart from that the water in the wash solutions contained no ytterbium salts.

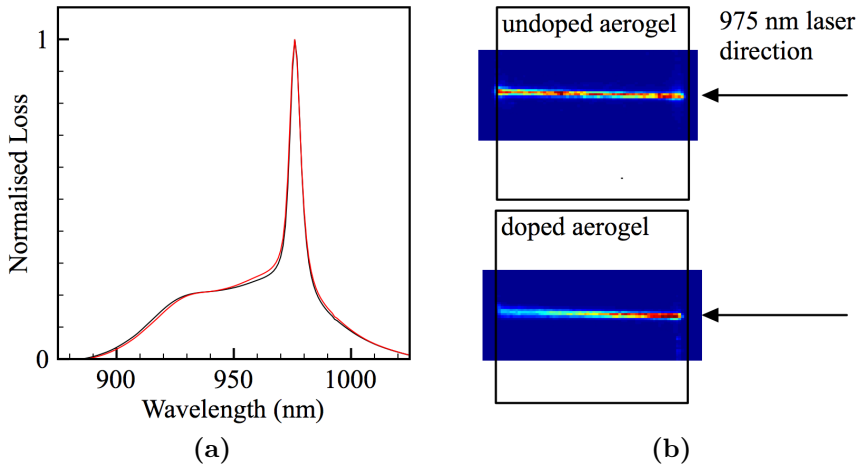

Figure 6.21: (a) The spectra of aerogel doped with Yb^{3+}. The aerogels both cause ~ 12 dB of absorption, and the normalised spectra are similar shapes despite one (red line) being made hydrophobic and the other not. (b) A 975 nm laser at low power was collimated and launched through undoped and ytterbium-doped aerogels is imaged from the side. The undoped aerogel causes almost no loss of the laser light, compared to the 5 dB caused by the doped aerogel.

Since aerogel causes Rayleigh scattering, beams in the aerogel are quite clearly visualised. Light from a 975 nm laser operating at low power was roughly collimated using a 10× microscope objective and launched through first undoped and then doped aerogel that had enough Yb^{3+} to cause 5 dB/cm attenuation at

975 nm. The scattered light was imaged using a linear InGaAs camera, and the false-colour images from the camera are shown in Fig. 6.21(b). The undoped aerogel causes almost no measurable attenuation in the scattered light. The doped aerogel causes approximately a 5 dB loss across the whole sample, and the loss is approximately the same for all parts of the sample. This implies that the dopant is homogeneously distributed throughout the aerogel.

Using a highly doped aerogel and a high power CW laser at 975 nm, we were able to observe fluorescence of Yb^{3+}. Fig. 6.22 shows a comparison between the fluorescence observed in a ytterbium-doped aerogel and the collection of scattered light from an undoped aerogel. The 975 nm laser light was focused on a point 2 mm into the aerogel, and the scattered light from that point was imaged onto a multimode fibre using a large lens. The multimode fibre was attached to an optical spectrum analyser for spectral measurements. The side-scattered light contains some components due to the laser, so for comparison we measured the spectrum of scattered light in an undoped aerogel. The difference between the two spectra is due to the ytterbium ion fluorescence in the aerogel host.

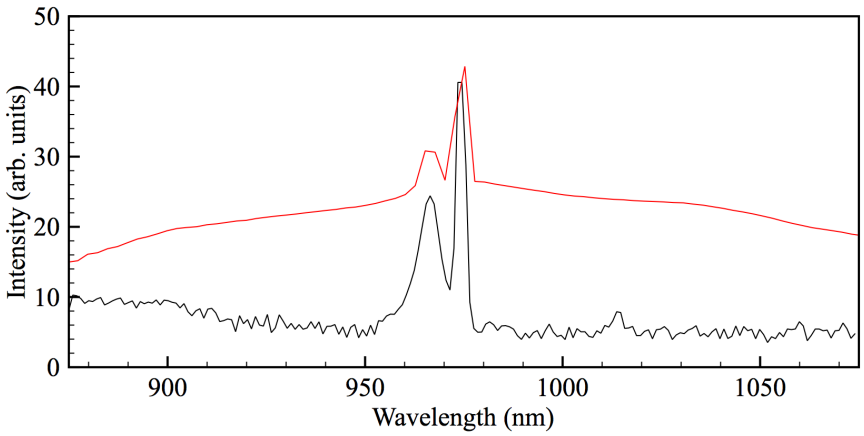

Figure 6.22: The complete (fluorescence + scattering) side-scattered spectrum of ytterbium doped aerogel (red line) compared with the side-scattered spectrum of an undoped aerogel (black line).

Whilst the fluorescence is quite strong, the spectrum is considerably different from what has been observed in bulk glasses (recall Fig. 6.16). There is quite a lot of upconversion to shorter wavelengths than 975 nm, which is presumably due to multiple-photon processes and non-radiative transitions. This could be

caused by interactions with either nearby Yb^{3+} ions or hydroxyl ions, both of which are known to cause this effect in other lanthanide-doped glasses made by sol-gel methods [168, 184]. We have not measured the fluorescence lifetime in these aerogels, but if there are large sources of quenching then we would expect it to be short.

The optical properties of the ytterbium-doped aerogel are intriguing. Particularly promising is the high amount of ytterbium in the network compared to the amount of glass. Therefore, if the aerogel could be made into consolidated glass without clustering and taking care to remove the hydroxyl surfaces (discussed in some detail in chapter 4), we believe this would exceed the maximum Yb^{3+} concentration available by other methods. In that case, we believe it would be a valuable technological development with uses in the fabrication of laser rods and fibre preforms.

It is clear there is scope for plenty of further investigation. Primarily, a better understanding of the process and limitations of doping the alcogel with ytterbium could make the procedure more efficient. The following could play a role in improving efficiency: various different anions (chloride, acetate, nitrate); mopping up the anions in some other chemical reaction (according to Tillotson *et al.* [174], propylene odixe can be used to remove HCl generated as Yb^{3+} ions become joined to the network); and different acidic or basic environments. Alternatively, various treatment methods to change the environment around the Yb^{3+}, such as adding more silica to the internal surfaces or investigating different coverings of hydrophobic groups, will hopefully shed more light on the environment of the Yb^{3+}. Methods of consolidation, taking care to remove the hydroxyl ions, can be pursued for making highly-doped glasses. Finally, further investigation into the active optical properties, such as fluorescence spectrum and lifetime measurements, will continue to inform us on the usefulness of the ytterbium doped aerogels. Once the ytterbium system is better understood, doping and co-doping other lanthanide ions should be straightforward, as their chemical properties are very similar.

Finally, we note that the solution-doping method is easily compatible with the two-step method we developed for doping aerogel with unaggregated GNPs. Fig. 6.23 shows a combined spectrum for a two-step aerogel made with 100 nm

GNPs in the sol, and solution-doped with Yb^{3+} to give a signal of comparable strength. We hope to exploit the success of co-doping GNPs and lanthanide ions to investigate gain an ideal plasmonic system.

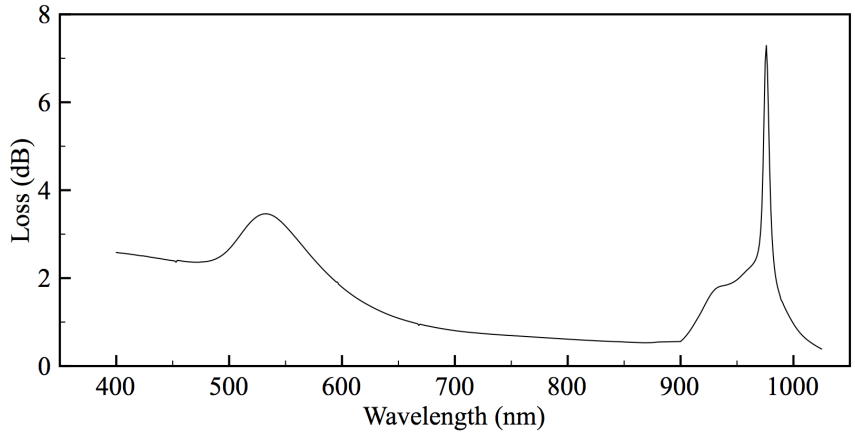

Figure 6.23: The spectrum of aerogel doped with 100 nm GNPs and Yb^{3+} ions.

6.4 Conclusion

We have developed several methods for doping aerogel, allowing us to alter its optical properties.

To create aerogel doped with gold nanoparticles, we developed a two-step method for making alcogel that can prevent aggregation. The local environment of the GNPs has been understood with the help of computational modelling of the nanoparticle's plasmonic properties. Such plasmonic aerogels are a natural candidate for exploring active plasmonic systems, as they offer access to well-separated single GNPs in an air-like matrix. They also appear to have a slight contribution to electronic nonlinearity. We hope that other nanoparticles, such as silver, platinum, quantum dots, LaF_3:Yb crystals, etc. could also be incorporated into aerogel using a similar method.

Aerogel doped with Yb^{3+} ions can be made using two methods. In the first method, acid catalysis can be used to create a clear sol containing dissolved ytterbium acetate salt. As the alcogel forms, the ytterbium becomes locked in the

network and is unable to escape even during high-temperature SCD. In the second method, diffusing ytterbium acetate solution into alcogel creates doped aerogel with exceedingly high concentrations of ytterbium. We see some potential for this aerogel to be consolidated into fully dense glass, with a very high concentration of Yb^{3+} ions evenly dispersed in the bulk. We believe the chemistry of erbium is similar enough to ytterbium that it could be incorporated into aerogel using the same method. Co-doping (either with erbium and ytterbium, or erbium and gold nanoparticles) could have technological applications as a gain medium or in lasers.

In the following two chapters, we will discuss incorporating aerogel as an element in a waveguide. It is important to note that the methods we have developed for doping aerogel could be used to make doped aerogel in waveguides. Although we have not yet done so, we hope to investigate the properties of doped aerogel in waveguides in the near future. This is particularly interesting in light of the nonlinear results, as the propagation of light through aerogel in a waveguide is not limited by the focus or Rayleigh range of lenses.

Chapter 7

Tapers in aerogel

This chapter describes the fabrication and optical properties of tapered fibres embedded in aerogel. Aerogel can be used to encapsulate a variety of tapered fibre devices because of its material compatibility and low refractive index. The tapered fibres benefit from the protection provided by the aerogel; it improves long-term stability (verified over 2 months) by preventing dust and water from damaging the fragile taper waist. Tapered fibres as small as 700 nm have be encapsulated in hydrophobic aerogel with attenuation <0.03 dB/mm. We have demonstrated that encapsulated tapered fibres have applications as fused couplers, evanescent sensors, and nonlinear light sources.

7.1 Motivation

Tapered optical fibres are made by heating and stretching a fibre over several centimetres to form a thin waist. If the transition regions between the full-sized fibre and the waist are gradual enough then the tapers can be adiabatic (low-loss), even when they have subwavelength dimensions. As the taper waist decreases in size, the spatial extent of the light field as a fraction of the fibre size continually grows. Eventually, it exceeds the total dimension of the fibre and some fraction of the light is guided in the evanescent field in the air around the glass.

The control over evanescent field makes tapers useful for devices such as evanescent sensors [185] and high-Q resonators [101, 186, 187] (each of which is explained in more detail in sec. 7.3). The principal operation of these devices is to cause well-controlled optical loss via interactions with the evanescent field. However, since the field is weakly confined, tapers are susceptible to other sources of loss that do not contribute to device functionality. The two most common problems are dust, which causes scattering and absorption loss, and moisture, which can lead to cracks forming in the tapered region of the fibre. Additionally, devices that contain loops require support completely along the fibre, as their optical properties are very sensitive to vibrations and movement.

Packaging for tapered fibre devices is therefore essential for their success. The most popular way for packaging tapered fibre devices is by suspending them in a hermetically sealed environment. This method is relatively cheap and adequate for the needs of the telecommunications industry, and is *de facto* the method for packaging fused fibre couplers (sec. 7.3.1). It provides protection from contaminants and mechanical strength, at the expense of being able to access the fibres once the package is formed.

Suspending fibres in a sealed package does not provide the mechanical stability required for making high-Q resonators from loops of fibre, and completely prohibits evanescent sensing applications. A second packaging option of encapsulating the tapers in a "low-index" material like Teflon partially addresses these problems. (The refractive index of Teflon is ≈ 1.3 [188].) The fibres are stabilised, but at the cost of a large increase in optical loss (for submicron dimension tapers) and a large change in the waveguide dispersion, a key parameter in nonlinear op-

tics. Encapsulated tapers with a 900 nm waist have 2 dB/mm additional loss at 1550 nm, dropping to 0.4 dB/mm for 1000 nm diameter tapers [185, 188]. This is particularly noticeable in the characteristics of loops, where the resonant wavelengths can shift by >200 nm [186].

Although not permeable itself, if the Teflon is a sufficiently thin coating on one side of a fibre or loop then the evanescent field will still feel weak effects from the external medium. A loop made with a hollow in the centre can sense changes in the refractive index with a sensitivity of 40 nm per unit change in refractive index [101]. Additional sensing functionality using the addition of biolayers has recently been proposed but remains unobserved [185].

Encapsulating tapered fibre devices in hydrophobic aerogel would create a protective package that can be used for almost any type of fibre device because of its material compatibility and refractive properties. The aerogel structure creates a package that is between the two existing approaches: microscopically, the fibre is suspended by the sub-wavelength elements all along its length, but macroscopically the effect is that the taper is completely encapsulated in the aerogel. The compatibility between the two silica glass materials means the device should be stable over a large temperature range. The low refractive index means that the waveguide dispersion is virtually unchanged, which is vital for fused couplers, loops, and nonlinear light sources. The porous nature of the aerogel can be exploited in gas-sensing experiments, but the pores are narrow enough to prevent dust from reaching the fibre and causing loss.

The aerogel can offer more than just a protective box for the tapered fibre. The previous chapter on doped aerogel shows its potential as a host for active optical elements. These aerogels, in intimate contact with the taper waist, could provide a true 3D distribution of dopants within the evanescent field. Depending on the application, dopants could be used to provide sensitivity to different gases, optical gain or lasing, and plasmonic resonances.

7.2 Method

In this section, we describe the process we have developed for encapsulating a tapered fibre in aerogel. Tapered fibres with low optical loss are made on our taper rig, and then transferred to a specially designed holder so they can be immersed in sol. The sol transforms to a rigid alcogel after 10 min, with the fibre fixed inside. At this point, it is made into aerogel using the method we described in sec. 5.2.1. This method can be used to encapsulate a variety of tapered fibre devices in aerogel.

7.2.1 Recap: making tapered fibres

The taper rig is described in more detail in sec. 3.2, here we just recap the operation and important results. Our tapered fibres are made by heating and stretching standard single mode fibre (Corning SMF-28) in an oxy-butane flame. The motion of the flame and the stages used to pull the fibre are controlled by a computer program, which calculates their movements based on the desired shape and size of the taper. Before tapering, the region of the fibre to be processed is stripped of coating and cleaned with acetone. It is held on the pulling stages using a double fibre clamp, and various v-grooves can be used depending on the size of fibre being tapered.

Using our taper rig it is possible to make low loss tapers with very small dimensions. Leon-Saval *et al.* [94] reported on tapers with 280 nm waists, up to 30 mm long and with only 0.01 dB/mm attenuation. They also verified using SEM images of a 620 nm taper that the diameters calculated using the taper rig software were indeed being made in the fibres (to within the resolution of the SEM).

7.2.2 Holder design

The holder used for casting sol around a tapered fibre has a significant impact on the whole fabrication process. Key parameters are: the size of tapers that can be accommodated, the fibre clamping mechanism, the diffusion length for solvent

exchange, and the materials used. As we have previously discussed (sec. 5.1) Leon-Saval demonstrated embedded tapered fibres in aerogel using PTFE moulds, but the fibres were bent so that they survived the embedding process despite the shrinkage of the aerogel. These fibres were lossy because of the bends, so new holders with a straight configuration were required.

Leon-Saval made additional holders for straight tapered fibres from large blocks of PTFE provided by the Department of Chemical Engineering. The block was cut and machined to contain a cavity 50 mm long, 10 mm wide, and 20 mm deep. The short sides of the cavity had 10 mm×1 mm slots cut into them for the fibre, and small wedges of PTFE wrapped in PTFE plumber's tape were jammed in the gaps to stop the sol from leaking out. Fig. 7.1 is a photograph of one of these holders.

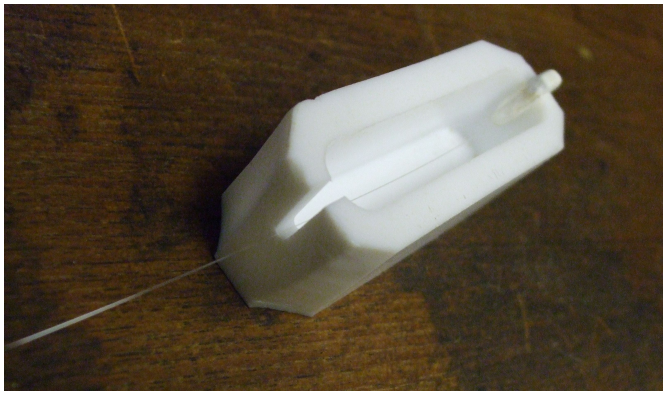

Figure 7.1: An early design of tapered fibre holder made from PTFE.

This holder design had several problems, which we recount in order of increasing severity: the depth of the holder meant that supercritical exchange took a long time; the fibre clamping mechanism made it difficult to hold very small tapers without them breaking; and the sol leaked from the clamping points anyway. By investigating simple holder designs (without fibres), we also discovered that the PTFE block from which the holders were made in some way prevented the formation of monolithic aerogels.

The contamination led us to develop holder designs with aluminium and eventually have them made in stainless steel. We used aluminium for the design steps because it is easy to machine, so moulds could be made cheaply and quickly on site. After settling on a final design, we had stainless steel holders fabricated as

the aluminium oxidises and degrades after repeated uses.

Problem. *holder depth*

The 20 mm depth of the cavity in the initial holders meant long solvent exchange times were required. Our initial design for the low-temperature SCD rig could only supply CO_2 at the bottle pressure, and was not controlled via computer. Having only bottle pressure CO_2 reduces the practical working temperature and increases the time it takes for solvent exchange to >60 h. Since the rig was not under automated control, such long drying times were virtually impossible.

Solution. *shallower holders, removable bases*

Thinner samples require much less time for solvent exchange. Halving the thickness does not alter the mechanical rigidity of the final aerogel, but reduces the exchange time by a factor of four. Using the most current version of the supercritical drying rig (operating above the supercritical point of CO_2) samples with a 10 mm diffusion length are possible, but diffusion is still slow. Making the aerogel thinner than this reduces its rigidity, and increases the likelihood of damaging the tapered fibre.

Creating a 10 mm deep mould with a removable base allows diffusion from both sides, halving the distance required for solvent exchange. Alcogel in a holder with this dimensions has the same diffusive properties to those formed in cuvettes, where we know solvent exchange is complete in less than 4 h. The alcogel cracks when the base-plate is removed because of a force holding the two together. The intended operation can be restored by placing a thin PTFE film between the base and the holder body, so the alcogel is not in contact with a removable metal part. We have used this style of holder to make monolithic aerogel.

Problem. *the fibre clamping mechanism*

The pushed-down slot-filler used to clamp the fibre in place and prevent sol from leaking was a poor design. The force caused by pushing down on the fibre caused tension and broke small tapers before alcogel was added. Additionally, a small amount of leakage around the sides and through the bottom was inevitable,

even if the piece felt tightly wedged. This is partially because the PTFE thread-seal tape is not designed to be impermeable by methanol, and partly because the fibre caused a slight gap where sol could leak out. Although the leakage is small, we established that it caused significant cracking extending far into the eventual aerogel.

Solution. *a rubber-based flat clamp*

Both of these problems can be solved using a more intricate clamping system. Initially we tried a holder that was formed of two 5 mm thick plates that sealed together by two rubber elements. However, the rubber seals swelled and out-gassed as the CO_2 depressurised, breaking the fibre. We identified a type of PTFE-impregnated high-temperature rubber that was materially compatible with CO_2 and did not out-gas during the depressurisation. However, this rubber is more difficult to machine and is unsuitable for such large seals as were used in separated holders. A more compact fibre clamp design was required.

Inspired by the gas-cells used for loading fibre cores with liquids and gases (chapters 8 and A), we tried a clamping mechanism that sealed by screwing in a small circular rubber element containing the fibre. Although this provided an excellent seal, it often caused the fibre to break because of the torsion on the fibre as the screw was tightened.

Finally, we adopted a flat clamp that sealed the around the fibre using a small pad of the CO_2 resistant rubber. The clamp has a v-groove cut in it that is large enough to fit the two fibres of a fused coupler. Everywhere else, the seal is provided by metal-on-metal contact from tightly screwing the clamp into position. A picture of one of these clamps is shown in Fig. 7.2(a). The shape was chosen so that the clamp separates from the base of the holder in the easiest way. Submicron diameter tapered fibres can be clamped straight in our holders and embedded in aerogel without breaking.

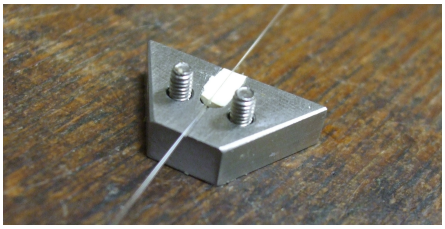

(a)

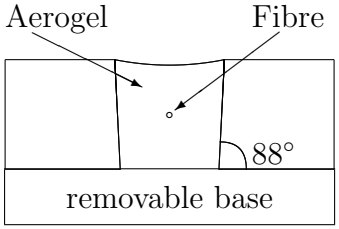

(b)

Figure 7.2: (a) A photograph of one of the clamps we use to hold the fibre in our holders and prevent the sol from leaking out. (b) A schematic of the holder cross-section, showing the 2° wedge applied to the long sides.

Problem. *removing aerogel from the holder*

Good aerogel remains quite firmly in the holders after supercritical drying, and requires a firm push to remove. However, pushing the aerogel often results in it bending slightly, and can cause the fragile taper to break.

Solution. *a 2° wedge shape*

We machined the two longest edges of the holder into a wedge shape, so that the aerogel was easier to remove from the holder. The cross-section of the wedged sides is shown in Fig. 7.2(b). The short edges of the holder were not angled as this would alter the fibre clamping mechanism.

7.2.3 Making the aerogel

We have adopted the following variations to our standard low-temperature SCD procedure (sec. 5.2.1) as our process for making aerogel-encapsulated tapered fibres. The molar ratio of TMOS : methanol : water used in the sol is 1 : 3 : 4, and the catalyst volume is adjusted to give gelation in 10 min. The resulting aerogel has a slightly higher density aerogel with improved strength and lower shrinkage. Low shrinkage is important so that the taper is not damaged or broken by the build-up of forces during SCD.

The fibre is clamped into the holder, and the sol is poured in as depicted in Fig. 7.3. (We have removed the nearer fibre clamp for this picture to make

it easier to see.) Laying a thin piece of the PTFE film on top of the sol helps reduce ambient drying from the surface. Alternatively, the holder can be kept in a saturated atmosphere of methanol with a similar effect. After gelation, the alcogel in the holder is immersed in methanol with the base left in place. Subsequent washing steps are according to our regular procedure, and can be with our without the base. A washing step in methanol and HMDS makes the resulting aerogel hydrophobic.

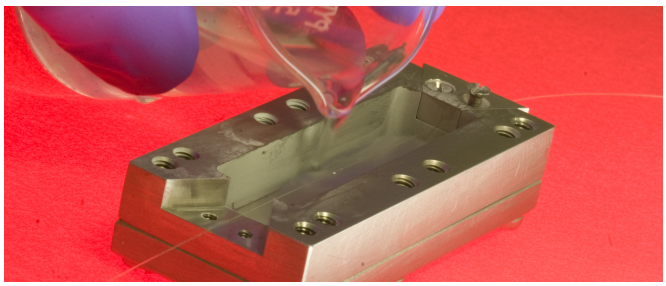

Figure 7.3: Liquid sol is added to a holder, where it becomes alcogel with the fibre *in situ*.

Supercritical drying

Low-temperature SCD is preferred to the other drying methods because it produces aerogel with low shrinkage and is compatible with the polymer coating on the fibre. A tapered fibre in alcogel is stood on its long side in the autoclave, with 100–200 ml excess methanol to minimise cracking caused by the solvent exchange process. Liquid CO_2 is introduced to cover the sample completely, and the pressure is slowly pumped up to 80 bar. This pressure is high enough to keep the CO_2 liquid, as we do not switch on the heaters until later in the cycle. The system is held at constant pressure, while the low flow rate continues for 4 h. After the solvent is fully exchanged, we increase the pressure to 100 bar and the temperature to 40 °C so that the fluid in the pores becomes supercritical. After 30 min of equilibration in the critical state, we slowly return the vessel to ambient pressure over 3 h.

The low-temperature SCD procedure we have just described has given us the highest success rate and was used to make most of the devices described in sec. 7.3. Using supercritical solvent conditions for exchange, as described in sec. 5.2.5, can

reduce the exchange time. The slow depressurisation minimises the stress on the fibre during this stage of drying, which reduces the chance of the taper breaking.

Tapered fibre in aerogel

We have encapsulated tapers of many different sizes in aerogel, from fused couplers (~ 40 µm waist region) to nanowires 700 nm in diameter. Fig. 7.4 shows a photograph of a 6 cm long, 10 µm diameter taper coupled to a red laser via the left hand fibre pigtail. The aerogel causes some scattering of the red light in the taper waist, clearly visible against the blue illumination of the aerogel block. The SEM image (inset) shows the intimate contact between the aerogel and a tapered fibre.

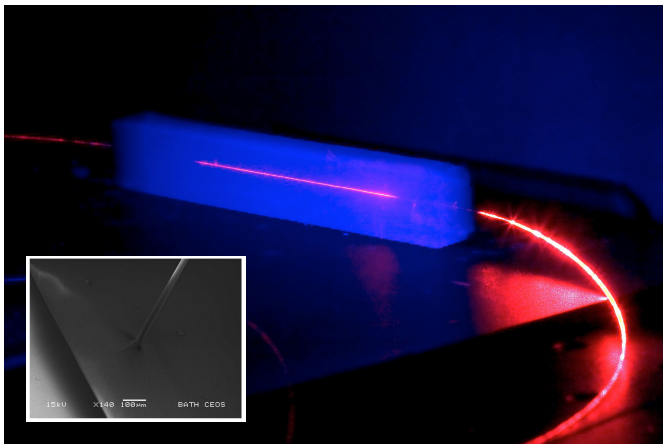

Figure 7.4: A tapered fibre with a 6 cm long, 10 µm diameter waist encapsulated in a hydrophobic aerogel. The aerogel was illuminated using a blue LED torch, and the fibre is coupled to a red laser diode. (Inset) SEM of a tapered fibre embedded in aerogel.

Aerogel-encapsulated tapered fibres have low loss and excellent long-term stability. The transmission loss spectra for 10 mm long, 10 µm and 1 µm diameter tapered fibres embedded in hydrophilic aerogel are plotted in Fig. 7.5(a). In the 1 µm taper, the spectrum has a double-peak at 1366 and 1383 nm from a combination of free and hydrogen-bonded OH resonances [139, 189]; i.e. the taper is sensing the effect of the aerogel. Hydrophobic aerogel reduces shrinkage and even smaller tapers can be encapsulated with lower loss. The transmission loss spectrum in Fig. 7.5(b) is for a 20 mm, 800 nm taper encapsulated in hydrophobic

aerogel, measured immediately after supercritical drying. The overall loss is less than for the 1 μm taper measured in Fig. 7.5(a) despite the waist being narrower and longer. The region of the spectrum from 1510–1545 nm was measured again 15 days later and is plotted for comparison in red. The increase in transmission loss is below the measurement error of 0.1 dB.

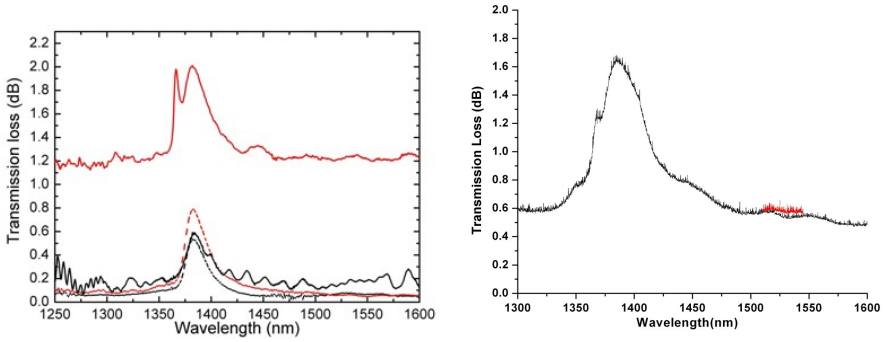

(a) **(b)**

Figure 7.5: (a) Transmission spectra of tapered fibres in air (broken line) and in aerogel (solid line), for waist diameters of 10 μm (black) and 1 μm (red). (b) The loss of an encapsulated 800 nm taper immediately after fabrication (black curve, full span) and 15 days later (red curve, between 1510 and 1545 nm).

7.3 Tapered fibre devices in aerogel

7.3.1 Fused couplers

Fused couplers are widely used basic components in optical communications and other fibre systems. They are made by tapering (heating and stretching) two bare fibres together to form a common fused waist, in which light can couple from one fibre to the other [99]. The waist is very thin and its optical characteristics are sensitive to bending and other stresses [190–193], so the coupler must be carefully packaged to protect and stabilise it.

A typical primary package (Fig. 7.6) comprises a silica rod to which the fibres at both ends of the coupler are fixed by epoxy, with the coupler waist suspended in air in between [190, 191]. A further, secondary, package protects the delicate waist

and the primary package. Thermal stresses are reduced because rod and fibres are made from the same material (silica), and having air around the waist minimises thermo-optic changes in coupling. However, epoxy can degrade when exposed to elevated temperatures and high humidity, and the couplers are typically only tested to 85 °C [191–193]. Epoxy-free primary packages have been made by fusing the fibres to the glass substrate [192, 193], but thermal characteristics above 85 °C were not reported and the coupler waist remained unsupported over its length.

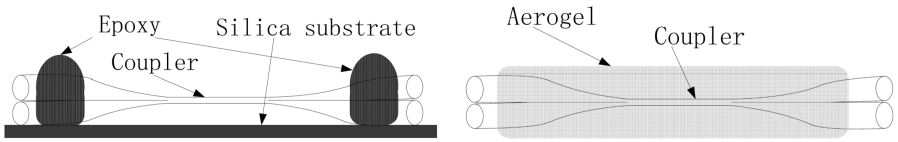

Figure 7.6: (a) Schematic picture of the existing package used for fused couplers. The coupler is fixed by epoxy to a silica bar so that there is material compatibility. This is then fixed to a secondary package for ruggedisation. (b) An aerogel package for fused couplers. The coupler waist is completely supported by the aerogel. A secondary package could be applied to ruggedise the aerogel if required.

We have made an epoxy-free hydrophobic aerogel package for fused couplers made from SMF-28 fibre. The coupler was held in a holder and immersed in sol, which soon became a wet-gel. Thereafter we followed a normal procedure to make hydrophobic aerogel by low-temperature SCD (sec. 5.2.1).

The splitting and loss spectra of the encapsulated coupler are plotted in Fig. 7.7. The splitting ratio changed by less than 1% at 1550 nm during the encapsulation process, and was 50 : 50 at 1538 nm. The large dip in excess loss at 1383 nm is characteristic of tapering in a flame that produces water vapour. Away from this the excess loss is only 0.2 dB, of which only 0.1 dB was introduced by the aerogel. These results show that the encapsulation process has little effect on the coupler, because the aerogel is behaving refractively like air.

The change in splitting ratio at 1310 nm, as the fibre was heated up to 250 °C and cooled back down again, is plotted in Fig. 7.7(c). The splitting ratio varied within ±1%, and the excess loss varied by <0.05 dB. This is comparable to the stability of our laser source. The temperature range of the measurement

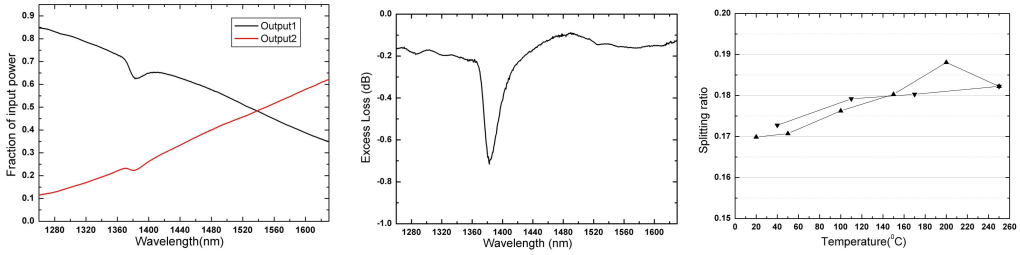

(a) **(b)** **(c)**

Figure 7.7: (a) Splitting and (b) excess loss of a fused coupler embedded in aerogel. (c) The change in splitting ratio at 1310 nm as the fibre is heated up to 250 °C (▲) and cooled back down (▼).

was restricted by our equipment, and higher temperatures below the sintering temperature of the aerogel (∼800 °C) should continue with a similar trend.

Using a hydrophobic aerogel significantly enhances the thermal stability of fused coupler packages, without degrading the other optical properties. Though not rugged, this package also performs some functions of a secondary package by shielding the coupler waist from contamination, handling and gross mechanical disturbances. The extra processing is clearly not appropriate for a routine low-cost component, but the extended stability, support for the entire coupler waist, waterproofing, temperature range and light weight could make this a suitable package for couplers intended for extreme service such as in water or in space.

7.3.2 Evanescent-field gas sensing

Submicron tapers (nanowires) carry a significant fraction of the light power in the evanescent field. In Fig. 7.8(a) we have plotted this fraction at 1550 nm for different diameter nanowires as a function of the external refractive index. When surrounded by air, an 800 nm nanowire carries around 50% of the light outside of the fibre, and the evanescent field extends 250 nm into the surrounding environment. Increasing the external index by encapsulating the nanowire in aerogel results in a small increase in external field, but if the encapsulant is Teflon then the evanescent power rises to 85% and the spatial extent of the field rises to 600 nm.

In air, the loss of a 750 nm nanowire rises (approximately) linearly by 0.3 dB/h

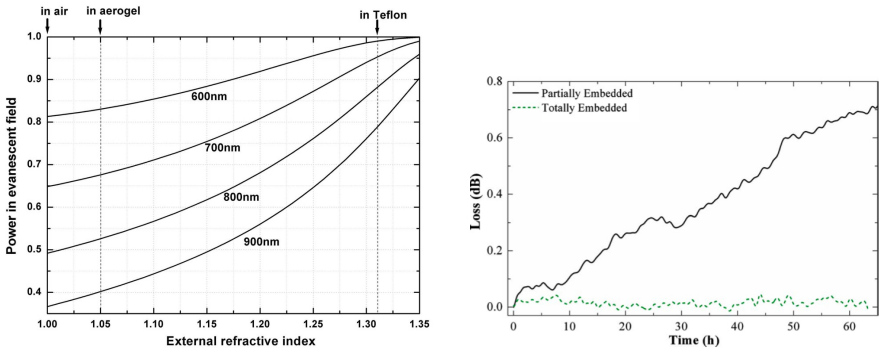

(a) **(b)**

Figure 7.8: (a) Calculated fraction of power in the evanescent field of the fundamental mode at 1550 nm wavelength versus external refractive index, for the nanowire diameters marked. (b) The increase in loss of a tapers partially and wholly encapsulated in Teflon, from [185].

[185], but when encapsulated in aerogel or Teflon the loss of the nanowires does not increase with time. However, for evanescent spectral-based sensing, gas molecules must come close enough to interact with the guided light field. If the nanowire is encapsulated in Teflon, then the Teflon coating must be thinner than 600 nm for light to feel any effect from the gas. One way to achieve this is by only partially encapsulating a nanowire in Teflon, but this reduces the time-dependent loss rather than eliminating it, Fig. 7.8(b). The increase in loss comes because the evanescent field has been re-sensitised to dust and contaminants, by the very requirement that it can interact with gases (although damage due to bending and moisture in the air is significantly reduced).

Aerogel encapsulants are unique because they are permeable to gases, so they can have macroscopic dimensions without significantly affecting the sensitivity. We have performed simple experiments on bulk aerogel with various gases that show diffusion in aerogel is comparable to that in air. Leventis *et al.* [145] have reported that the diffusion coefficient of oxygen in aerogel is $1 - 2\,\mathrm{mm}^2/\mathrm{s}$, only one order of magnitude less than unimpeded diffusion in air. Acetylene (C_2H_2) has a conveniently-distinctive absorption spectrum, and should diffuse similarly in our aerogel because the gases' molecular masses and the aerogels' pore sizes are similar.

We demonstrated gas sensing by placing an aerogel-encapsulated 800 nm ta-

pered nanowire in a test chamber into which acetylene gas could be introduced and removed at atmospheric pressure. The familiar signature of acetylene appeared in the transmission spectrum, Fig. 7.9, with a peak absorption as much as 2 dB at maximum concentration. The change was completely reversible, the induced loss returning to zero when the acetylene was removed. The response time was 16 ± 3 s for diffusion in both directions, consistent with the estimated diffusion time through 5 mm of aerogel [145].

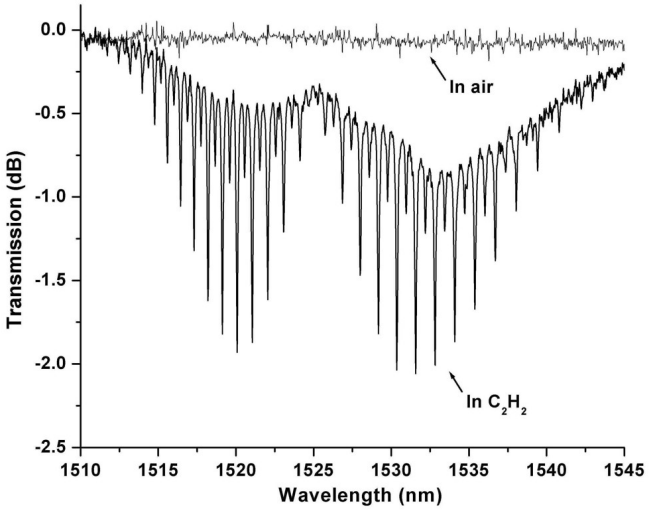

Figure 7.9: Steady-state transmission spectra of a nanofibre with waist length 20 mm and diameter 800 nm embedded in aerogel, after the surrounding air was replaced by acetylene (C_2H_2) gas at atmospheric pressure, and after the acetylene was replaced by air again. The spectra are relative to the transmission before the acetylene was first introduced.

The narrow pores of the aerogel filter particulates from the air that would otherwise cause loss, but water vapour can still diffuse into the aerogel and approach the nanofibre surface. However, the process of making the aerogel surfaces hydrophobic by the modification of surface hydroxyl groups with trimethylsilyl ones also causes the same modification on the nanofibre itself and protects it from water adsorption and condensation. This inhibits the formation of the surface cracks thought to cause loss (and indeed mechanical weakness) [185, 188]. We have observed that a 700 nm nanowire encapsulated in aerogel was stable even after two months, compared to a normal life of just a few hours.

Packaging sub-micron tapered fibres in aerogel exploits the highly porous nature and low refractive index of the aerogel for applications in evanescent gas sensing. The fabrication method has the added benefit of making the tapered fibre hydrophobic, so the aerogel and fibre is protected from damage caused by water vapour as well as immersion in liquid. This could be exploited for sensing gases dissolved in aqueous solutions, where the gas can diffuse through the aerogel pores but the liquid cannot. The range of gases for sensing can be extended by doping the aerogel, for example following the method of [145] to make the device sensitive to oxygen. Aerogel-encapsulated nanowires therefore make an entirely new class of evanescent-field sensors a reality for a variety of medical or defence applications.

7.3.3 Knotted tapers

When thin tapered fibres are looped up or tied in a knot, the strong coupling at the overlapping region creates a resonator with high Q-values from a few thousand to a few million [101, 186, 187]. These loops have been generating interest in fields as wide as sensing, cavity QED, and nonlinear optics [101]. However, if a loop moves or is bent even by a small amount, the resonant wavelength of the cavity changes and the properties have to (at the very least) be recalibrated. As we discussed in chapter 4, an aerogel-loop-aerogel 'sandwich' provided a temporary solution to this problem [102], but fails to prevent the ingress of moisture or gross movement. Encapsulation is key to realising the useful potential of these devices.

Encapsulation in polymers such as Teflon protects and stabilises the microfibre loops. The tapers used in making loops are generally $> 1\,\mu$m in diameter [186, 194], so the excess loss caused by the encapsulation remains manageable. However, the change in the evanescent field caused by the polymer encapsulant significantly alters the coupling condition and blue-shifts the resonant wavelengths [186]. Encapsulation in low-index aerogel should not significantly shift the strong coupling wavelengths, and we still do not expect it to introduce much excess loss to the device.

We encapsulated a knot made from a $4\,\mu$m diameter tapered fibre in a hydrophobic aerogel. The picture in Fig. 7.10 shows the loop illuminated with light

from a red diode laser coupled into the right hand pigtail. The circular shape is clearly visible, with a very slight distortion to the upper right hand quadrant. We are currently investigating the optical properties of encapsulated knots and hope to report further on them soon.

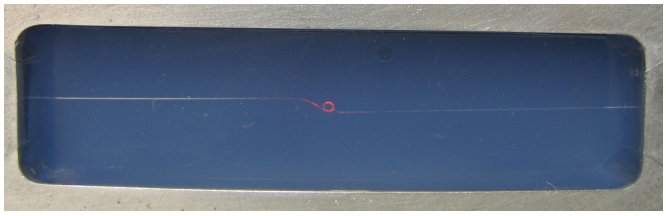

Figure 7.10: A tapered fibre knot encapsulated in hydrophobic aerogel, illuminated with light from a 635 nm fibre coupled source.

7.3.4 Supercontinuum generation

Optical fibres make an ideal medium for observing nonlinear effects because they have low loss and a small effective area [22, 85]. However, the buildup of nonlinear effects in conventional fibres is limited by the high normal group velocity dispersion at visible wavelengths [22]. PCFs and tapered fibres can be designed to have anomalous group velocity dispersion at a chosen wavelength. These can both be used to generate a broadband, visible, optical continuum (supercontinuum) from 400–1600 nm [22, 100, 195]. Whereas supercontinuum in PCF has become widely a commercialised product, in tapered fibres it remains relatively unexploited. This is in part because tapered fibres must be packaged carefully and are optically degraded by dust settling on the fibres surface.

The calculated dispersive properties of a 1 μm diameter taper in air and aerogel are plotted in Fig. 7.11(a), and the broadened supercontinuum spectra of 1 cm tapers in those environments are plotted in (b). The supercontinua were generated in the tapered fibres by launching light from a pulsed 800 nm Ti:sapphire laser (170 fs pulse duration, 76 MHz repetition rate) into the embedded taper via a similar length of input fibre.

The spectral broadening observed in these tapers was only ~ 200 nm because the taper diameter was designed for a relatively large field overlap (4%) with the external medium to emphasise any differences introduced by the encapsulation

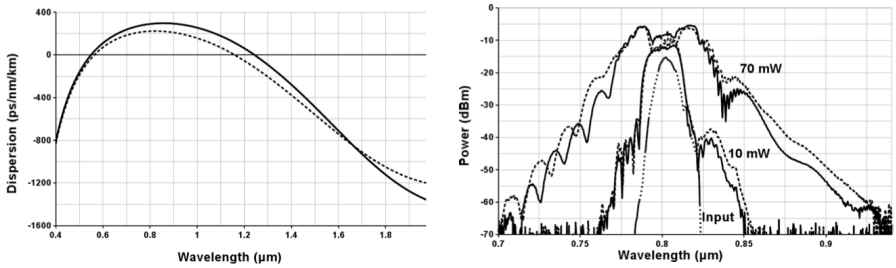

(a) **(b)**

Figure 7.11: (a) Calculated dispersion for a 1 μm waist diameter tapered fibre in air (solid) and aerogel with $n_{\mathrm{agl}} = 1.05$ (dotted). (b) Output supercontinuum for a tapered fibre with a waist 1 cm long and 1 μm in diameter in air (solid) and in aerogel (dashed) at 10 mW and 70 mW output power together with spectrum of incident laser light (dotted line with dashes).

process. The spectra show that the aerogel-embedded taper behaves similarly to air, which is expected from the similarity of the calculated dispersion. By calculating the effect of the power propagating in the evanescent field around our tapers, we expect to observe increased nonlinearity (and therefore more spectral broadening) if the n_2 of the aerogel is more than two orders of magnitude greater than that of silica. Since we have observed similar spectral broadening in air and aerogel, our measurements suggest that the electronic nonlinearity of our aerogels is small.

The 1 μm waist diameter taper in aerogel survived for over a week, with no noticeable loss, when removed from its container and left in a lab. It was eventually broken by user mishandling. This is in contrast to a 1 μm taper in air that severely degrades over time (> 3 dB loss in 1 h).

We made second embedded taper with an 800 nm diameter waist. The dispersion calculation for this fibre surrounded by air, aerogel and Teflon is plotted in Fig. 7.12(a). We have included the material dispersion of silica and Teflon [196] in these calculations, but neglected the dispersion of aerogel since it is small (sec. 2.4.3). This figure shows that the zero-dispersion wavelength of this taper is 510 nm in air and 530 nm in aerogel, whereas in Teflon the dispersion is always strongly normal and never zero. We could therefore demonstrate visible single-mode supercontinuum generation (Fig. 7.12(b)) in a 20 mm long taper pumped by

a pulsed green laser, as in [94] but with hydrophobic aerogel to protect the taper and indefinitely extend its lifetime. The output spectrum was unchanged after half an hour, whereas an unencapsulated nanofibre would have been destroyed in this time by laser-induced heating at surface scatter points caused by dust or cracks.

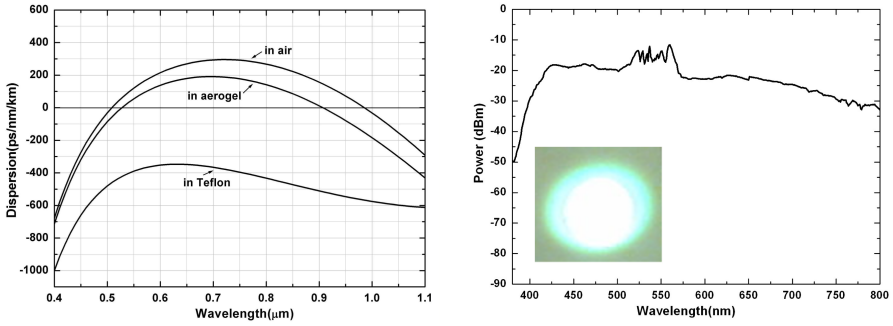

(a) **(b)**

Figure 7.12: (a) Calculated dispersion for a 800 nm waist diameter tapered fibre in air, aerogel and Teflon. (b) Output supercontinuum for a tapered fibre with a 2 cm long and nm in diameter in aerogel with an output power of 5.7 mW. Inset is a photograph of the output far field pattern.

7.4 Conclusion

Encapsulation of tapered fibres in hydrophobic aerogel overcomes key impediments to their exploitation in optical nanowires and devices, including: degradation over time; encapsulation-induded loss; undesirable changes in light confinement and dispersion; thermal sensitivity; and movements in unsupported structures. The aerogel is a rigid barrier to particulate contaminants, waterproof on macroscopic and molecular scales, potentially self-cleaning, permeable to gases, and optically like air. We have demonstrated some of these improvements with a gas sensor, a fused coupler with enhanced thermal stability, and a supercontiuum source. It should also be possible to exploit other optical properties of the aerogel itself, including the ability to functionalise it with dopants as we have previously discussed in chapter 6.

Chapter 8

Aerogel core waveguide

This chapter describes the fabrication and properties of an aerogel waveguide in the core of hollow photonic crystal fibre. The linear properties are discussed in detail, and then some preliminary nonlinear results are presented. The fibre provides mechanical protection enabling what we believe is the largest aspect ratio of any aerogel, $\sim 30{,}000:1$. Light is guided in the aerogel core, with a measured attenuation of 0.2 dB/cm at 1540 nm. At this wavelength, the waveguide operates in a single mode. The structure guides light by different mechanisms depending on the wavelength. At long wavelengths, the effective index of the cladding is below the aerogel index of 1.045 and guidance is by total internal reflection (TIR). At short wavelengths, where the effective cladding index exceeds 1.045, a photonic bandgap can guide the light instead. There is a small region of crossover, where both index- and bandgap-guided modes were simultaneously observed.

8.1 Motivation

Incorporating aerogel into a waveguide gives interaction lengths limited by the attenuation of the material rather than, say, the Rayleigh length of a focused free-space beam. In the previous chapter, we saw how aerogel could be used to enhance tapered fibres several centimetres long. The aerogel behaves refractively like air, with little perturbation of the guided mode. In sufficiently small tapers, a large component of evanescent electromagnetic field extended far into the aerogel. However, the evanescent field is weak. In order to study intensity-dependent interactions, it would be advantageous to confine light to a small waveguide core made of aerogel. Since aerogel has the lowest refractive index of any solid, guidance by TIR at an interface with another solid is impossible.

Hollow core fibres (HC-PCFs, sec. 3.3.2) use a microstructure cladding to confine light in a region of low refractive index. The core of these fibres can be filled with gas for enhanced laser interactions by tight transverse confinement and long interaction lengths [197–199]. This technique enables weak optical effects, such as stimulated Raman scattering in hydrogen or electromagnetically induced transparency (EIT) in acetylene, to be visible at low powers (this is discussed further in appendix A). All fibre gas-cells, where the HC-PCF is hermetically sealed to industry standard SMF-28 fibre [200], use these interactions in stable and portable devices.

If the core of a HC-PCF is filled with a material of a higher refractive index than the effective index of the cladding, then light can be confined by TIR. Liquids have a high enough index for this to occur for almost arbitrary cladding structures. Water [201], ethanol [202], and toluene [203] have all been used to fill PCFs. In these papers, the focus has been on the nonlinear properties of the filled fibres, e.g. for supercontinuum generation.

The refractive index of aerogel is a little larger than that of a gas, but a lot smaller than that of a liquid. If it is used to fill a hollow-core PCF, then it will cause a significant perturbation to the structure of the waveguide. Therefore, the optical properties of an aerogel filled HC-PCF will strongly depend on the fibre's microstructure. Although the refractive index of aerogel is very low, in carefully selected PCFs the effective cladding index is even lower. In these fibres, at least

for some wavelengths, the aerogel can confine light by TIR.

8.2 Method for making filled fibre

8.2.1 Selecting a fibre

Bandgap guiding hollow-core fibres (sec. 3.3.2) can confine light of a narrow wavelength range in a low index core. Understanding the properties of the fibre cladding at different wavelengths helps us to understand why the waveguide only operates over a narrow range. We selected a fibre with a bandgap at visible wavelengths, and simulated an idealised version of the cladding structure using an in-house modelling package [111]. Fig. 8.1(a) shows an image of a cladding cell taken using a scanning electron microscope (SEM). The SEM is used to measure the relative thickness of the glass struts and the curvature of their intersections, as a fraction of the pitch of the fibre $\Lambda = 1.8\,\mu$m. These measurements are used to generate the computerised approximation of the cladding unit-cell, and the photonic density of states (DOS, sec. 3.3.2) for different effective index modes, Fig. 8.1(b & c).

The red regions of the simulated DOS plot mark effective indices, where no cladding modes exist. The black arrow marks the bandgap at the air line, where modes with an effective index $n_{\text{eff}} \approx 1$ are confined in a hollow core defect. The simulation parameters were adjusted until the bandgap matched that measured in the real fibre. In this case, the bandgap extends from 550–750 nm.

At long wavelengths, the effect of the microstructured cladding is "washed out". The largest effective index of a cladding mode (the fundamental space-filling mode), approaches the refractive index of an effective medium calculated from the weighted average of the materials' dielectric constants [106]. From measurements of the structure, we calculated the air-filling fraction of this fibre to be 94%, so $n_{\text{fsm}} \to 1.0325$. In our simulation, we find that $n_{\text{fsm}} < 1.035$ for wavelengths longer than 1350 nm.

Raising the refractive index of the core material is equivalent to moving up the DOS plot, starting at $n = 1.00$. Modes with higher effective index n_{eff} can

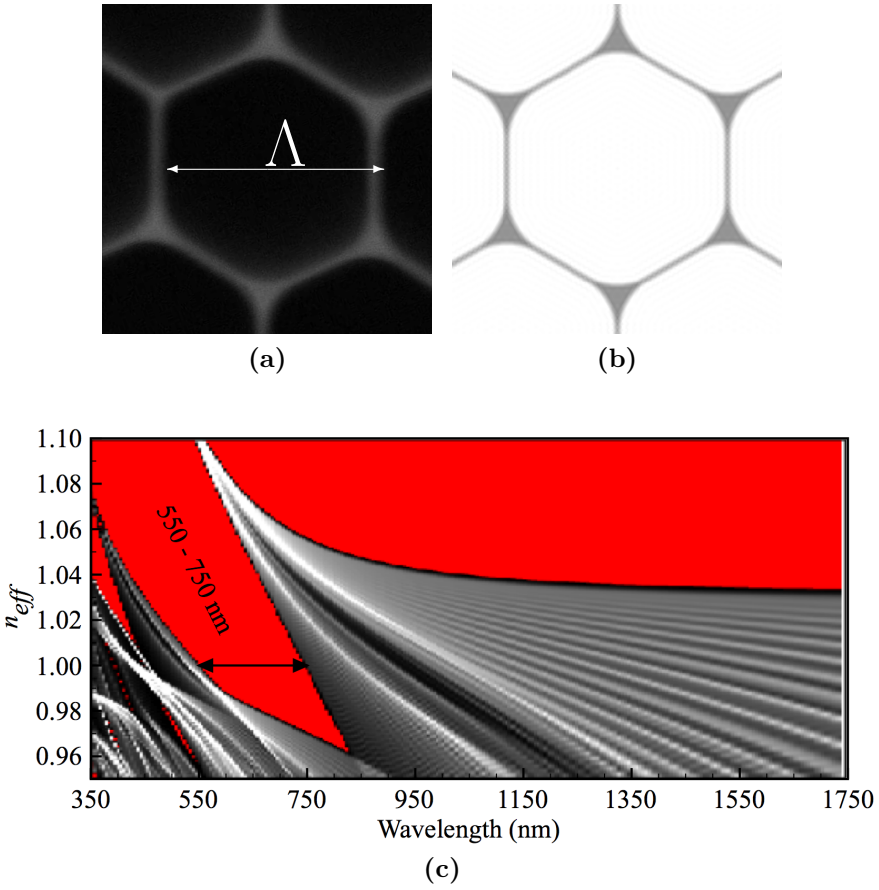

Figure 8.1: (a) Actual and (b) simulated cladding structures of the HC-PCF. (c) The DOS plot for the idealised fibre cladding. On this plot, regions of white are highly populated with modes, and darker regions represent fewer modes. Red regions are combinations of effective index and wavelength where there are no cladding modes.

become guided in the core. Significantly, if the air core is replaced with a material that has a refractive index above n_{fsm}, then modes with $n_{\text{fsm}} < n_{\text{eff}} < n_{\text{core}}$ will be confined to the core by TIR rather than by a bandgap. Since the refractive index of aerogel is also related to the weighted average of the silica and glass' dielectric constants, this means that the aerogel must contain more glass than the PCF cladding to enable TIR guidance at some wavelength.

The fibre we have chosen fits the two most important criteria for TIR guidance in an aerogel core: first, the air-filling fraction is low enough that using our normal

procedures we can make aerogel of a higher index; and second, the structures are small enough that the cladding behaves as essentially an effective medium for wavelengths longer than 1350 nm. Filling this fibre with aerogel, we hoped to see broadband guidance caused by total internal reflection in the infrared and a shifted and enlarged bandgap for some visible wavelengths.

8.2.2 Selecting an aerogel

We chose to fill our HC-PCF with aerogel that had $n_{\mathrm{agl}} = 1.045$, the index marked by the blue line in Fig. 8.2. In region A, bounded by the aerogel index and n_{fsm}, the aerogel should guide light by TIR. Within the bandgap guided region (marked B), there should be many modes because the difference between the core index and the band below it is large. Modes with high spatial frequency (lower n_{eff}) could even be confined in the very bottom tip of the bandgap at around 800 nm.

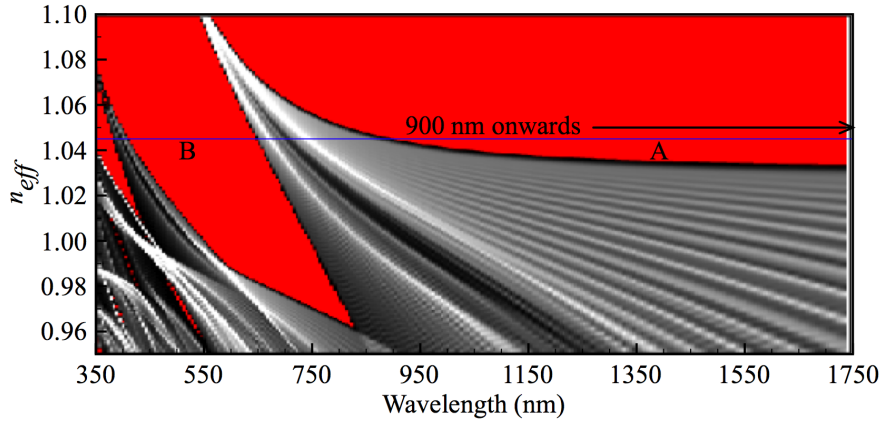

Figure 8.2: The expected regions of guidance in hollow-core PCF with an aerogel core of refractive index 1.045.

The fibre can be used as a mould to form aerogel *in situ* inside the core. The first step of filling is to suck the sol into the core hole. When the sol turns to rigid alcogel the filling process stops. The core of the fibre is very small, so filling reasonable lengths of fibre takes a long time. Making a sol with a long gel time allows longer sections of fibre to be filled with aerogel, at the expense of a slight increase in the attenuation of the aerogel.

Once the core of a HC-PCF is filled with alcogel, any solvent exchange or

removal can only occur by diffusion through the fibre ends. Since both ends are open, the diffusion length is half the fibre's actual length. This needs to be considered during solvent exchange and supercritical drying (SCD) as both processes scale badly with diffusion length. A quick calculation predicts that solvent exchange in 20 cm fibre would take around 50 days. This makes low-temperature SCD prohibitively time-consuming, especially as solvent exchange with liquid CO_2 requires temperature and pressure control. High-temperature SCD is more tolerant to residual chemicals from the initial sol, and doesn't require solvent substitution, so it is naturally more suited to these long, thin samples.

Considering all the above factors, we made sol with a molar ratio of TMOS : MTMS : methanol : water : ammonia of $1 : 0.11 : 2 : 4.5 : 3.3 \times 10^{-3}$. The MTMS co-precursor ensures the resulting aerogel is hydrophobic after high-temperature SCD. The ammonia concentration results in gelation after 40 min. With this molar ratio, the target density (in the event of no shrinkage) is 0.20 g/cm^3, which corresponds to a porosity (air fraction) of 91%.

8.2.3 Filling the fibre with sol

A schematic of the equipment used to fill fibre with sol is shown in Fig. 8.3. One end of the fibre was attached to a windowed vacuum cell, and light from a red HeNe laser was launched into the core. The other end of the fibre was dipped in a test tube containing the sol. As it was drawn into the fibre, the sol scattered the laser light in a spot that moved gradually until gelation after ~ 40 min. The scattering spot indicates the fullness of the fibre, and helps to determine when gelation has occurred.

Fixing one end of the fibre to a vacuum pump creates a driving pressure difference, which draws liquid at the other end into the fibre like sucking through a straw. The liquid fills the large holes more quickly than small ones, in proportion to the square of the radius. Since the sol becomes rigid everywhere at nearly the same time, the filling length in the large holes is longer. Given the size difference between the core and cladding holes in most HC-PCFs, this is sufficient to separate a region of ~ 30 cm where only the core is filled with alcogel.

Alternatively, to ensure that only the core was filled with sol, the ends of the

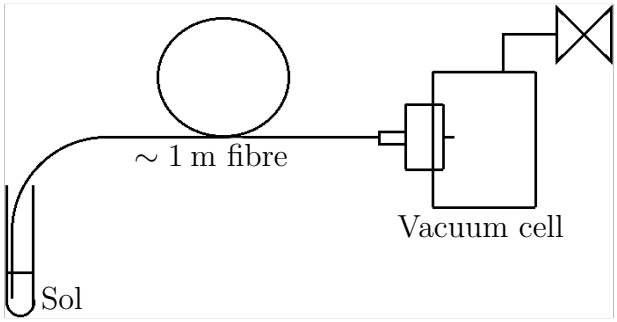

Figure 8.3: A schematic of the equipment used for filling fibre with sol. The sol becomes rigid after about 40 min, filling around 0.5 m of the fibre with alcogel.

PCF could be heated using a Vytran splicer. This collapses the cladding holes but not the core [204], isolating the sol from the vacuum pump in the cladding holes without significantly altering flow in the core. We used this method during the initial experiments but found that, for the fibre we selected, the hole-size discrimination proved enough and the cladding collapse was not required. Other more complex techniques can be employed to selectively fill different cladding holes [203, 205, 206], for example to create coupled cores or tighter light confinement.

8.2.4 SCD

The alcogel-filled fibre and a similar macroscopic alcogel in a test-tube were dried using our high-temperature SCD rig (see sec. 5.2.4). The vessel was filled with 400 ml of methanol and heated to 280 °C over 2 h, reaching a maximum pressure of 105 bar before we started to slowly vent the methanol. The pressure was evenly released over an hour, and the vessel left to cool for 4 h before removing the aerogel and the filled fibre.

8.2.5 Aerogel-filled HC-PCF

The macroscopic aerogel was used to determine the properties of the aerogel in the fibre. The refractive index was 1.045 ± 0.005, as measured using refraction from a cylinder (described on p. 113), and the density of the aerogel was $0.19\,\mathrm{g/cm^3}$. The aerogel was hydrophobic and able to support water drops on the external

surface. The linear shrinkage during supercritical drying was 5%.

The scanning electron micrographs of Fig. 8.4 show unfilled and core-filled fibres. Fig. 8.4(c) shows the aerogel slightly proud of the PCF endface. This difference in cleaving planes was typical, but the aerogel was equally often recessed by a similar amount.

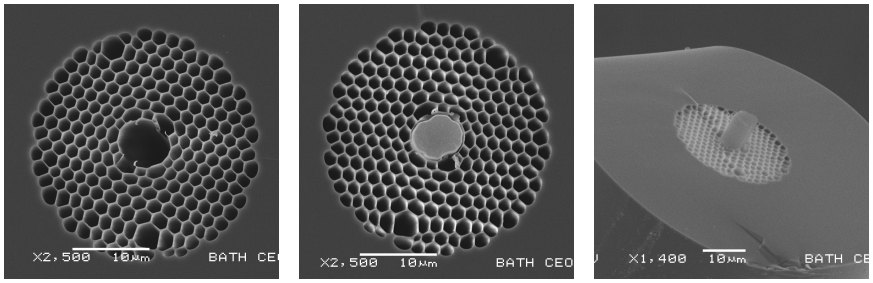

(a) **(b)** **(c)**

Figure 8.4: SEMs of a hollow-core PCF with the core (a) empty and (b) filled with aerogel. (c) Tilted image of (b), where the aerogel core sticks out from the fibre.

8.3 Optical properties

8.3.1 Attenuation

The attenuation of the aerogel-filled fibre was measured using the cutback technique. Light from a broadband LED source was coupled into ~ 20 cm of fibre using a $10\times$ microscope objective. The near-field pattern at the output was imaged on a linear infrared (InGaAs) camera through one of a succession of 10 nm bandpass filters in turn, checking that the light was in the core. The output was refocused for each wavelength, but the input stayed fixed. Then 6.5 cm of fibre was cut off without disturbing the launch optics, and a new set of output images obtained. Since the camera was linear, the image data could be used to calculate loss. The resulting spectrum is shown in Fig. 8.5(a); the minimum attenuation was 0.2 dB/cm at 1540 nm and there is an increase in loss at ~ 1400 nm corresponding to OH in the aerogel.

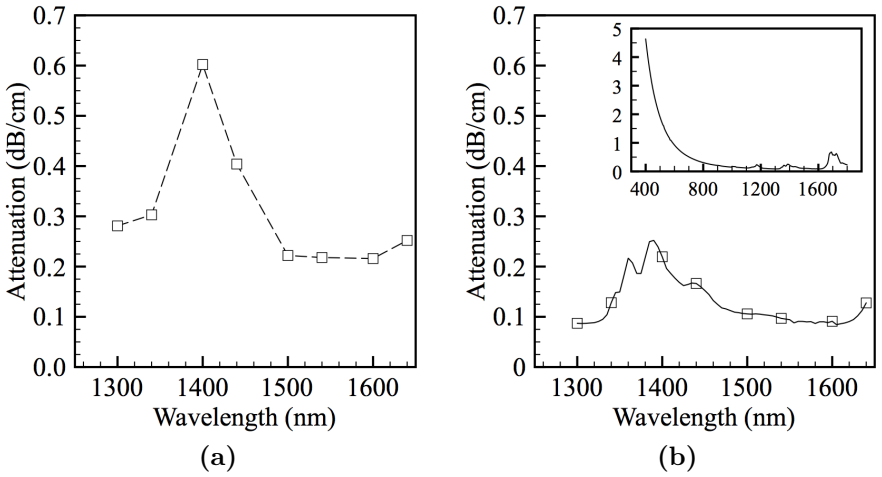

Figure 8.5: (a) Measured attenuation of the aerogel-filled fibre at 8 discrete wavelengths. (b) Measured attenuation through similar bulk aerogel with the same key wavelengths picked out. (inset) Broader attenuation spectrum of the same aerogel.

The loss of an aerogel with the same density, made by casting the sol in a glass cuvette and dried using high-temperature SCD, is presented over the same range for ease of comparison in Fig. 8.5(b). The spectra both show an absorption feature at ~ 1400 nm, albeit with less detail in the fibre where only two data-points are overlapping it. The attenuation in the aerogel-filled fibre is approximately twice the attenuation we have observed in bulk aerogel.

The difference between the measured attenuation in the waveguide and the bulk aerogel could be due to scattering caused by imperfections in the waveguide. However, it is more likely to be due to the difference in the gel times of the two aerogels; 40 min for the aerogel in the filled fibre and only 15 min for the aerogel in a cuvette used for spectral measurements. Alternatively, the difference could be because of measurement errors. Sources of measurement error include a slight disturbance in the launch optics when making the cut-back measurement on the fibre, and errors in the attenuation measurement of the bulk aerogel caused be measuring some component of diffuse transmittance.

We measured the transmission spectrum of 20 cm unfilled and aerogel-filled fibre from 350–1750 nm using a supercontinuum light source and an optical spectrum analyser (OSA), Fig. 8.6(upper). (The lower part of the figure is the same

DOS plot as before, to aid comparison.) The transmission spectrum measured by the OSA is good for examining broad spectral features, as the OSA has a large dynamic range and can quickly scan a broad wavelength range. However, it is unsuitable for measuring loss, because the uncertainties in coupling can dominate over the attenuation in the small lengths of fibre we are using.

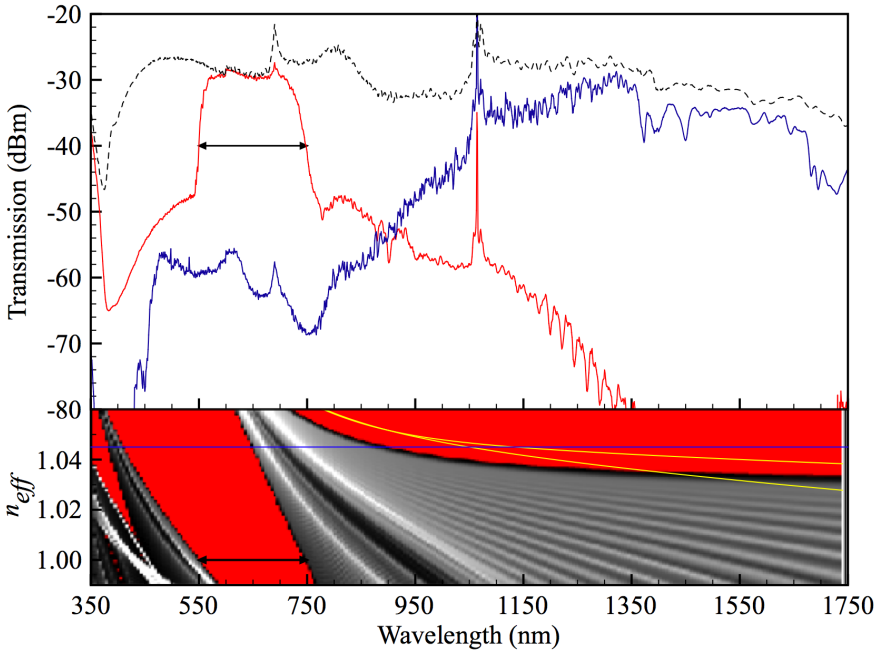

Figure 8.6: The transmission spectra for the supercontinuum source (black dashed curve), the unfilled fibre (red curve) and the aerogel-filled fibre (blue curve). The supercontinuum source shows sharp spectral features at 1064 nm and 690 nm, which are repeated in the other spectra. For ease of comparison, the DOS and simulated n_{eff} for the modes of the waveguide are plotted in the same figure (yellow lines).

The arrows from 550–750 nm mark the wavelength range where bandgap-guided modes can have an effective index $n_{\text{eff}} \approx 1$. In the unfilled fibre, this wavelength range corresponds to a region of low loss. However, higher-order bandgap modes with lower n_{eff} can be guided outside of this range in the 'pit' of the bandgap. In the air filled fibre, the effect of the extended bandgap guidance in higher order modes is not really visible in the transmission spectrum, probably because they are hard to excite.

The aerogel-filled fibre has high transmission at IR wavelengths longer than

1200 nm, consistent with guiding light by TIR. The short-wavelength part of the filled fibre's transmission spectrum can be explained by considering the loss caused by the aerogel and the DOS of the fibre. Starting at short wavelengths, the sharp shoulder of the transmission is probably due to Rayleigh scattering in the aerogel. The spectrum is relatively flat until the transmission starts to dip at 620 nm, coincident with the long-wavelength edge of the shifted bandgap. At this wavelength, there are no longer bandgap-guided modes with an effective index close to the refractive index of aerogel, however, the bandgap pit is much deeper and there are higher-order modes that can be excited (albeit with higher loss). The transmission continues to decrease until 750 nm, as more of the higher-order bandgap modes become similarly cut off.

The transition region between bandgap and index guiding rises almost linearly, and can not be explained using our simple picture. For a more complete understanding, we need to examine the modes of the fibre more carefully.

8.3.2 TIR modes

Light from the supercontinuum source was butt-coupled into the filled fibre and the output was imaged on a linear infrared (InGaAs) camera. The wavelengths of interest were selected using 10 nm bandpass filters. The output near-field pattern at 1540 nm measured by the InGaAs camera shows a Gaussian-like fundamental mode in the core, which we call the 'aerogel mode', Fig. 8.7(a). Imaging the output field at progressively shorter wavelengths shows that the intensity distribution significantly changes as light becomes more confined in the core surround.

The same simulation tool we used to calculate the DOS can be used to find the modes of an idealised version of the full structure. The aerogel core defect is included in the simulation by cutting out the seven central cladding cells and replacing them with a region of refractive index $n_{\mathrm{agl}} = 1.045$. The simulated core boundary was modified so that every other strut was twice as thick as a normal cladding strut, matching the properties of the core-wall observed in SEM images. The modelled output field distribution of the highest effective index mode at the specified wavelengths is shown in Fig. 8.7(b). The simulated and observed light patterns evolve in a similar way, becoming more confined in the core-surround as

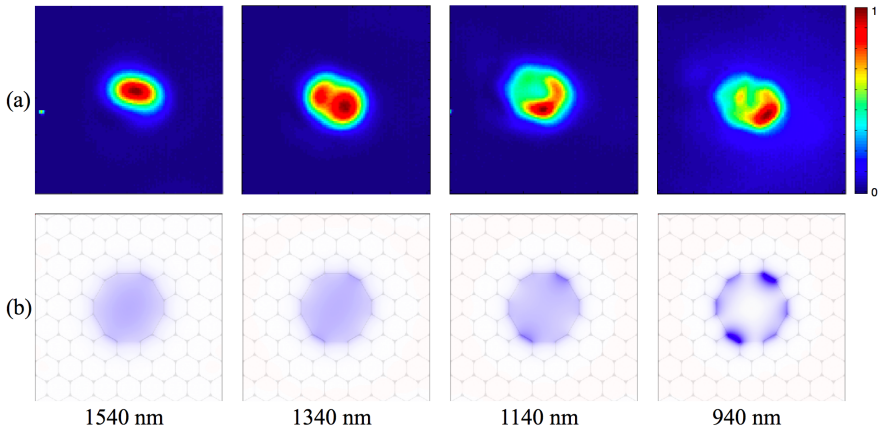

Figure 8.7: (a) Measured near-field images of the fibre at four wavelengths. (b) Simulated mode patterns at the same wavelengths (within 10 nm) superimposed on the simulated structure.

the wavelength decreases.

Using mode simulations for wavelengths from 750–1750 nm, we have calculated the dispersion for the first two modes of the waveguide and plotted them on the DOS of Fig. 8.6 (yellow lines). The aerogel core operates in a single mode (bar polarisation degeneracy) for wavelengths longer than 1450 nm. At wavelengths shorter that this, the waveguide supports higher order modes. The short, sharp peaks in the measured transmission spectrum are characteristic of mode-beating and they only appear at wavelengths that our simulation predicts the fibre will support multiple modes. This is evidence of higher order modes in the transmission spectrum of the filled fibre.

The light pattern of the first higher order mode is peaked in the core-surround at all wavelengths, hence we call it the 'core-surround mode'. The calculated intensity pattern of this mode is plotted in Fig. 8.8(a). The similarity of between this light pattern and that observed in the aerogel-mode at short wavelengths (Fig. 8.8(b) and the orthogonal degenerate mode) implies that both the aerogel and core-surround modes have similar n_{eff}. Studying the mode dispersion very carefully reveals a mode crossing at 950 nm. At this point, the core-surround mode becomes the fundamental mode of the waveguide and the aerogel-mode is now the first higher order mode! Plotting the vector fields, Fig. 8.8, shows the mode-crossing is permitted as the modes have very different symmetries. The

aerogel-mode has an HE_{11}-like vector direction, whereas the core-surround mode is more like a TE_{01} mode.

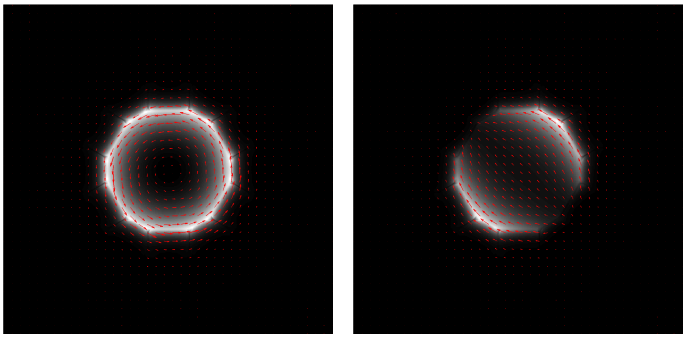

(a) **(b)**

Figure 8.8: The intensity profile and electric field vector direction of the (a) core-surround and (b) aerogel modes in the simulated waveguide at 1000 nm. The aerogel mode is one of a degenerate pair of modes with orthogonal polarisations.

The light patterns of the higher order modes show how the filled fibre can guide light even when n_{fsm} rises above the aerogel refractive index. However, for wavelengths shorter than 1150 nm, the mode index exceeds the aerogel index and the field becomes evanescent in the aerogel. This wavelength roughly coincides with the continual decrease in transmission in Fig. 8.6, from 1150–750 nm.

8.3.3 Bandgap modes

Within the wavelength range of the bandgap, imaging the near-field at 550 nm (using a Si CCD camera) produces a complex pattern that is very sensitive to small changes in the launch optics. Snapshots for three different excitations show different amounts of many complex modes being excited, Fig. 8.9 (a–c). This is typical of a multimode waveguide, and not surprising given that the bandgap pit is deep enough (1.045–1.00) to support many modes. The fibre's DOS plot, reproduced in Fig. 8.9(d), is marked with white boxes indicating the effective indices of some of the bandgap modes at 550 nm. The simulation in accurate enough to predict modes with a similar intensity distribution to those observed, one of which is plotted in Fig. 8.9(e).

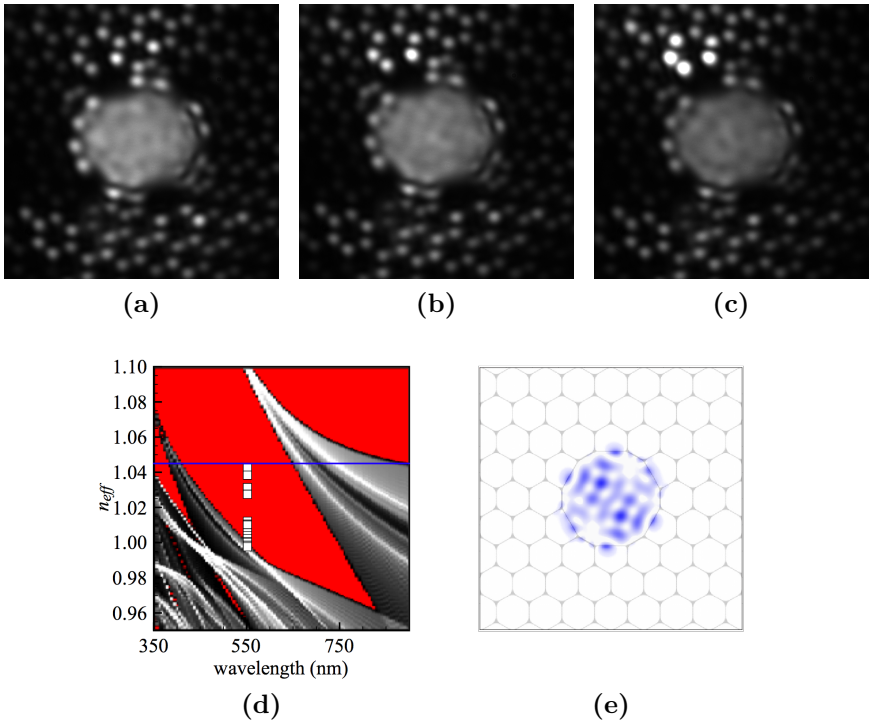

Figure 8.9: (a–c) Bandgap modes of the filled fibre at 550 nm, where slightly different excitation has been achieved by small changes in the launch optics. (d) The bandgap region of the DOS plot of the fibre where each white box marks a mode effective index from simulation at 550 nm. (e) An example of one of the calculated modes with the lowest effective index.

8.3.4 Mode coexistance

As modes become localised in the glass core-surround, their effective indices rise above the refractive index of the aerogel. This extends the regime of index guidance, albeit with higher loss, to shorter wavelengths that overlaps with the long-wavelength edge of the bandgap pit. In fact at 750 nm we observed two distinct guided modes, Fig. 8.10. The first was localised in the core-surround with a low spatial frequency in the aerogel, presumably guided by total internal reflection. The second was concentrated in the aerogel with a high spatial frequency and hence a low effective index, presumably guided by the bandgap.

Coexisting guidance mechanisms in solid-core PCFs have been predicted computationally by Yan and Shum [207] and Perrin *et al.* [208]. Solid-core PCFs

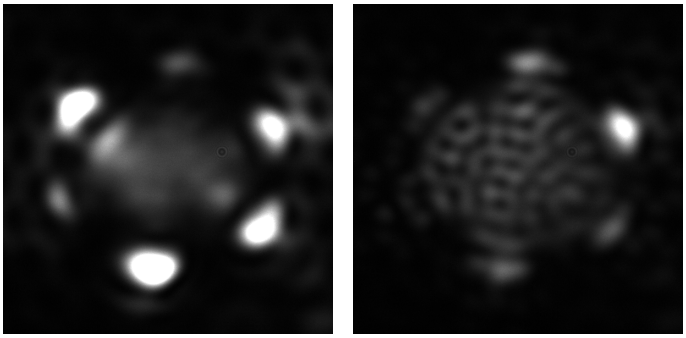

(a) **(b)**

Figure 8.10: Images of an index-guided mode (a) and a bandgap mode (b) excited by altering the light coupled into the filled fibre. Both of these modes were observed at 750 nm.

naturally guide because of the index step, but can also have high-order modes confined in the cladding bandgaps. The simulations in these papers show the modes are realistically hard to excite and have much greater loss than the ones guided by TIR. Similar reasoning holds for hollow-core fibres filled with liquid: bandgap modes which may be 'valid' are in actuality almost impossible to excite because they have exceedingly high spatial frequencies.

Yan and Shum [207] extend the work to lower-index cores by replacing the solid core with a second photonic crystal structure. This microstructured core significantly reduces the number of index guided modes so that (apart from degeneracy) the second waveguide mode is confined by bandgap effects from the outer cladding. This is similar to our filled fibre, where the refractive index of the core is provided by using aerogel instead of a microstructure.

However, these reports are all only theoretical predictions. If our interpretation is correct, then we believe our results to be the first observation of coexisting index- and bandgap-guided modes.

8.3.5 Nonlinear properties

We recall from sec. 2.4.4 that the refractive index of a material that exhibits Kerr nonlinearity depends on the intensity of the incident light [85] such that $n = n_0 + n_2 I$ where n_0 and n_2 are the linear and nonlinear refractive index, and I

is the intensity. As we have previously discussed, Seo *et al.* [18] measured the n_2 of aerogel to be $\sim -1.5 \times 10^{-15}\,\mathrm{m^2/W}$. This value is approximately five orders of magnitude larger than the n_2 of bulk silica and has the opposite sign, causing the refractive index to depress at high intensities rather than increase. Given that the refractive index of aerogel is already small, the reported nonlinear index is large enough to cause a significant perturbation. In the aerogel waveguide, the nonlinear perturbation would cause the refractive index to depress below the effective index of the cladding for intensities above $10^{13}\,\mathrm{W/m^2}$, equivalent to peak powers of $\sim 100\,\mathrm{kW}$ when focused into the small aerogel core.

We investigated the nonlinear properties of the aerogel-filled fibre using the output of an optical parametric amplifier (OPA) tuned to 1550 nm and pumped using a pulsed Ti:Sapphire laser source. The pulse duration was 120 fs, the repetition rate was 250 kHz, and the average power was 50 mW (this equates to a peak power of 1.6 MW). The output of the OPA passed through some polarisation optics to allow power control, and then was coupled into the aerogel-filled fibre using a 10× microscope objective. The output of the fibre was first imaged on an InGaAs camera to confirm that the light was in the core, and then coupled into the OSA using a butt-coupled multimode fibre.

If the Kerr nonlinearity of the aerogel is $\mathcal{O}(10^{-15})\,\mathrm{m^2/W}$ then, for realistic powers, we would expect to see the aerogel mode migrating into the core-surround as the power is increased. We imaged the near-field output of the fibre through a 1550 nm bandpass filter to ensure that light was coupling into the core at low power. We increased the power up to the maximum available in the laser, but the measured near-field output mode at that wavelength did not significantly change shape. Therefore, we conclude that the nonlinear refractive index does not significantly depress the refractive index of the aerogel and "switch off" the waveguide. Although this does not completely rule out a large nonlinear refractive index (it just means that n_2 is not large *and* negative), it does cast doubt over the reported value for n_2.

However, with high input powers we saw new wavelength generation in the fibre, which glowed a blue-green colour as shown in Fig. 8.11(a). Imaging the visible light through a 500 nm bandpass filter onto a silicon CCD camera (Fig. 8.11(b)) showed a near-field pattern similar to the bandgap guided modes discussed in

sec. 8.3.3. The output spectrum of the filled fibre at high power is plotted as the red line in Fig. 8.11(c). It shows that the peak wavelength of the blue light is 513 nm. For comparison, we measured the transmission spectrum of the fibre using a low input power. This is plotted as the black line in the same subfigure. The central wavelength of the spectrum is at 1543 nm, and no wavelengths below 1400 nm or above 1650 nm are transmitted at this power.

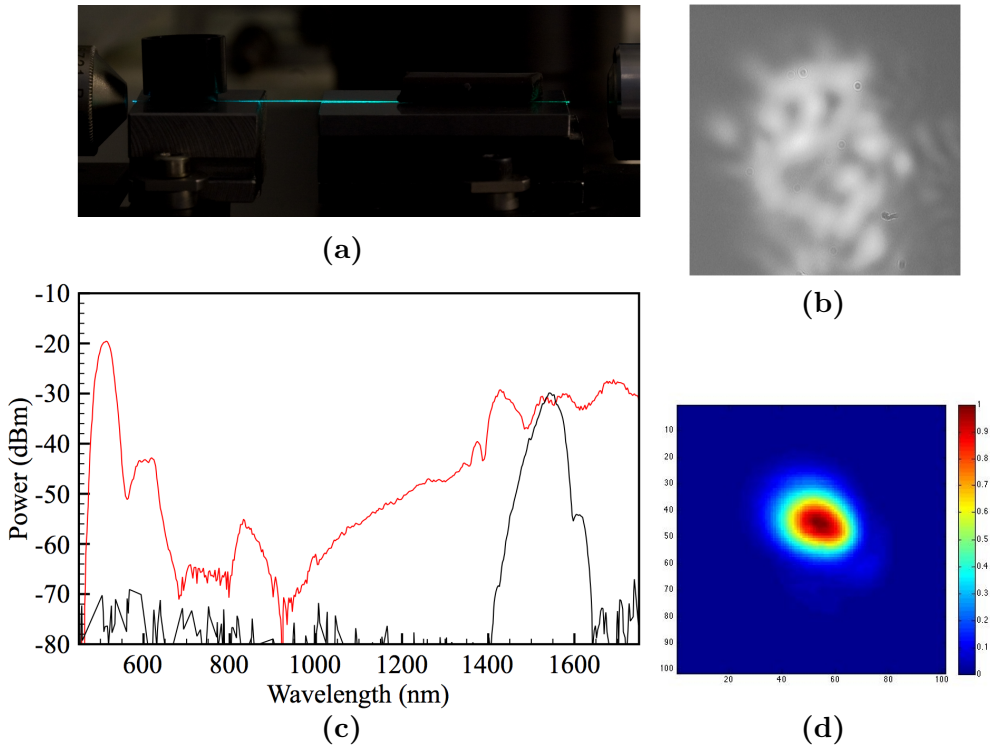

Figure 8.11: (a) The aerogel-filled fibre glows blue when illuminated (from the right) with light from the OPA at 1550 nm. (b) The near-field output of the fibre, imaged through a 10 nm bandpass filter with a central wavelength of 500 nm. (c) The output spectra of the aerogel-filled fibre at low (black line) and high (red line) powers. (d) The near-field output of the fibre imaged at 1650 nm.

The wavelength of the blue-green light generated in the waveguide suggests some kind of third harmonic generation process. The generation of new wavelengths is consistent with an electronic contribution to nonlinearity. From our linear investigation of the waveguide, we know that there is a small component of the electromagnetic field that propagates in the glass. However, near-field mode

images of the wavelengths generated by nonlinear processes, like those plotted in Fig. 8.11(b & d), have light patterns that suggest the light may be generated in the aerogel core.

8.4 Bandgap shifting

The blue-shift of the bandgap for the fibre discussed in the previous sections is complicated by high attenuation in the aerogel at visible wavelengths. A second fibre with an infrared bandgap shows the shift much more clearly, although the index-guided modes in this fibre are only core-surround type modes.

A fibre with an infrared bandgap from 950–1175 nm was filled with an aerogel that had a refractive index $n_{\mathrm{agl}} \approx 1.04$. SEMs of this fibre show that it has an almost identical air-filling fraction to the fibre discussed previously, but the pitch is $\Lambda = 2.9\ \mu\mathrm{m}$. The simulated DOS for this fibre is presented in Fig. 8.12(a). The vertical purple line marks the pump wavelength of the supercontinuum source used in measuring the real fibre and the horizontal blue lines mark the refractive index of air and aerogel.

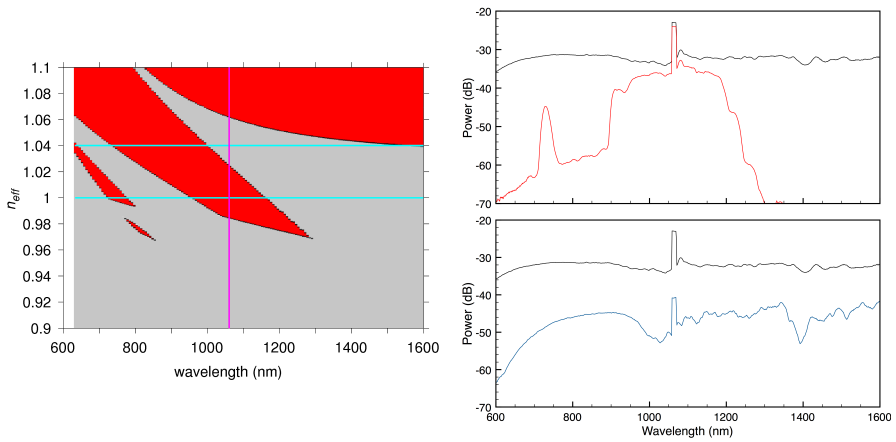

(a) **(b)**

Figure 8.12: (a) DOS simulation for a second fibre filled with aerogel. (b) Measured transmission in the (upper) unfilled and (lower) filled fibre clearly shows a shift in the bandgap to shorter wavelengths. The black line on each is the spectrum of the supercontinuum source used in the measurement.

The DOS matches the transmission spectrum of the unfilled fibre well, including a small secondary bandgap at 700 nm that is observed because the fibre is quite short. Looking at the DOS plot for the filled fibre (upper blue line) suggests that there is no index-guided mode in the aerogel over the wavelength range we can observe; however, the modes in the core surround are still permitted. The index-guided mode clearly has a component of mode-field in the aerogel, as there is strong evidence of the OH absorption in the transmission spectrum.

The simulation predicts that in the aerogel-filled fibre the bandgap will shift to 700–1000 nm. The transmission spectrum of the filled fibre shows a blue-shift of the bandgap in reasonable agreement with these wavelengths. Observations of the bandgap modes (both measured and simulated) have some mode-field components in the core-surround. We believe this is because the core-surround is thicker than in the fibre we discussed previously.

8.5 Conclusion

We have demonstrated a waveguide with an aerogel core, using a photonic crystal fibre to provide a cladding with an effective index low enough to confine light by total internal reflection. The waveguide offers unparallelled ability to probe the properties of aerogel with tightly confined light over long interaction lengths. This is particularly important in the field of nonlinear optics, as demonstrated by our measurements of new wavelength generation in the waveguide.

There are many possibilities for further study of aerogel-filled waveguides, using different aerogel or different fibres. Filling the waveguide with other types of aerogel, for example doped aerogels (discussed in chapter 6) or alumina aerogels will add different optical functionality to the waveguide. Plasmonic aerogel could be used in creating a new class of plasmonic sensors, aided by the long interaction lengths and benefits of easy integration with fibre networks. It could also enhance the nonlinear optical properties of the waveguide. Making aerogel in different host fibres will alter the optical properties of the waveguide. Kagomé-lattice fibres have broadband guidance and no surface modes, and could presumably confine light in an aerogel core in the same way. Fibres made so that the whole structure

was ‘cladding’ could have multiple aerogel-filled holes to investigate linear and nonlinear coupling properties. Cobweb fibre, with a large core hole suspended from the jacket by narrow webs, could be efficient at confining light by TIR over a much wider wavelength range.

Chapter 9

Conclusion

This thesis presents the integration of aerogel with two fibre optic technologies. The aerogel acts as an optical component of the waveguide in both cases; either as a cladding or waveguiding core.

Aerogel clad tapered fibres are an exciting new class of devices, where the aerogel protects the fragile fibre but itself causes only a small perturbation to the light in the fibre. We have developed the methods for encapsulating tapered fibres in aerogel with low loss, 0.3 dB/mm at 1310 nm for a 750 nm diameter taper. The low refractive index of aerogel means the waveguide modes are relatively unchanged in their dispersion. This is confirmed by generating a supercontinuum spectrum in an encapsulated 800 nm taper using a 530 nm pump laser. We have also embedded fused couplers, and observed a $< 1\%$ change in the splitting ratio after the encapsulation process. We have shown how the open network of the aerogel can be exploited to enable tapered fibres to function as evanescent gas sensors.

Aerogel core waveguides can transmit light through unprecedented lengths of aerogel in a single mode. We formed an aerogel waveguide inside a selectively-filled hollow-core photonic crystal fibre, which protects the aerogel and provides a low-index cladding that causes light guidance by total internal reflection over a range of infrared wavelengths. The filled fibre can also guide light over a different wavelength range by photonic bandgaps, and at the point of overlap between the two guidance regimes we have observed coexisting bandgap and index-guided

modes.

To make these composite materials we had to develop methods for producing transparent aerogel with high optical quality in a way that was compatible with the fibre. This involved making a sol, casting the sol to incorporate the fibres, waiting for gelation, and extracting the solvent under supercritical conditions.

Starting from fabrication procedures found in the literature, we developed methods for making aerogel with high optical quality. We built two rigs for supercritical drying. One is suitable for making encapsulated tapers without damaging the coated fibre, the other is suitable for drying aerogels with long diffusion lengths, such as those cast in the core of a fibre. Either rig can be used for making bulk aerogels without fibres. The type of sol we used depended on the supercritical drying conditions. By studying the literature, we implemented and developed several recipes for each drying procedure that could be used to produce hydrophobic aerogel with control over gel time and density. The optical properties of these aerogels are comparable to the best reported in the literature.

We investigated several different types of mould into which we could cast our sol. For producing pieces of aerogel without fibres, we discovered that PMMA cuvettes held their shape during casting but softened to the point where the alcogel could be removed after approximately 2 days in a wash solution of pure methanol. Removing the alcogel from the cuvettes allowed us to speed up the supercritical drying cycle without having to compromise on the dimensions or surface quality of the final aerogel. The shape and surface quality of aerogel cast in cuvettes is ideal for measuring optical properties such as transmission or refractive index. Alternative moulds for the sol included glass cuvettes, petri dishes and test tubes. The core of a hollow-core PCF, and custom-designed aluminium and stainless steel holders were used to make the aerogel-fibre composites.

Aerogel made in PMMA cuvettes has some natural birefringence caused by the exposed surface of the sol during gelation. The birefringence varies spatially throughout the sample, so quarter and half wave retardation can be measured for different wavelengths simply by moving the aerogel. Thus, we propose the aerogel can be used similarly to a Babinet compensator, but with minimised Fresnel back reflections because of the low refractive index.

We modified the optical properties of aerogel by including two different dopants.

The first dopant we used was gold nanoparticles, which have a broad spectral feature centred at ~ 530 nm caused by a surface plasmon resonance. The exact surface plasmon wavelength depends on the size and shape of the nanoparticles and their local environment. We developed a method for incorporating the gold nanoparticles so that they were well dispersed in the aerogel. The surface plasmon wavelength was shifted to shorter wavelengths, but this shift could not be explained using effective medium approximations for the aerogel. We modelled the doped aerogel as gold nanoparticles coated in a 5 nm layer of silica in air 'pores', and got an excellent fit for the surface plasmon wavelength. The same model worked for alcogel and toluene-filled wet gel when we changed the index of the pore fluid to match methanol or toluene. Thus, we concluded that the structure of the doped aerogel is as if the gold nanoparticles are coated in a thin layer of silica.

The other dopant we used was ytterbium, which has a narrow resonance centred at 975 nm. We developed a method to dope alcogel by diffusing ytterbium acetate into the pores. The ytterbium ions stayed in the alcogel after several solvent exchanges, and their effects could be measured in the aerogel after supercritical drying. The attenuation due to absorption by the ytterbium could be varied up to ~ 12 dB/cm simply by diffusing different amounts of ytterbium acetate into the aerogel.

9.1 Future work

We hope the work presented in this thesis, and the equipment and methods we have developed, enables further study of integrated aerogel-fibre devices. Here, we propose some experiments that build directly on this work, and identify a few areas of study that could increase the usefulness of our techniques.

Perhaps the most obvious future experiments involve combining doped aerogel with our techniques for making fibre-based waveguides. The simplest way of doing this is to encapsulate a sub-micron tapered fibre in aerogel doped with gold nanoparticles. This should not be technologically challenging, as the methods and

equipment for doing this experiment are fully developed. Studying the optical effects of a plasmonic aerogel cladding on the evanescent field around a thin taper would help probe the effects of the electric-field enhancement at the surface of the nanoparticles. This would help prove the modelling of plasmonic aerogel, and could also be used for sensing experiments as the light is easy to collect and measure because it is guided by the fibre.

Alternatively, GNP-doped aerogel could be added to an aerogel-core waveguide. The tight light confinement and long interaction lengths could significantly aid our understanding of nonlinearity in plasmonic materials. This would then enable measurements of some of our proposed applications, such as gas sensing or SERS.

It would be premature at the moment to add lanthanide-doped aerogel to the fibre waveguides we have developed, as there is still much to learn about these during their formation and as aerogels. The continuation of this work should focus on understanding the mechanism by which the lanthanide is taken up by the gel, the importance of the anion in the process, and the local environment of the lanthanide ion. Once we have a better understanding of this, then we can try to observe optical gain in the doped aerogel. Only then would we be ready to investigate this type of aerogel as the core of a waveguide, possibly with the view of making a fibre-laser with an aerogel core.

Concurrently, optical investigations of co-doping gold nanoparticles with erbium are of interest because of an overlap in the erbium absorption spectrum and the field enhancement of the surface plasmon resonance around the nanoparticles. This could lead to enhancements in the erbium absorption, and make more efficient lasing materials. It could also lead to an efficient method for making co-doped glasses by consolidating the aerogel or alcogel. This is an interesting fabrication approach for trying to observe plasmonic enhanced gain or lasing.

Of course, doped aerogel is not limited to the two dopants we have already chosen to investigate. Other dopants of interest include quantum dots, laser and fluorescent dyes, molecules with non-linear optical properties, and molecules sensitive to particular elements such as oxygen. The last class of dopants are particularly useful for extending the range and sensitivity of the evanescent field gas sensor encapsulated in aerogel.

We believe that the optical properties of aerogel can be further optimised for light transmission, particularly in the infrared telecom band. Currently, loss at visible wavelengths is caused by Rayleigh scattering, and loss at IR wavelengths is dominated by absorption due to molecules in the aerogel. Different methods of making alcogel such as surfactant templating, which has better control over the pore size, could lead to some reduction in the Rayleigh scattering properties of the aerogel. The reduction in scattering loss at visible wavelengths could be a significant benefit to aerogels doped with gold nanoparticles. At IR wavelengths, most of the loss comes from light absorption by OH on the surface. Reducing the water content, for example by making aerogel from heavy water (D_2O), could shift the resonant absorption away from the key telecom band and correspondingly reduce the attenuation. This would be particularly interesting for applications of the filled fibre, where propagation over significant distances is predominantly limited by the loss in the aerogel.

The reported optical nonlinearity of aerogel is significant because it is unexpectedly large, and has the opposite sign to fully dense silica glass. It is therefore of interest to verify whether this measurement is correct, using either z-scan measurements or a different method for measuring nonlinearity. If the reported value is confirmed (particularly the sign of the nonlinearity) then interesting waveguide structures could be designed that can exploit this property.

Extending the tapered fibre coating to thin films between a few hundred nanometres and a few hundred microns could help extend their usefulness both in the plasmonic community and for medical gas sensing. Thin films comparable to the scale of the fibre could be used to prevent the tapers from touching plasmonic structures, while allowing coupling via the evanescent field. Alternatively, thicker films of a few hundred microns would greatly reduce the response time of gas sensors, whilst still preventing bulk scattering elements like dust from causing loss. Rapid response times are vital in many gas-sensing applications.

Finally, we propose an experiment based on the work presented in Appendix A on hollow-core fibre used for making gas cells. Current interactions between gas and laser light cause a resonant absorption spectrum, the lineshape of which depends only on the pressure of the gas. However, there is some evidence that interactions between laser light and gas confined in aerogel causes a change in the

lineshape resulting in a narrower spectral feature. This means that aerogel-filled fibre could have applications in frequency metrology and quantum optics.

Appendix A

Coupling to hollow-core PCF using tapers

This appendix describes a significant body of work by the author and colleagues that is not related to the rest of this thesis. It describes different taper transitions that can be used for coupling light between solid and hollow-core fibres of different dimensions. We have investigated several types of taper transitions to create a better match between the fibres. The motivation for this work was the observation of quantum-optic phenomena in gas-laser interactions, enhanced by hollow core fibres of unconventionally large dimensions. Therefore, the dual purpose of using taper transitions to splice these hollow fibres with solid fibre is to improve the optical coupling and to provide a hermetic seal for the gas. The same techniques could be useful for coupling to aerogel-filled fibres, and there is some evidence to suggest that aerogel-gas-laser interactions could be of interest in similar experiments.

A.1 Motivation

Hollow-core photonic crystal fibre (HC-PCF) has enabled the longstanding wish of transporting tightly focused laser beams in a gas without the constraints of diffraction, making it an excellent host for interactions between gas and laser light [92]. In particular, it makes the observation of quantum-optics effects such as electromagnetically induced transparency (EIT) [209] and saturable absorption (SA) [210] possible at low powers [198–200, 211]. A further useful feature of a fibre-based host is the ability to integrate them in an all-fibre system by the development of a photonic microcell (PMC) [92, 200, 212]. The PMC provides a robust, compact, portable and low-loss waveguiding platform for quantum optics and frequency stabilization, with applications in metrology [200] and gas-laser systems [197–199, 213].

In most previous studies, PMCs have been made using bandgap-guiding PCF (sec. 3.3.2). The comparable core diameters of this HC-PCF and SMF enabled splice losses of < 1 dB [212]. However, this fibre has three drawbacks. Firstly, it only guides light within the relatively narrow wavelength range of the bandgap. This means that specialised fibre is needed for each gas, and any nonlinear effects are limited. Secondly, the diameter of the core d_c is limited by the light guidance mechanism ($d_c \approx 10$ μm for 7-cell HC-PCF designed to guide at 1550 nm). The collision rate between gas molecules and the core wall (which at low pressure scales approximately as d_c^{-1} [214]) dominates dephasing effects so the small size limits the minimum achievable linewidth of a spectral feature. For acetylene-filled fibre with a 10 μm core this limit is ~ 26 MHz [214]. Finally, residual structural asymmetries and strong coupling to surface modes lift the degeneracy between the polarizations of the guided mode. The resulting modal beating causes asymmetric and irregular absorption profiles, degrading the visibility of a spectral feature [215].

Kagomé-lattice PCF (sec. 3.3.3) solves these problems by confining light in the hollow core by a different mechanism. The kagomé lattice cladding traps light in the core because the transverse fields of the core mode and cladding modes are mismatched [92, 114]. Typical kagomé fibres can guide over a wide range of wavelengths in cores with diameters up to 80 μm [105], which can reduce

the linewidth due to gas-wall collisions by $\approx 8\times$ compared to a 10 µm core. Knabe *et al.* [211] recently used acetylene-filled kagomé fibre to create a saturable absorption feature with a FWHM of 8 MHz and measure the absolute frequency of the P(13) $\nu_1 + \nu_3$ transition with an accuracy better than 10 kHz. The strong inhibited coupling between core and cladding modes in kagomé fibres [114] leads to an extremely flat transmission spectrum, free from mode beating effects.

However, the large size of kagomé fibre (the outer diameter is 315 µm for a 19-cell defect core) complicates integration into all-fibre systems. The diameter of the fibre's microstructured region exceeds the 125 µm diameter of SMF-28, so direct splices between them would be weak and not provide a hermetic seal. Also, the difference in core sizes leads to butt-coupling losses of > 3.5 dB due to mode field mismatch. Finally, the larger core speeds diffusion of contaminants into the fibre, inhibiting fabrication of low-pressure PMCs.

There are several ways to improve the mode-field overlap at the boundary of SMF and PCF, thus reducing the coupling loss. The use of a bridge-fibre, with a mode-field in between that of the two fibres to be spliced, can reduce the overall loss despite introducing an extra splice junction [216]. Dopant diffusion in solid fibres can alter the mode-field diameter in such a way that coupling is improved, especially for splices between SMF and multimode fibres [216]. Xiao *et al.* [217] developed a splicing technique that caused an expansion in the mode-field of a PCF with a small solid core, and the subsequent splice loss dropped from 3 dB to 0.9 dB. Alternatively, tapering the fibres can result in low-loss splices [216, section 8.2.6].

We have investigated two techniques for improved coupling and hermetic sealing between the large kagomé fibres and SMF-28. Firstly (sec. A.2.1), we tapered the kagomé fibre so that it matched the outer dimensions of the SMF. This created a hermetic seal on splicing (the SMF completely covers the microstructure) and improved the mode-field overlap. Secondly (sec. A.2.2), we tapered SMF and inserted it into the core of the kagomé fibre. The mode-field of the tapered SMF had a better overlap with the mode-field of the kagomé fibre, and the reflections from the end-face could be used to observe multiple pass interference effects.

A.2 Tapers, micromirrors, and PMCs

We used three designs of kagomé fibre for the work described in this section. The first fibre had a 315 μm outer diameter (OD) and a 70 μm core diameter, made by excluding the 19 central holes when stacking the fibre (19-cell). The second fibre had a 200 μm OD and a 40 μm core, made by inflating the central hole (1-cell). These two fibres are pictured in Fig. A.1(b, 1 & 2); they were both tapered and used for making PMCs as described in sec. A.2.1. The third fibre had a 136 μm OD and a 23 μm core, again made from an inflated central hole. This fibre is pictured in Fig. A.5(b); it was used as the PCF host for micromirrors, forming a cavity or a multi-pass PMC as described in sec. A.2.2.

A.2.1 Tapered kagomé fibres

In this section we describe how we tapered kagomé fibres for use in PMCs. The kagomé fibres are tapered so that the outer and core diameters are a better match to SMF-28. The tapered kagomé fibre is cleaved in the waist region, then spliced onto SMF-28.

The procedure for fibre tapering is discussed in sec. 3.2. Tapering the kagomé fibre quickly in a relatively 'cold' flame should reduce the amount of deformation to the fibres' microstructures. However, the fibres have such large ODs that the normal holding mechanism (with blu-tack or clamps) does not provide sufficient force to prevent them from slipping rather than tapering. This makes the tapers slightly sausage-shaped, and causes excess loss. Adding an elastic band over the fibre clamps increases the gripping force, and the sausage-shape is eliminated in most of the tapers.

A labelled schematic of the tapers is shown in Fig. A.1(a). We made tapers with $d_w = 125$ μm from both the 19-cell and 1-cell kagomé fibres. The tapers were lossy, but still allowed some transmission because of their broadband guidance property. Some of the tapers were cleaved close to the narrow end of the transition region, in preparation for splicing. Scanning electron micrographs (SEMs) of the cleaved tapers, Fig. A.1(b), indicate the amount of deformation introduced during the tapering process. The core of the 19-cell fibre has altered into a more

rounded and relatively larger defect. The microstructure of the 1-cell fibre is almost unchanged by the tapering process.

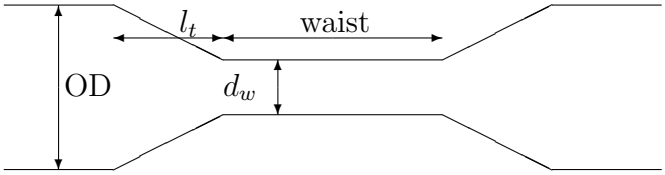

(a)

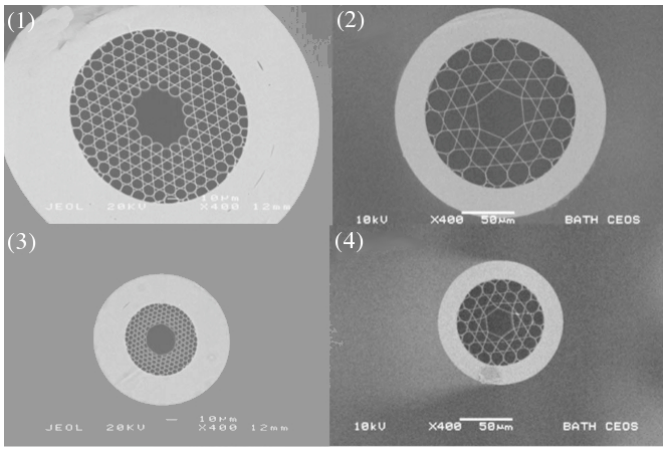

(b)

Figure A.1: (a) A schematic of the shape of tapered fibre. (b) SEMs of (1) the 19-cell and (2) the 1-cell kagomé fibres. (3) and (4) SEMs of the same fibres, tapered and cleaved in the waist. All the SEMs were taken at the same magnification.

Changing the length of the transition region alters the amount of coupling loss. When making SMF tapers, long transition regions help ensure the fundamental mode of the fibre evolves smoothly into the fundamental mode of the taper waist (adiabatic tapers). The coupling loss from SMF-28 to kagomé fibre through different length taper transitions is plotted in Fig. A.2(a). Long transitions have the same loss as butt-coupling to the untapered fibre, despite the smaller core increasing the mode-field overlap. *Shorter* transitions reduced the butt-coupling loss by a factor of three.

This result appears surprising when compared to the SMF case. However, it is worth remembering that the core-guided mode in HC-PCF is not the fundamental mode of the waveguide (there are cladding modes with greater β), so arguments about adiabaticity are misleading. In fact, the mode order of the core-guided

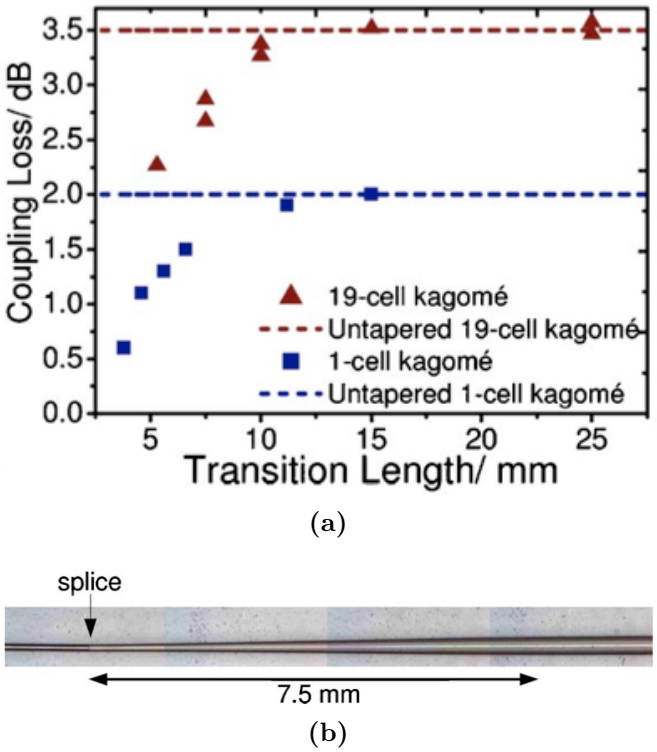

Figure A.2: (a) The loss of butt-coupling SMF to tapered kagomé fibre with different transition lengths. (b) Micrograph of a 19-cell fibre (right) tapered from OD 315 µm to d_w 125 µm over a 7.5 mm transition length and spliced to SMF (left).

mode will change along the transition. When the fibre gets smaller, the number of modes with higher β decreases; hence, strictly speaking, for light to stay in the core the transition must not be adiabatic. Shorter transitions also reduce the propagation distance through regions of higher loss caused by deformations during the tapering process and the shifting band-structure of the kagomé fibre.

The shortest transitions we could make were 4 mm; trying to make transitions shorter than this resulted in the sausage-shape reappearing. As the transition length approaches zero, the loss should rise to the untapered value, so we could be at the optimum length in any case.

The additional loss of the fibre coupling due to deformations during the splicing process is typically 0.2 dB. Fig. A.2(b) is a composite image of the SMF, splice, and transition to the full-size 19-cell kagomé fibre. We achieved total splice losses from the SMF as low as 0.6 dB to the 1-cell fibre (l_t = 3.8 mm) and

2 dB to the 19-cell fibre ($l_t = 6$ mm). These compare to the lowest-reported loss of 0.9 dB for a splice between SMF and bandgap-guiding HC-PCF.

Applications: an acetylene-filled PMC

To demonstrate the usefulness of our new splicing technique, we made a PMC filled with low-pressure acetylene. Our collaborators used this PMC to observe both electromagnetically induced transparency (EIT) and saturable absorption (SA) [209, 210].

The PMC was made from the 1-cell kagomé fibre. The fibre was tapered in two places approximately 6.5 m apart. One end was cleaved and spliced to SMF to provide a hermetic seal. The other end was attached to a pressure cell so that it could be evacuated and filled with acetylene to the required pressure. The helium technique [212] was used to prevent the ingress of air while the second taper was cleaved and spliced. The splice losses were non-reciprocal (presumably due to multimode propagation in the kagomé fibre), and the lowest PMC losses were achieved when the output splice was to a large-core multimode fibre. The total PMC insertion loss was 6 dB, including the loss from the fibre and both of the splices (but not considering insertion back into a single mode system).

Two tunable external-cavity diode lasers (ECDLs) provided the probe and coupling beams necessary to enable the observation of EIT, Fig. A.3(a). The beams are combined using a 50/50 coupler spliced to the PMC. A typical probe trace is shown in Fig. A.3(a) for a coupling laser power of 250 mW. The EIT feature has a height of 16% and a FWHM of 25 MHz. The graphs of Fig. A.3(b) show the evolution of the EIT feature's height and width with coupling laser power for 1-cell kagomé fibre and (for comparion) 7-cell bandgap fibre. Considerably narrower and higher features are achieved in the kagomé fibre compared to those observed in the smaller core of the bandgap fibre.

In a slightly different configuration, Fig. A.4, the reflected probe technique [218] was used to create a sub-Doppler SA feature, reducing the number of components and the alignment required. This feature had a line width of 110 MHz, measured from the trace in Fig. A.4. Such a large line width compared to the 20 MHz linewidth expected for this core diameter and gas pressure [218] is due

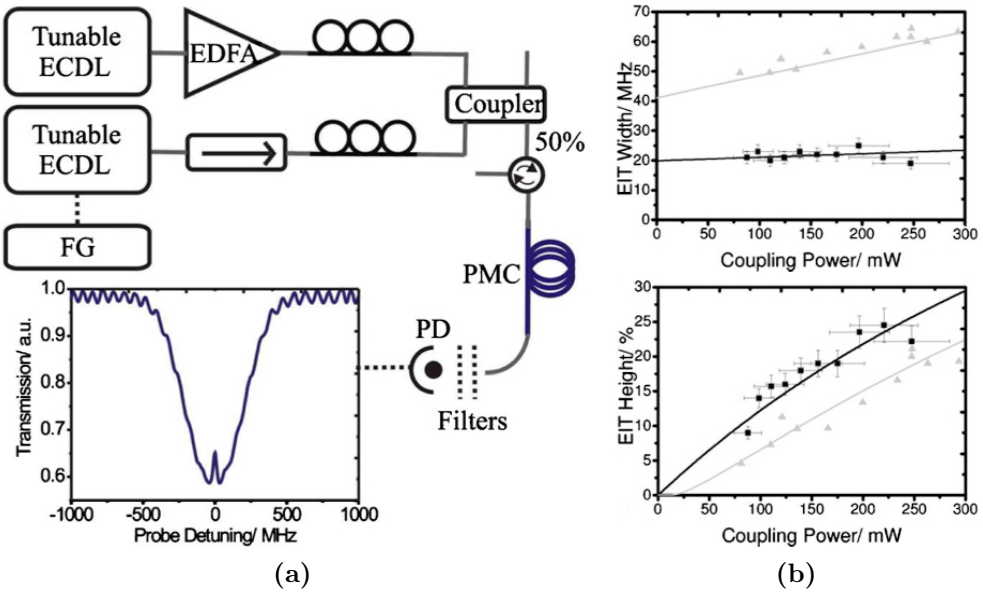

Figure A.3: (a) Experimental setup for observing EIT in our PMC: EDFA, erbium-doped fibre amplifier; FG, function generator; PD, photodiode. (b) EIT feature width and height as a function of laser coupling power. Experimental 1-cell kagomé fibre data (black points) are compared to experimental 7-cell bandgap data (grey points) and theoretical fits (black and grey lines respectively).

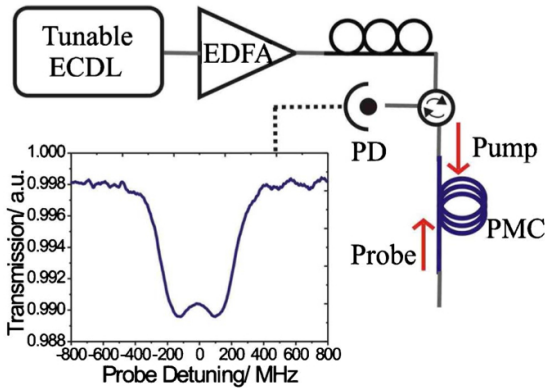

Figure A.4: Experimental setup used to create and observe SA in our PMC for a pump power of 250 mW in line P25 of the acetylene $\nu_1 + \nu_3$ spectrum. Probe beam is created through reflection from the second kagomé fibre to SMF splice.

to power broadening, which is induced by the use of extremely high pump power of 250 mW. This power level was required to have a measurable probe signal because of the very small contrast (1%) of the probed acetylene absorption line on one hand and the strong etalon effect on the other hand. Nevertheless, this etalon effect could be solved by an angled splice at the input [219], and the SA generation indicates clearly the judiciousness of such a PMC.

A.2.2 Micromirrors

The core of kagomé fibre is large enough that a tapered piece of SMF will fit inside of the core, pictured schematically in Fig. A.5(a). For the experiments described in this section, we used the 1-cell kagomé fibre shown in Fig. A.5(b), with a 136 µm OD and a 23–26 µm core diameter. Fig. A.5(c) shows an SMF taper being inserted several millimetres into the core of the kagomé fibre and fixed in place by a cladding collapse. The kagomé fibre and cleaved SMF taper were positioned using the alignment stages of a Vytran splicer. Then, the stages were used to push the taper tip gently into the hollow core. The stages were move to close to the end of their travel, to get the taper tip as deep into the core as possible. Finally, we used the heating element of the fusion splicer to collapse the cladding, holding the taper tip firmly in place. We initially conceived this type of fibre junction as a method to improve the coupling between SMF and kagomé fibre by increasing the mode overlap.

Fig. A.6(a) is a plot of the mode-field size versus the dimension of a tapered fibre, from [216]. For tapered fibres around 20 µm, the mode fills more than half of the taper waist. Fig. A.6(b, c, & d) are the measured near-field mode-images at 1550 nm of regular SMF, the 1-cell kagomé fibre, and the tapered SMF. The size of the mode in the tapered fibre is much closer to that in the kagomé fibre than in the untapered fibre, so the coupling loss should be less.

The tapered fibre tip is inserted far enough into the kagomé fibre that the heat used to collapse the cladding has no effect on it other than to anchor it in place. This means that the end of the tapered fibre can be coated with thin metal films and hermetically sealed in place without degrading the reflection from the surface. The reflection from the tip can be controlled using different coatings and

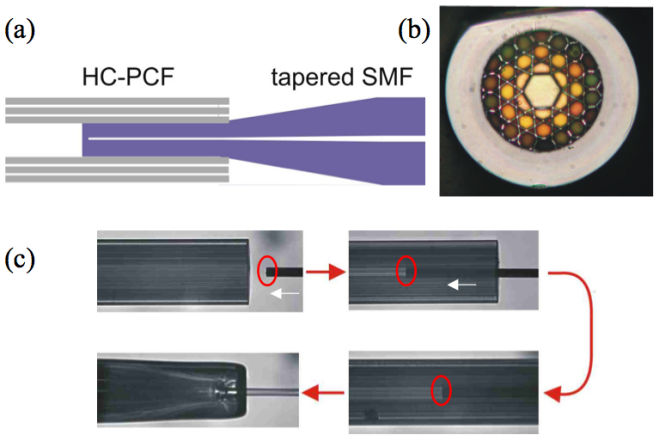

Figure A.5: (a) Schematic of the micromirror concept. (b) Optical micrograph of the 1-cell kagomé fibre. (c) Micromanipulation of the mirror (position circled) as it is inserted into the kagomé fibre core.

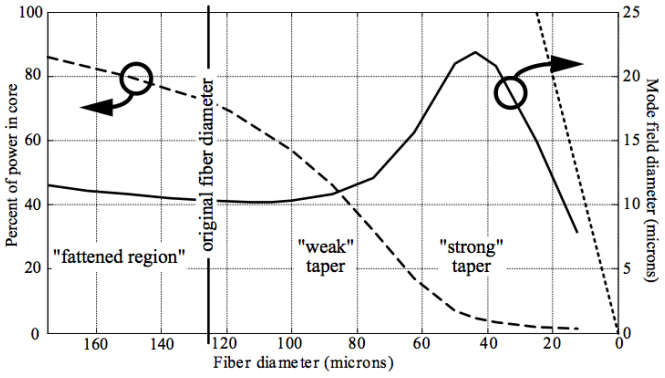

(a)

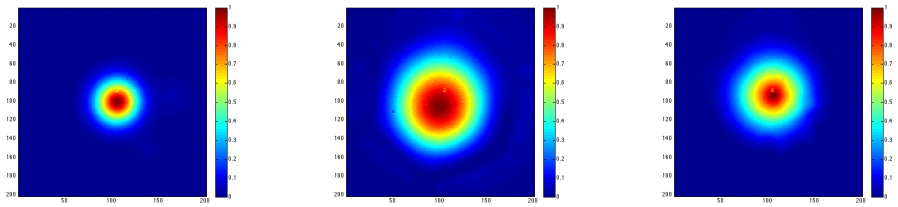

(b) (c) (d)

Figure A.6: (a) The mode-field diameter and fraction of power in the core for different sized tapers, from [216, p. 223]. (b, c & d) Measured near-field images of the mode-field at the output of regular SMF, the 1-cell kagomé fibre from Fig. A.5(b), and an SMF taper/micromirror. The dashed line is the outer diameter of the taper for easy comparison.

thicknesses. In fact, even the uncoated fibre has a 4% reflection, which can be used for making a cavity (discussed later in this section). The most intriguing uses arise from this reflection (combined with the improved coupling efficiency), so we have named this component a micromirror.

To calibrate the reflectivity of thin-film coatings, light from a continuous wave laser (1540 nm) is launched, via a fibre circulator, into the input of the kagomé fibre which is angle-spliced beforehand to untapered SMF to reduce Fresnel reflection at this junction [219] (Fig. A.7(a)). The reference reflected power is measured at the third port of the circulator when an uncoated, untapered piece of SMF-28 is butt-coupled to the output of the kagomé fibre. The uncoated SMF-28 is then replaced by silver-coated untapered and tapered SMF-28 samples. The transmission through the mirror junction is measured using a photodetector at the SMF-28 output.

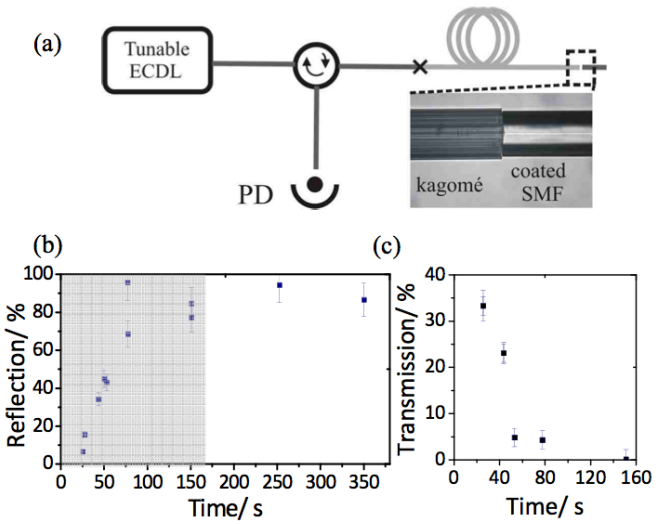

Figure A.7: (a) Set-up for reflection measurements. (b & c) Reflection and transmission from the SMF-28, as functions of coating time.

By evaluating the losses in our system, we estimate that the butt-coupled untapered and uncoated SMF reflected 3.4% of the HC-PCF output power back into the core. Using this estimate, as a reference we deduce that a maximum reflectivity of 95% was achieved using untapered silver coated SMF, butt-coupled to kagomé HC-PCF. This is indicated in Fig. A.7(b), which shows that the reflectivity increases with coating evaporation time until a plateau occurs at a time of

100 s corresponding to an estimated film thickness of ~ 20 nm. The corresponding transmission measurements are shown in Fig. A.7(c) and indicate significant scattering loss due to the coating deposition. This can be attributed to our very basic coating procedure and could be overcome by using existing fibre-tip coating procedures (e.g. [220]). Upon splicing, the reflection dramatically decreased to 2%, well *below* the reflection achieved with an uncoated fibre. This is due to degradation of the silver coating during the splicing process.

For the tapered fibre, the maximum reflectivity achieved was 85% upon silver-coating. This was measured with the micromirror being inserted ~ 1 mm into the kagomé fibre core. The reduction in reflectivity of a taper compared to the coated untapered fibres is believed to be due to two main sources. Firstly, the surface roughness of the cleaved taper is likely to be higher than the roughness of cleaved untapered SMF, because of water penetration during the taper process and the mechanical fragility of the taper. To eliminate the water produced by the taper rig flame, carbon monoxide can be burnt with oxygen as a dry heat source [221]. Secondly, an untapered fibre reflects all the light coming out of the kagomé fibre, including higher order and cladding modes, whereas the taper will favourably reflect the fundamental core mode.

Upon fusion, the reflectivity of the (coated) micromirror remained unchanged indicating that in this configuration there is no degradation to the silver coating when the taper is fused in place. These results show that using a micromirror the range of possible reflective coatings can be expanded in order to maximize the reflectivity from the end face of the micromirror.

Applications: SA and cavity formation in kagomé PCF

The appeal of a micromirror should be obvious from the saturable absorption experiment discussed in sec. A.2.1. Increasing the reflected probe means that the power and associated power broadening are significantly reduced. We used a micromirror with a 25% reflection to provide the probe for the experiment in Fig. A.8. The fibre collapse around the micromirror was left incomplete to allow evacuation and acetylene loading into the kagomé fibre core. The plotted transmission is for a pump power of 97 mW and an acetylene pressure of 0.5 mbar.

The sub-Doppler feature width is 25 MHz, which is similar to the previously published results for a fibre of similar core size [222]. The compactness of this SA device could further be enhanced by using the helium loading technique [212] to remove the kagomé fibre from the vacuum system and fully collapse the core around the micromirror.

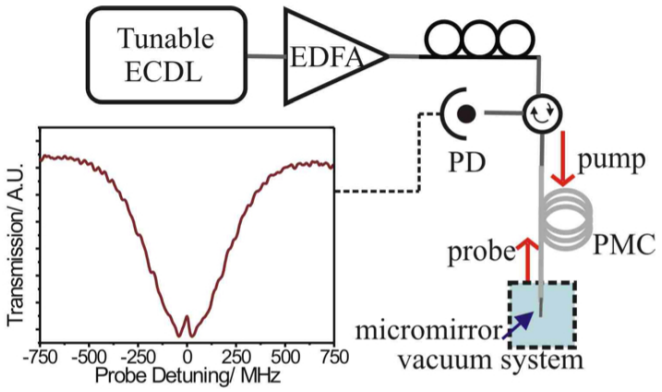

Figure A.8: The experimental setup used to obtain saturable absorption using a micromirror to provide the reflected probe beam. The sub-Doppler feature observed has a FWHM of 25 MHz.

We used two uncoated micromirrors to form a microcavity within a 3 mm length section of the kagomé fibre. The micromirrors were inserted into each end of the kagomé fibre core and the cavity length was adjusted using the alignment features of the Vytran splicer. One of the micromirrors (the back micromirror) was fixed in place by collapsing the HC-PCF as described previously, whilst the other (front) mirror was kept freely running so the cavity length could be scanned over several values. The position of the front micromirror could be tuned within the alignment range of the splicer. An optical image of a microcavity formed in this way with a cavity length of 340 μm is shown in Fig. A.9(a). The end faces of the micromirrors are clearly visible.

The cavity spectral characteristics were measured in reflection and recorded on an optical spectrum analyzer (OSA) with a resolution of 0.02 nm. The reflection spectrum for this cavity is shown in Fig. A.9(b). This was obtained by recording the optical output from a fibre circulator, which was spliced to the end of the non-tapered section of the micromirror. Fig. A.9(c) shows the reflection spectrum from a cavity of only 30 μm at a resolution of 0.5 nm. Cavity lengths

were initially determined through measurements taken with an optical microscope and subsequently corroborated using the cavity free spectral range.

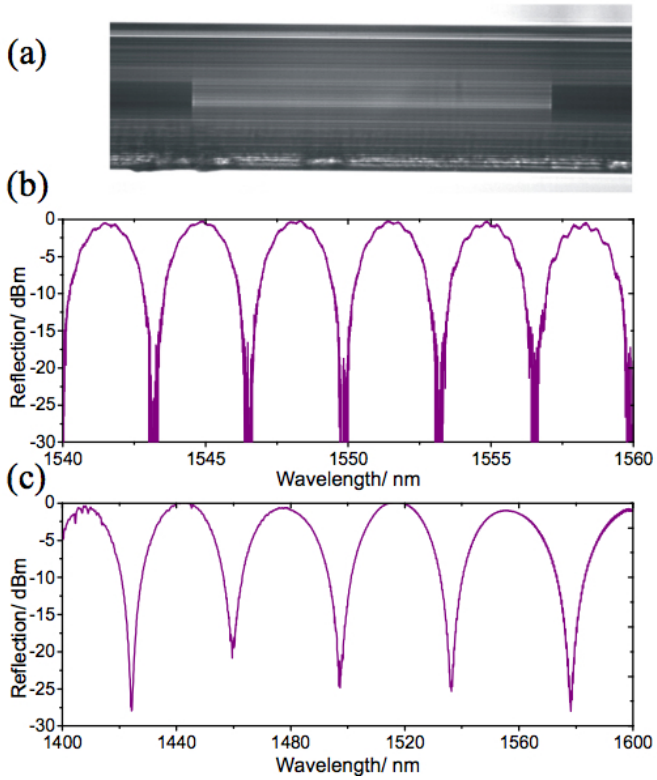

Figure A.9: (a) Example cavity formed from two uncoated micromirrors inserted into the core of the kagomé fibre, cavity length $L = 340\,\mu m$. (b) Reflection from cavity shown in (a). (c) Reflection from cavity with $L \approx 30\,\mu m$. (Note the different wavelength scales.) Traces recorded on OSA and normalized using light source spectrum

The experimental spectrum shows fringe contrasts as high as 28 dB (i.e. 0.998), which is the best performance reported so far for a cavity formed using reflections at a silica-air interface [223] and, to the best of our knowledge, is the highest contrast demonstrated in a HC-PCF cavity. This extremely high fringe visibility is indicative of the excellent mode field matching at the cavity interfaces. Having micromirrors with better quality metal films so that the scattering component is reduced could lead to very high finesse cavities with applications in cavity quantum electrodynamics (CQED) [220] or sensing [223].

A.3 Acetylene absorption in aerogel

When some gas molecules are sufficiently confined, then quantum mechanical effects can alter the absorption spectrum so that they have very narrow spectral features [224]. Our collaborators suggested measuring the spectrum of acetylene in bulk aerogel, to see if confining the gas in the aerogel's ~ 40 nm pores caused a change in the shape of the absorption lines. In order to do this, we made a rod of aerogel that fitted inside their windowed vacuum chamber. The chamber and aerogel were evacuated, and then acetylene was added to a pressure of 53 mbar. An ECDL was tuned to the R11 (12699.91 /cm [225]) absorption line of acetylene, and the output was collimated and directed through the chamber.

The transmission spectrum of the acetylene was measured with the beam going through just the vacuum chamber, and is plotted as the red curve in Fig. A.10. The beam was then realigned so that it passed through the aerogel in the chamber, and the measured transmission spectrum is plotted as the black curve on the same figure. The curves have been shifted on the transmission axis so that the peaks overlap. The spectral line shape measured through the aerogel is narrower than that measured through just the chamber, presumably due to the gas being confined in the pores. Therefore, adding acetylene to aerogel-filled hollow-core fibres could lead to enhanced PMCs with even narrower spectral features.

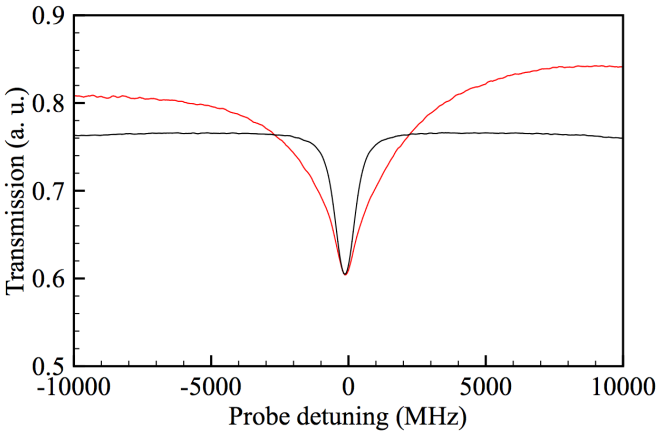

Figure A.10: The spectrum of a single acetylene absorption line measured with 53 mbar pressure in a vacuum chamber (red line) and in an aerogel (black line).

A.4 Conclusion

We have made a low loss, low pressure, large-core kagomé fibre photonic microcell. Fibre tapering overcame the outer diameter mismatch and minimised coupling losses between the kagomé fibre and the SMF and MMF at the input and output. Tapering reduced the input coupling loss by more than 3× to 0.6 dB. Such a PMC was used to demonstrate the advantages of large-pitch kagomé fibre microcells for reducing the contribution of the core walls on the width of any spectral features produced by EIT or saturable absorption spectroscopy. The narrow spectral features produced in these PMCs have applications in quantum optics and frequency metrology.

We have also demonstrated a technique for fabricating micromirrors using tapered SMF. The micromirrors are designed to fit inside the core of a kagomé lattice HC-PCF and are shown to be suitable for providing a controllable reflection within the HC-PCF geometry. Using a silver coated micromirror, saturable absorption spectroscopy was recorded in a compact system, similar to that in the tapered PMC, but with lower power and less power broadening. Furthermore, a low finesse microcavity was demonstrated, using two uncoated micromirrors, which had record fringe visibility. By optimizing the coating deposition procedure, it is suggested that applications in CQED and sensing are possible.

We have measured the shape of the R11 acetylene absorption line in aerogel. There is a clear perturbation to the line shape, which we believe arises from the confinement of the acetylene within the small pores of the aerogel. The main absorption of the acetylene is narrower than the same line measured with no aerogel, indicating promise for forming narrow spectral features. This narrow feature means that using some aerogel-filled fibre (chapter 8) as the basis for a PMC could have similar applications in frequency metrology and quantum optics. The coupling mechanisms we have developed in this chapter, particularly for the tapered gas cell, should help us in developing this new component.

References

[1] J Fricke. "Aerogels." *Sci. Am.*, **258**(5): p. 92 (1988).

[2] J Fricke and A Emmerling. "Aerogels - preparation, properties, applications." *Struct. Bond.*, **77**: pp. 37–87 (1992).

[3] G M Pajonk. "Transparent silica aerogels." *J. Non-Cryst. Solids*, **225**(1): pp. 307–314 (1998).

[4] A C Pierre and G M Pajonk. "Chemistry of aerogels and their applications." *Chem. Rev.*, **102**(11): pp. 4243–4265 (2002).

[5] S S Kistler. "Coherent expanded aerogels and jellies." *Nature*, **127**: p. 741 (1931).

[6] S S Kistler. "Coherent expanded aerogels." *J. Phys. Chem.*, **36**(1): pp. 52–64 (1932).

[7] J Phalippou, T Woignier and M Prassas. "Glasses from aerogels .1. the synthesis of monolithic silica aerogels." *J. Mater. Sci.*, **25**(7): pp. 3111–3117 (1990).

[8] P H Tewari, A J Hunt and K D Lofftus. "Ambient-temperature supercritical drying of transparent silica aerogels." *Mater. Lett.*, **3**(9-10): pp. 363–367 (1985).

[9] S J Teichner and G A Nicolaon. "Method of preparing inorganic aerogels." U.S. Patent 3,672,833 (1972). Orignially reported in Bull. Soc. Chim. Fr. (1968).

[10] S J Teichner, G A Nicolaon, M A Vicarini and G E E Gardes. "Inorganic oxide aerogels." *Adv. Colloid Interface Sci.*, **5**(3): pp. 245–273 (1976).

[11] M Cantin *et al.* "Silica aerogels used as Cherenkov radiators." *Nucl. Instrum. Methods*, **118**(1): pp. 177–182 (1974).

[12] J Fricke, (Editor) *Aerogels*. Springer Proc. Phys. 6. Springer, Berlin, Heidelberg, New York (1985).

[13] C J Brinker, K D Keefer, D W Schaefer and C S Ashley. "Sol-gel transition in simple silicates." *J. Non-Cryst. Solids*, **48**(1): pp. 47–64 (1982).

[14] T M Tillotson and L W Hrubesh. "Transparent ultralow-density silica aerogels prepared by a 2-step sol-gel process." *J. Non-Cryst. Solids*, **145**(1-3): pp. 44–50 (1992).

[15] L Kocon, F Despetis and J Phalippou. "Ultralow density silica aerogels by alcohol supercritical drying." *J. Non-Cryst. Solids*, **225**(1): pp. 96–100 (1998).

[16] R Deshpande, D M Smith and C J Brinker. "Preparation of high porosity xerogels by chemical surface modification." U.S. Patent 5,565,142 (1996).

[17] NASA. "Stardust website." (1999). URL `http://stardust.jpl.nasa.gov/home/index.html`.

[18] J T Seo *et al.* "Large pure refractive nonlinearity of nanostructure silica aerogel." *Appl. Phys. Lett.*, **82**(25): pp. 4444–4446 (2003).

[19] J T Seo *et al.* "Highly porous silica nanoaerogels for ultrafast nonlinear optical applications." *Advanced Si-Based Ceramics and Composites*, **287**: pp. 352–357 (2005).

[20] J T Seo *et al.* "Large optical nonlinearity of highly porous silica nanoaerogels in the nanosecond time domain." *J. Korean Phys. Soc.*, **48**(6): pp. 1395–1399 (2006).

[21] JT Seo *et al.* "Polarization-resolved cubic nonlinearity and optical power limiting of highly porous silica nanoaerogels." In *Nanotechnology Materials and Devices Conference*, vol. 1, pp. 534 –535. IEEE (2006).

[22] J K Ranka, R S Windeler and A J Stentz. "Visible continuum generation in air-silica microstructure optical fibers with anomalous dispersion at 800 nm." *Opt. Lett.*, **25**(1): pp. 25–27 (2000).

[23] J M Stone and J C Knight. "Visibly "white" light generation in uniform photonic crystal fiber using a microchip laser." *Opt. Express*, **16**(4): pp. 2670–2675 (2008).

[24] L M Tong *et al.* "Assembly of silica nanowires on silica aerogels for microphotonic devices." *Nano Lett.*, **5**(2): pp. 259–262 (2005).

[25] C J Brinker and G W Scherer. *Sol-gel science : the physics and chemistry of sol-gel processing.* Academic Press, Boston (1990).

[26] R K Iler. *Chemistry of Silica - Solubility, Polymerization, Colloid and Surface Properties and Biochemistry.* John Wiley & Sons (1979).

[27] C J Brinker. "Hydrolysis and condensation of silicates - effects on structure." *J. Non-Cryst. Solids*, **100**(1-3): pp. 31–50 (1988).

[28] J Livage and C Sanchez. "Sol-gel chemistry." *J. Non-Cryst. Solids*, **145**(1-3): pp. 11–19 (1992).

[29] W Vogelsberger *et al.* "A model for viscosity in the early stages of the sol-gel transformation." *J. Non-Cryst. Solids*, **145**(1-3): pp. 20–24 (1992).

[30] A Roig *et al.* "Silica aerogels by supercritical extraction." *J. Eur. Ceram. Soc.*, **18**(9): pp. 1141–1143 (1998).

[31] A Soleimani Dorcheh and M H Abbasi. "Silica aerogel; synthesis, properties and characterization." *J. Mater. Process. Technol.*, **199**(1-3): pp. 10–26 (2008).

[32] NASA. "Stardust news item, world record aerogel." (2002). URL `http://stardust.jpl.nasa.gov/news/news93.html`.

[33] A H Boonstra and T N M Bernards. "The dependence of the gelation time on the hydrolysis time in a 2-step SiO_2 sol-gel process." *J. Non-Cryst. Solids*, **105**(3): pp. 207–213 (1988).

[34] J Fricke and G Reichenauer. "Structural investigation of SiO_2 - aerogels." *J. Non-Cryst. Solids*, **95-6**: pp. 1135–1142 (1987).

[35] G W Scherer, J Gross, L W Hrubesh and P R Coronado. "Optimization of the rapid supercritical extraction process for aerogels." *J. Non-Cryst. Solids*, **311**(3): pp. 259–272 (2002).

[36] F Schwertfeger, W Glaubitt and U Schubert. "Hydrophobic aerogels from $Si(OMe)_4$/$MeSi(OMe)_3$ mixtures." *J. Non-Cryst. Solids*, **145**(1-3): pp. 85–89 (1992).

[37] S Haereid *et al.* "Thermal and temporal aging of TMOS-based aerogel precursors in water." *J. Non-Cryst. Solids*, **185**(3): pp. 221–226 (1995).

[38] M A Einarsrud and E Nilsen. "Strengthening of water glass and colloidal sol based silica gels by aging in TEOS." *J. Non-Cryst. Solids*, **226**(1-2): pp. 122–128 (1998).

[39] M A Einarsrud *et al.* "Strengthening of silica gels and aerogels by washing and aging processes." *J. Non-Cryst. Solids*, **285**(1-3): pp. 1–7 (2001).

[40] S Haereid, M Dahle, S Lima and M A Einarsrud. "Preparation and properties of monolithic silica xerogels from TEOS-based alcogels aged in silane solutions." *J. Non-Cryst. Solids*, **186**: pp. 96–103 (1995).

[41] S Haereid, E Nilsen and M A Einarsrud. "Properties of silica gels aged in TEOS." *J. Non-Cryst. Solids*, **204**(3): pp. 228–234 (1996).

[42] F Ehrburgerdolle, J Dallamano, E Elaloui and G M Pajonk. "Relations between the texture of silica aerogels and their preparation." *J. Non-Cryst. Solids*, **186**: pp. 9–17 (1995).

[43] NIST. "Chemical webbook: Methyl alcohol." (2008). URL `http://webbook.nist.gov/cgi/inchi/InChI=D1S/CH4O/c1-2/h2H,1H3`.

[44] G W Scherer. "Stress development during supercritical drying." *J. Non-Cryst. Solids*, **145**(1-3): pp. 33–40 (1992).

[45] S Yoda *et al.* "TiO_2-impregnated SiO_2 aerogels by alcohol supercritical drying with zeolite." *J. Non-Cryst. Solids*, **225**(1): pp. 105–110 (1998).

[46] B M Gauthier, S D Bakrania, A M Anderson and M K Carroll. "A fast supercritical extraction technique for aerogel fabrication." *J. Non-Cryst. Solids*, **350**: pp. 238–243 (2004).

[47] Mark A McHugh and Val J Krukonic. *Supercritical Fluid Extraction.* 2nd edn. Elsevier (1994).

[48] J Fricke. *The unbeatable lightness of aerogels: Take 10 parts of metal oxide, 90 parts of air, mix well - and watch industry fall upon the product with glee*, vol. 1858. New Scientist (1993).

[49] NIST. "Chemical webbook: Carbon dioxide." (2008). URL `http://webbook.nist.gov/cgi/inchi/InChI=D1S/CO2/c2-1-3`.

[50] P B Wagh *et al.* "Comparison of some physical properties of silica aerogel monoliths synthesized by different precursors." *Mater. Chem. Phys.*, **57**(3): pp. 214–218 (1999).

[51] N Husing, F Schwertfeger, W Tappert and U Schubert. "Influence of supercritical drying fluid on structure and properties of organically modified silica aerogels." *J. Non-Cryst. Solids*, **186**: pp. 37–43 (1995).

[52] M J van Bommel and A B de Haan. "Drying of silica-gels with supercritical carbon-dioxide." *J. Mater. Sci.*, **29**(4): pp. 943–948 (1994).

[53] G Rogacki and P Wawrzyniak. "Diffusion of ethanol-liquid CO_2 in silica aerogel." *J. Non-Cryst. Solids*, **186**: pp. 73–77 (1995).

[54] M J van Bommel and A B de Haan. "Drying of silica aerogel with supercritical carbon-dioxide." *J. Non-Cryst. Solids*, **186**: pp. 78–82 (1995).

[55] J M Moses, R J Willey and S Rouanet. "Development and processing of aerogels in a windowed autoclave." *J. Non-Cryst. Solids*, **145**(1-3): pp. 41–43 (1992).

[56] A V Rao, M M Kulkarni, D P Amalnerkar and T Seth. "Super-hydrophobic silica aerogels based on methyltrimethoxysilane precursor." *J. Non-Cryst. Solids*, **330**(1-3): pp. 187–195 (2003).

[57] K H Lee, S Y Kim and K P Yoo. "Low-density, hydrophobic aerogels." *J. Non-Cryst. Solids*, **186**: pp. 18–22 (1995).

[58] A V Rao and G M Pajonk. "Effect of methyltrimethoxysilane as a co-precursor on the optical properties of silica aerogels." *J. Non-Cryst. Solids*, **285**(1-3): pp. 202–209 (2001).

[59] A V Rao *et al.* "Synthesis and characterization of hydrophobic silica aerogels using trimethylethoxysilane as a co-precursor." *J. Sol-Gel Sci. Technol.*, **27**(2): pp. 103–109 (2003).

[60] A V Rao, M M Kulkarni, D P Amalnerkar and T Seth. "Surface chemical modification of silica aerogels using various alkyl-alkoxy/chloro silanes." *Appl. Surf. Sci.*, **206**(1-4): pp. 262–270 (2003).

[61] A V Rao, S D Bhagat, H Hirashima and G M Pajonk. "Synthesis of flexible silica aerogels using methyltrimethoxysilane (MTMS) precursor." *J. Colloid Interface Sci.*, **300**(1): pp. 279–285 (2006).

[62] H Yokogawa and M Yokoyama. "Hydrophobic silica aerogels." *J. Non-Cryst. Solids*, **186**: pp. 23–29 (1995).

[63] A P Rao and A V Rao. "Improvement in optical transmission of the ambient pressure dried hydrophobic nanostructured silica aerogels with mixed silylating agents." *J. Non-Cryst. Solids*, **355**(45-47): pp. 2260–2271 (2009).

[64] A P Rao, A V Rao and U K H Bangi. "Low thermalconductive, transparent and hydrophobic ambient pressure dried silica aerogels with various preparation conditions using sodium silicate solutions." *J. Sol-Gel Sci. Technol.*, **47**(1): pp. 85–94 (2008).

[65] G W Scherer, S Haereid, E Nilsen and M A Einarsrud. "Shrinkage of silica gels aged in TEOS." *J. Non-Cryst. Solids*, **202**(1-2): pp. 42–52 (1996).

[66] A Bisson *et al.* "Drying of silica gels to obtain aerogels: Phenomenology and basic techniques." *Drying Technol.*, **21**(4): pp. 593–628 (2003).

[67] H Tamon, T Sone and M Okazaki. "Control of mesoporous structure of silica aerogel prepared from TMOS." *J. Colloid Interface Sci.*, **188**(1): pp. 162–167 (1997).

[68] L W Hrubesh. "Aerogel applications." *J. Non-Cryst. Solids*, **225**(1): pp. 335–342 (1998).

[69] R Caps and J Fricke. "Infrared radiative heat-transfer in highly transparent silica aerogel." *Sol. Energy*, **36**(4): pp. 361–364 (1986).

[70] K Tajiri and K Igarashi. "The effect of the preparation conditions on the optical properties of transparent silica aerogels." *Sol. Energy Mater. Sol. Cells*, **54**(1-4): pp. 189–195 (1998).

[71] G M Pajonk, E Elaloui, B Chevalier and R Begag. "Optical transmission properties of silica aerogels prepared from polyethoxidisiloxanes." *J. Non-Cryst. Solids*, **210**(2-3): pp. 224–231 (1997).

[72] S Yoda *et al.* "Effects of ethanolamines catalysts on properties and microstructures of silica aerogels." *J. Non-Cryst. Solids*, **208**(1-2): pp. 191–198 (1996).

[73] M Rubin and C M Lampert. "Transparent silica aerogels for window insulation." *Sol. Energy Mater.*, **7**(4): pp. 393–400 (1983).

[74] A Beck *et al.* "Radiation transport and image transmission through aerogels." *J. Non-Cryst. Solids*, **186**: pp. 232–237 (1995).

[75] A Emmerling *et al.* "Relationship between optical transparency and nanostructural features of silica aerogels." *J. Non-Cryst. Solids*, **185**(3): pp. 240–248 (1995).

[76] N Husing and U Schubert. "Aerogels airy materials: Chemistry, structure, and properties." *Angew. Chem. Int. Ed.*, **37**(1-2): pp. 23–45 (1998).

[77] P Wang *et al.* "Optical investigations of silica aerogels." *J. Non-Cryst. Solids*, **145**(1-3): pp. 141–145 (1992).

[78] P Carter. "The aerogel radiator of the HERMES RICH on behalf of the HERMES collaboration." *Nucl. Instrum. Methods Phys. Res. Sec. A*, **433**(1-2): pp. 392–395 (1999).

[79] D Richter and D Lipka. "Measurement of the refractive index of silica aerogel in vacuum." *Nucl. Instrum. Methods Phys. Res. Sec. A*, **513**(3): pp. 635–638 (2003).

[80] T Bellunato *et al.* "Refractive index of silica aerogel: Uniformity and dispersion law." *Nucl. Instrum. Methods Phys. Res. Sec. A*, **595**(1): pp. 183–186 (2008).

[81] A F Danilyuk *et al.* "Recent results on aerogel development for use in Cherenkov counters." *Nucl. Instrum. Methods Phys. Res. Sec. A*, **494**(1-3): pp. 491–494 (2002).

[82] P Wang *et al.* "Density and refractive-index of silica aerogel after low-temperature and high-temperature supercritical drying and thermal treatment." *J. Phys. D: Appl. Phys.*, **27**(2): pp. 414–418 (1994).

[83] M F Villoro *et al.* "Measurement of the dispersion law for hydrophobic silica aerogel sp-25." *Nucl. Instrum. Methods Phys. Res. Sec. A*, **480**(2-3): pp. 456–462 (2002).

[84] T Bellunato *et al.* "Refractive index dispersion law of silica aerogel." *Eur. Phys. J. C*, **52**(3): pp. 759–764 (2007).

[85] G P Agarwal. *Nonlinear Fiber Optics*. 4th ed edn. Academic Press, Boston (2006).

[86] Y Nabekawa *et al.* "All-solid-state high-peak-power Ti:sapphire laser system above 5 kHz repetition rate." *Appl. Phys. B*, **70**: pp. S171–S179 (2000).

[87] M Sheik-Bahae *et al.* "Sensitive measurement of optical nonlinearities using a single beam." *IEEE J. Quantum Electron.*, **26**(4): pp. 760–769 (1990).

[88] A W Snyder and J D Love. *Optical waveguide theory*. Kluwer Academic Publishers, Boston, Dordrecht, London (2000).

[89] J A Buck. *Fundamentals of Optical Fibers*. Wiley series in pure and applied optics, 2nd edn. Wiley, Hoboken, New Jersey (2004).

[90] P St J Russell. "Photonic crystal fibers." *Science*, **299**(5605): pp. 358–362 (2003).

[91] P St J Russell. "Photonic-crystal fibers." *J. Lightwave Technol.*, **24**(12): pp. 4729–4749 (2006).

[92] F Benabid, P J Roberts, F Couny and P S Light. "Light and gas confinement in hollow-core photonic crystal fibre based photonic microcells." *J. Eur. Opt. Soc. Rapid Comm.*, **4** (2009).

[93] B Mellish. "Single mode fibre structure." Creative commons (2010). URL `http://en.wikipedia.org/wiki/File:Singlemode_fibre_structure.svg`.

[94] S G Leon-Saval *et al.* "Supercontinuum generation in submicron fibre waveguides." *Opt. Express*, **12**(13): pp. 2864–2869 (2004).

[95] T A Birks and Y W Li. "The shape of fiber tapers." *J. Lightwave Technol.*, **10**(4): pp. 432–438 (1992).

[96] T A Birks. "Fibre transitions and tapering." (2010). URL `http://www.bath.ac.uk/physics/groups/cppm/tapers.php`.

[97] J D Love. "Spot size, adiabaticity and diffraction in tapered fibers." *Electron. Lett.*, **23**(19): pp. 993–994 (1987).

[98] G Kakarantzas, L Prill-Sempere and P St J Russell. "Up-tapering of optical fibers using a conventional flame tapering rig." In *Conference on Lasers and Electro-Optics*, p. CFK2. Optical Society of America (2007).

[99] T Bricheno and A Fielding. "Stable low-loss single-mode couplers." *Electron. Lett.*, **20**(6): pp. 230–232 (1984).

[100] W J Wadsworth *et al.* "Supercontinuum generation in photonic crystal fibers and optical fiber tapers: a novel light source." *J. Opt. Soc. Am. B: Opt. Phys.*, **19**(9): pp. 2148–2155 (2002).

[101] G Brambilla *et al.* "Optical fiber nanowires and microwires: fabrication and applications." *Adv. Opt. Photon.*, **1**(1): pp. 107–161 (2009).

[102] F Xu. *Optical Fibre Nanowire Devices.* Ph.D. thesis, University of Southampton (2007).

[103] L M Tong *et al.* "Subwavelength-diameter silica wires for low-loss optical wave guiding." *Nature*, **426**(6968): pp. 816–819 (2003).

[104] R Amezcua-Correa *et al.* "Control of surface modes in low loss hollow-core photonic bandgap fibers." *Optics Express*, **16**(2): pp. 1142–1149 (2008).

[105] F Couny, F Benabid and P S Light. "Large-pitch kagomé-structured hollow-core photonic crystal fiber." *Opt. Lett.*, **31**(24): pp. 3574–3576 (2006).

[106] T A Birks, J C Knight and P St J Russell. "Endlessly single-mode photonic crystal fiber." *Opt. Lett.*, **22**(13): pp. 961–963 (1997).

[107] R F Cregan *et al.* "Single-mode photonic band gap guidance of light in air." *Science*, **285**(5433): pp. 1537–1539 (1999).

[108] J C Knight, J Broeng, T A Birks and P St J Russel. "Photonic band gap guidance in optical fibers." *Science*, **282**(5393): pp. 1476–1478 (1998).

[109] A Wang *et al.* "All solid photonic bandgap fiber based on an array of oriented rectangular high index rods." *Opt. Express*, **14**(22): pp. 10844–10850 (2006).

[110] T A Birks *et al.* "Full 2-d photonic bandgaps in silica/air structures." *Electron. Lett.*, **31**(22): pp. 1941–1943 (1995).

[111] G J Pearce, T D Hedley and D M Bird. "Adaptive curvilinear coordinates in a plane-wave solution of maxwell's equations in photonic crystals." *Phys. Rev. B*, **71**(19) (2005).

[112] F Poletti. "Hollow core fiber with an octave spanning bandgap." *Opt. Lett.*, **35**(17): pp. 2837–2839 (2010).

[113] P S Light *et al.* "Double photonic bandgap hollow-core photonic crystal fiber." *Opt. Express*, **17**(18): pp. 16238–16243 (2009).

[114] F Couny *et al.* "Generation and photonic guidance of multi-octave optical-frequency combs." *Science*, **318**(5853): pp. 1118–1121 (2007).

[115] Y Wang, F Couny, P J Roberts and F Benabid. "Low Loss Broadband Transmission in Optimized Core-shape Kagomé Hollow-core PCF." In *Conference on Lasers and Electro-Optics*, p. CPDB4. Optical Society of America (2010).

[116] C Yeh. *Handbook of fiber optics: theory and applications*. Academic Press, Boston (1990).

[117] J M Stone. *Photonic crystal fibres and their applications in the nonlinear regime*. Ph.D. thesis, University of Bath (2009).

[118] L C Klein, (Editor) *Sol-Gel technology for thin films, fibers, preforms, electronics, and specialy shapes*. Noyes Publications, Park Ridge, N.J. U.S.A. (1988).

[119] L Costa and D Kerner. "High purity glass forms by a colloidal sol-gel process." *J. Sol-Gel Sci. Technol.*, **26**(1-3): pp. 63–66 (2003).

[120] J B MacChesney *et al.* "Optical fibres using sol-gel silica overcladding tubes." *Electron. Lett.*, **33**(18): pp. 1573–1574 (1997).

[121] J B MacChesney *et al.* "Optical fibers by a hybrid process using sol-gel silica overcladding tubes." *J. Non-Cryst. Solids*, **226**(3): pp. 232–238 (1998).

[122] M Arimondi and G S Roba. "Process for manufacturing a microstructured optical fibre." U.S. Patent 7,779,651 (2001).

[123] Evonik Industries AG. "AEROSIL® homepage." (2010). URL `http://www.aerosil.com/product/aerosil/en/Pages/default.aspx`.

[124] D Kominsky. *Development of Random Hole Optical Fiber and Crucible Technique Optical Fibers*. Ph.D. thesis, Virginia Polytechnic Institute and State University (2005).

[125] G A Sprehn, L W Hrubesh, J F Poco and P H Sandler. "Aerogel-clad optical fiber." U.S. Patent 5,684,907 (1997).

[126] P H Sandler, C J Hailey, G Sprehn and K P Ziock. "GRABIT: A large-area, broad-bandwidth, gamma-ray imaging spectrometer for astrophysics." *IEEE Trans. Nucl. Sci.*, **43**(1): pp. 278–282 (1996).

[127] K Tsubaki *et al.* "Optical fiber." U.S. Patent 5,790,742 (1996).

[128] H Yokogawa *et al.* "Side-face illuminating optical fiber." U.S. Patent 6,154,595 (1998).

[129] H R Fraval and C J Brinker. "Fluid light guide having hydrophobic aerogel cladding layer." U.S. Patent 6,984,093 (2001).

[130] E Mazur, L M Tong and R R Gattass. "Subwavelength-diameter silica wires for low-loss optical waveguiding." U.S. Patent 7,620,281 (2008).

[131] G Kakarantzas, S G Leon-Saval, T A Birks and P St J Russell. "Low-loss deposition of solgel-derived silica films on tapered fibers." *Opt. Lett.*, **29**(7): pp. 694–696 (2004).

[132] R Williams. *Design of SFE rig for the drying of an aerogel*. Master's thesis, University of Bath (2006).

[133] S G Leon-Saval. "Notes on making aerogel at the University of Bath." (2007). Personal communication.

[134] T A Birks *et al.* "Aerogels in fibre optics." EPSRC Grant EP/F018622/1 (2007).

[135] J G Liu *et al.* "Critical properties of binary and ternary mixtures of hexane plus methanol, hexane plus carbon dioxide, methanol plus carbon dioxide, and hexane plus carbon dioxide plus methanol." *J. Chem. Eng. Data*, **48**(6): pp. 1610–1613 (2003).

[136] E Hecht. *Optics*. 4th ed edn. Pearson Education, Inc. as Addison Wesley, San Francisco (2002).

[137] W Theiss. "Optical properties of porous silicon." *Surf. Sci. Rep.*, **29**(3-4): pp. 95–192 (1997).

[138] R T Bise and D J Trevor. "Surface absorption in microstructured optical fibers." vol. 1800, p. 2 (2004).

[139] D Wolverson. "Resonant absorption of molecules under excitation with visible light." (2010). Personal communication.

[140] C F Bohren and D R Huffman. *Absorption and Scattering of Light by Small Particles*. Wiley Inter-Science, New York, U. S. A. (1998).

[141] P Bhupathi *et al.* "Aerogel waveplates." *Opt. Express*, **17**(13): pp. 10599–10605 (2009).

[142] A Beck, R Caps and J Fricke. "Scattering of visible-light from silica aerogels." *J. Phys. D: Appl. Phys.*, **22**(6): pp. 730–734 (1989).

[143] J Pollanen *et al.* "Globally anisotropic high porosity silica aerogels." *J. Non-Cryst. Solids*, **354**(40-41): pp. 4668–4674 (2008).

[144] R Dorn, S Quabis and G Leuchs. "Sharper focus for a radially polarized light beam." *Phys. Rev. Lett*, **91**(23) (2003).

[145] N Leventis *et al.* "Durable modification of silica aerogel monoliths with fluorescent 2,7-diazapyrenium moieties. sensing oxygen near the speed of open-air diffusion." *Chem. Mater.*, **11**(10): pp. 2837–2845 (1999).

[146] Stefan A Maier. *Plasmonics: fundamentals and applications*. 1st edn. Springer, New York (2007).

[147] S K Eah *et al.* "Plasmon scattering from a single gold nanoparticle collected through an optical fiber." *J. Non-Cryst. Solids*, **86**(3) (2005).

[148] J A Creighton, C G Blatchford and M G Albrecht. "Plasma resonance enhancement of Raman-scattering by pyridine adsorbed on silver or gold sol particles of size comparable to the excitation wavelength." *J. Chem. Soc., Faraday Trans 2*, **75**: pp. 790–798 (1979).

[149] J F Li *et al.* "Shell-isolated nanoparticle-enhanced Raman spectroscopy." *Nature*, **464**(7287): pp. 392–395 (2010).

[150] R F Souza *et al.* "Nonlinear optical properties of Au nanoparticles colloidal system: Local and nonlocal responses." *Appl. Phys. Lett.*, **92**(20) (2008).

[151] D D Smith, L A Snow, L Sibille and E Ignont. "Tunable optical properties of metal nanoparticle sol-gel composites." *J. Non-Cryst. Solids*, **285**(1-3): pp. 256–263 (2001).

[152] M Haruta. "Size- and support-dependency in the catalysis of gold." *Catal. Today*, **36**(1): pp. 153–166 (1997).

[153] T Yazawa *et al.* "Preparation and optical property of monolithic silica-gel uniformly dispersed with gold colloid from aqueous-solution." *J. Non-Cryst. Solids*, **170**(1): pp. 105–108 (1994).

[154] Y Tai *et al.* "Preparation of gold cluster/silica nanocomposite aerogel via spontaneous wet-gel formation." *Adv. Mat.*, **13**(21): pp. 1611–+ (2001).

[155] M L Anderson *et al.* "Colloidal gold aerogels: Preparation, properties, and characterization." *Langmuir*, **15**(3): pp. 674–681 (1999).

[156] C A Morris *et al.* "Silica sol as a nanoglue: Flexible synthesis of composite aerogels." *Science*, **284**(5414): pp. 622–624 (1999).

[157] G Reichenauer and G W Scherer. "Nitrogen sorption in aerogels." *J. Non-Cryst. Solids*, **285**(1-3): pp. 167–174 (2001).

[158] P B Johnson and R W Christy. "Optical-constants of noble-metals." *Phys. Rev. B*, **6**(12): pp. 4370–4379 (1972).

[159] D D Smith, L Sibille, R J Cronise and D A Noever. "Surface plasmon resonance evaluation of colloidal silver aerogel filters." *J. Non-Cryst. Solids*, **225**(1): pp. 330–334 (1998).

[160] D D Smith *et al.* "Noble metal immersion spectroscopy of silica alcogels and aerogels." *J. Porous Mater.*, **7**(4): pp. 499–508 (2000).

[161] Matthew Pelton, Javier Aizpurua and Garnett Bryant. "Metal-nanoparticle plasmonics." *Laser Photonics Rev.*, **2**(3): pp. 136–159 (2008).

[162] F Tam, C Moran and N J Halas. "Geometrical parameters controlling sensitivity of nanoshell plasmon resonances to changes in dielectric environment." *J. Phys. Chem. B*, **108**(45): pp. 17290–17294 (2004).

[163] C L Nehl, H W Liao and J H Hafner. "Optical properties of star-shaped gold nanoparticles." *Nano Lett.*, **6**(4): pp. 683–688 (2006).

[164] K Aslan, J R Lakowicz, H Szmacinski and C D Geddes. "Metal-enhanced fluorescence solution-based sensing platform." *J. Fluorescence*, **14**(6): pp. 677–679 (2004).

[165] S Murai, K Fujita, K Nakanishi and K Hirao. "Fabrication of dye-infiltrated macroporous silica for laser amplification." *J. Non-Cryst. Solids*, **345**: pp. 438–442 (2004).

[166] M Sheik-Bahae, A A Said and E W van Stryland. "High-sensitivity, single-beam n_2 measurements." *Opt. Lett.*, **14**(17): pp. 955–957 (1989).

[167] P Urquhart. "Review of rare-earth doped fiber lasers and amplifiers." *IEEE Proceedings – J. Optoelectronics*, **135**(6): pp. 385–402 (1988).

[168] A J Berry and T A King. "Characterization of doped sol-gel derived silica hosts for use in tunable glass lasers." *J. Phys. D: Appl. Phys.*, **22**(10): pp. 1419–1422 (1989).

[169] J E Townsend, S B Poole and D N Payne. "Solution-doping technique for fabrication of rare-earth-doped optical fibers." *Electron. Lett.*, **23**(7): pp. 329–331 (1987).

[170] E J A Pope and J D MacKenzie. "Nd-doped silica glass 1. structural evolution in the sol-gel state." *J. Non-Cryst. Solids*, **106**(1-3): pp. 236–241 (1988).

[171] W V Moreshead, J L R Nogues and R H Krabill. "Preparation, processing, and fluorescence characteristics of neodymium-doped silica glass prepared by the sol-gel process." *J. Non-Cryst. Solids*, **121**(1-3): pp. 267–272 (1990).

[172] S Grandi and L Costa. "Lanthanide-doped $SiO_2-Al_2O_3$ aerogels and densified glasses." *J. Non-Cryst. Solids*, **225**(1): pp. 141–145 (1998).

[173] J Bouaziz, D Bourret, A Sivade and C Grill. "Phase-separation during isothermal sintering of (1-x)SiO_2-xLn_2O_3 aerogels." *J. Non-Cryst. Solids*, **145**(1-3): pp. 71–74 (1992).

[174] T M Tillotson, W E Sunderland, I M Thomas and L W Hrubesh. "Synthesis of lanthanide and lanthanide-silicate aerogels." *J. Sol-Gel Sci. Technol.*, **1**: pp. 241–249 (1994). 10.1007/BF00486167.

[175] W Xu *et al.* "Green up-conversion emission from Er^{3+} ion doped into sol-gel silica glasses under red-light (647.1 nm) excitation." *J. Phys. Chem.*, **99**(13): pp. 4447–4450 (1995).

[176] W Strek *et al.* "Spectroscopic properties of erbium doped silica glasses obtained by sol-gel method." *J. Alloys Compd.*, **275**: pp. 420–423 (1998).

[177] T Woignier *et al.* "The use of silica aerogels as host matrices for chemical species - Different ways to control the permeability and the mechanical properties." *J. Non-Cryst. Solids*, **350**: pp. 299–307 (2004).

[178] A Biswas *et al.* "Er^{3+}-doped multicomponent sol-gel-processed silica glass for optical signal amplification at 1.5 μm." *Appl. Phys. Lett.*, **82**(15): pp. 2389–2391 (2003).

[179] S A C Glauser and H W H Lee. *Aerogels - A New Material for Emissive Display Applications*. Tech. rep., Lawrence Livermore National Laboratory (1997).

[180] H M Pask *et al.* "Ytterbium-doped silica fiber lasers - versatile sources for the 1-1.2 μm region." *Ieee Journal of Selected Topics In Quantum Electronics*, **1**(1): pp. 2–13 (1995).

[181] C Florea and K A Winick. "Ytterbium-doped glass waveguide laser fabricated by ion exchange." *J. Lightwave Technol.*, **17**(9): pp. 1593–1601 (1999).

[182] Y Tai, M Watanabe, J Murakami and K Tajiri. "Composite formation of thiol-capped au nanoparticles and mesoporous silica prepared by a sol-gel method." *J. Mater. Sci.*, **42**(4): pp. 1285–1292 (2007).

[183] A V Deshpande, L V Jathar and J R Rane. "Effect of method of preparation and drying time on photophysical properties of coumarin 1 laser dye embedded in hcl catalysed sol-gel glasses." *J. Non-Cryst. Solids*, **356**(1): pp. 1–7 (2010).

[184] G E Malashkevich *et al.* "Influence of freon heat treatment on optical properties of Er-doped silica-gel glasses." *Acta Phys. Pol. A*, **90**(2): pp. 419–421 (1996).

[185] Na Lou *et al.* "Embedded optical micro/nano-fibers for stable devices." *Opt. Lett.*, **35**(4): pp. 571–573 (2010).

[186] G Vienne, Y Li and L Tong. "Effect of host polymer on microfiber resonator." *IEEE Photonics Technol. Lett.*, **19**(17-20): pp. 1386–1388 (2007).

[187] M Sumetsky. "Basic elements for microfiber photonics: Micro/nanofibers and microfiber coil resonators." *J. Lightwave Technol.*, **26**(1-4): pp. 21–27 (2008).

[188] F Xu and G Brambilla. "Preservation of micro-optical fibers by embedding." *Jpn. J. Appl. Phys.*, **47**(8): pp. 6675–6677 (2008).

[189] M R Miner, B Hosticka and P M Norris. "The effects of ambient humidity on the mechanical properties and surface chemistry of hygroscopic silica aerogel." *J. Non-Cryst. Solids*, **350**: pp. 285–289 (2004).

[190] I J Wilkinson. "Wear-out failure-mechanism in fused-fiber couplers." *Electron. Lett.*, **29**(12): pp. 1137–1139 (1993).

[191] I Plitz and M P Dugan. "Reliability concerns addressing the use of structural adhesives in optical devices." In *Proc. 9th Annual NFOEC*, pp. 295–303 (1993).

[192] C M Fitzgerald, C V Cryan, K P Oakley and CD Hussey. "All-silica pacakge for tapered couplers." *Electron. Lett.*, **27**(25): pp. 2329–2331 (1991).

[193] H S Daniel, D R Moore and V J Tekippe. "A glass solder process for packaging fibre optic components." In *Proc. EFOC&N*, pp. 126–129 (1994).

[194] F Xu and G Brambilla. "Demonstration of a refractometric sensor based on optical microfiber coil resonator." *Appl. Phys. Lett.*, **92**(10) (2008).

[195] T A Birks, W J Wadsworth and P St J Russell. "Supercontinuum generation in tapered fibers." *Opt. Lett.*, **25**(19): pp. 1415–1417 (2000).

[196] Min K Yang, Roger H French and Edward W Tokarsky. "Optical properties of teflon® af amorphous fluoropolymers." *J. Micro/Nanolithog. MEMS MOEMS*, **7**(3) (2008).

[197] F Benabid, J C Knight, G Antonopoulos and P S Russell. "Stimulated raman scattering in hydrogen-filled hollow-core photonic crystal fiber." *Science*, **298**(5592): pp. 399–402 (2002).

[198] S Ghosh, J E Sharping, D G Ouzounov and A L Gaeta. "Resonant optical interactions with molecules confined in photonic band-gap fibers." *Phys. Rev. Lett*, **94**(9) (2005).

[199] F Benabid, P S Light, F Couny and P St J Russell. "Electromagnetically-induced transparency grid in acetylene-filled hollow-core PCF." *Opt. Express*, **13**(15): pp. 5694–5703 (2005).

[200] F Benabid *et al.* "Compact, stable and efficient all-fibre gas cells using hollow-core photonic crystal fibres." *Nature*, **434**(7032): pp. 488–491 (2005).

[201] K Nielsen *et al.* "Selective filling of photonic crystal fibres." *J. Opt. A: Pure Appl. Opt.*, **7**(8): pp. L13–L20 (2005).

[202] S Yiou *et al.* "Stimulated Raman scattering in an ethanol core microstructured optical fiber." *Opt. Express*, **13**(12): pp. 4786–4791 (2005).

[203] M Vieweg, T Gissibl and H Giessen. "Selectively filled photonic crystal fibers." In *Conference on Lasers and Electro-Optics*, p. CThB2 (2010).

[204] L M Xiao *et al.* "Fabrication of selective injection microstructured optical fibers with a conventional fusion splicer." *Opt. Express*, **13**(22): pp. 9014–9022 (2005).

[205] Y Y Huang, Y Xu and A Yariv. "Fabrication of functional microstructured optical fibers through a selective-filling technique." *Appl. Phys. Lett.*, **85**(22): pp. 5182–5184 (2004).

[206] A Witkowska *et al.* "All-fiber anamorphic core-shape transitions." *Opt. Lett.*, **31**(18): pp. 2672–2674 (2006).

[207] M Yan and P Shum. "Guidance varieties in photonic crystal fibers." *J. Opt. Soc. Am. B: Opt. Phys.*, **23**(8): pp. 1684–1691 (2006).

[208] M Perrin, Y Quiquempois, G Bouwmans and M Douay. "Coexistence of total internal reflexion and bandgap modes in solid core photonic bandgap fibre with intersticial air holes." *Opt. Express*, **15**(21): pp. 13783–13795 (2007).

[209] S E Harris, J E Field and A Imamoglu. "Nonlinear optical processes using electromagnetically induced transparency." *Phys. Rev. Lett*, **64**(10): pp. 1107–1110 (1990).

[210] M de Labachelerie, K Nakagawa and M Ohtsu. "Ultranarrow ($^{13}C_2H_2$) saturated-absorption lines at 1.5 μm." *Opt. Lett.*, **19**(11): pp. 840–842 (1994).

[211] K Knabe *et al.* "10 kHz accuracy of an optical frequency reference based on ($^{12}C_2H_2$)-filled large-core kagomé photonic crystal fibers." *Opt. Express*, **17**(18): pp. 16017–16026 (2009).

[212] P S Light, F Couny and F Benabid. "Low optical insertion-loss and vacuum-pressure all-fiber acetylene cell based on hollow-core photonic crystal fiber." *Opt. Lett.*, **31**(17): pp. 2538–2540 (2006).

[213] F Couny, P S Light, F Benabid and P St J Russell. "Electromagnetically induced transparency and saturable absorption in all-fiber devices based on ($^{12}C_2H_2$)-filled hollow-core photonic crystal fiber." *Opt. Comm.*, **263**(1): pp. 28–31 (2006).

[214] J E M Haverkort, H G C Werij and J P Woerdman. "Numerical study of light-induced drift of Na in noble-gases." *Phys. Rev. A*, **38**(8): pp. 4054–4063 (1988).

[215] N V Wilding, P S Light, F Couny and F Benabid. "Experimental comparison of electromagnetically induced transparency in acetylene-filled kagomé and triangular lattice hollow core photonic crystal fiber." In *Conference on Lasers and Electro-Optics*, pp. 1 –2 (2008).

[216] A D Yablon. *Optical Fiber Fusion Splicing*, vol. 103 of *Springer series in optical sciences*. Springer, Berlin Heidelberg New York (2005).

[217] L M Xiao, W Jin and M S Demokan. "Fusion splicing small-core photonic crystal fibers and single-mode fibers by repeated arc discharges." *Opt. Lett.*, **32**(2): pp. 115–117 (2007).

[218] K Knabe, R Thapa, B R Washburn and K L Corwin. "Reflected pump technique for saturated absorption spectroscopy inside photonic bandgap fibers." In *Conference on Lasers and Electro-Optics*, pp. 1 –2 (2007).

[219] F Couny, F Benabid and P S Light. "Reduction of Fresnel back-reflection at splice interface between hollow core PCF and single-mode fiber." *IEEE Photonics Technol. Lett.*, **19**(13-16): pp. 1020–1022 (2007).

[220] D Hunger *et al.* "A fiber Fabry-Perot cavity with high finesse." *New J. Phys.*, **12** (2010).

[221] T A Birks, R P Kenny, K P Oakley and C V Cryan. "Elimination of water peak in optical fiber taper components." *Electron. Lett.*, **26**(21): pp. 1761–1762 (1990).

[222] R Thapa *et al.* "Saturated absorption spectroscopy of acetylene gas inside large-core photonic bandgap fiber." *Opt. Lett.*, **31**(16): pp. 2489–2491 (2006).

[223] Y J Rao *et al.* "Micro Fabry-Perot interferometers in silica fibers machined by femtosecond laser." *Opt. Express*, **15**(21): pp. 14123–14128 (2007).

[224] R H Dicke. "The effect of collisions upon the doppler width of spectral lines." *Phys. Rev.*, **89**(2): pp. 472–473 (1953).

[225] D Biswas, B Ray, S Dutta and P N Ghosh. "Diode laser spectroscopic measurement of line shape of $(\nu(1) + 3\nu(3))$ band transitions of acetylene." *Appl. Phys. B*, **68**(6): pp. 1125–1130 (1999).